Final Report On Project

Single-stage Earth-orbital Reusable Vehicle

SPACE SHUTTLE FEASIBILITY STUDY

volume 2
contract NAS8-26341
aerodynamic model testing
june 30, 1971

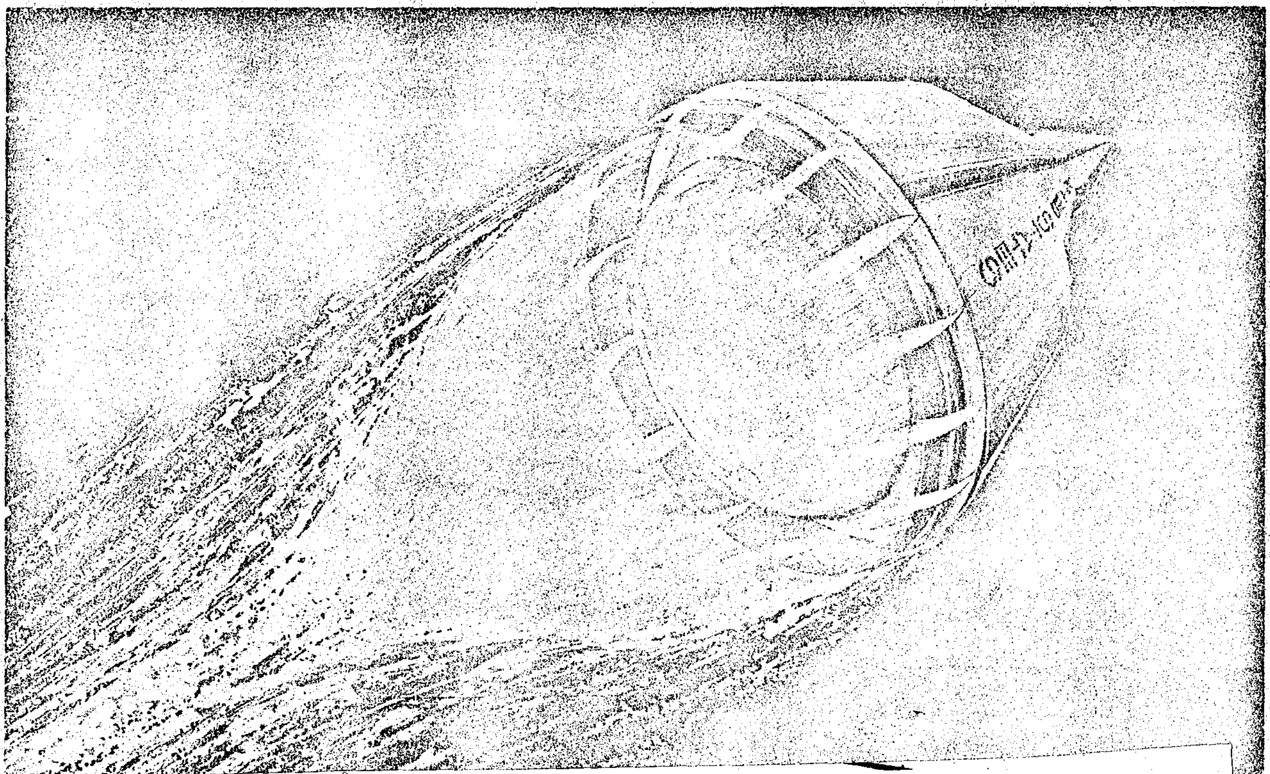

(NASA-CR-124173) SINGLE-STAGE EARTH-ORBITAL REUSABLE VEHICLE SPACE SHUTTLE FEASIBILITY STUDY. VOLUME 2: AERODYNAMIC MODEL TESTING Final Report (Chrysler Corp.) 252 p GP-0 CSCL 22A F3/30
X73-10295
Unclas
17395

SPACE DIVISION CHRYSLER CORPORATION NEW ORLEANS, LOUISIANA

TR-AP-71-4

DRD MA-095-U4 TR-AP-71-4

Final Report On Project

SINGLE-STAGE EARTH-ORBITAL REUSABLE VEHICLE

SPACE SHUTTLE FEASIBILITY STUDY

volume 2 contract NAS8-26341

aerodynamic model testing june 30, 1971

approved: C. E. Tharratt
C.E. Tharratt
Project Manager - SERV

CHRYSLER CORPORATION SPACE DIVISION
P.O. BOX 29200
NEW ORLEANS, LOUISIANA

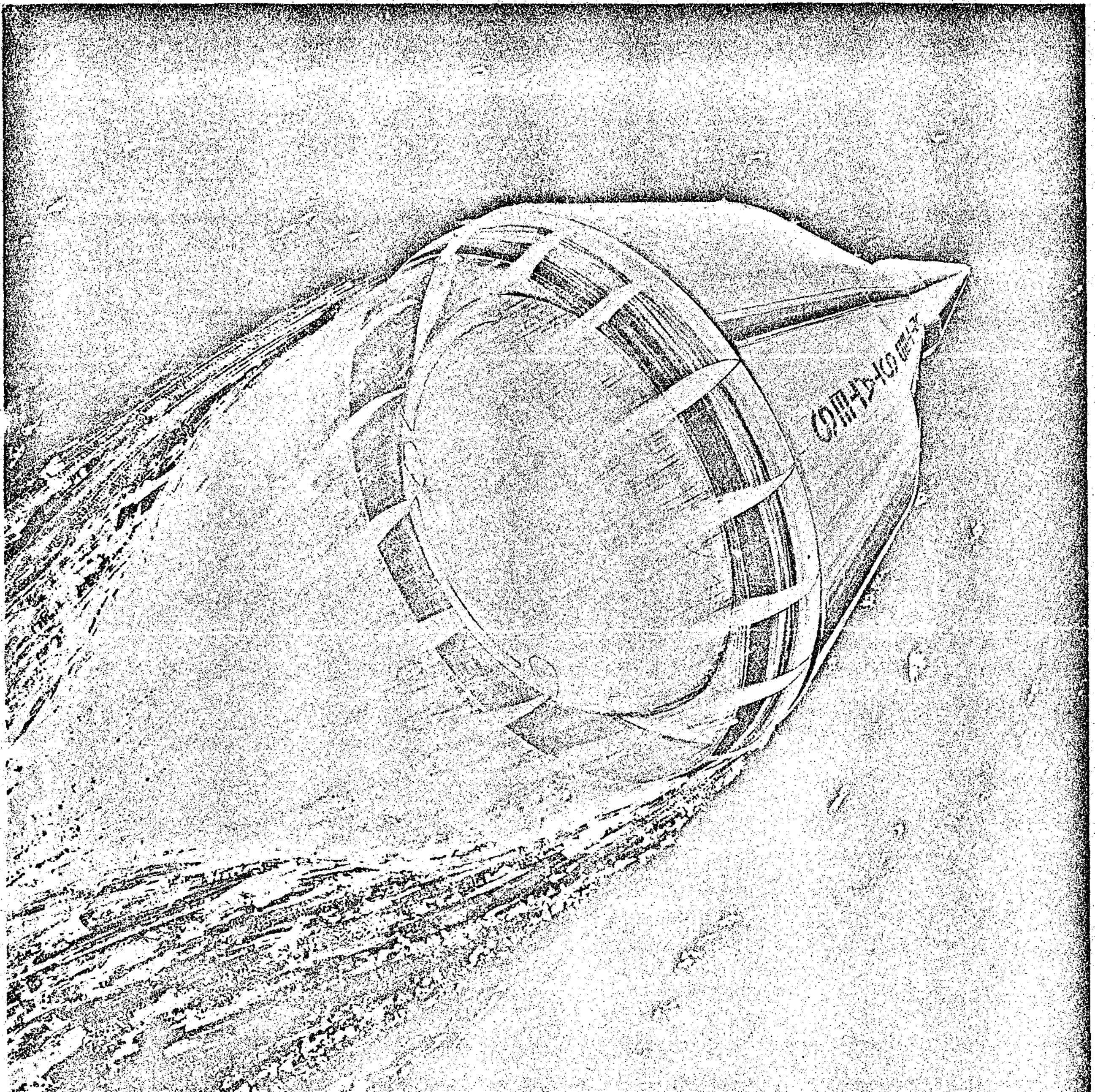

II

FOREWORD

This volume is one of a 6-volume final report of the Study of a Single-stage Earth-orbital Reusable Vehicle (SERV). The study was conducted by the Chrysler Corporation Space Division (CCSD) for the National Aeronautics and Space Administration, George C. Marshall Space Flight Center under Contract NAS8-26341. The purpose of the study was to evaluate the potential of SERV as the boost element of a candidate space transportation system. To establish the SERV potential, five key technical areas affecting concept feasibility were identified for examination: engine performance, aerodynamic characteristics, thermal protection, subsystem weights, and the landing method. The results of these analyses are published in a final report consisting of the following six volumes:

Volume 1	Summary
Volume 2	Aerodynamic Model Testing
Volume 3	Concept Evaluation
Volume 4	Vehicle Definition
Volume 5	Operations Definition
Volume 6	Resources

Chrysler gratefully acknowledges the cooperation and support of North American Rockwell Corporation, Rocketdyne Division, who under subcontract assisted in the model test, and analyzed the test results of the uniquely integrated SERV engine-to-structure concept. Rocketdyne also generated parametric engine data and designed the SERV aerospike engine. Chrysler also acknowledges the support and technical assistance received from Detroit Diesel Allison Division of General Motors Corporation who provided parametric engine data for advanced technology direct lift gas turbine engines and the AVCO Systems Division who provided design and cost data for thermal protection systems. In addition, acknowledgement is made to the following NASA and DOD agencies for their cooperation during wind tunnel testing: NASA-Ames, NASA-LaRC, NASA-MSFC, and AF-AEDC.

The study was managed and supervised by:

Charles E. Tharratt	Study Manager
William R. Baldwin	Principal Systems Analyst
John H. Wood	Principal Performance Analyst
Arthur P. Raymond, III	Principal Program Analyst

of the Chrysler Corporation Space Division, supported by Robert E. Schnurstein of the North American Rockwell Corporation, Rocketdyne Division. The study was conducted under the direction of Robert J. Davies, NASA study manager.

PRECEDING PAGE BLANK NOT FILMED

TABLE OF CONTENTS

Paragraph Page

Section 1 - INTRODUCTION

Section 2 - ASCENT BASE FLOW TEST

Section 3 - ASCENT CONFIGURATION FORCE TESTS

Section 4 - DESCENT CONFIGURATION FORCE TESTS

APPENDIX

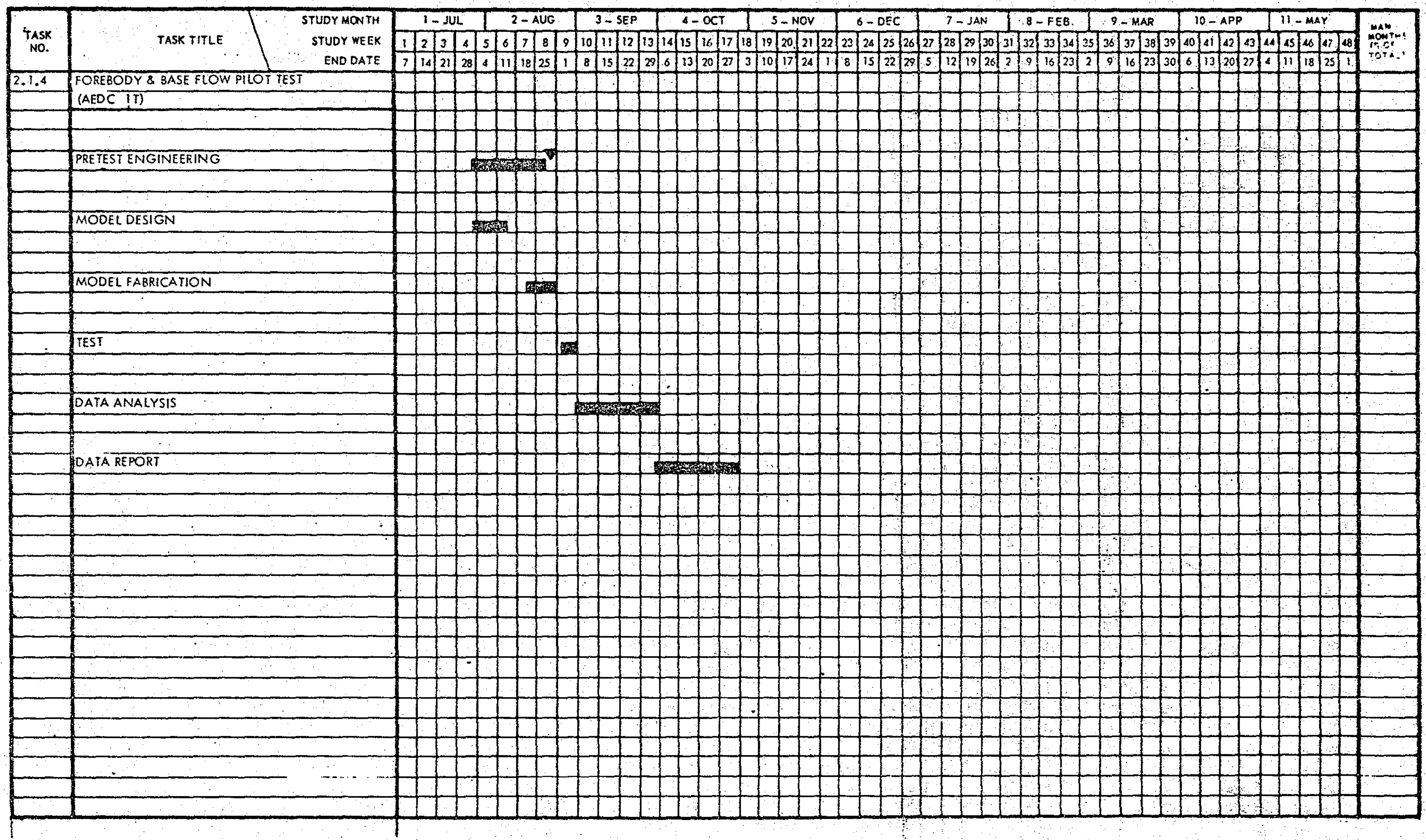

Figure 1.1(a). Task 2 Wind Tunnel Test Program

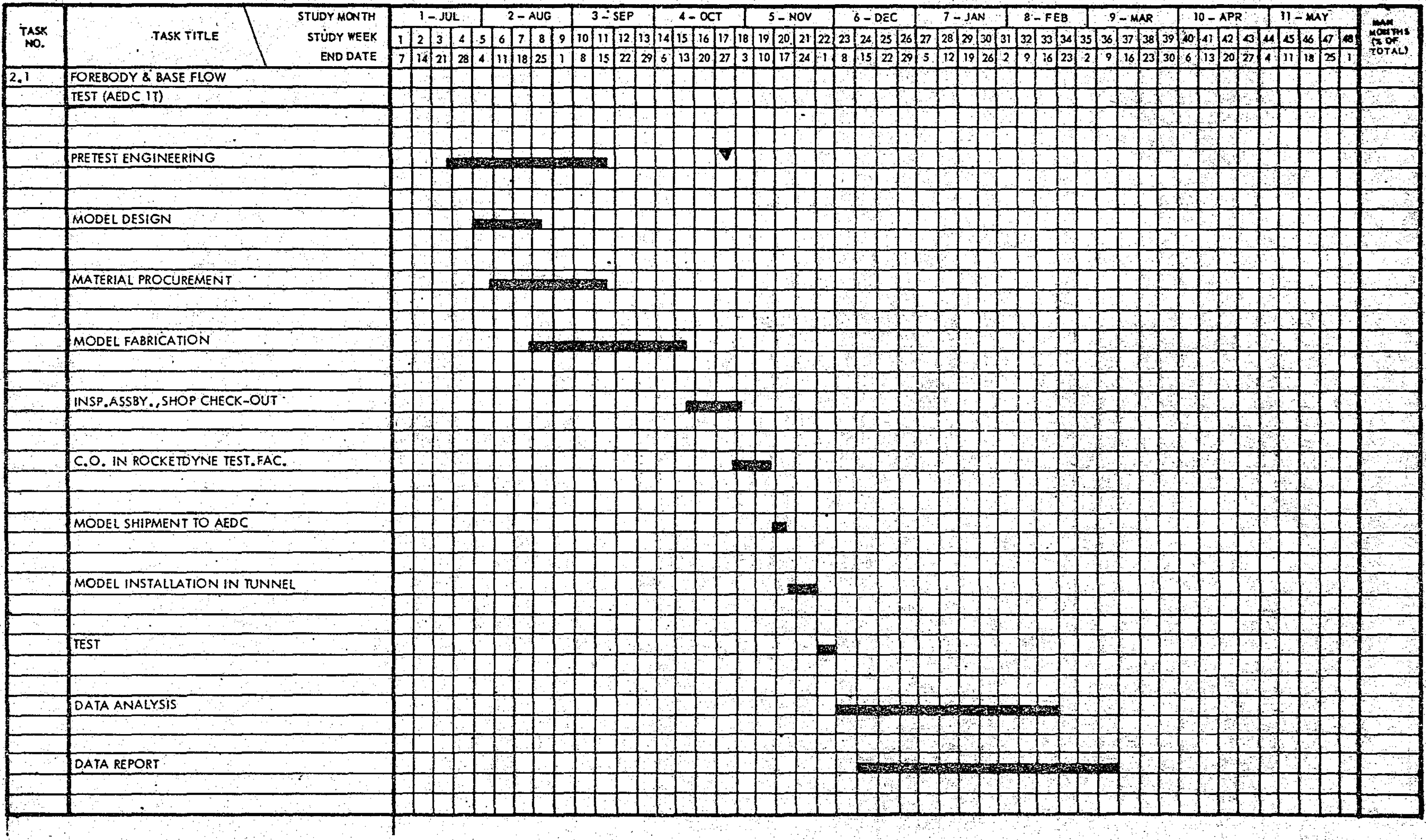

Figure 1.1(b). Task 2 Wind Tunnel Test Program

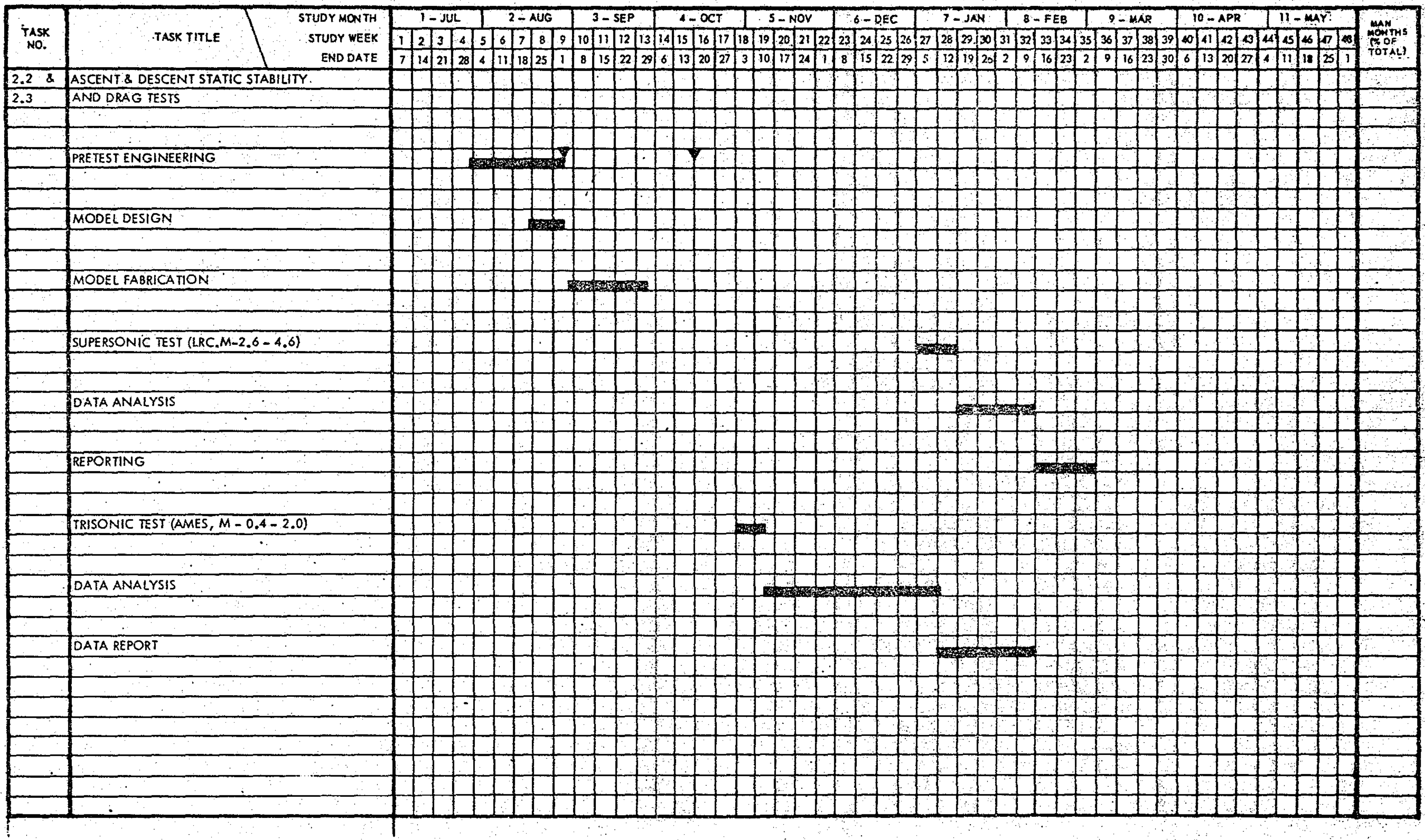

Figure 1.1(c). Task 2 Wind Tunnel Test Program

Table 1-1. Nomenclature

A_{REF} - reference area, $A_{REF} = \frac{\pi D_{REF}^2}{4}$ (ft^2)

C_A - aerodynamic axial force coefficient, $C_A = \frac{\text{Axial Force}}{q_\infty \ A_{REF}}$

C_{A_F} - forebody aerodynamic axial force coefficient

C_D - aerodynamic drag coefficient, $C_D = \frac{\text{DRAG FORCE}}{q_\infty \ A_{REF}}$

C_M = CLM - aerodynamic pitching moment coefficient,

$$C_M = \frac{\text{MOMENT}}{q_\infty \ A_{REF} \ D_{REF}},$$

referenced to vehicle station X/D = 0, unless otherwise noted

C_{M_α} - gradient of aerodynamic pitching moment coefficient with angle of attack (α), $\frac{d\,C_M}{d\,\alpha}$

C_N - aerodynamic normal force coefficient,

$$C_N = \frac{\text{Force Normal to Longitudinal Axis}}{q_\infty \ A_{REF}}$$

C_{N_α} - gradient of normal force coefficient with angle of attack (α),

$$\frac{d\,C_N}{d\,\alpha}$$

CP/D - location along longitudinal axis where normal force must be located to produce aerodynamic pitching moment, $CP/D = C_M/C_N$, (measured from vehicle station X/D = 0)

C_P - pressure coefficient, $C_P = \frac{P - P_\infty}{q_\infty}$

$D = D_{MAX}$ - maximum diameter across heat shield (feet)

Table 1-1. Nomenclature (Continued)

D_{REF} - reference diameter (in most cases $D_{REF} = D = D_{MAX}$, reference diameter is defined where used)

L/D - aerodynamic lift-to-drag ratio, $L/D = \frac{C_L}{C_D}$

$(L/D)_T$ - lift-to-drag ratio at static aerodynamic trim condition

$\overset{\circ}{m}_p$ - primary aerospike engine mass flow rate

$\overset{\circ}{m}_s$ - secondary aerospike engine mass flow rate

M - Mach number

M_∞ - ambient freestream Mach number

P_B - base pressure

P_{BE} - mean base heat shield region pressure

P_{B_V} - mean base pressure (over area outside of engine nozzle perimeter)

P_C - aerospike engine chamber pressure

P_L - local pressure (psia or psfa)

P_∞ - ambient pressure (psia or psfa)

R_B - heat shield surface radius

r_C - heat shield corner radius

Table 1-1. Nomenclature (Continued)

r_c/D	ratio of heat shield corner radius to maximum diameter across heat shield
R_B/D	ratio of heat shield surface radius to maximum diameter across heat shield
S	Reference area, $S = A_{ref}$
X, Z	longitudinal and lateral axis coordinates
X/D	longitudinal axis location, measured from the center of the heat shield surface, nondimensionalized by the reference diameter, D
Z/D	lateral distance from the vehicle centerline nondimensionalized by the reference diameter, D
α	wind angle of attack (angle between freestream velocity vector and the reference axis)
α_T	static aerodynamic trim angle of attack
η_V	vehicle thrust performance factor
π	constant 3.14159

Model Configuration Code

B_1	45°/25° frustum baseline ascent configuration centerbody with balance cavity on centerline
B_2	45°/25° frustum baseline descent configuration centerbody with balance cavity on centerline
B_3	45°/25° frustum baseline descent configuration centerbody with balance cavity rotated 16°
B_4	45°/25° frustum baseline descent configuration centerbody with balance cavity rotated 32°
D_2	Ascent configuration base ring with aerospike engine doors open 25°
D_3	Ascent configuration base ring with aerospike engine doors open 45°
D_4	Descent configuration baseline reentry heat shield with 11% radius aerospike engine doors closed
D_6	Descent configuration reentry heat shield with aerospike engine doors removed
D_7	Descent configuration reentry heat shield with one quadrant of 11% radius aerospike engine doors at various angular openings
F_1	Large generalized payload forebody - 2.2 inch max. dia., model scale
F_2	Large personnel module payload - 1.5 inch max. dia., model scale
F_3	Winged payload - 1.24 inch max. total span, model scale
F_4	Small personnel module payload - 1.5 inch max. dia., model scale
O	Reentry configuration with no afterbody payload attached

removal of aerospike engine protection doors. A load cell was used to measure the net vehicle axial force and extensive pressure measurements with selected temperature measurements were made.

A pilot test was conducted in the AEDC 1-foot PWT to investigate the best model support mounting technique to be used in the 16T PWT base flow test. This test utilized a 0.156 percent scale model simulating the test conditions at which the larger scale test was to be conducted. The effect on base pressure of forward strut-sting mounting systems was compared to the effect produced by aft sting mounting systems. From this test, it was concluded that a forward floor-mounted strut-sting mounting system could be advantageously employed with a minimum influence on base pressure magnitudes and symmetry.

Scale model force tests were conducted in the NASA Ames 6-foot Supersonic Wind Tunnel (SWT) and the Langley Unitary Plan Wind Tunnel (UPWT) to define the aerodynamic flight performance characteristics of both the ascent and descent vehicles. These were to determine the aerodynamic stability characteristics, normal force, axial force, and pitching moment through the complete flight Mach number range of 0.4 to 4.64. No testing of the descent vehicle above Mach 4.64 was conducted as it was considered adequate for Task 4 vehicle definition requirements to extrapolate the higher supersonic Mach number data to the reentry hypersonic Mach range by application of reference Apollo data and hypersonic flow theory.

In the ascent portion of these tests, 0.55 percent scale models of the SERV baseline configuration with the various payload options were utilized. The models were approximately 6 inches in maximum cross-section diameter. Tests of the descent configuration utilized similar 0.55 percent scale models of a maximum diameter of 6 inches in the heat-shield-first reentry and deceleration attitude. The influence of descent configuration geometric parameters such as removal of engine doors, afterbody geometry, heat shield corner radius, and using the aerospike engine protection doors as flaps were investigated. Aerodynamic force characteristics of the ascent configurations were tested through an angle-of-attack range of -4 to +16 degrees, while the descent configurations were tested from +4 to -50 degrees in the subsonic and transonic range (utilizing offset stings), and from -6 to -34 degrees angle-of-attack range in the higher supersonic regime.

Figure 1-2 presents the test conditions of Reynolds number versus Mach number for all aerodynamic tests conducted, with a comparison of the full scale flight Reynolds number for a typical trajectory. As is so often the case, all tests were conducted at simulated Reynolds numbers well below the full scale values.

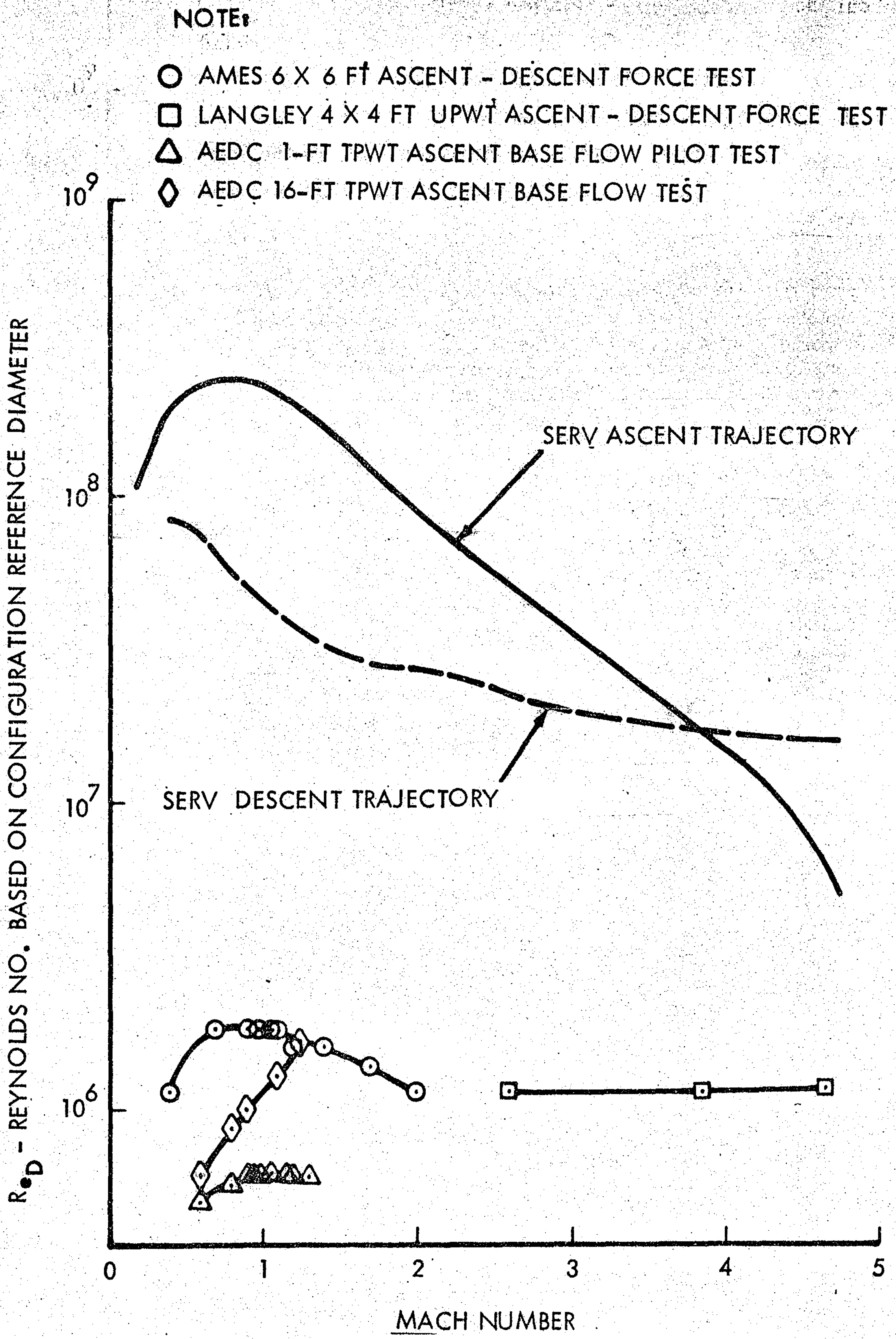

Figure 1-2. Wind Tunnel Test Conditions For SERV Investigations Compared With Full-scale Conditions

Section 2

ASCENT BASE FLOW TEST

2.1 PILOT MODEL TEST

The objective of this test was to determine experimentally the effect on base pressures of various model mounting supports and nose shapes of a 0.156 percent scale model of the SERV ascent configuration in the transonic region. The results of this test were used in determining the mounting of the 2.5 percent cold-flow-model of SERV in the AEDC 16T PWT. The 0.156 percent scale model test was conducted in the AEDC 1-foot PWT (reference 12). Sketches of the configurations tested are shown in figures 2.1-1 through 2.1-4.

The model was designed by Chrysler and, under subcontract, was fabricated from aluminum and stainless steel by Microcraft, Inc. of Tullahoma, Tennessee. Ten orifices were located on the model, 6 static orifices in the vertical centerline of the model base and 4 flow orifices on the shoulder of the forebody, each 90 degrees apart (figures 2.1-3 and 2.1-5).

2.1.1 TEST PROCEDURE

The model was mounted in the test section by two methods,sting mounted from the base of the model and strut mounted from the nose of the model. With the model sting mounted, three nose shapes were tested; a large diameter payload of cargo module, an extended personnel module, and an extended nose. With the model strut-mounted, two forward sting lengths were tested, one was a length that located the base of the model 1.70 strut chord lengths (3.03 inches) from the tailing edge of the strut and the other located the base of the model 3.74 strut chord lengths (6.66 inches) from the trailing edge of the strut. The strut was mounted to the side wall of the test section. Photographs of the model, strut mounted and sting mounted, are shown in figures 2.1-6 and 2.1-7. Testing was performed at angles of attack of 0, -5 and -10 degrees from Mach numbers of 0.6 to 1.30. A detailed description of the test plan is presented in reference 1.

Several problems developed during testing. Due to the limited space in the model, it was nearly impossible to keep the flexible tubing which connected the pressure orifices to the pressure transducers from kinking inside the model with the result that several orifices were inoperative. With the model strut mounted, the tunnel had to be opened and part of the tunnel wall removed in order to change the angle-of-attack, resulting in a lengthy downtime and therefore limiting the angle-of-attack data obtained. The model was not mounted in front of the tunnel window so shadowgraphs and/or Schieren pictures of flow characteristics could not be obtained.

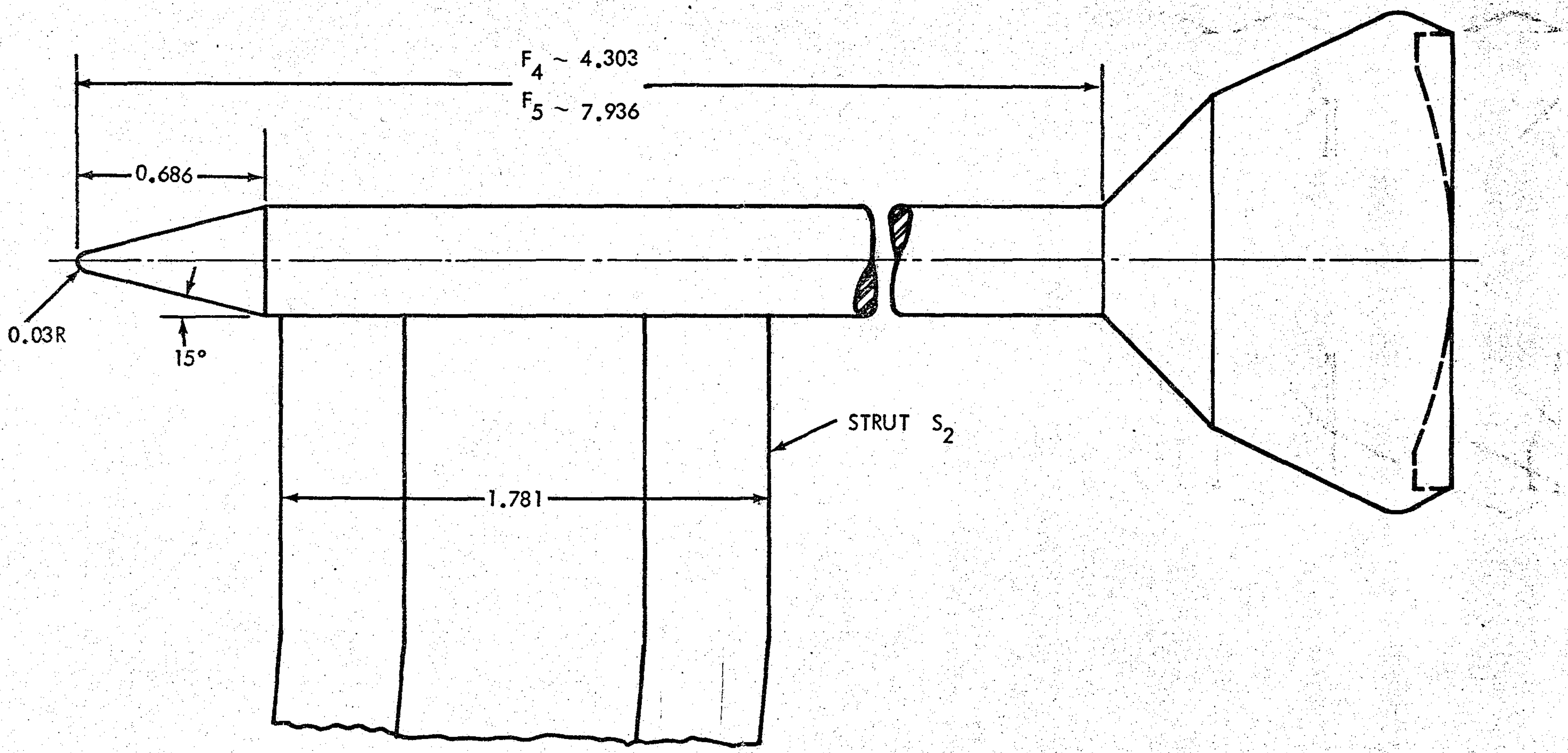

Figure 2.1-1. SERV Model Strut Mounted

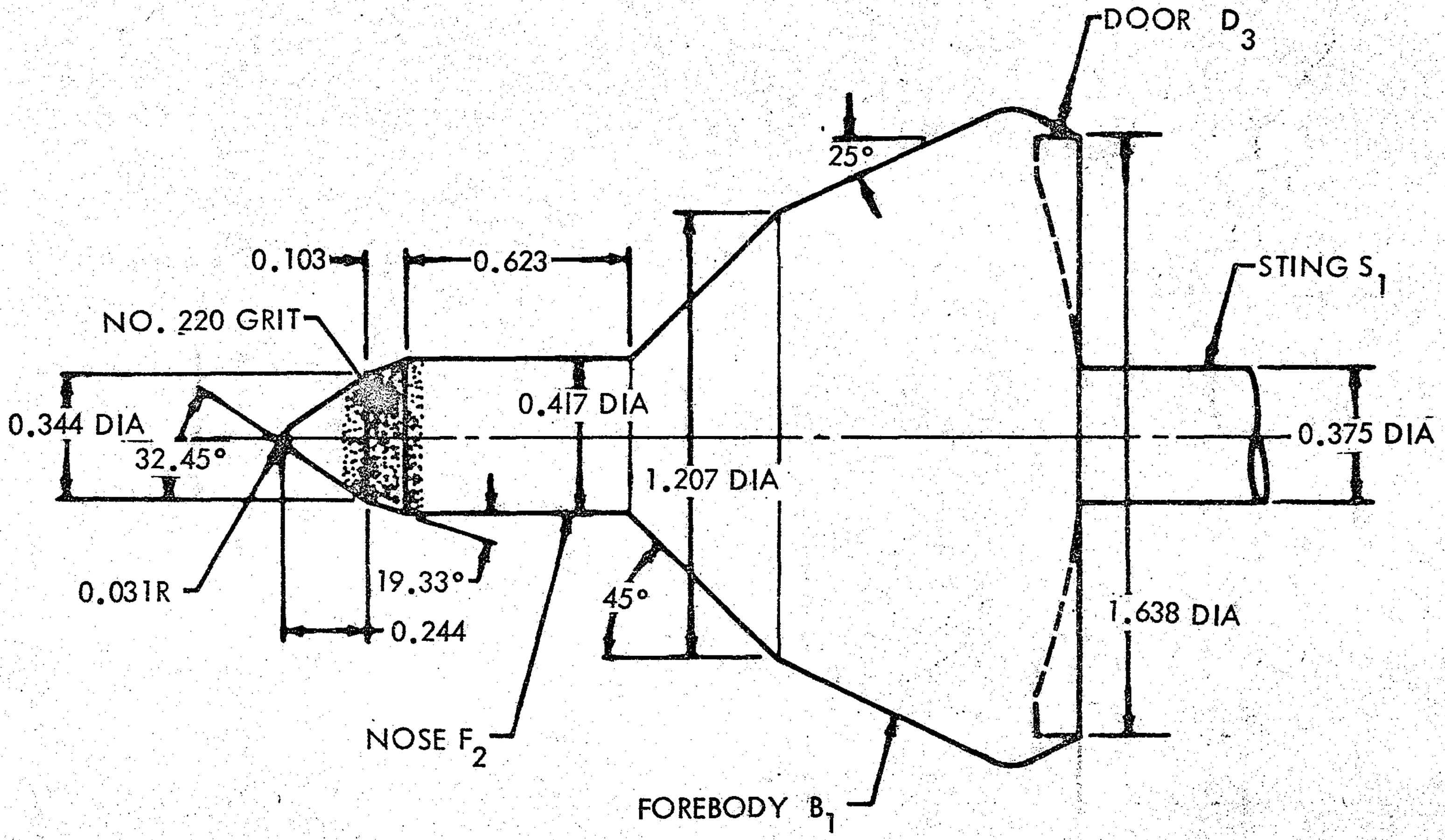

Figure 2.1-2. SERV With Extended Personnel Module

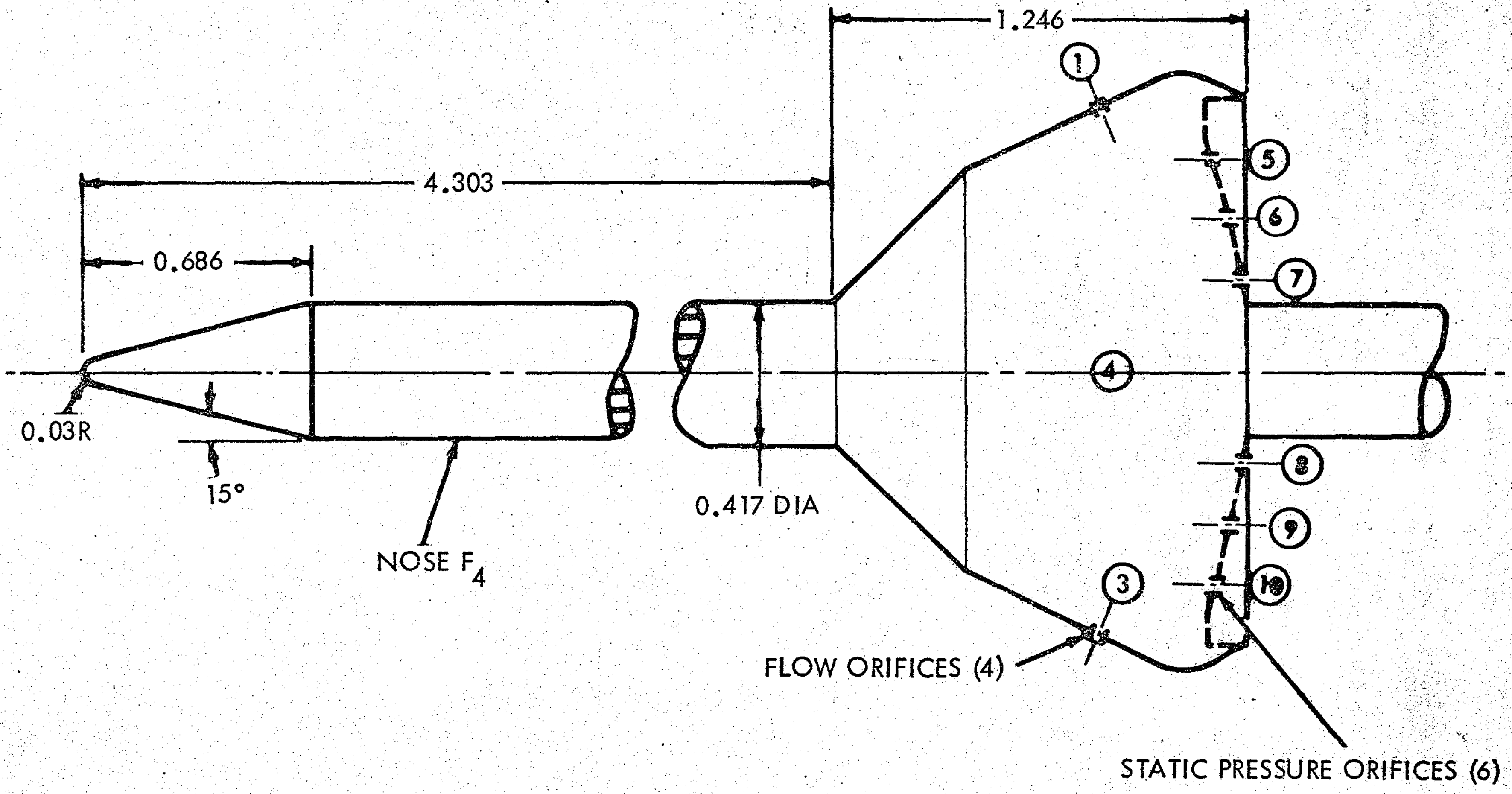

Figure 2.1-3 SERV Model With F_4 Nose

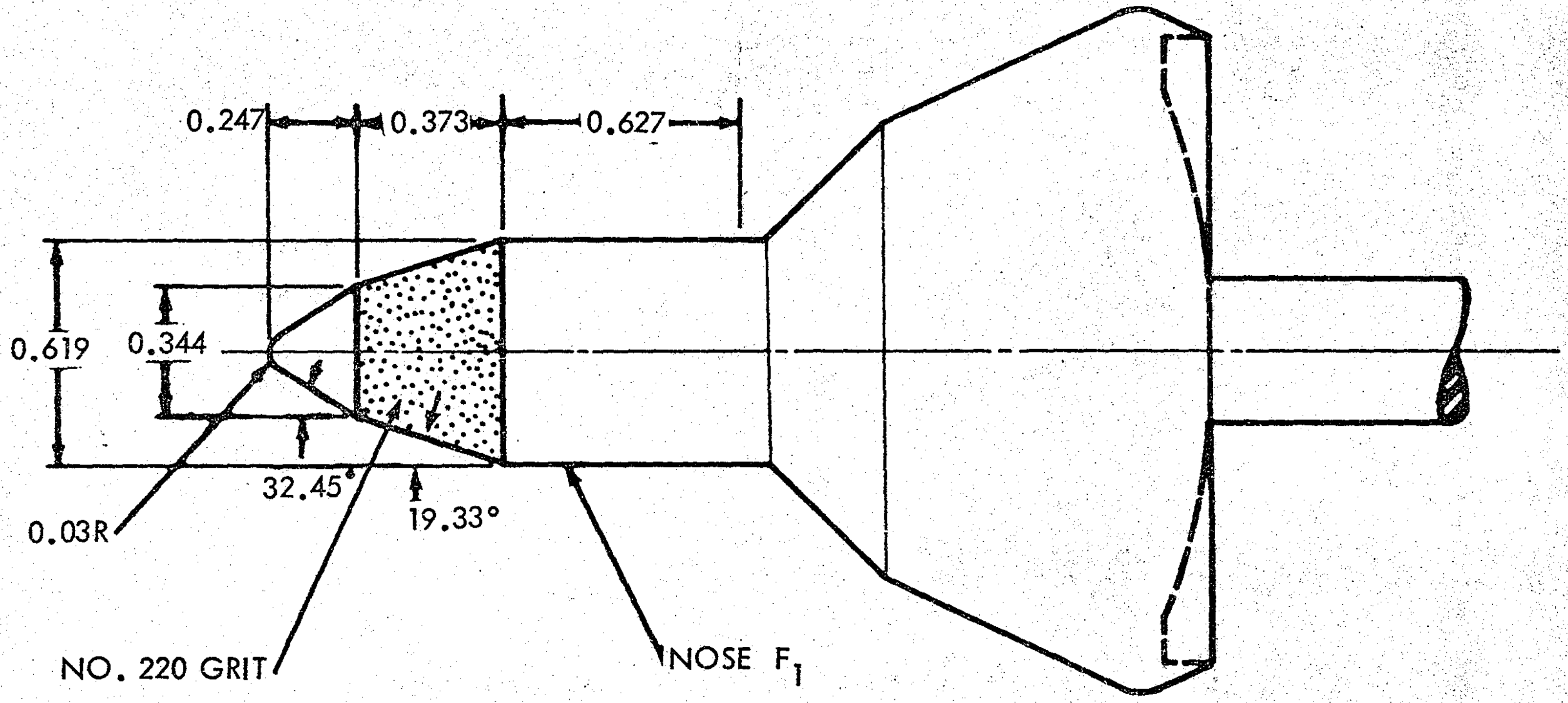

Figure 2.1-4 SERV With Large Payload

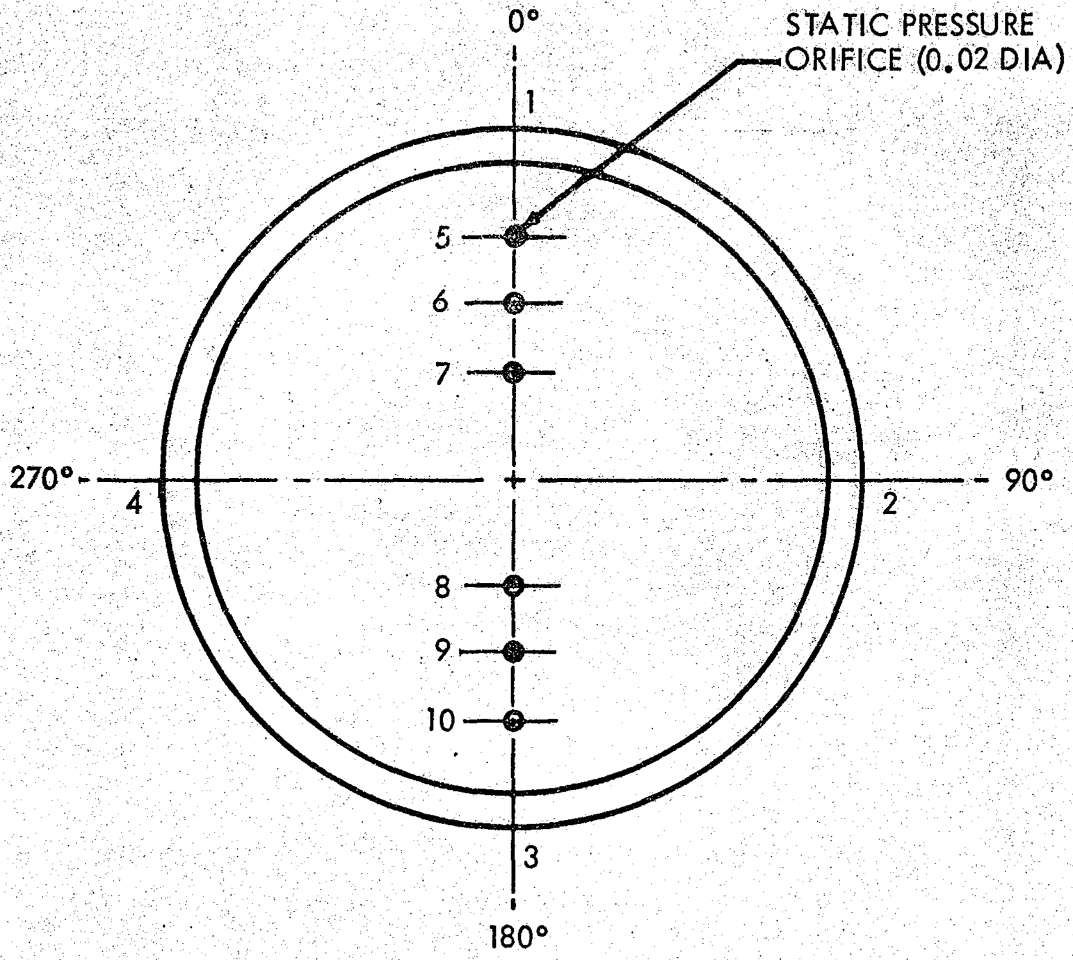

Figure 2.1-5 Base Static Pressure Orifices

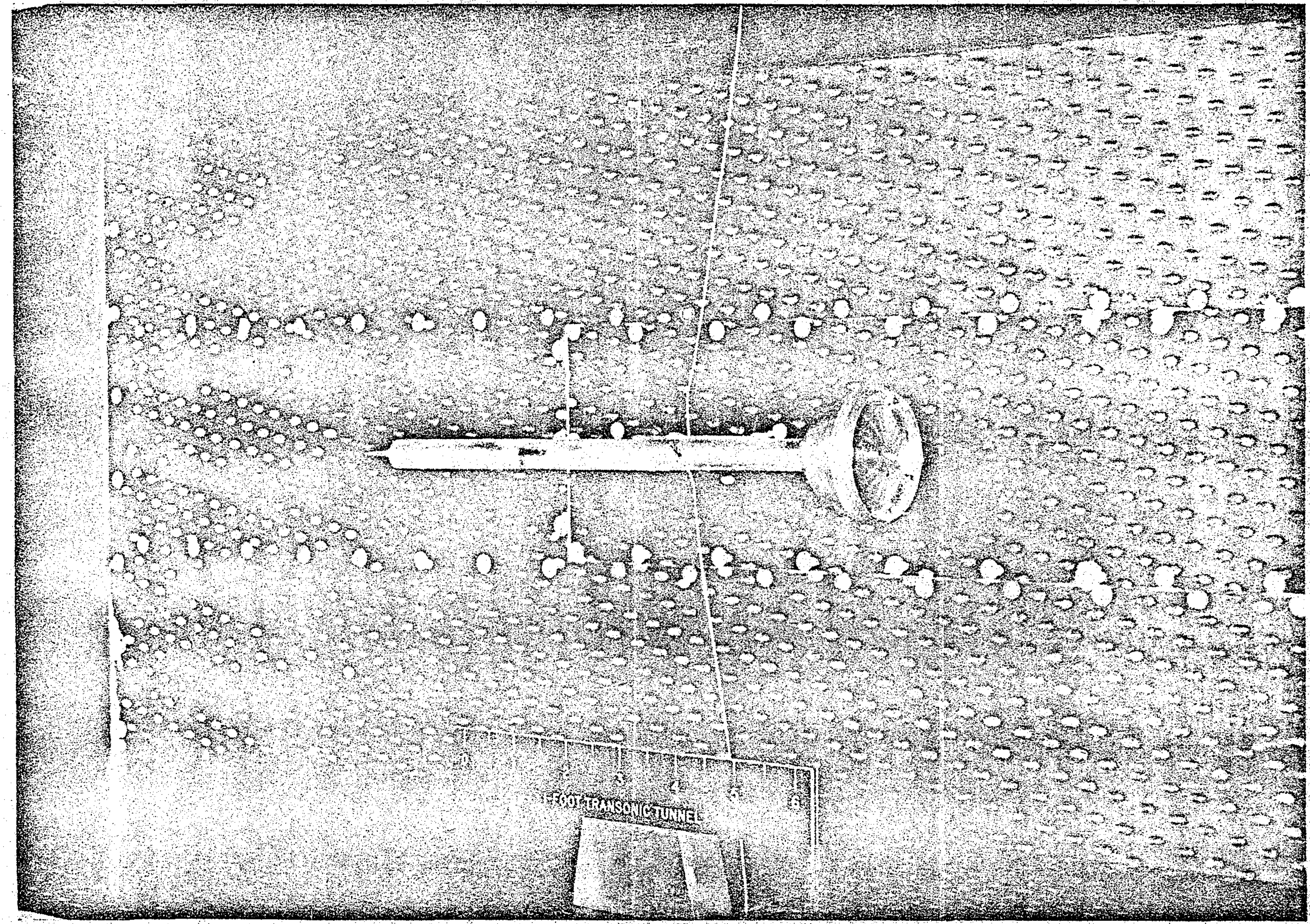

Figure 2.1-6 SERV I Strut Mounted With F_5 Nose

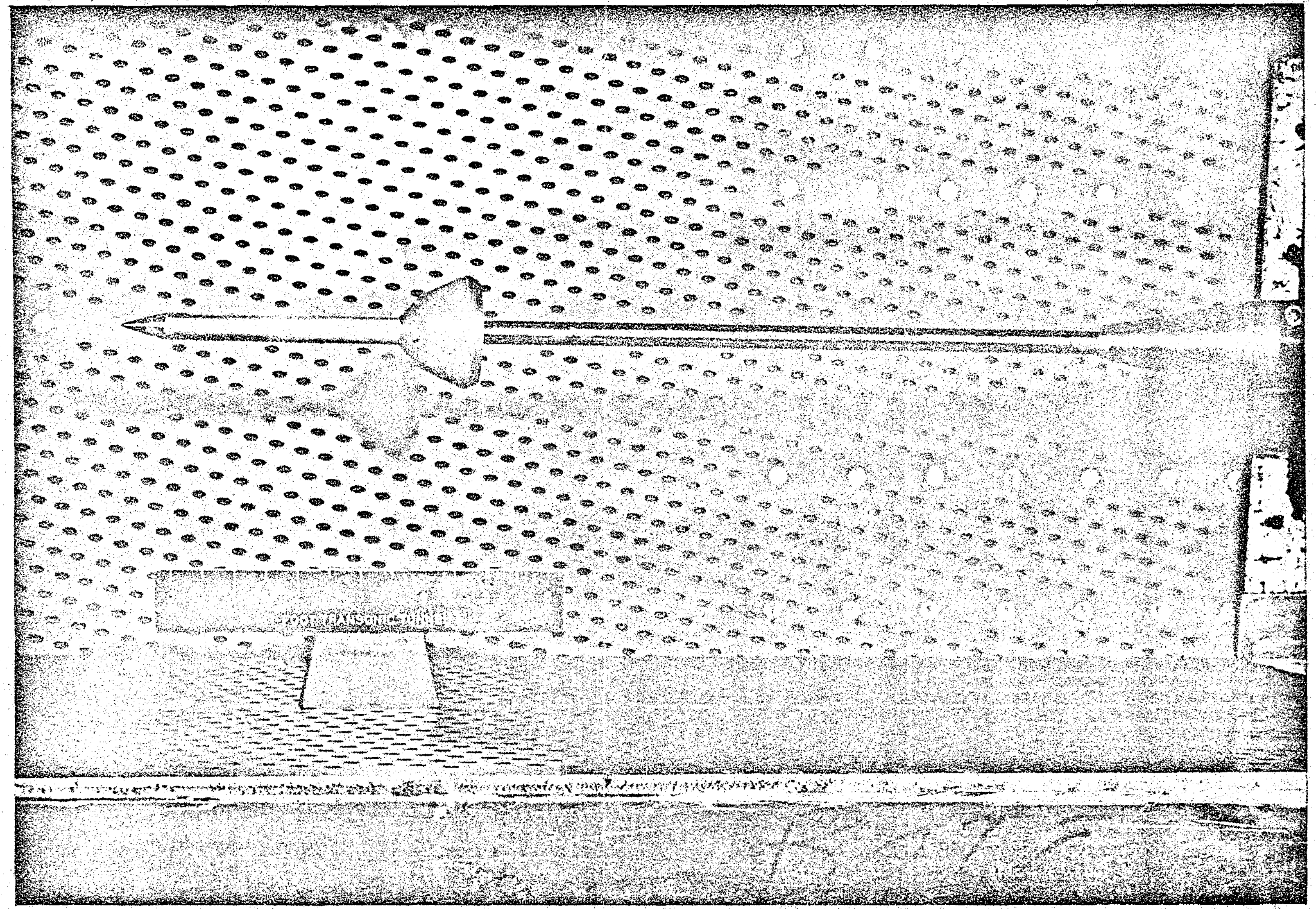

Figure 2.1-7 SERV I Sting Mounted With F_4 Nose

2.1.2 RESULTS AND DISCUSSION

Only pressure data were obtained from this test, and figure 2.1-8 presents the base pressure ratio (P_b/P_∞) plotted versus radial diameters (R/D) at zero angle-of-attack for the various configurations tested. These data show that in the transonic region, the long nose sting on the strut-mounted model had less influence on the model base pressures than the shorter nose sting. With the model sting-mounted from the base, the length of the nose had no effect on the base pressures. The short nose sting was tested with the model both strut and sting mounted and the data showed slightly less effect on the base pressures with the model sting mounted. Figure 2.1-9 presents pressure coefficient data (Cp) obtained on the forebody with the model strut mounted. These were the only forebody pressure data obtained during the test. The pressures on the forebody were more positive with the short nose sting than with the long nose sting. Complete results and analysis of the wind tunnel test are presented in reference 2.

The method selected to mount the 2.5 percent cold-flow scale model in the AEDC 16T PWT was the strut mount with the long nose sting. The strut mounting was selected because with the sting mounted in the base and with aerospike engine exhaust out the base, the flow would impinge on the sting and even the smallest sting could give erroneous results. Also, due to the requirement of routing the air supply into the model, the sting would have been of a diameter that could have resulted in large base pressure errors. Because the differences in the effect on base pressures between the front strut mount and the aft sting mount were small, and because the long nose sting had less effect on the base pressures than the short nose sting, it was decided that the front strut mount with the long nose sting would have the least effect on the base flow characteristics.

2.2 COLD-FLOW MODEL TEST

In order to adequately define the aerospike engine performance and resulting net vehicle axial forces during ascent flight, it was necessary to determine the flow characteristics of the engine with its large-area-ratio at open wake operating pressure ratio under the influence of a simulated flight slipstream over the blunt forebody configuration. Small-scale, cold-flow engine-model wind tunnel slipstream testing had proven to be an inexpensive and accurate means of verifying these characteristics on past programs as discussed in appendix A. Cold-flow engine wind tunnel tests, under well controlled simulation conditions, had been used to establish the flow characteristics and performance trends of typical aerospike nozzles operating in a slipstream. The experience gained by the reference testing, noted in appendix A, provided valuable guidelines for defining the necessary model scaling and testing techniques.

A test program was conducted in the AEDC 16T PWT from December 3 through December 8, 1970, utilizing a 2.5 percent scale model of the SERV baseline geometry, incorporating a high expansion ratio, short length aerospike engine. The test was conducted in still air and in a slipstream simulating flight altitude conditions and freestream Mach numbers from 0 to 1.25. These tests did not duplicate completely the pressure ratios of an actual trajectory. The resultant data were to establish sufficient magnitudes and trends to extrapolate analytically to the higher pressure ratio flight conditions. Reference 3 presents a complete pretest plan for this program and references 4 through 7 and appendix A

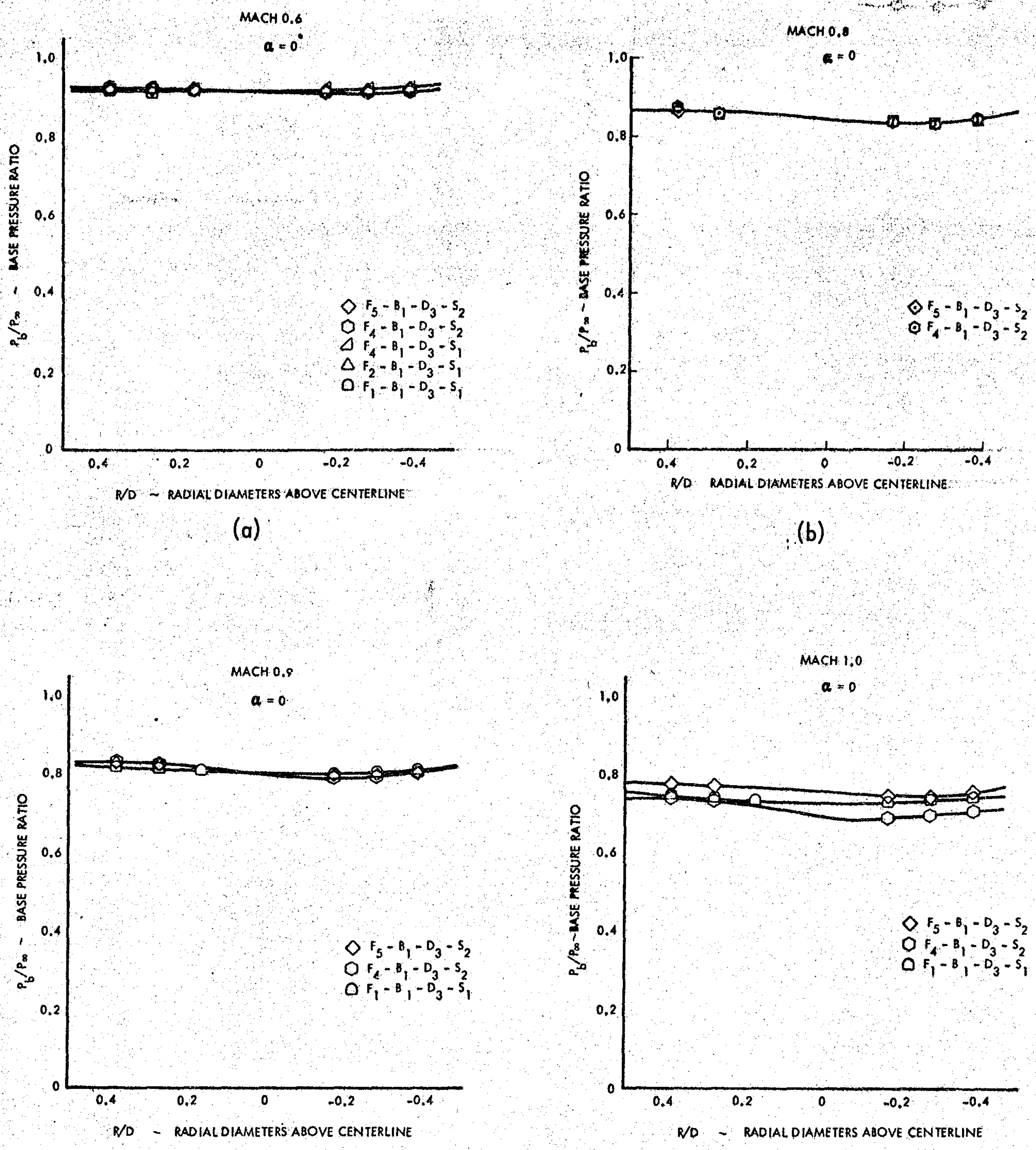

(c) (d)

Figure 2.1-8. SERV I Base Pressure AEDC 1T Tunnel

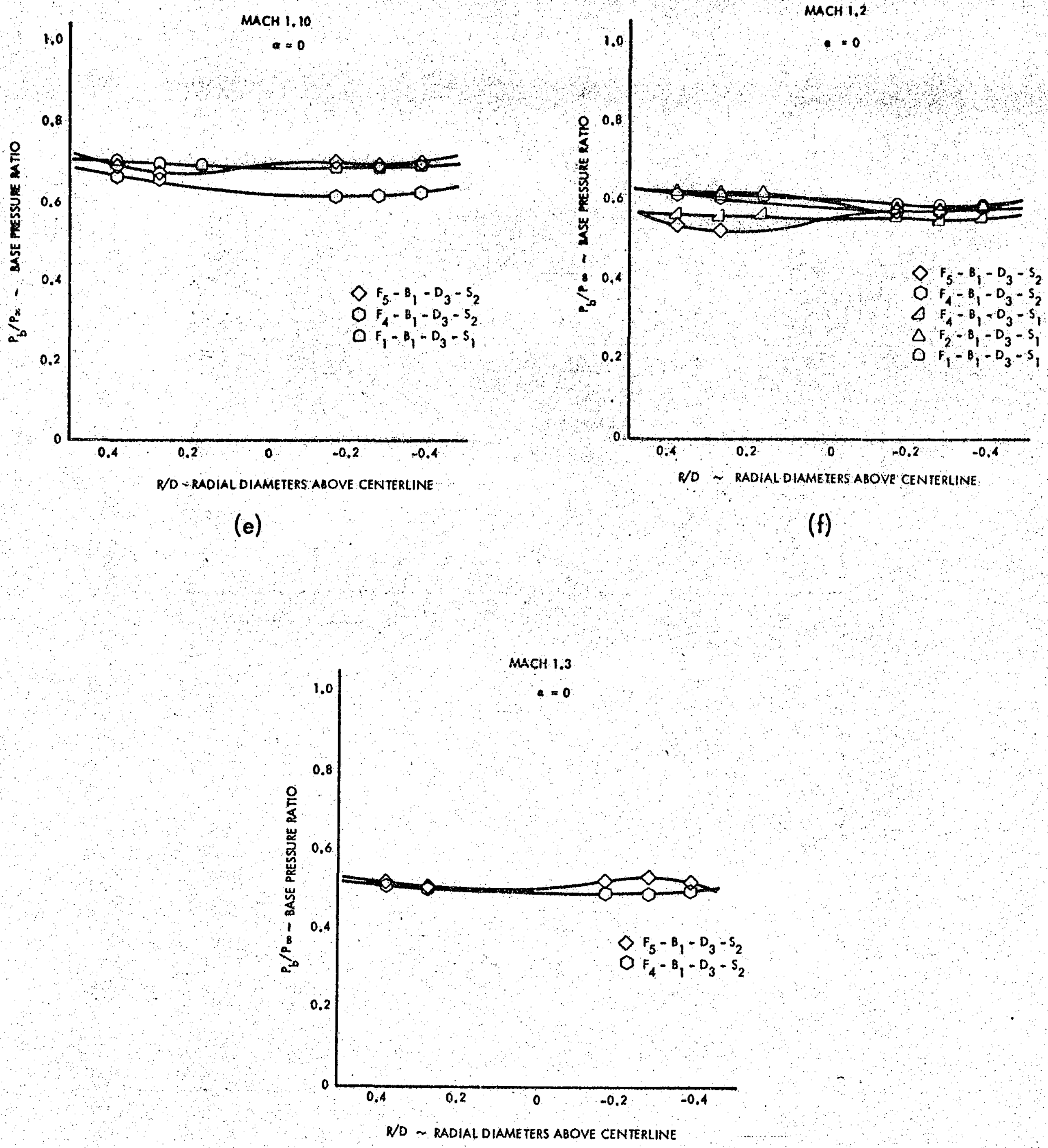

(e)

(f)

(g)

Figure 2.1-8. SERV I Base Pressure AEDC 1T Tunnel (continued)

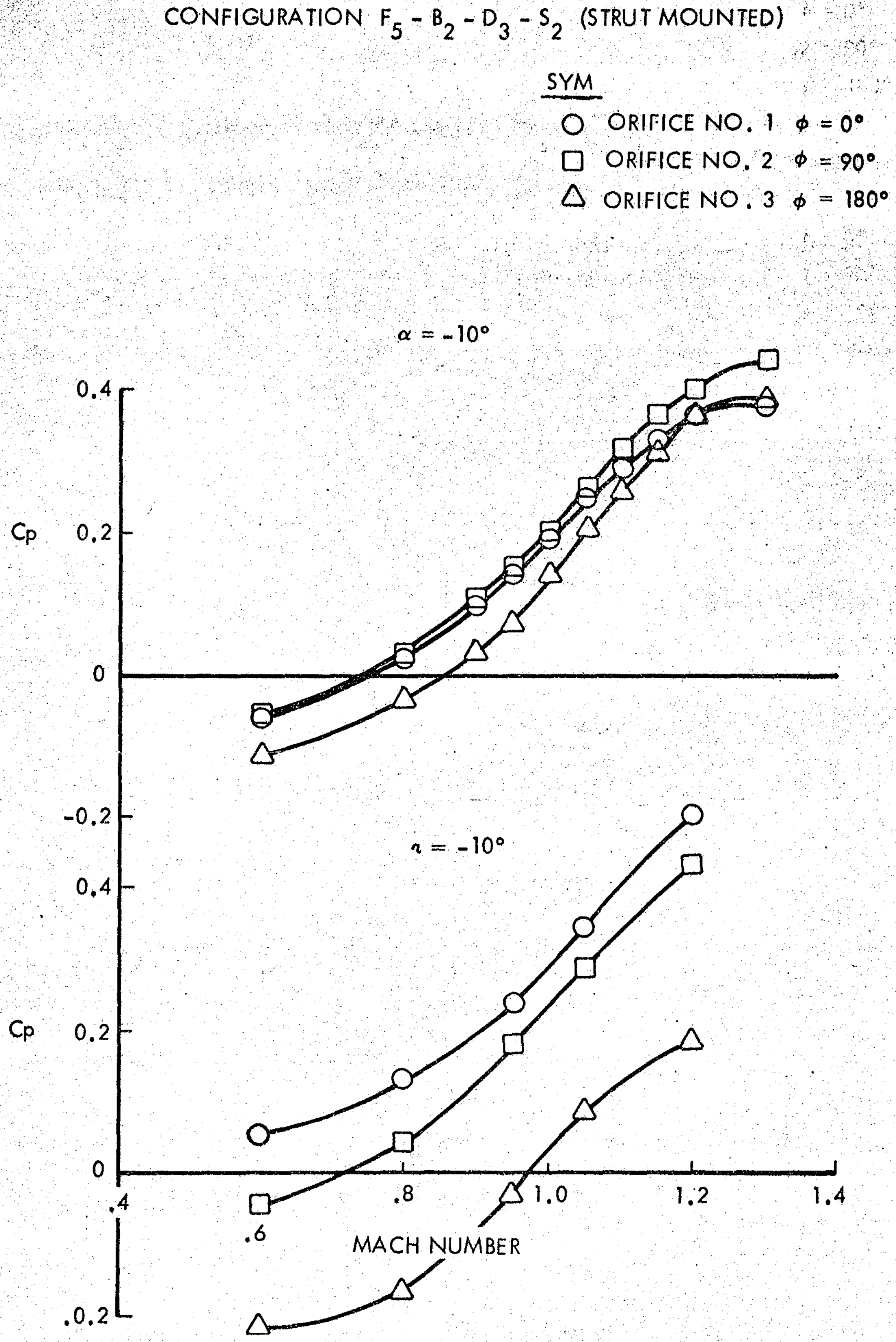

Figure 2.1-9(a). SERV I Forebody Pressures - AEDC 1T Tunnel

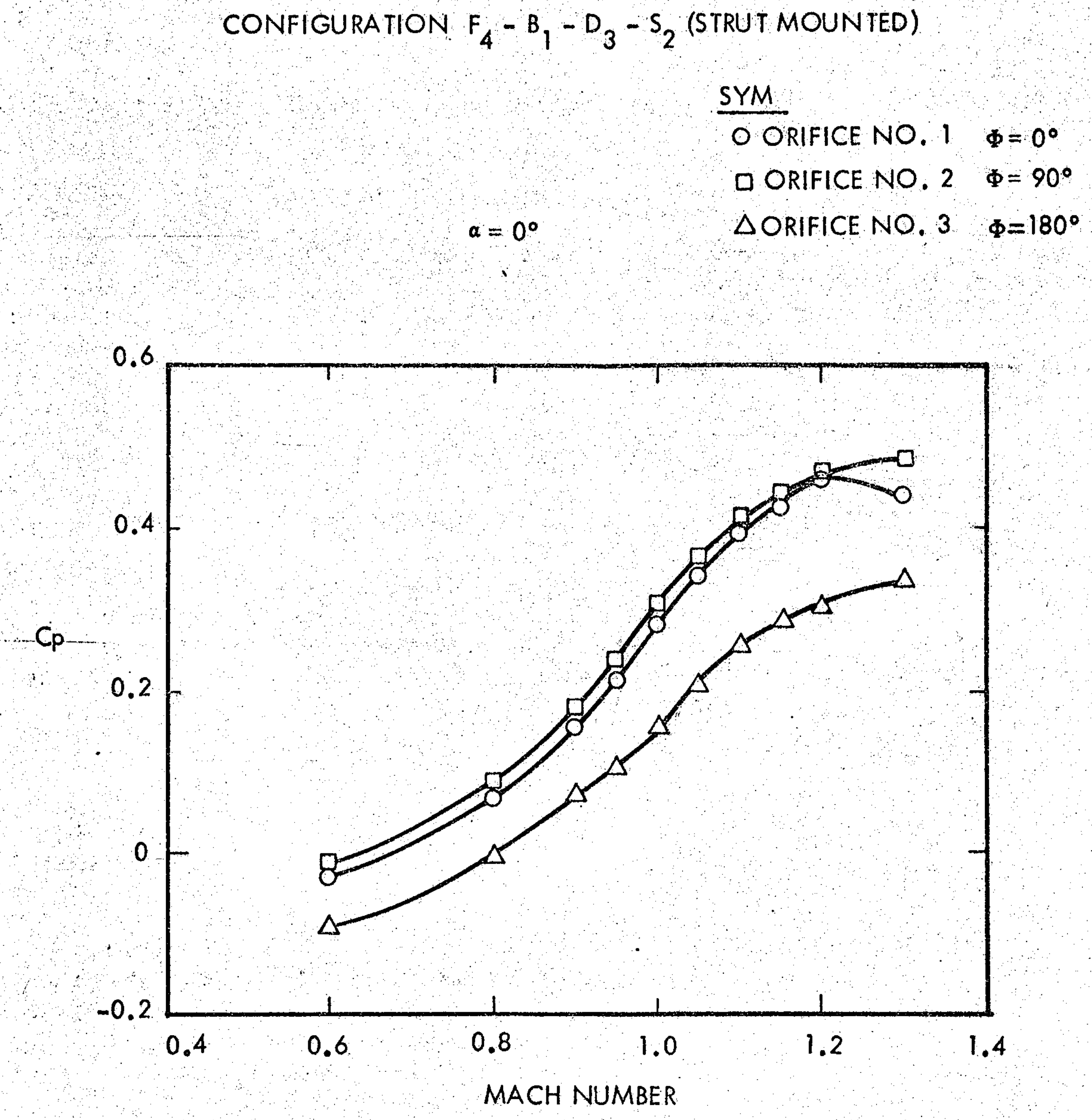

Figure 2.1-9(b). SERV I Forebody Pressures AEDC 1T Tunnel

document the test data, analysis and results.

2.2.1 TEST FACILITY

The AEDC 16T PWT is a closed-circuit, continuous-flow tunnel capable of being operated at Mach numbers from 0.20 to 1.60. The test section is 16 by 16 feet in cross section and 40 feet long. The tunnel can be operated at stagnation pressures down to 120 psfa at specific Mach numbers. Perforated walls in the test section allow continuous operation through the Mach number range with a minimum of wall interference. A more detailed description of this test facility is presented in reference 12.

2.2.2 MODEL DESIGN AND FABRICATION

The test model was a 2.5 percent scale replica of the SERV baseline ascent vehicle. It had a physical diameter of approximately 27 inches at the base and was approximately 20 inches in length. A 417 area ratio aerospike engine, designed to use air as a test gas, was incorporated. The model was mounted on a forebody sting 126.5 in. long which was strut mounted to the tunnel floor. Aerospike engine thermal protection doors were attached to the outer perimeter of the aerospike engine nozzle flange. The model was instrumented with an axial force load cell, 163 static pressure taps, and 4 thermocouple gages. References 3 and 4, and appendix A present a more detailed description of the test model and instrumentation. Figures 2.2-1 and 2.2-2 illustrate the model geometry, instrumentation, and installation in the AEDC test facility.

The model was designed jointly by Chrysler and Rocketdyne and fabricated under subcontract to Rocketdyne. Final assembly was completed on November 4, 1970 and operational checkout was conducted in the Rocketdyne Rocket Nozzle Test Facility in Los Angeles, California, through November 10, 1970.

2.2.3 TEST PROCEDURE

The complete test plan followed in this program is published in reference 3. The model was tested with and without engine flow at freestream Mach numbers of 0, 0.6, 0.8, 0.9, 1.1, and 1.25. With engine flow, model chamber pressure was maintained at a nominal value of 400 psia. Tunnel pressure was varied to obtain a range of aerospike engine chamber pressure to freestream static pressure ratios at each Mach number. At each test condition, data were recorded with no engine flow, with primary engine flow, and with primary engine plus simulated secondary turbine exhaust flow. As mentioned previously, the altitude versus Mach number test conditions did not duplicate completely the full-scale trajectory. A comparison of the reference trajectory to test conditions is presented in figure 2.2-3.

There were three major problems incurred with this test program. First the axial force load cell readings indicated a significant bias due to the thermal stresses in the capillary spoke lines used to feed the high-pressure air from the center pipe to the outer combustion chamber annulus. This bias was a small percentage of net thrust, but it was especially significant when measuring engine-off axial force or drag, due to the very low tunnel freestream densities. This problem was solved by running a Mach number sweep at high tunnel total pressures to measure model axial forces without engine on. These data were then normalized to a drag coefficient to be used in the data reduction for engine thrust at the low tunnel density test conditions.

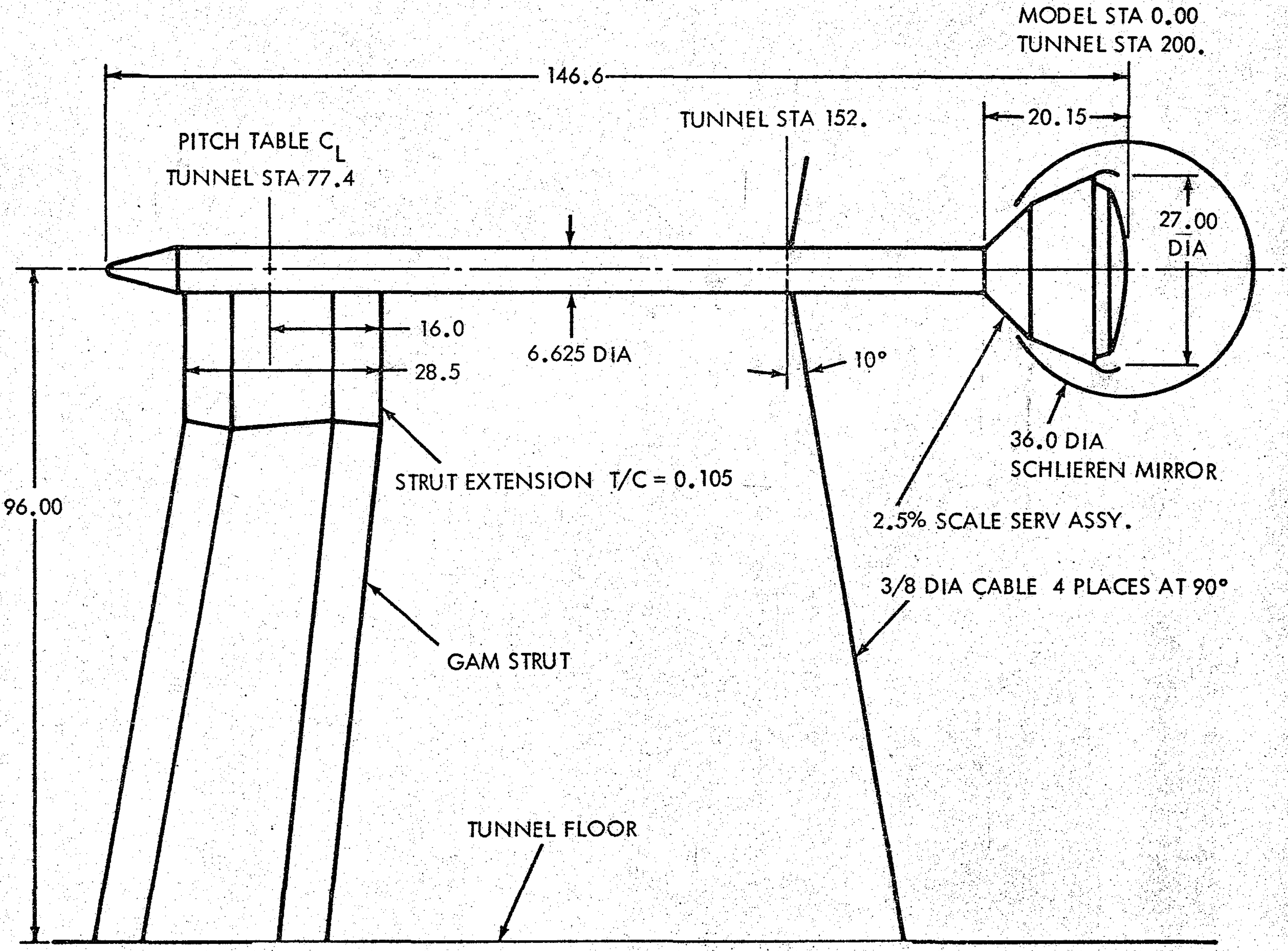

Figure 2.2-1(a). SERV Model Installed in AEDC 16T PWT

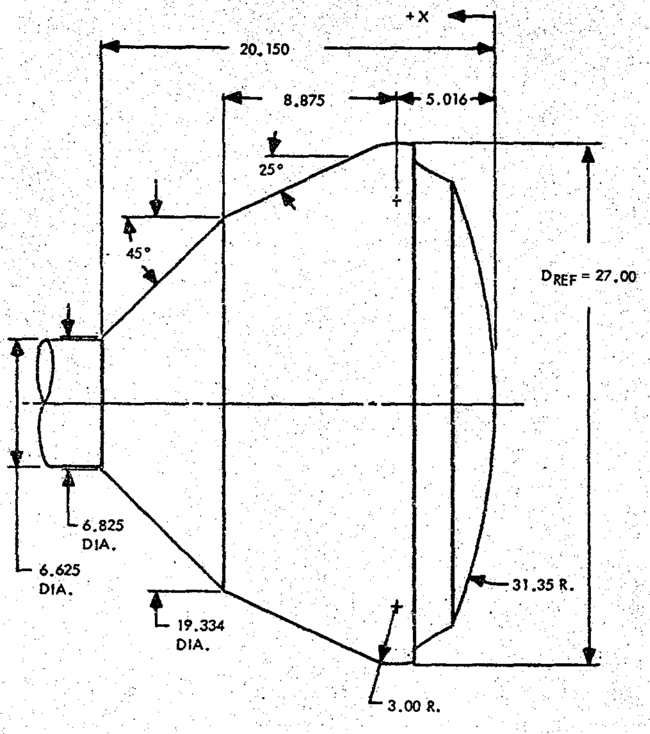

Figure 2.2-1(b). SERV 2½ Percent Base Flow Model Geometry

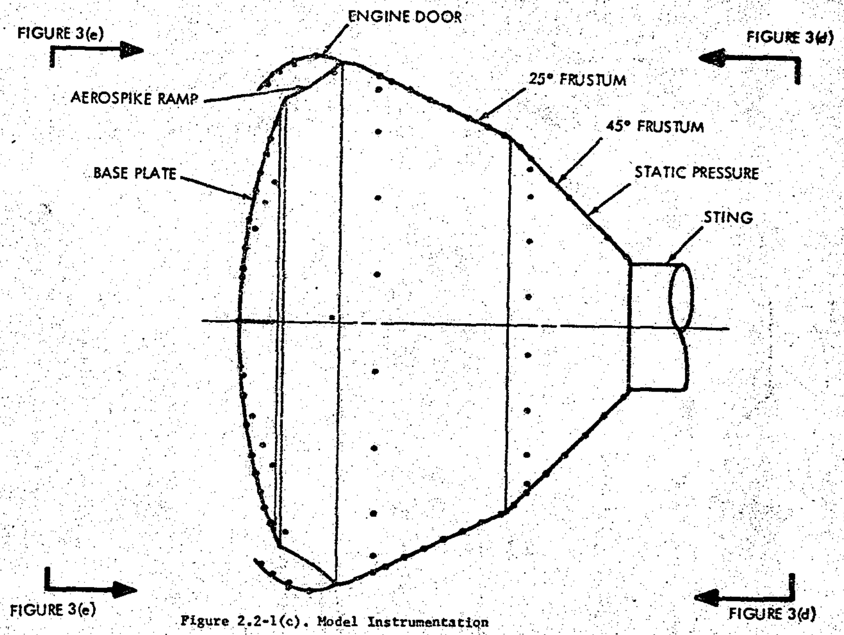

Figure 2.2-1(c). Model Instrumentation

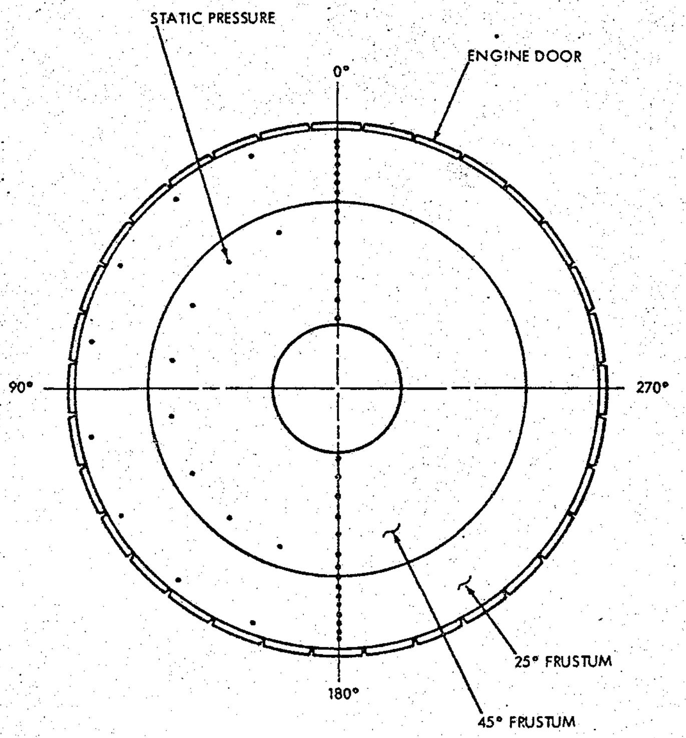

Figure 2.2-1(d). Forebody Instrumentation

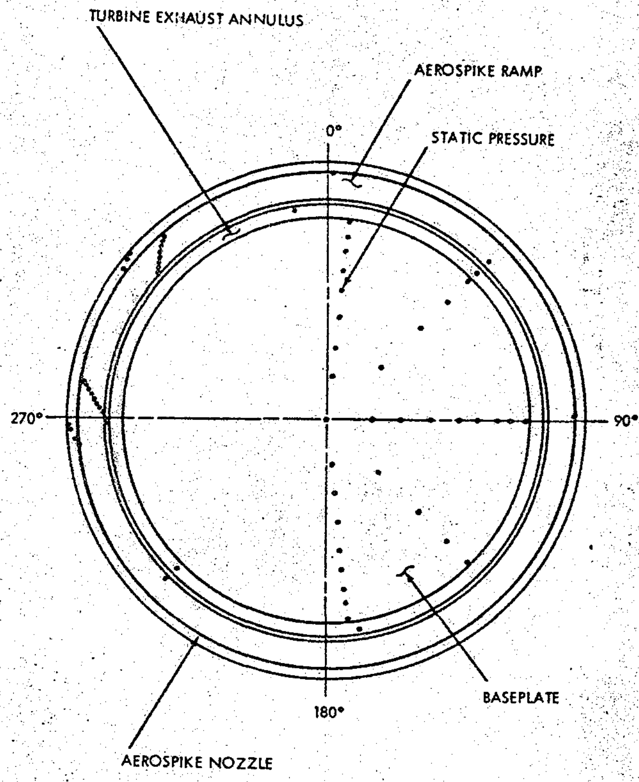

Figure 2.2-1(e). Base Instrumentation

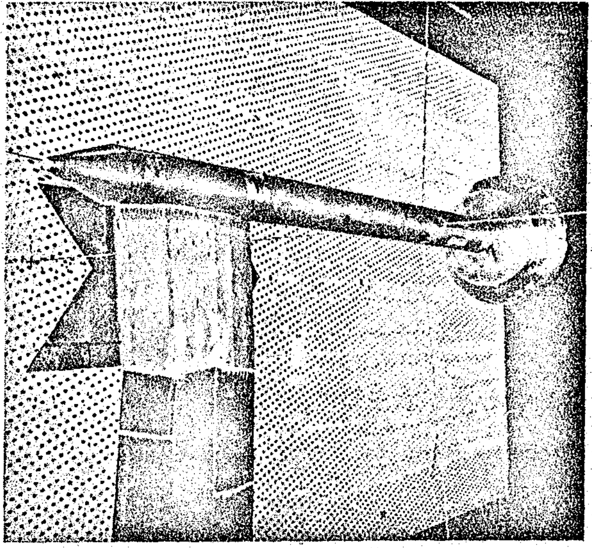

Figure 2.2-2(a). Model Installation

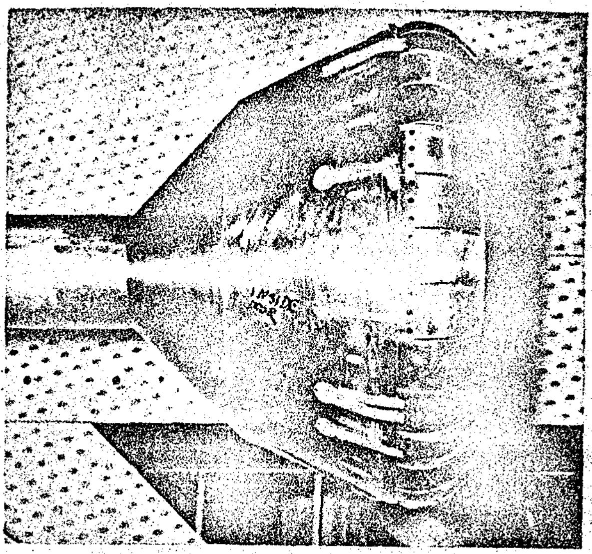

Figure 2.2-2(b). Model Installation

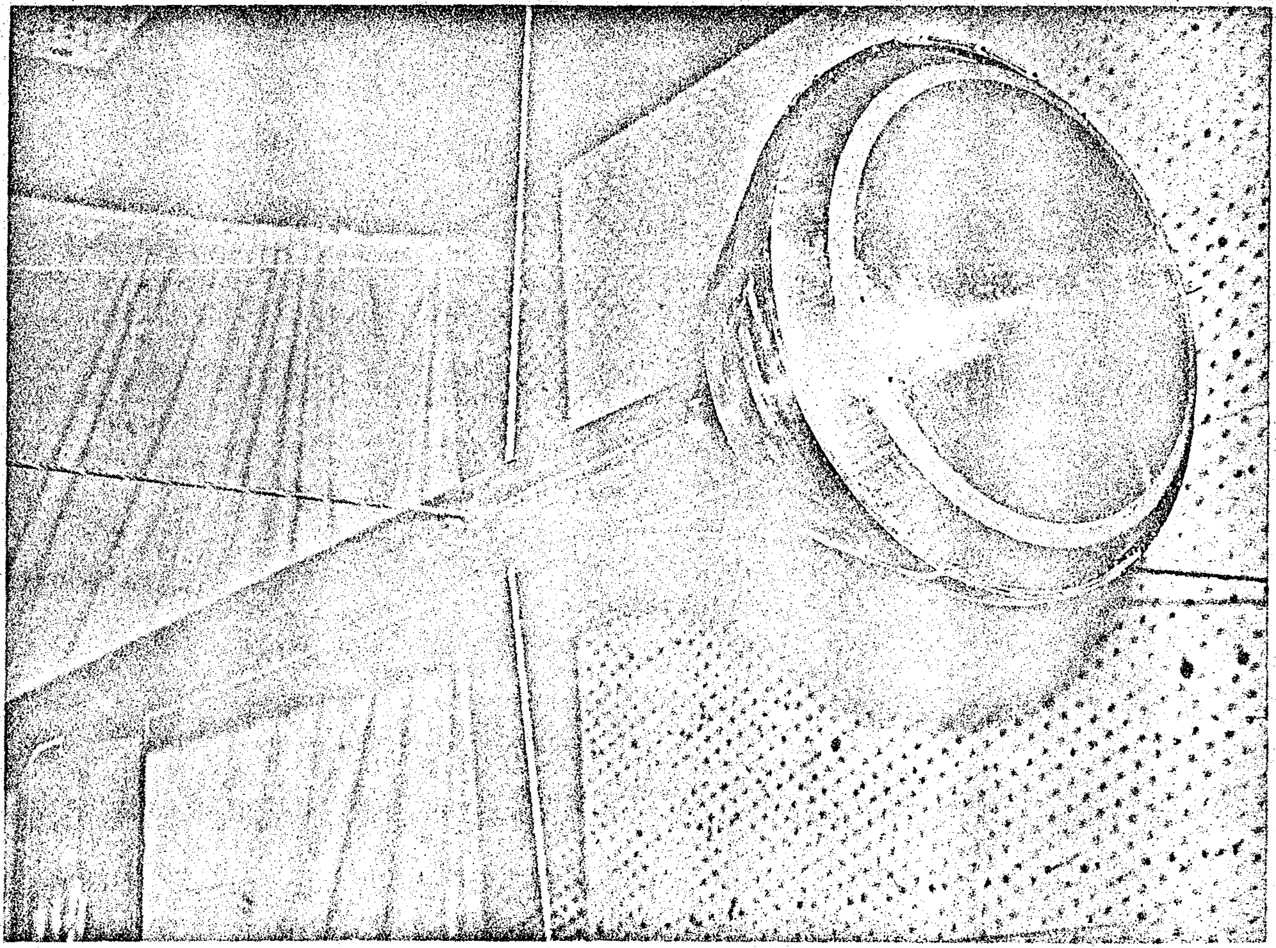

Figure 2.2-2(c). Model Installation At AEDC

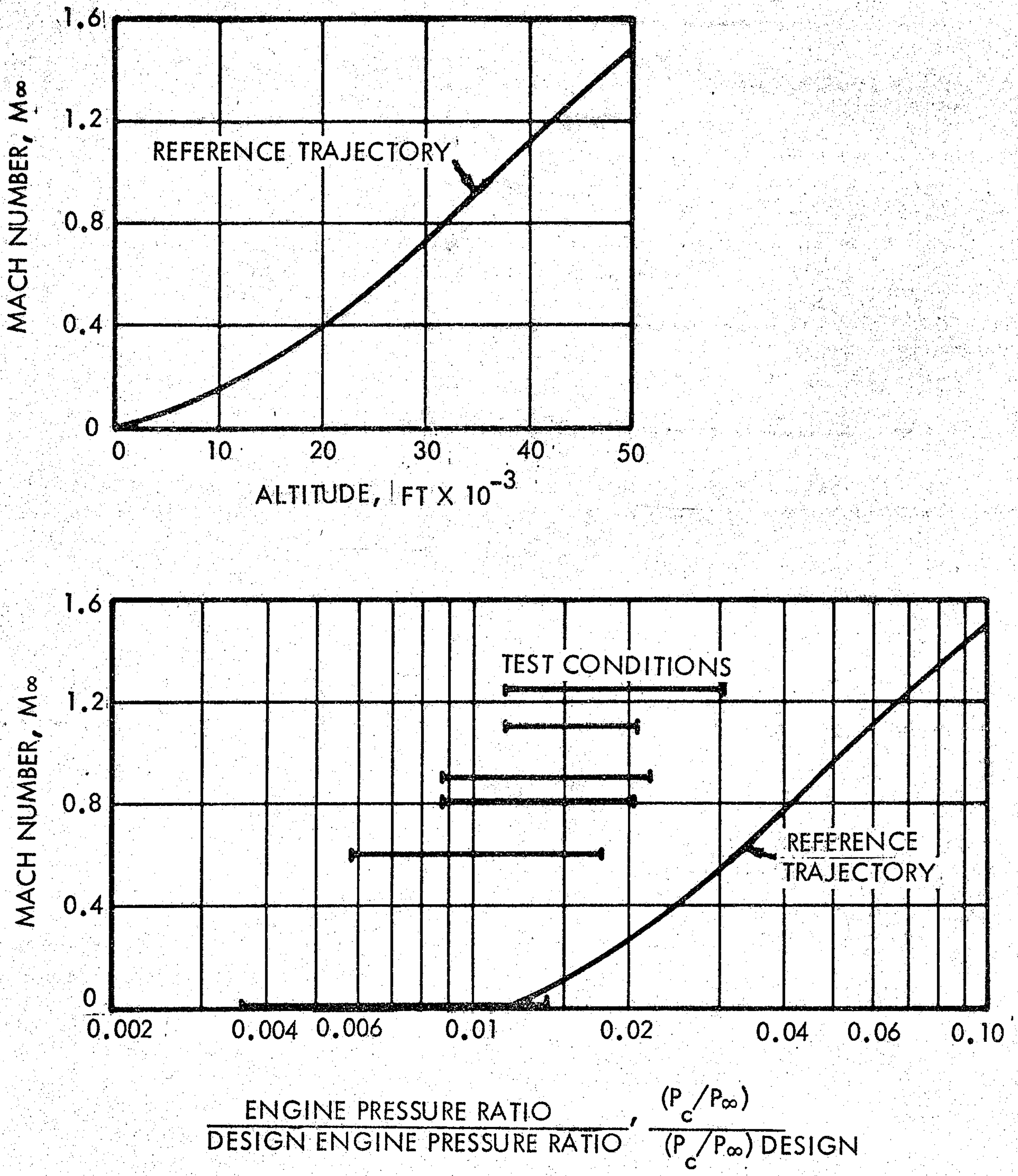

Figure 2.2-3. Reference Trajectory For The SERV Launch Vehicle

It became apparent after several attempts that it would be very difficult to hold the test section Mach number condition of 1.05 as required by the test plan. Therefore, a test Mach number of 1.1 was run in the place of 1.05.

In the last phases of testing a pressure seal in the facility started leaking; this made it impossible to achieve the minimum test section total pressure of 120 psfa. This resulted in the reduction of the doors-off altitude simulation for the final phases of testing.

With the exception of these difficulties, the test program was completed with excellent results. The test model functioned without failure throughout the complete program. Data acquisition was accomplished with a minimum of repeat conditions required. Schlieren photographs of the model base flow are presented in figure 2.2-4 at specific freestream Mach number and engine pressure ratio test conditions. The engine exhaust plume can be easily distinguished; however, the slipstream ambient flow is not visible due to its very low density for these test conditions (noted above).

2.2.4 RESULTS AND DISCUSSION

Complete listings of the test data in digitized form and graphic presentations have been published in references 5 through 7. Appendix A by Rocketdyne documents their analysis of the engine performance test data with the method of extrapolation to full scale.

It became apparent after preliminary analysis of test data that the engine jet exhaust impinged on the engine protection doors for engine pressure ratios, P_c/P_∞, of greater than 380. This had a tendency to alter engine performance, due to a high buildup in the base pressure. As impingement on the engine doors represented an intolerable design condition with respect to door loads and heating, the engine data with doors removed were used to evaluate engine performance and an incremental drag term was included for attachment of the engine doors for flight performance evaluation as discussed in volume 4.

The axial load cell measurements with engine on were used with the evaluated forebody drag and specific local surface pressure measurements to calculate net engine model thrust at each freestream Mach number and engine pressure ratio condition. Figure 2.2-5 presents these results in thrust coefficient form as a function of engine pressure ratio. There is a definite reduction in engine thrust performance with increasing freestream Mach number. This is typical of the influence of the blunt body base pressure trends which this vehicle should exhibit. The effect of the ambient slipstream of aerospike engine performance is determined by the expansion of the engine exhaust flow into the base. For all flight operating pressure ratios, the nozzle momentum thrust term and exhaust flow compression on the aerospike ramp are constant. Only expansion of the flow from the end of the ramp into the base region changes with altitude and slipstream effects. The low expansion pressures of the ambient flow expanding over the peripheral base geometry of the vehicle are reflected through the exhaust plume into the base region causing a reduction in the effective pressure acting on the base heat shield. As this region is considered a component of the total engine thrust, there is, therefore, a reduction in the engine thrust performance as compared to the condition of no slipstream ($M_\infty = 0$).

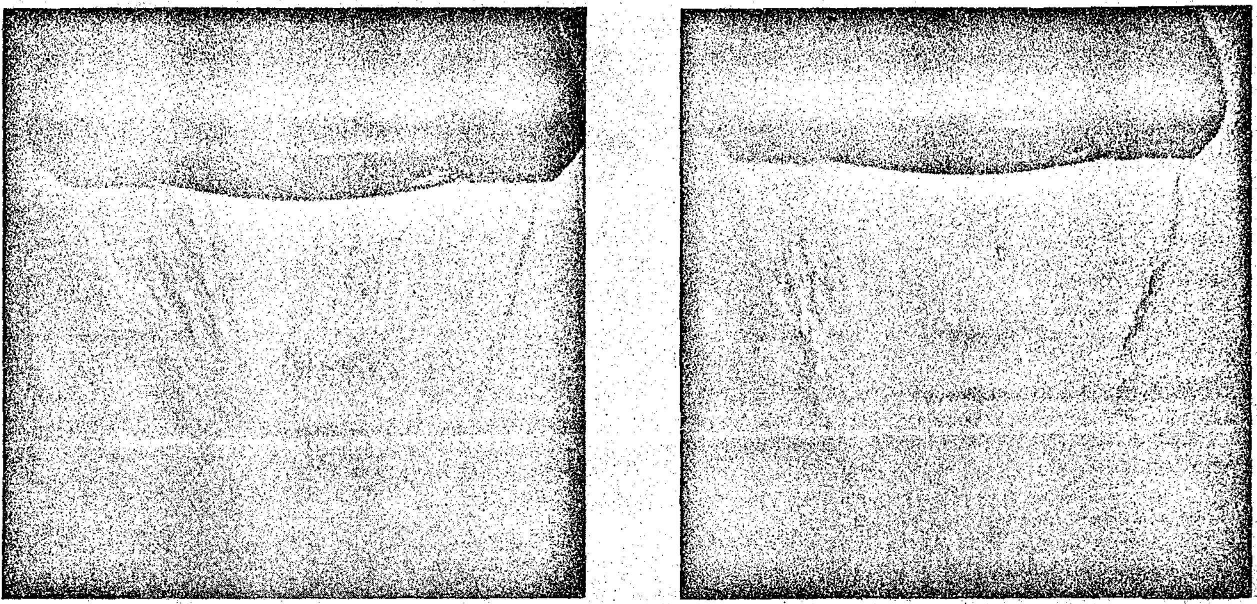

(a) $M_\infty = 0$; $\alpha = 0$; $P_c/P_\infty = 406$
ENGINE DOORS ON

(b) $M_\infty = 0.8$; $\alpha = 0$; $P_c/P_\infty = 491$
ENGINE DOORS ON

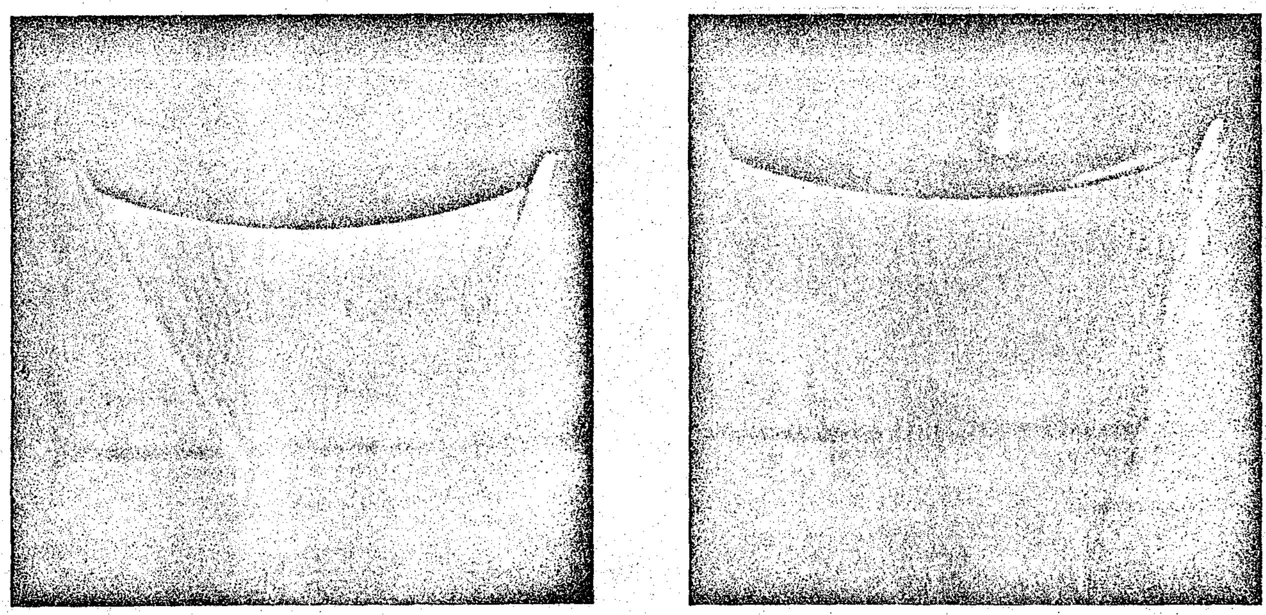

(c) $M_\infty = 0$; $\alpha = 0$; $P_c/P_\infty = 484$
ENGINE DOORS OFF

(d) $M_\infty = 0.6$; $\alpha = 0$; $P_c/P_\infty = 580$
ENGINE DOORS OFF

Figure 2.2-4. Schlieren Photograph of Model Base Flow

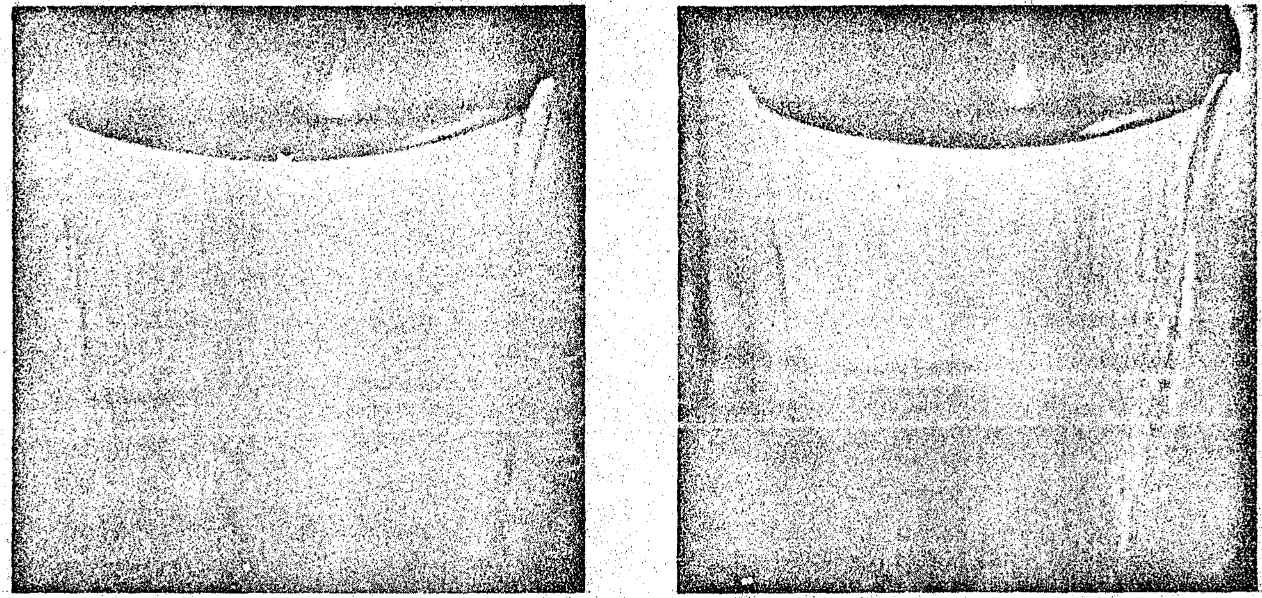

(e) $M_\infty = 0.9$; $\alpha = 0$; $P_c/P_\infty = 399$
ENGINE DOORS OFF

(f) $M_\infty = 1.1$; $\alpha = 0$; $P_c/P_\infty = 394$
ENGINE DOORS OFF

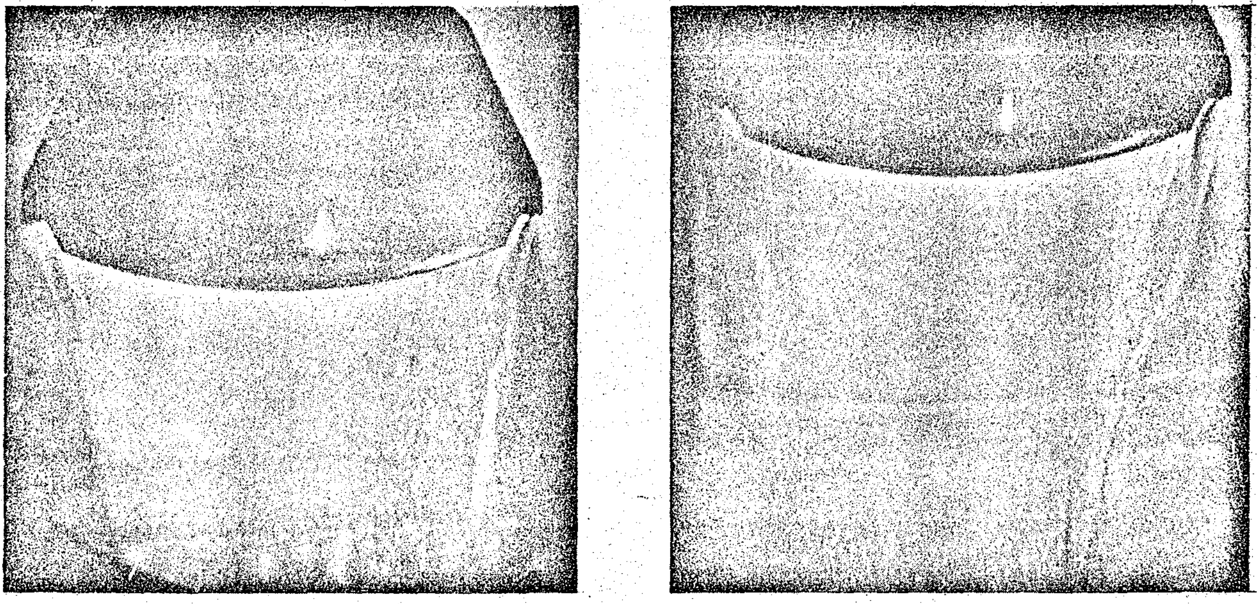

(g) $M_\infty = 1.25$; $\alpha = 0$; $P_c/P_\infty = 402$
ENGINE DOORS OFF

(h) $M_\infty = 1.25$; $\alpha = 0$; $P_c/P_\infty = 763$
ENGINE DOORS OFF

Figure 2.2-4. Schlieren Photograph of Model Base Flow (continued)

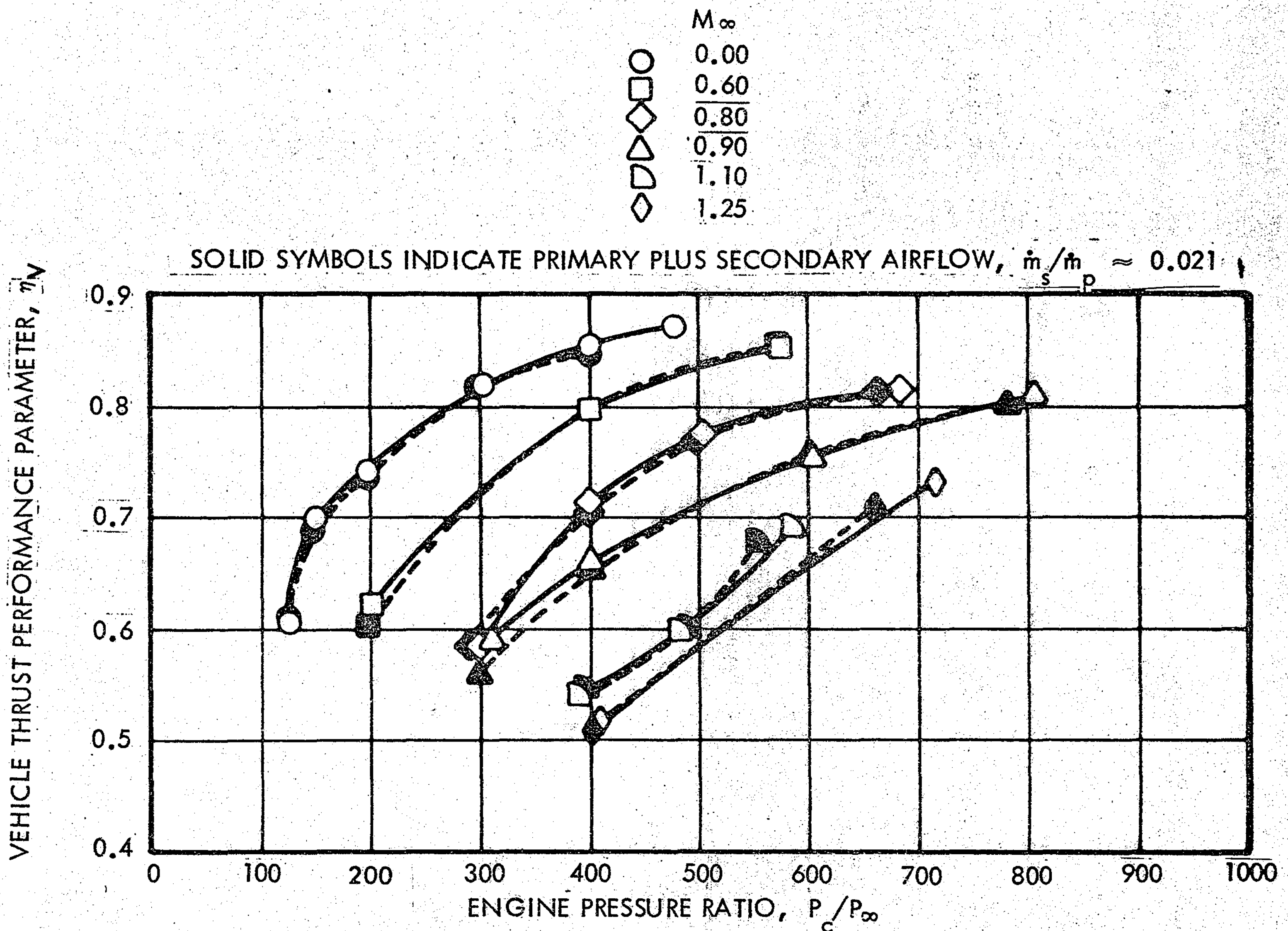

NOTE: REENTRY PROTECTION DOORS OFF

Figure 2.2-5. Variation Of Model Thrust Performance With Engine Pressure Ratio

Engine thrust performance increases with increasing pressure ratio and should increase with the addition of injection of turbine exhaust or secondary flow into the base. The increase in engine performance by secondary flow injection will be a small percentage, but should definitely be distinguishable. That was not always the result in this test; however, the turbine exhaust location and flow rate were fixed and no attempt was made at optimization.

Figure 2.2-6(a) shows mean base pressure ratio (P_{B_V}/P_∞) over the area outside of the engine nozzle perimeter. These pressure ratios are a direct function of the pumping action of the engine exhaust flow and the ambient slipstream expanding over the vehicle external geometry. They are seen to decrease with increasing slipstream Mach number, but have little variation (except M=0.6) with engine pressure ratio (P_c/P_∞) for the range tested. At M =0.0 the drop in this local pressure below ambient must be due solely to the pumping action of the engine.

The mean pressure ratios (P_{B_E}/P_∞) in the base heat shield region are shown in figure 2.2-6(b) as functions of flight Mach number and engine pressure ratio (P_c/P_∞). These too decrease with increasing freestream Mach number and reflect almost directly the reduction in engine thrust performance due to slipstream effects. Within the pressure ratio range tested, these pressures are also very nearly constant with increasing engine pressure ratio (P_c/P_∞). Secondary flow injection into the base definitely appears to increase the pressures in this region.

2.2.5 CONCLUSIONS

The most significant result of the SERV base flow test was that the engine exhaust jet and base flow field were typically characteristic of aerospike engines. The integrated SERV concept, with large area ratio at open wake and low engine pressure ratios, did not indicate any new or different trends from previous reference test data. Engine performance did prove to be sensitive to forebody geometry slipstream and the exhaust plume expanding into the base area. This of course was due to the large portion of engine thrust which is determined by these areas for SERV. The necessary data were acquired, however, to assess the influence of all these parameters for the specific SERV vehicle application, within the accuracy level of a Phase A feasibility study. The basis for extrapolation to full-scale flight performance was established and the comparison with original predictions was good (see appendix A for detailed analysis and discussion).

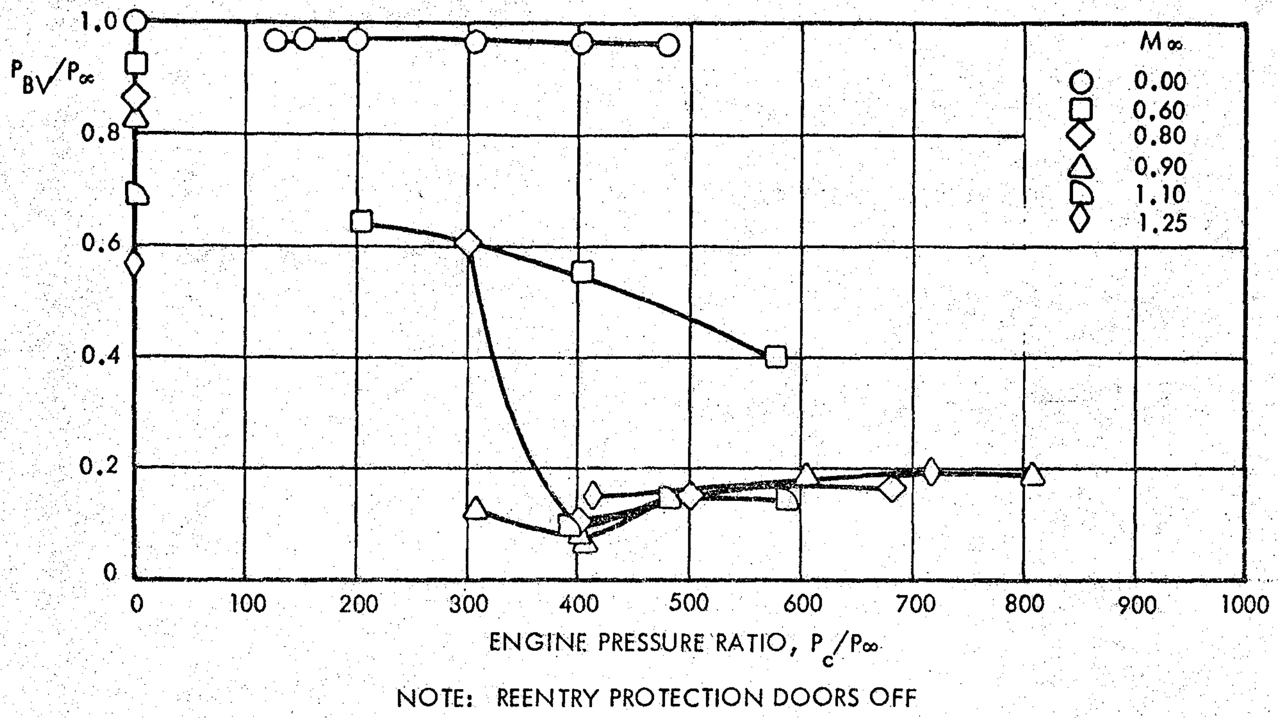

Figure 2.2-6(a). Variation of Area-Weighted Shroud Pressure with Engine Pressure Ratio

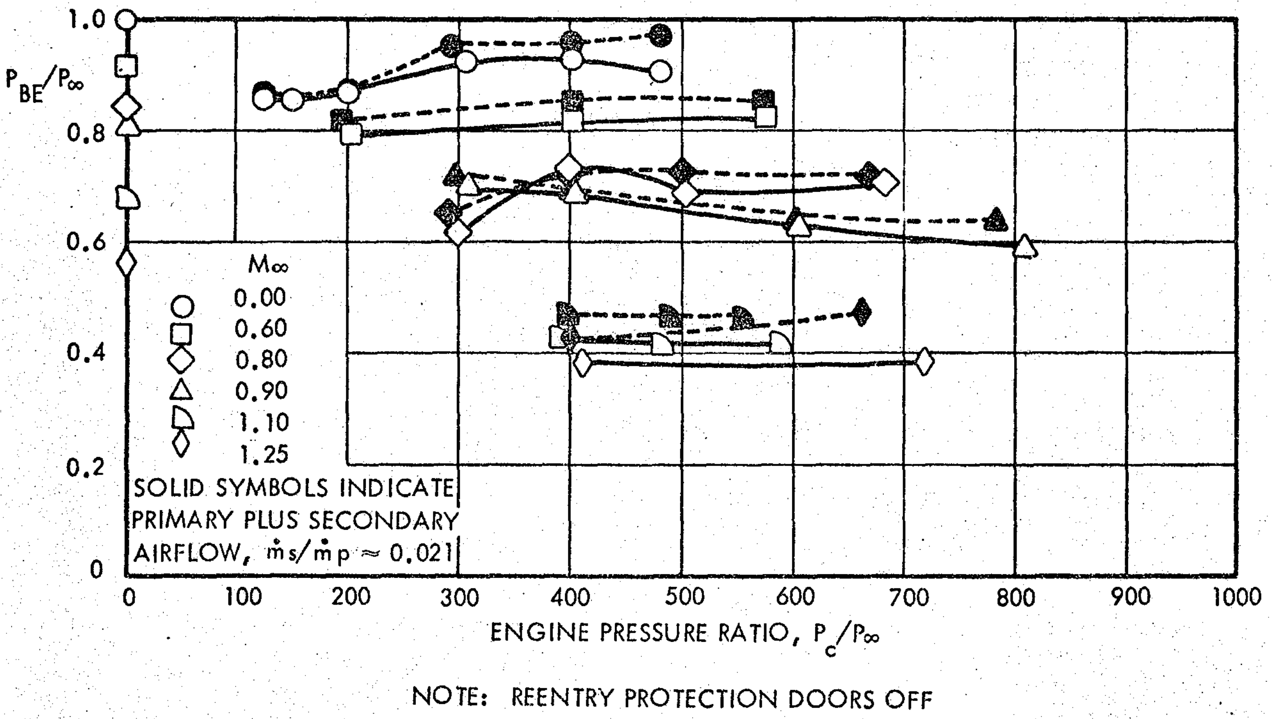

Figure 2.2-6(b). Variation of Area-Weighted Shroud Pressure with Engine Pressure Ratio

Section 3

ASCENT CONFIGURATION FORCE TESTS

3.1 TEST PLAN

To verify SERV vehicle payload capability and flight control requirements in the ascent mode, a definition of flight aerodynamic stability and drag characteristics was obtained from wind tunnel tests according to plans outlined in references 8 and 9. These experimental force tests conducted in the 6-foot Supersonic Wind Tunnel (SWT) and the Unitary Plan Wind Tunnel (UPWT) at NASA Ames Research Center and Langley Research Center, respectively; covered a combined Mach number range of 0.4 to 4.64 (subsonic to high supersonic). Lower Mach numbers of 0.4 to 2.0 were obtained in the Ames facility, while remaining supersonic speeds were acquired in the Langley facility. Angle-of-attack range for ascent mode testing varied from -4 to +16 degrees in both facilities.

Ascent configurations tested in these programs varied primarily in payload geometry with four different forebodies being considered. These were: Retracted Personnel Module (PM); Winged Spacecraft (MURP); Large Payload (LPL); and Extended Personnel Module (PM). An additional variation involved a change in degree of aerospike protection door opening.

3.2 MODEL DESIGN AND FABRICATION

The four ascent configurations having 25-degree aerospike engine door openings are illustrated in figure 3.2-1. Figure 3.2-1(e) shows the Extended Personnel Module configuration again but with engine doors open 45 degrees. The models were fabricated of stainless steel to 0.55 percent of full scale by Standard Tool and Die Inc. of Los Angeles, California. All were approximately 6 inches in diameter with the largest (LPL) having an overall length of 8.87 inches and the shortest (Retracted Personnel Module) 5.69 inches. All component model parts (including interchangeable reentry configuration parts) are illustrated in figure 3.2-2.

Pertinent model reference dimensions and areas for ascent configurations were: reference diameter of 6 inches; reference area of 28.26 square inches; and a base area of 21.23 square inches.

Model strengths were adequate to withstand anticipated maximum loads with a safety factor of four (4.0) based on material yield strength.

3.3 TEST PROCEDURE

The tunnel installation, typical in both facilities, is illustrated in figure 3.3-1. The models were sting mounted from a rear tunnel support system which

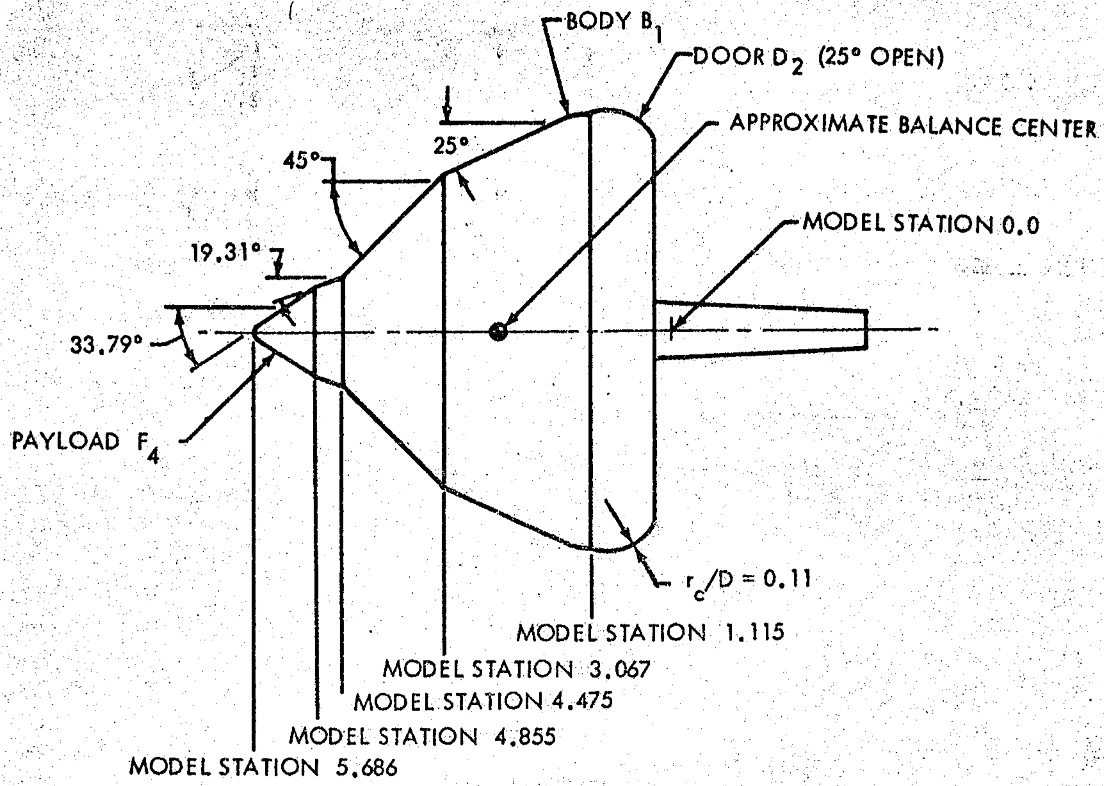

Figure 3.2-1(a). Retracted PM Payload Configuration - Model $F_4B_1D_2$

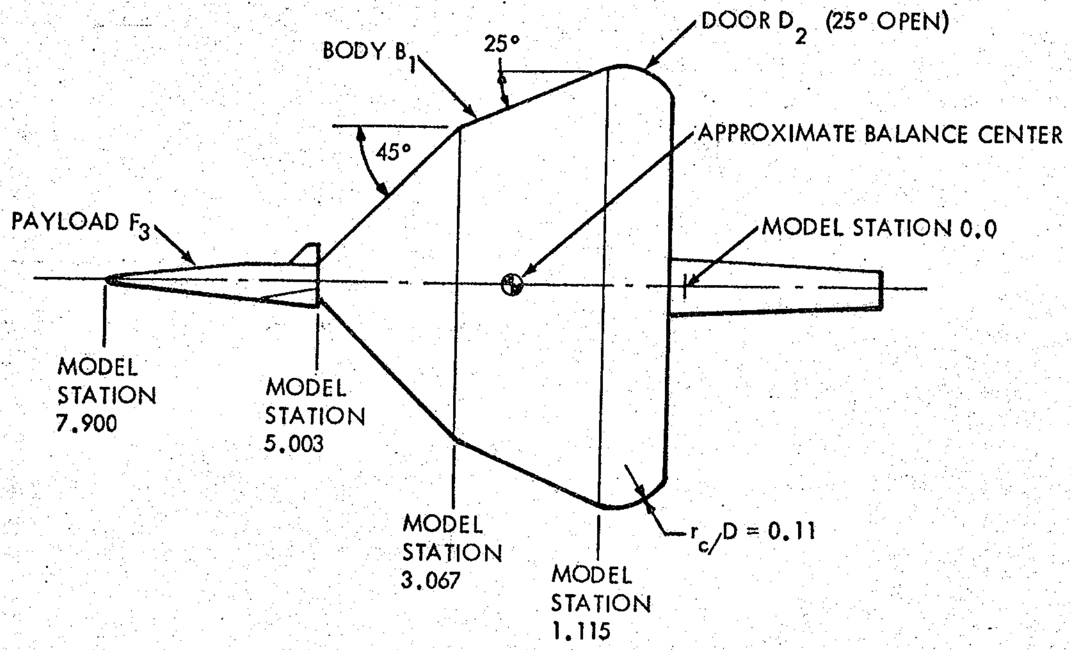

Figure 3.2-1(b). Winged Orbiter Payload Configuration - Model $F_3B_1D_2$

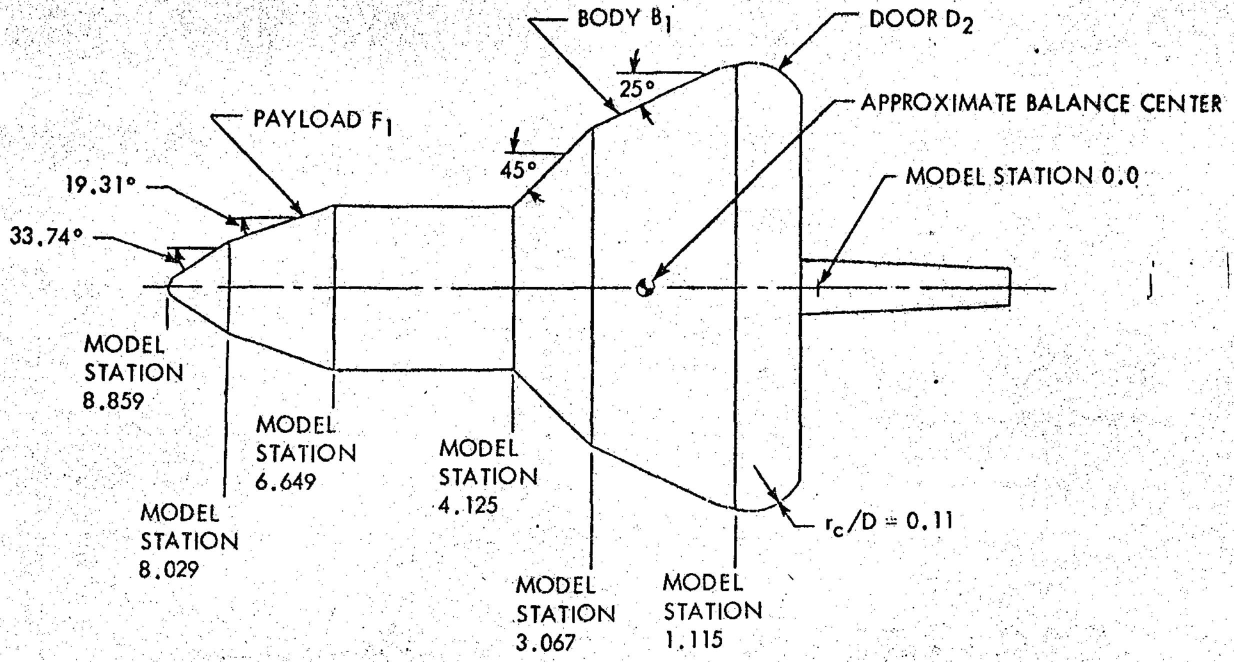

Figure 3.2-1(c). Large Payload (LPL) Configuration - Model $F_1B_1D_2$

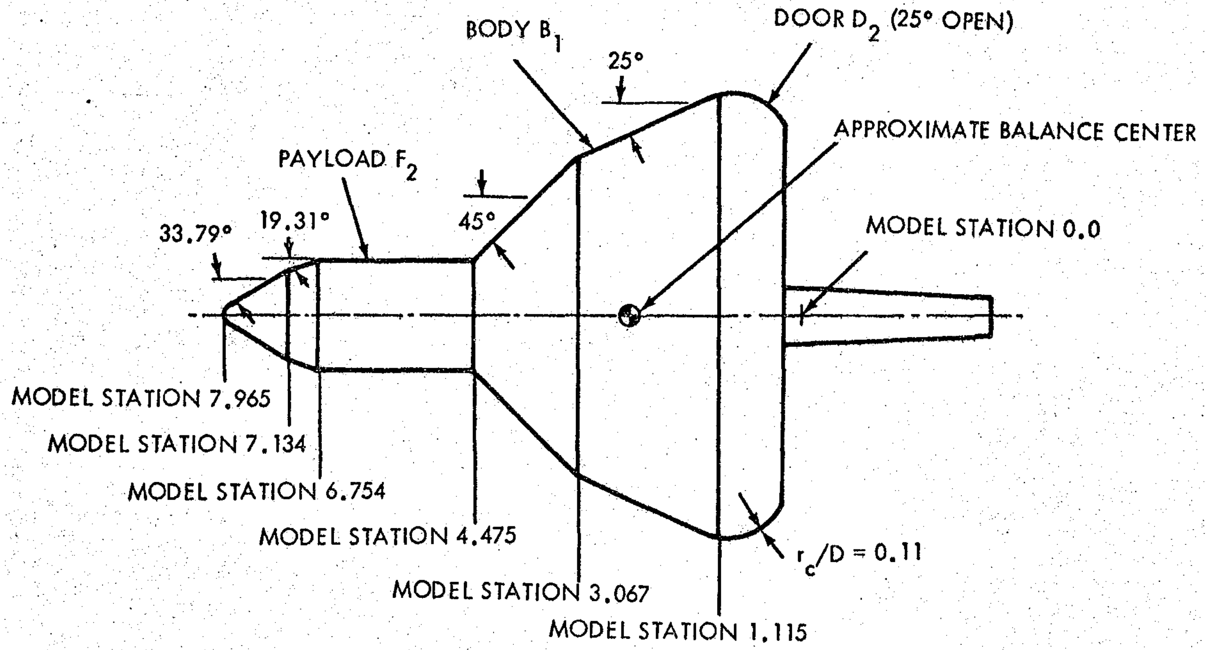

Figure 3.2-1(d). Extended Personnel Module Payload Configuration - Model $F_2B_1D_2$

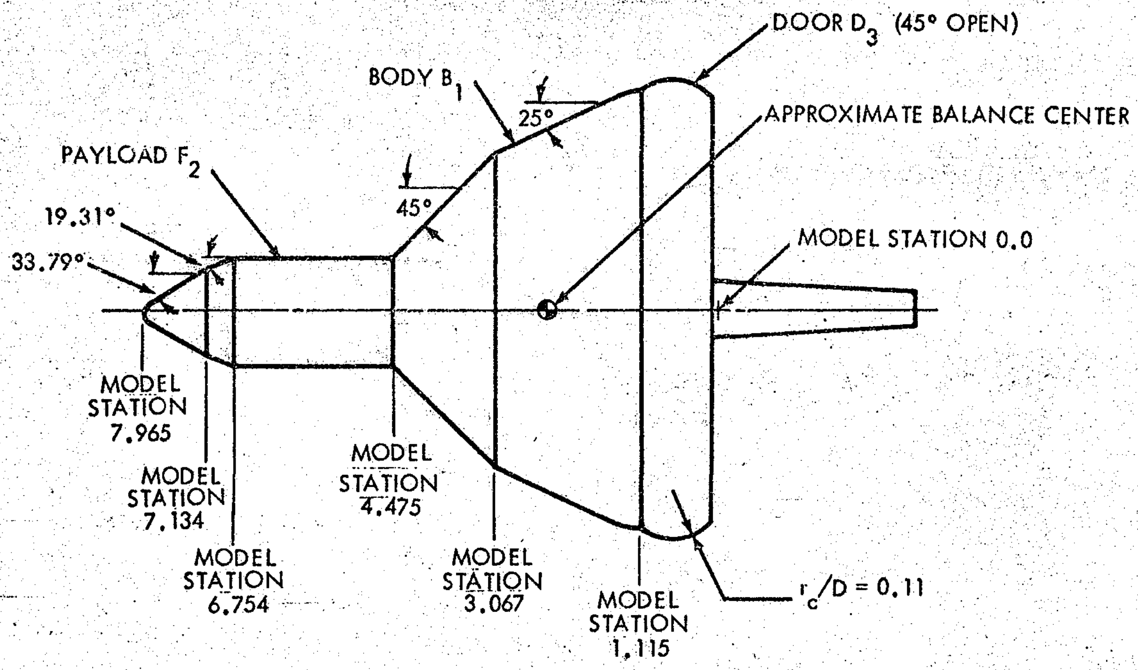

Figure 3.2-1(e). Extended Personnel Module Payload Configuration (Engine Doors Open 45°) - Model $F_2B_1D_3$

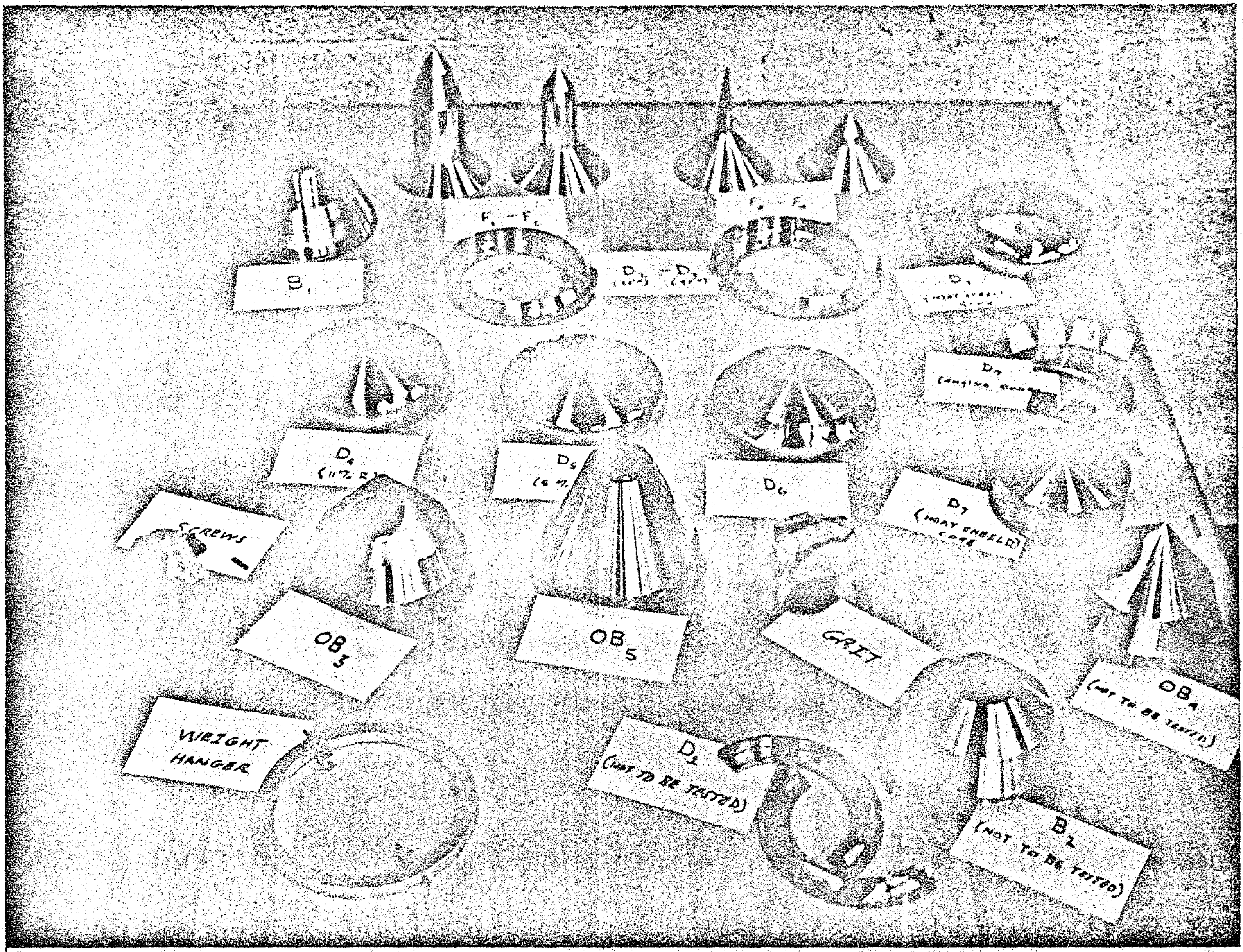

Figure 3.2-2. Model Components

Figure 3.3-1 Typical SERV Baseline Ascent Model Tunnel Installation

incorporated a Langley UT-22 strain gage balance and tubing for base cavity pressure measurement. The UT-22 balance measured three components: normal force, pitching moment and axial force. It was capable of sustaining maximum loads of 300 pounds in normal and axial directions and 300 inch pounds of pitching moment. Actual maximum loads encountered however were always less than these limits.

Data obtained from the UT-22 balance and pressure transducers were reduced to force, moment and base pressure coefficients defined as:

$$1)\quad C_N = \frac{\text{Normal Force}}{q_\infty S}$$

$$2)\quad C_M = \frac{\text{Pitching Moment}}{q_\infty SD}$$

$$3)\quad C_A = \frac{\text{Total Axial Force}}{q_\infty S}$$

$$4)\quad C_{A_B} = \frac{(P_\infty - (P_{b_1} + P_{b_2})/2)A_b}{q_\infty S}$$

where q_∞ = test section dynamic pressure, S = reference area, D= reference diameter, and A_b = ascent configuration base area.

Moments measured by the balance were initially referenced to its electrical center, and then transferred to model station 0.0 (figure 3.2-1). The transfer distance from the balance moment reference to the reference model station was measured by hanging weights with the balance installed. In addition to the above coefficients, Schlieren photographs of the shock wave systems were acquired at all conditions of interest.

Test run numbers, correlated with nominal Mach numbers and angle-of-attack ranges used in the testing, are shown in matrix form in table 3.3-1. Angle-of-attack ranges were generally covered in 2-degree steps.

No specific problems developed during the testing of ascent configurations. No significant bias or shift in the data was seen except in the pitching moment characteristics at Mach 0.4 for both MURP and Retracted PM configurations, more so for the latter model, however. This data bias was more of a serious problem in the reentry portion of the testing where offset stings were employed to achieve extended angle-of-attack ranges. In these cases, the magnitude of any data shift was often smaller than the accuracy limits of the balance.

3.4 DISCUSSION OF RESULTS

The results of these experimental investigations of SERV ascent configurations have been presented in detail in data reports (references 10 and 11). Aerodynamic characteristics given in these references were generally in agreement with predicted trends as estimated and derived by empirical and/or theoretical methods. Some sample characteristics from references 10 and 11 are shown in coefficient form in figures 3.4-1 and 3.4-2 as functions of angle-of-attack for a Mach number of 1.2 (peak dynamic pressure region) and a second at a high supersonic value of 4.64.

Normal Force Coefficient M= 1.205

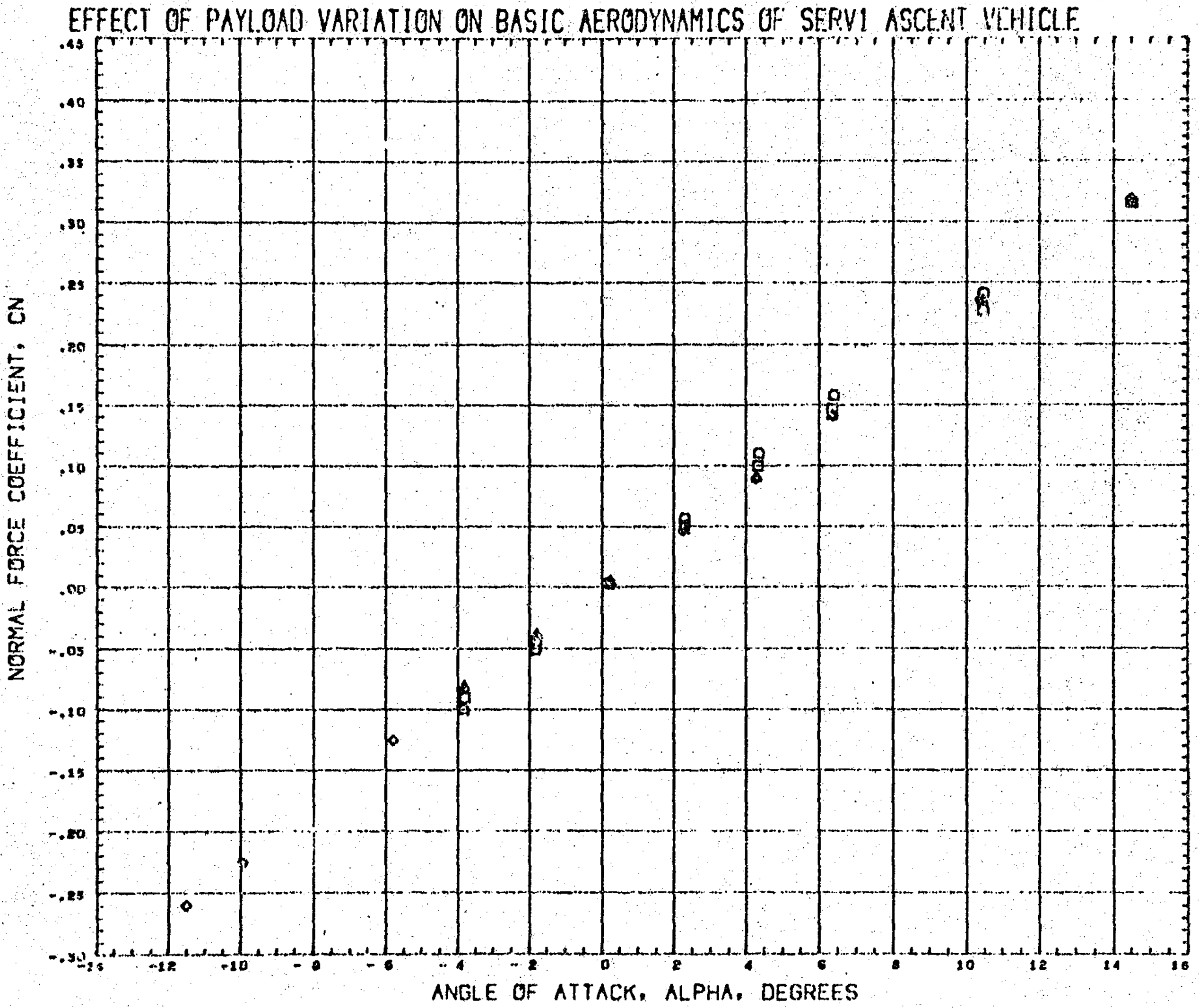

DATA SET	SYMBOL	CONFIGURATION DESCRIPTION
(BA0001)	○	AMES 66-522 CCSD SERVI ASCENT VEHICLE F1B1D2
(BA0002)	□	AMES 66-522 CCSD SERVI ASCENT VEHICLE F2B1D2
(BA0004)	♀	AMES 66-522 CCSD SERVI ASCENT VEHICLE F3B1D2
(BA0005)	Δ	AMES 66-522 CCSD SERVI ASCENT VEHICLE F4B1D2

MACH 1.205

PARAMETRIC VALUES

BETA 0.000 EDOOR 25.000
RC/D 0.110

REFERENCE INFORMATION

REFS	28.2744	SQ.IN.
REFL	6.0000	IN.
REFB	0.0000	IN.
XMRP	8.8590	IN.
YMRP	0.0000	IN
ZMRP	0.0000	IN.
SCALE	0.5500	PERCNT

Figure 3.4-1(a).

Pitching Moment Coefficient M= 1.205

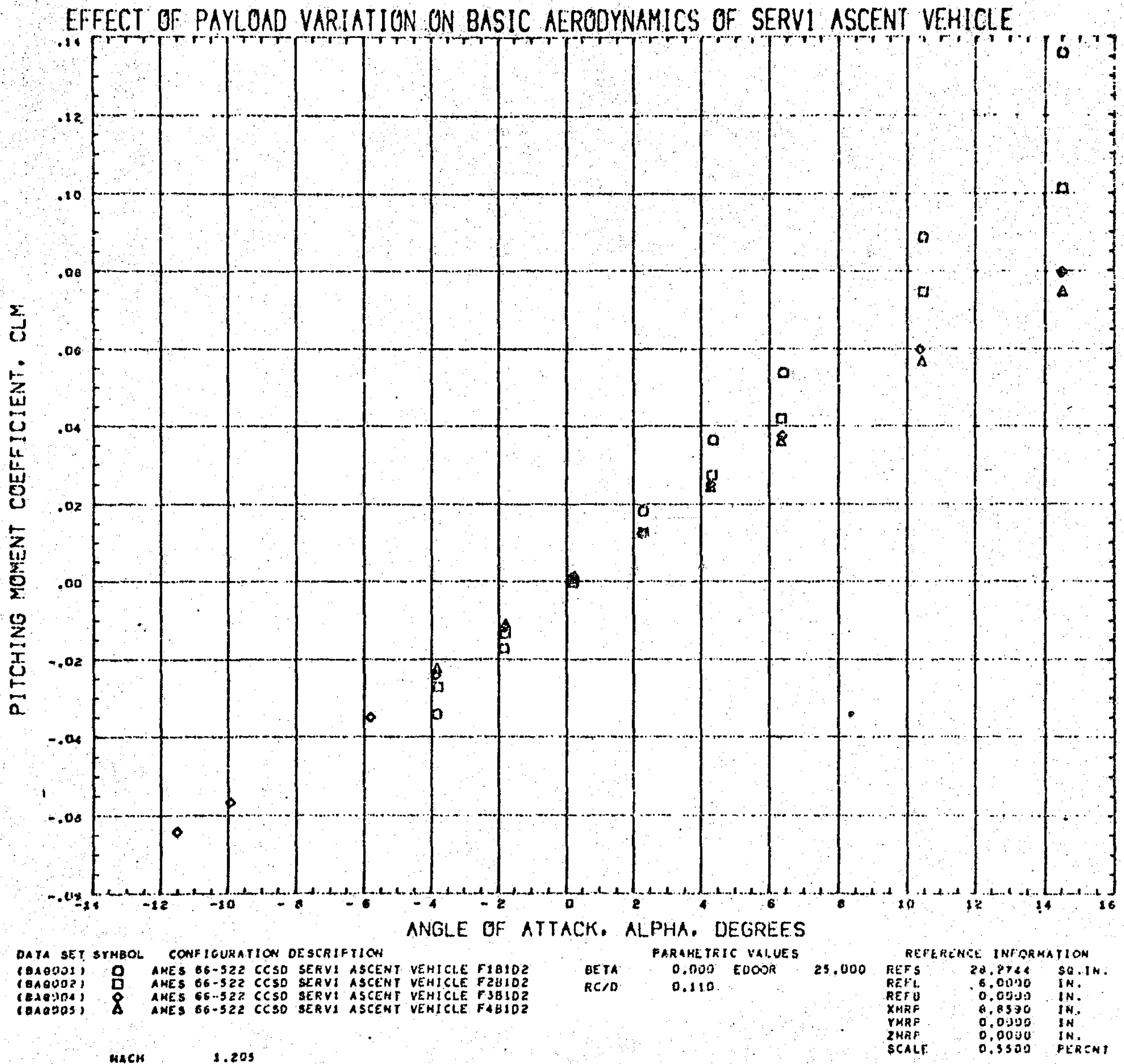

Figure 3.4-1(b).

Forebody Axial Force Coefficient M= 1.205

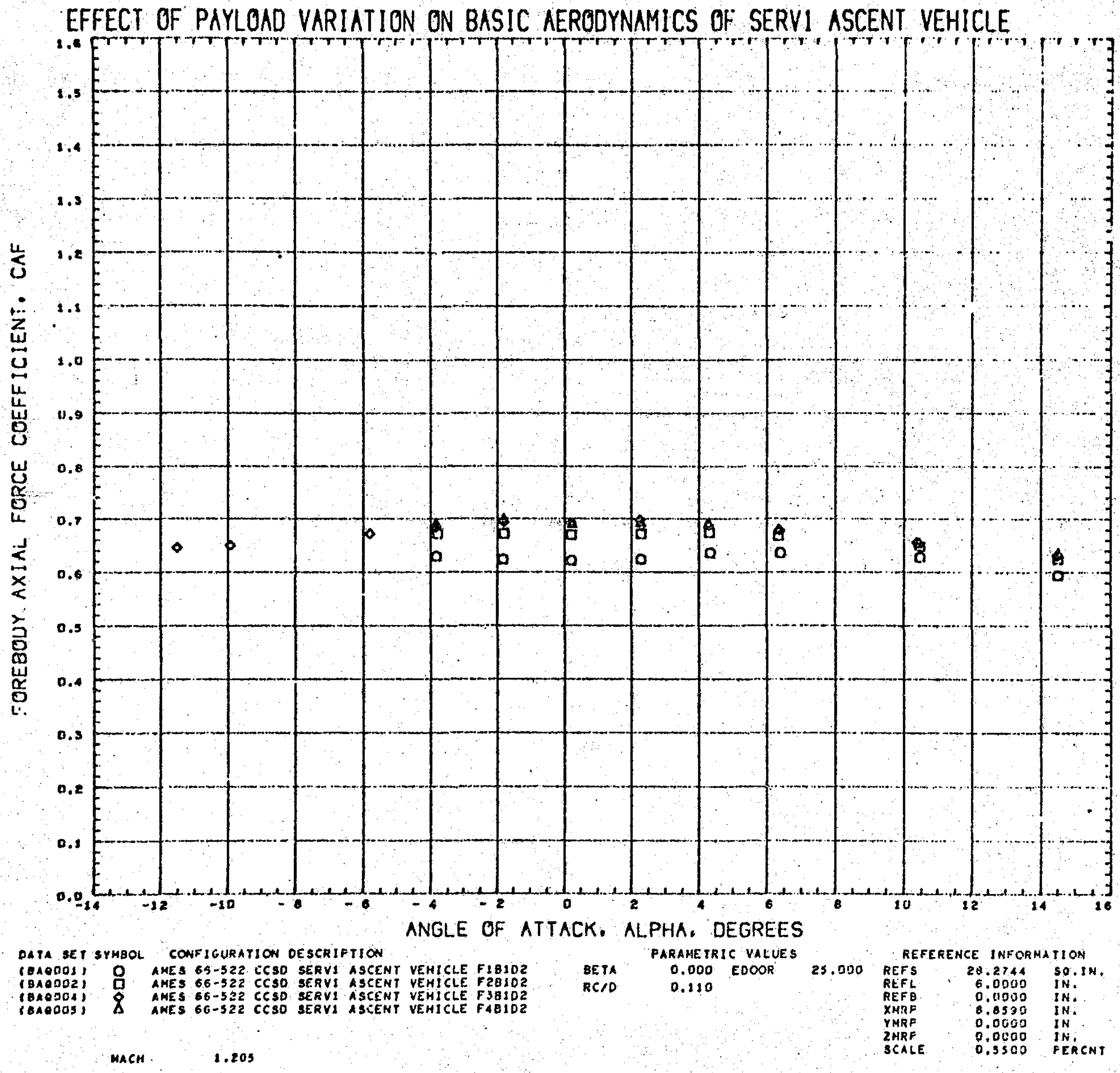

Figure 3.4-1(c).

Axial Force Coefficient M=1.205

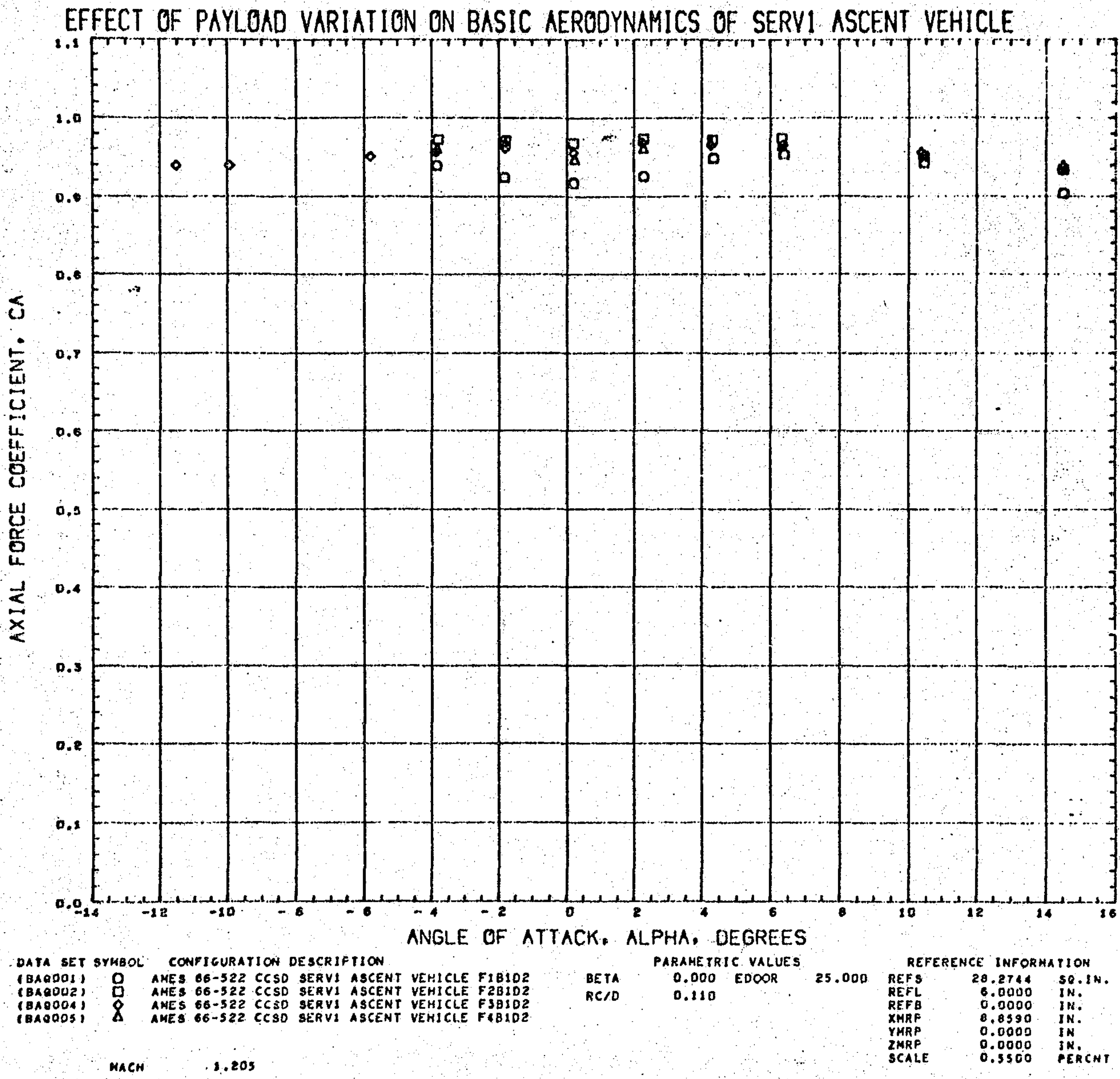

Figure 3.4-1(d).

Normal Force Coefficient M = 4.64

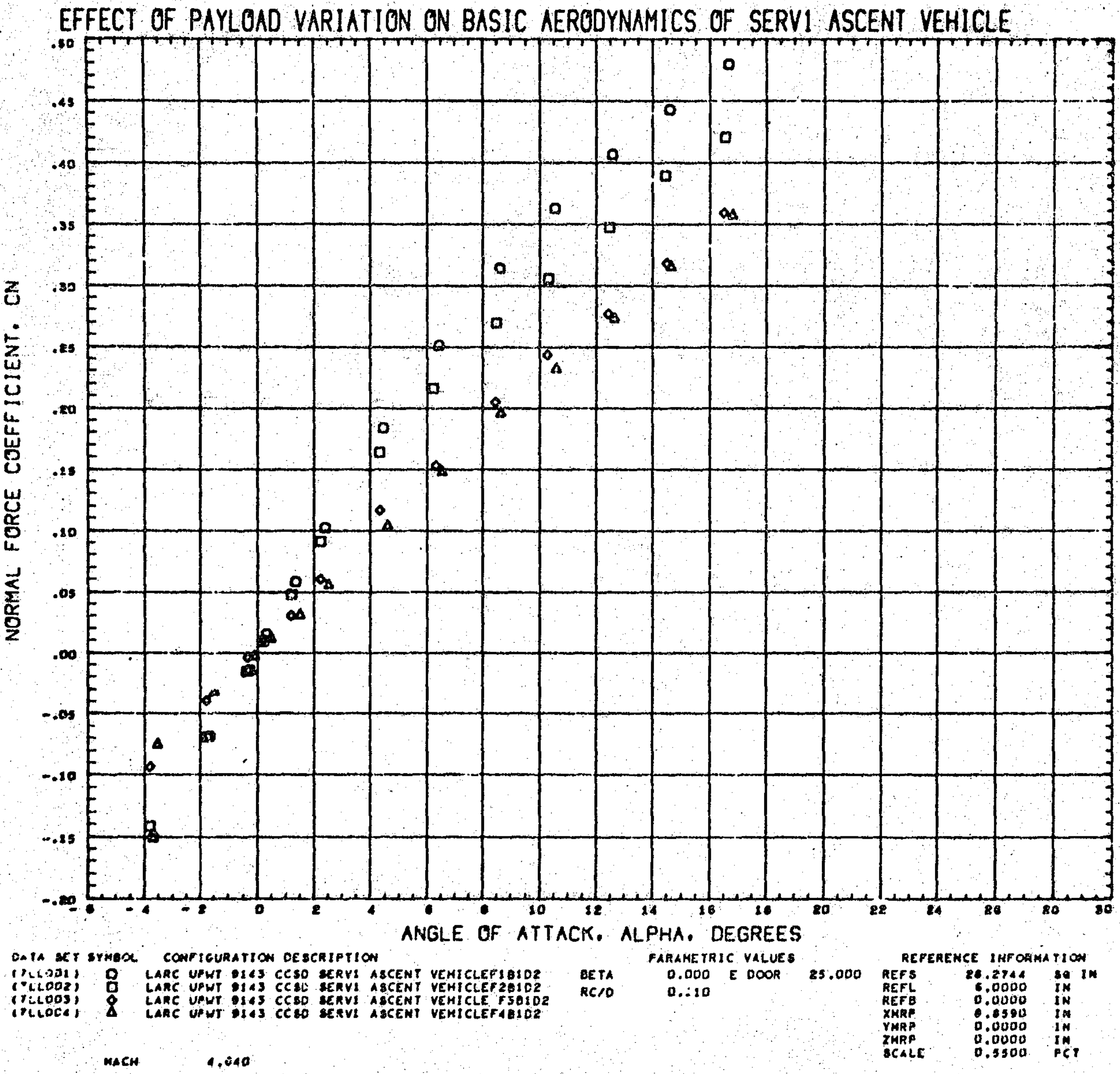

Figure 3.4-2(a).

Pitching Moment Coefficient M= 4.64

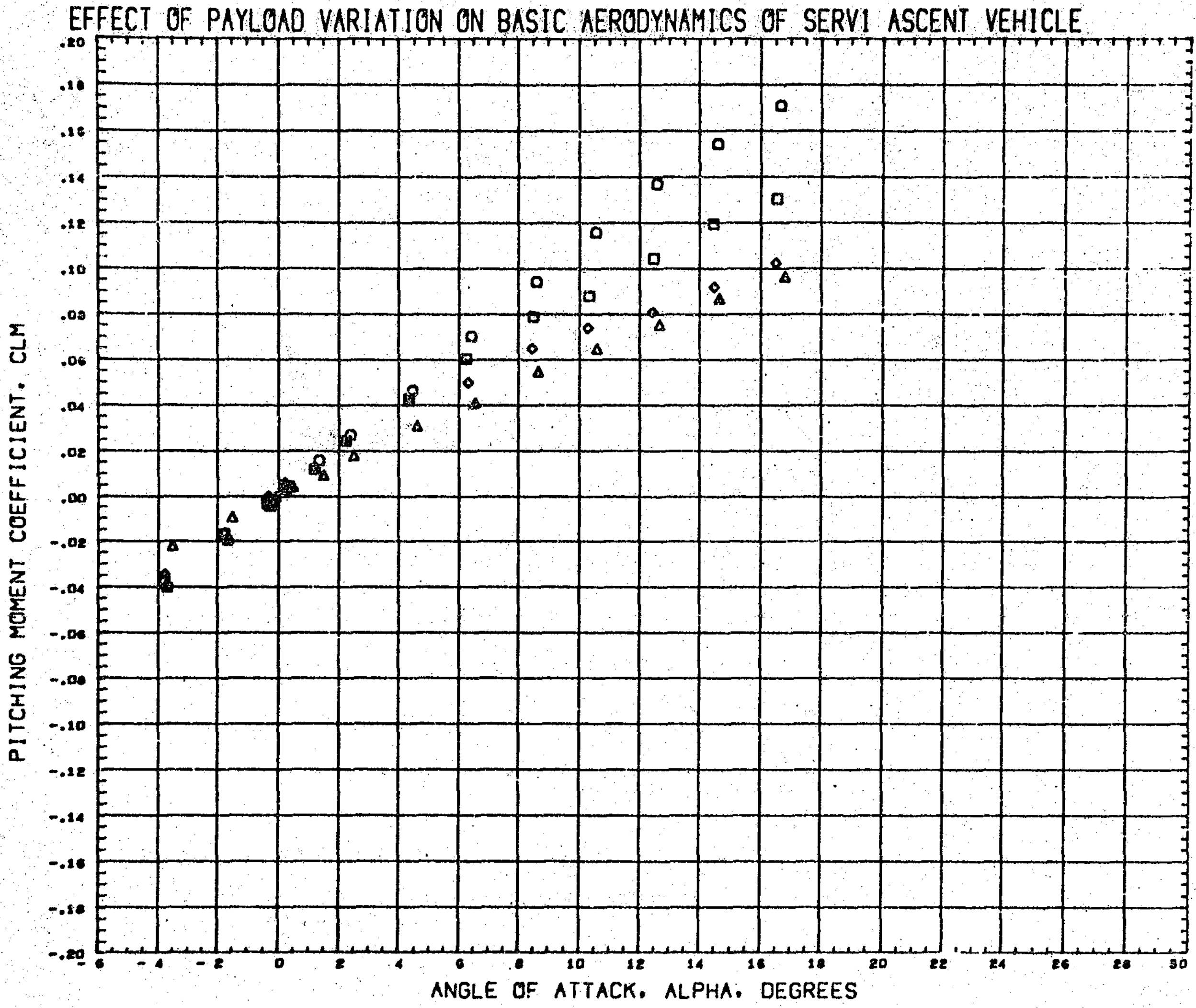

DATA SET	SYMBOL	CONFIGURATION DESCRIPTION
(7LL001)	○	LARC UPWT 9143 CCSD SERV1 ASCENT VEHICLEF1B1D2
(7LL002)	□	LARC UPWT 9143 CCSD SERV1 ASCENT VEHICLEF2B1D2
(7LL003)	◇	LARC UPWT 9143 CCSD SERV1 ASCENT VEHICLE F3B1D2
(7LL004)	△	LARC UPWT 9143 CCSD SERV1 ASCENT VEHICLEF4B1D2

MACH 4.640

PARAMETRIC VALUES

BETA	0.000	E DOOR	25.000
RC/D	0.110		

REFERENCE INFORMATION

REFS	28.2744	SQ IN
REFL	6.0000	IN
REFB	0.0000	IN
XMRP	8.8590	IN
YMRP	0.0000	IN
ZMRP	0.0000	IN
SCALE	0.5500	FCT

Figure 3.4-2(b).

Forebody Axial Force Coefficient M= 4.64

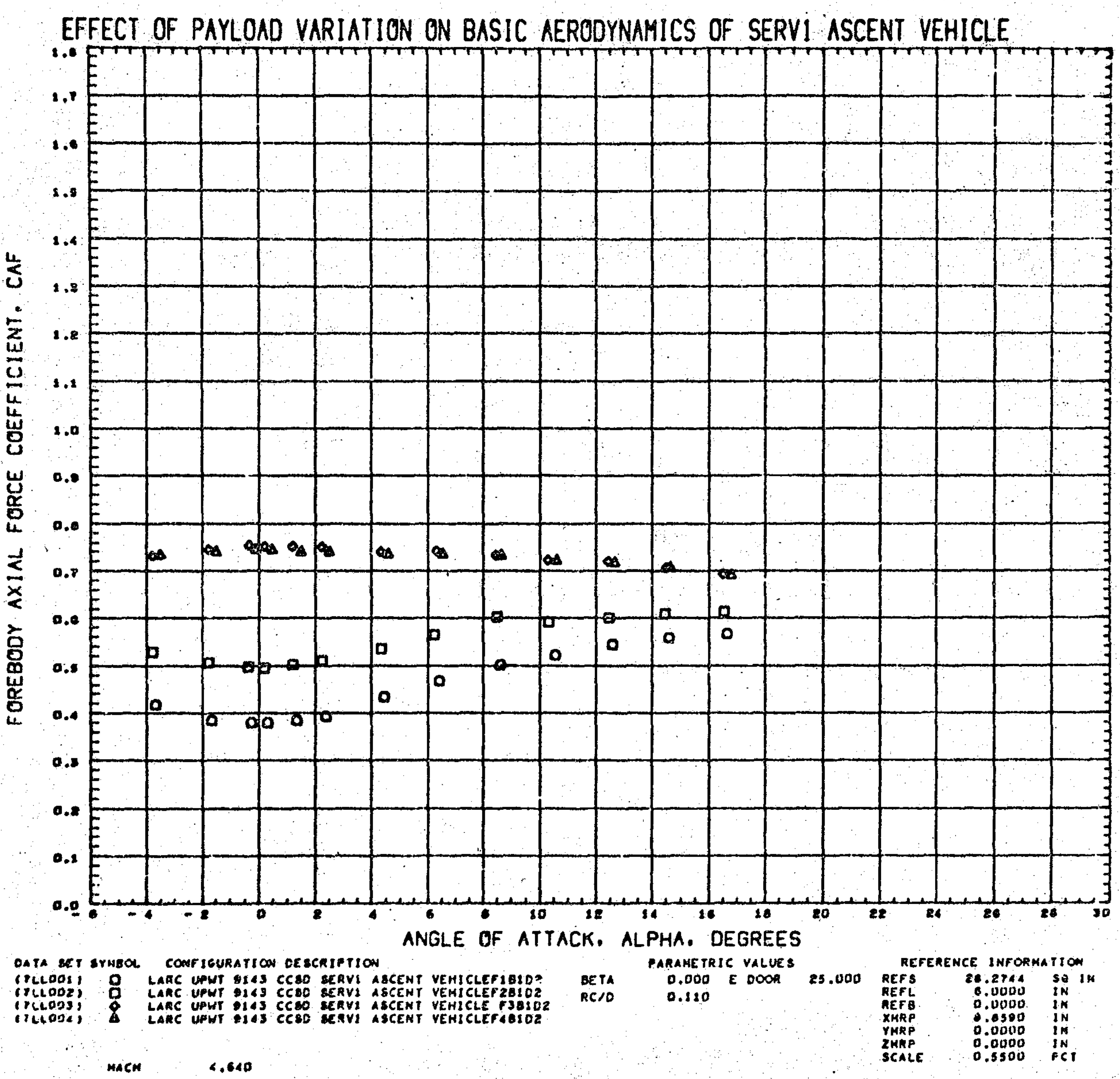

Figure 3.4-2(c).

Axial Force Coefficient M= 4.64

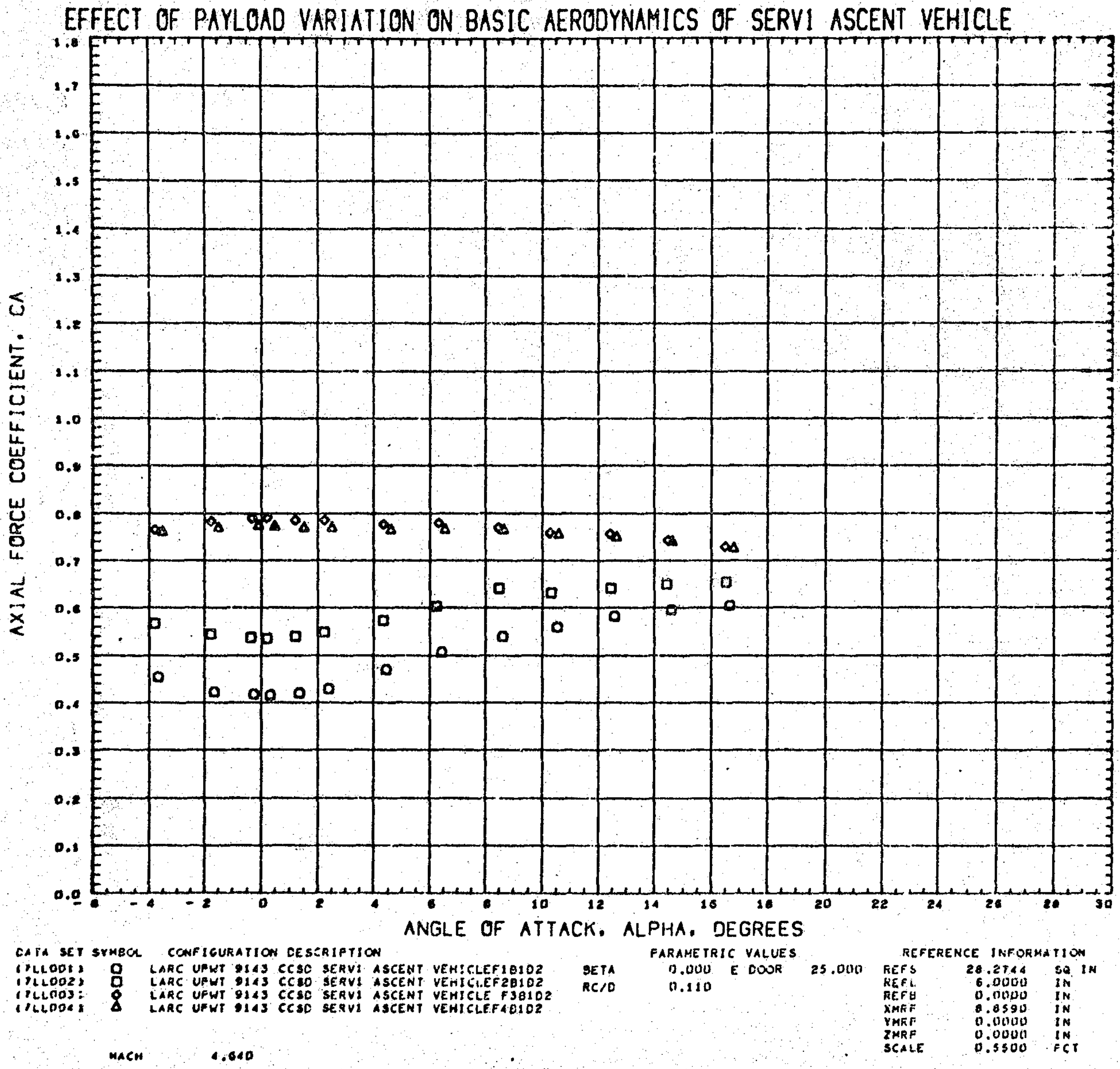

Figure 3.4-2(d).

Table 3.3-1. Test Log

ASCENT CONFIGURATION	TEST RUN NUMBERS (REFERENCES 3 and 4) AT MACH NO. (NOMINAL)													ANGLE-OF-ATTACK RANGE	TEST CONFIGURATION IDENTIFICATION CODE
	0.4	0.7	0.9	0.95	1.05	1.10	1.20	1.40	1.70	2.0	2.60	3.85	4.64		
RETRACTED PM PAYLOAD (25°)	50	49	48	47	46	45	44	43	42	41	10	11	12	A	$F_4B_1\ D_2$
MURP PAYLOAD (25°)	40	39	38	37	36	35	34	33	32	31	9	7	8	C (A)* A (L)*	$F_3B_1\ D_2$
LPL PAYLOAD (25°)		30	29	28	27	26	25	24	23	22	3	1	2	A	$F_1B_1\ D_2$
EXTENDED PM PAYLOAD (25°)	60	59	58	57	56	55	54	53	52	51	4	5	6	A	$F_2B_1\ D_2$
EXTENDED PM PAYLOAD (45°)	71	70	69	68	67	66	65	63	62	61	15	13	14	A	$F_2B_1\ D_3$

← AMES 6 FT → *(A) (Mach 0.4 to 2.0)

← LANGLEY UPWT → *(L) (Mach 2.60 to 4.64)

ANGLE-OF-ATTACK RANGE (2° INCREMENTS)
A (-4° TO 16°)
C (-12° TO 15°)

3.4.1 PAYLOAD VARIATION

Effects of payload variation at Mach numbers of 1.2 and 4.64 are presented in figures 3.4-1 and 3.4-2. At Mach 1.2, normal force (C_N) and axial force (C_A & C_{A_F}), coefficients exhibit trends for the various configurations that do not differ appreciably. The maximum observed deviations occur in the axial force in the $\pm 2^{\circ}$ angle-of-attack range. The effect of payload on pitching moment, however, at this transonic Mach number (figure 3.4-1(b)) is quite significant (beyond $\alpha = 2^{\circ}$). Differences due to payload at the higher Mach number are quite noticeable for all characteristics shown. Normal force and pitching moment coefficient magnitudes are generally highest for the configurations having the longer and wider forebodies. Conversely, this same class of vehicles produces minimum axial forces. In all characteristics shown here, the Retracted PM and MURP forebodies show similar levels of magnitude, indicating a small effect due to the more slender forebody of the MURP configuration.

Drag coefficients (at $\alpha = 0^{\circ}$) from references 10 and 11 have been plotted in figure 3.4-3 for the entire combined Mach number range of 0.4 to 5.0. In this figure, the base drag coefficient shown results from testing involving no simulation of engine operation and is constant for all configurations. It has no relationship to the power-on base pressure effects reported elsewhere. The effect of payload shape on these drag characteristics (figure 3.4-3) becomes significant beyond Mach 1.0 where divergences really begin, with the Retracted PM configuration (figure 3.2-1(a)) exhibiting the highest level, and the LPL configuration (figure 3.2-1(c)) showing the lowest level. While the Extended PM configuration (figure 3.2-1(d)) is not included in figure 3.4-3, it would show characteristics intermediate to LPL and MURP payload vehicles. (Total drag coefficient for this vehicle is presented in figure 3.4-6 in another comparison.)

Schlieren photographs (figures 3.4-4 and 3.4-5) from the Ames and Langley test facilities represent the flow characteristics about the various ascent configurations at the sample Mach numbers of 1.2 and 4.64. The previously discussed drag characteristics of the various vehicles may be correlated with these shock formations to some degree. At Mach 1.2, drag divergence due to payload has not yet occurred, so that little difference in the bow shock wave formations of the various payloads should be apparent. Examination of the sequence of Mach 1.2 pictures in figure 3.4-4 indicates this is true; however, the LPL configuration is beginning to display more obliqueness and a tendency toward the conical shock pattern associated with reduced drag (figure 3.4-4(c)). At the higher Mach number of 4.64, shock formations seen in figure 3.4-5 reflect the differences in drag seen in figure 3.4-3. The progression of the bow shock system from the near normal shock case of the short-length Retracted PM forebody to the increasingly more conical shock system of the longer nose payloads seen in the sequence of pictures (3.4-5(a) through 3.4-5(d)) corresponds to the regression in drag due to forebody shape seen in figure 3.4-3.

3.4.2 ENGINE DOOR OPENING

With the exception of some minor effect on the normal force at lower Mach numbers and higher angles-of-attack, an increase of engine door opening from 25 degrees to 45 degrees affects the base axial force primarily. The increase of about 25 percent in this parameter due to the increased opening, also increases the total drag coefficient by the differential between curves seen in figure 3.4-6 where door opening cases are compared.

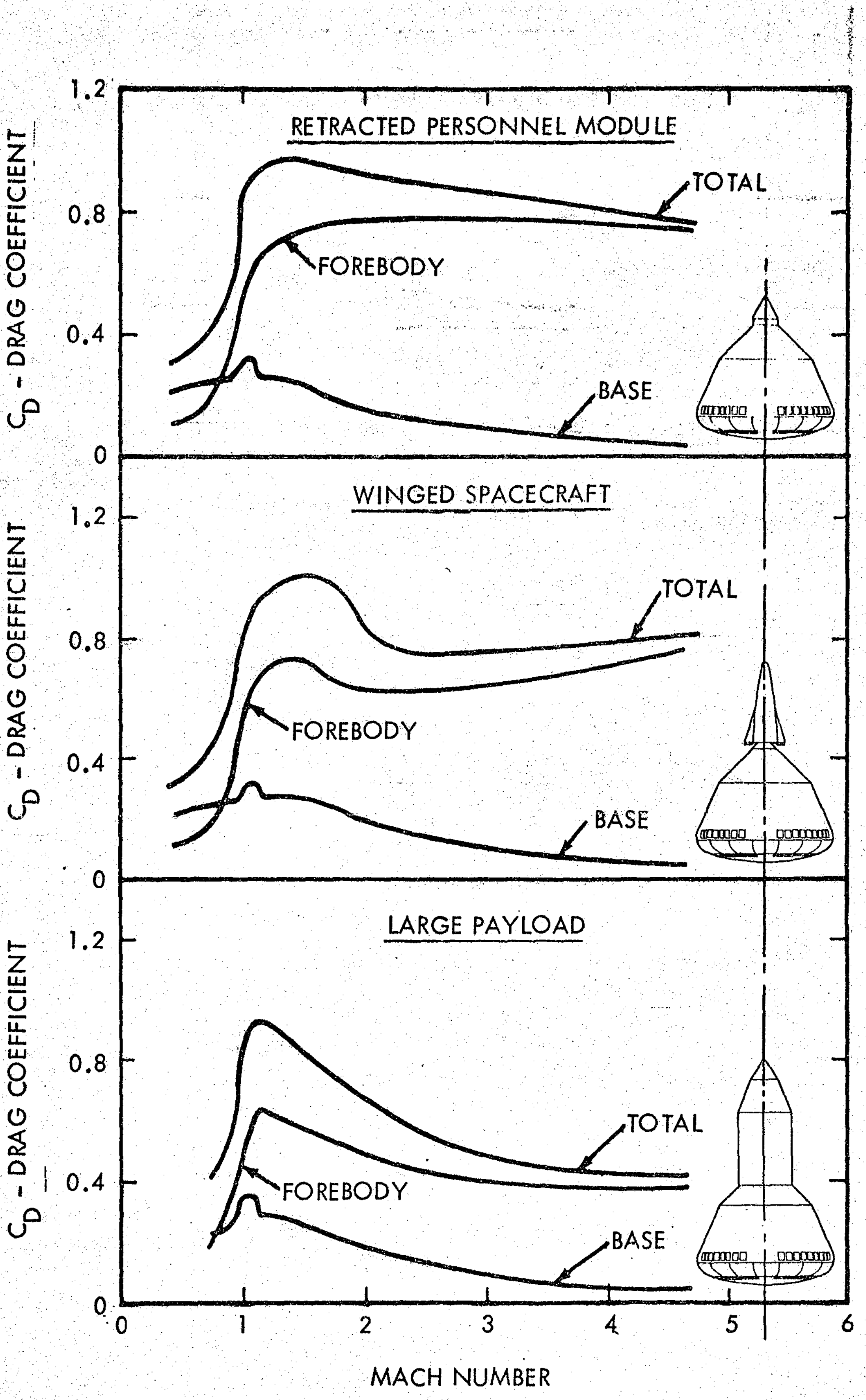

Figure 3.4-3. Power-Off Drag Characteristics of SERV (Task 2 Baseline) Ascent Vehicle (α= 0°) $C_D = D/qA_{REF}$

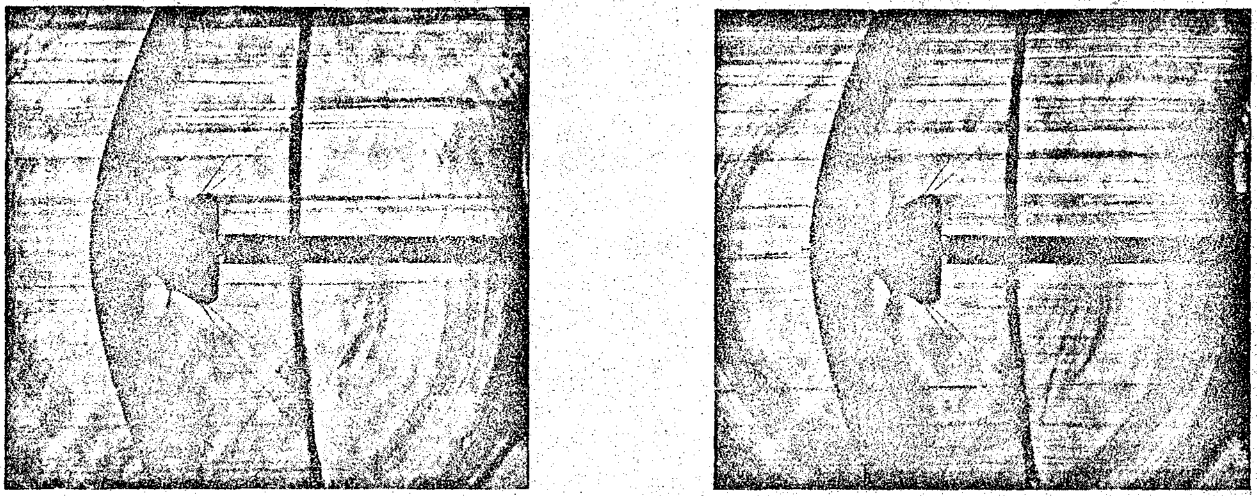

(a) RETRACTED PM

(b) MURP

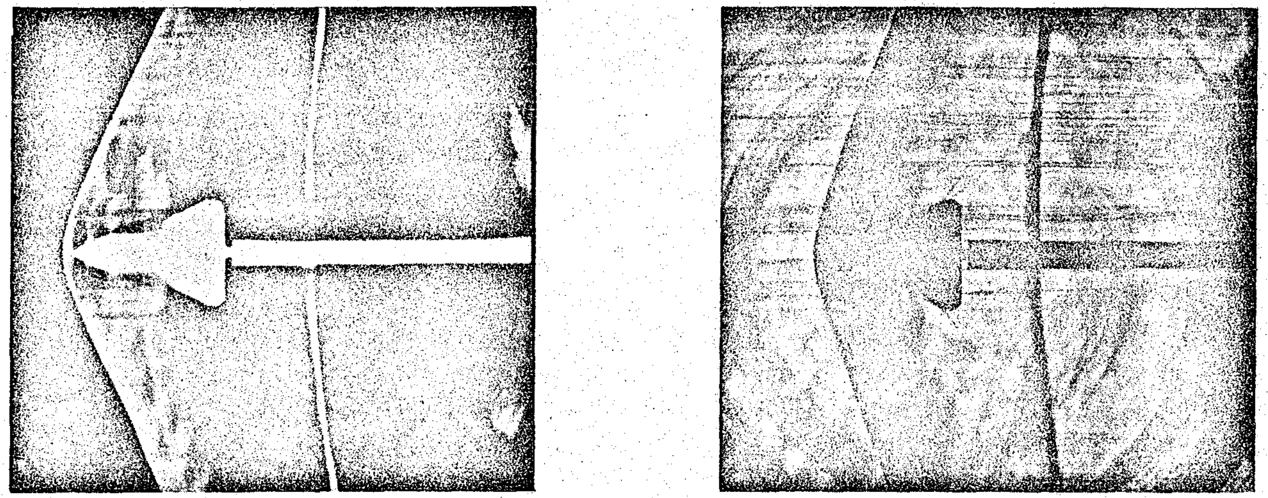

(c) LPL

(d) EXTENDED PM

Figure 3.4-4. Flow Characteristics for Various Ascent Configurations - Mach = 1.2

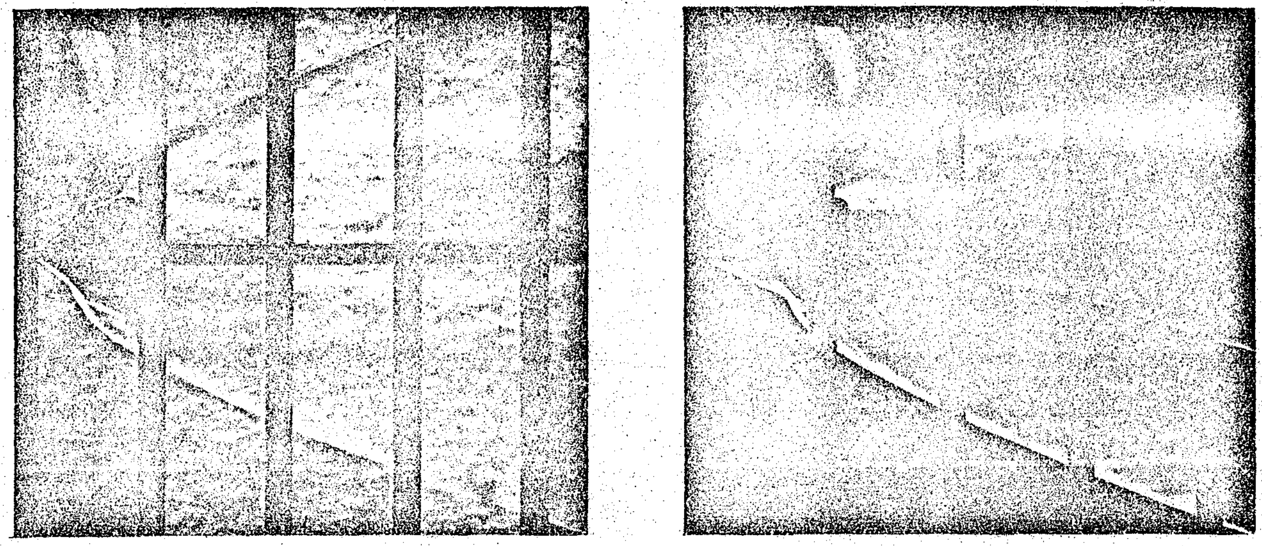

(a) RETRACTED PM

(b) MURP

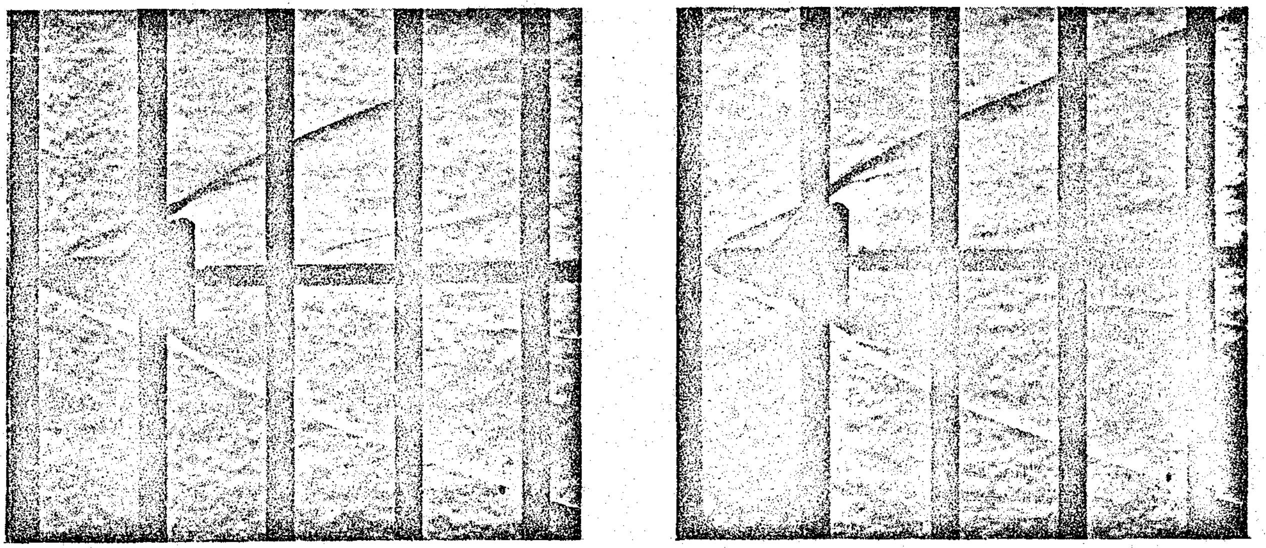

(c) LPL

(d) EXTENDED PM

Figure 3.4-5. Flow Characteristics for Various Ascent Configurations - Mach - 4.64

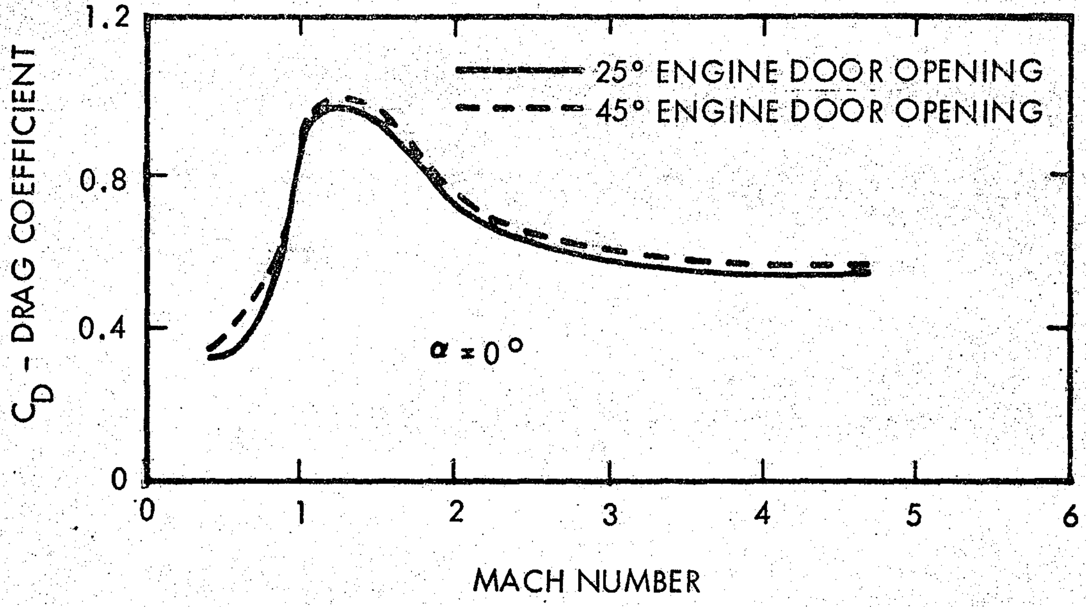

Figure 3.4-6. Effect Of Change In Engine Door Opening On Total Power-Off Drag Coefficient Of Extended Personnel Module Payload Configuration

3.4.3 STATIC STABILITY

The slope of normal force and pitching moment coefficient curves in the linear range of angle of attack ($\pm 4^{\circ}$ about zero), provide criteria which, when related properly, indicate the center of pressure location from the vehicle base and provide overall knowledge of vehicle stability. These characteristics are presented in figure 3.4-7.

Center of pressure locations shown in figure 3.4-7 agree generally with the predicted levels, with most payloads exhibiting marginal static stability characteristics in the range of 0.2 to 0.4 calibers forward of the vehicle base. Up to approximately Mach 1.5, normal force gradient ($C_{N}\alpha$) trends for all payload versions were somewhat similar; beyond this Mach number, however, trends were different from predicted with wide divergencies noted.

3.5 CONCLUSIONS

Conclusions were summarized in the following paragraphs.

Experimentally acquired data were generally in agreement with predicted trends.

At Mach numbers below 1.2, payload variation did not appreciably affect normal and axial force characteristics. At angles of attack greater than 2 degrees, the effect on pitching moment was quite significant.

At higher Mach numbers, payload shape has a significant effect on all aerodynamic characteristics. The longer, larger-diameter payload shapes produce the highest normal forces and pitching moments but produce minimum axial forces. The primary effect of a change in the opening of the aerospike engine doors from 25 degrees to 45 degrees is about a 25 percent increase in the engine-off base drag.

All payload shapes exhibit marginal static stability characteristics with center of pressure locations in the order of 0.2 to 0.4 calibers forward of the base.

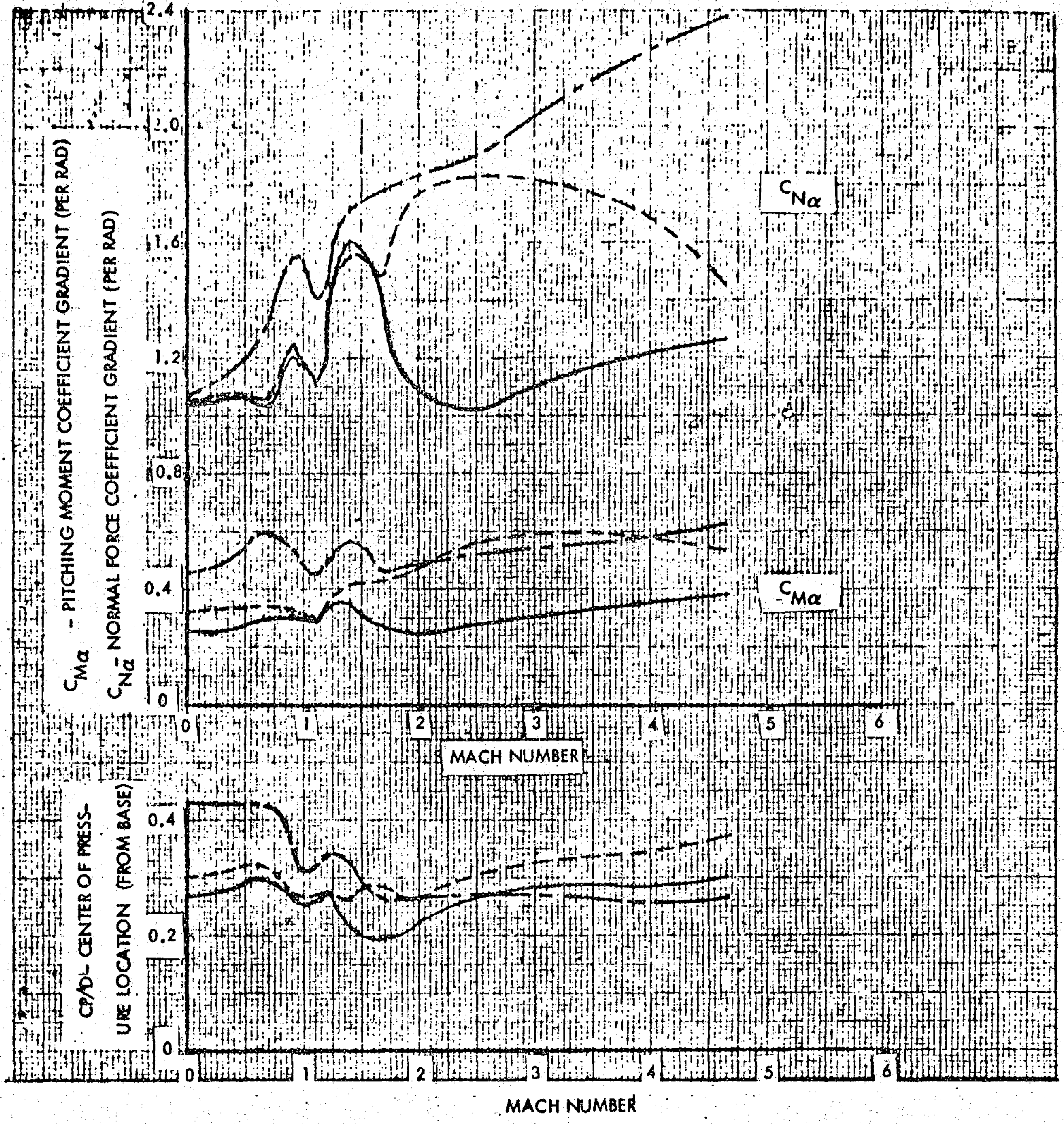

NOTES: A) $C_{M\alpha}$ AND CP/D REFERENCED TO STA 0

B) $A_{REF} = \frac{\pi D^2_{REF}}{4}$; D_{REF} = 88 FT

——— RETRACTED PERSONNEL MODULE

- - - - WINGED ORBITER

—·—·— LARGE CARGO MODULE

Figure 3.4-7. Static Stability Characteristics

Section 4

DESCENT CONFIGURATION FORCE TESTS

Descent performance of the SERV concept is contingent upon reentry aerodynamic drag, lift-to-drag ratio, and trim stability. In the lower supersonic through subsonic phase of flight, vehicle static aerodynamic stability characteristics are very important factors in minimized control system requirements. In order to determine these aerodynamic performance characteristics to the accuracy required to prove feasibility, wind tunnel force tests were conducted on parametric scale models of the SERV descent configuration.

These tests were conducted in the NASA Ames Research Center 6-foot SWT and Langley Research Center UPWT over a combined Mach number range of from 0.4 to 4.64. The higher Mach number data were used to extrapolate the performance characteristics to hypersonic Mach numbers through the use of applicable Apollo reference data and hypersonic flow theory. Geometric effects such as heat shield corner radius, afterbody configuration, removal of aerospike engine protection doors, and opening engine doors in the lower Mach range, were investigated.

4.1 TEST PLAN

Aerodynamic wind tunnel force tests were conducted using 0.55 percent scale models of the SERV descent baseline concept with specific geometric variations. The NASA Ames Research Center 6-foot SWT was utilized for the test Mach number range from 0.4 to 2.0. The Langley Research Center UPWT was used for the supersonic test Mach numbers 2.6 to 4.64. The higher Mach number tests were conducted for an angle-of-attack range of -6 to -34 degrees (heat-shield-down attitude) while the lower supersonic, transonic and subsonic tests were conducted at angles of attack from +4 to -50 degrees. A 3-component force balance was used to measure the aerodynamic parameters, normal force (C_N), axial force (C_A) and pitching moment (C_M). An offset sting mounting system was employed to achieve the complete angle-of-attack ranges. References 8 and 9 document in detail the original pretest plans. Both the Ames and Langley test facilities are continuous flow tunnels with the capability of accurate testing of this size model within their respective operating Mach ranges. The test Reynold's number conditions are defined by figure 1-2. References 13 and 14 provide detailed definition of the tunnel capabilities and operating systems.

4.2 MODEL DESIGN AND FABRICATION

The descent force models were 0.55 percent replicas of the SERV descent baseline configuration with parametric variations as illustrated in figure 4.2-1. The models were designed by Chrysler and fabricated under purchase order by Standard Tool and Die, Company of Los Angeles, California.

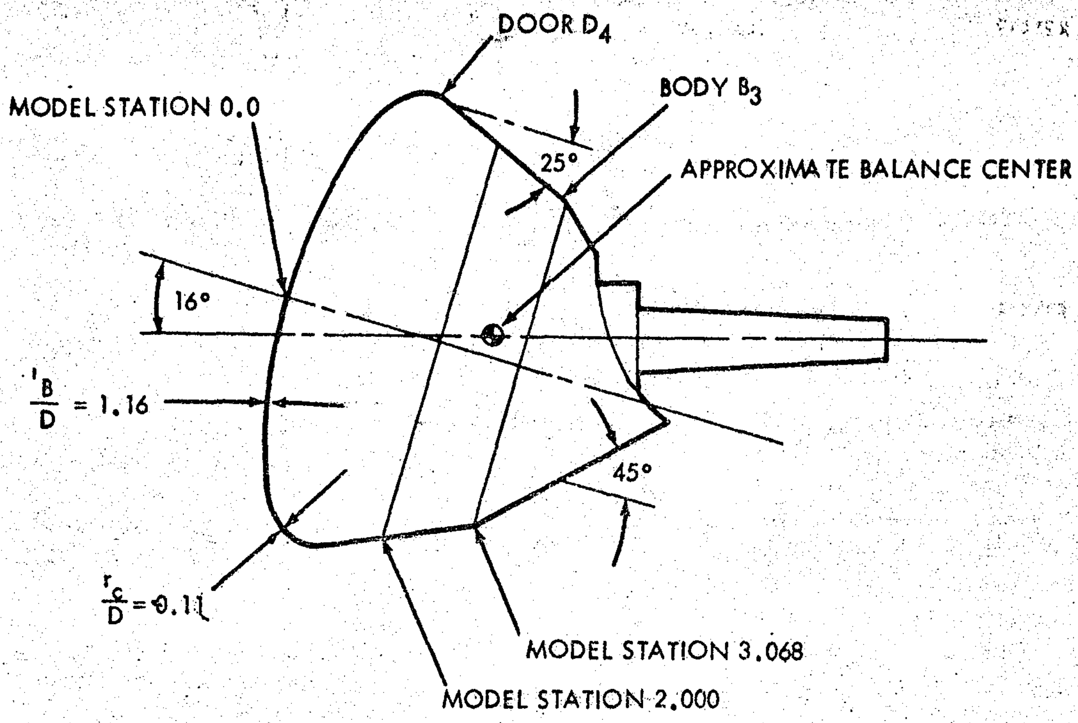

Figure 4.2-1(a). SERV Baseline Descent Configuration - Model OB_3D_4

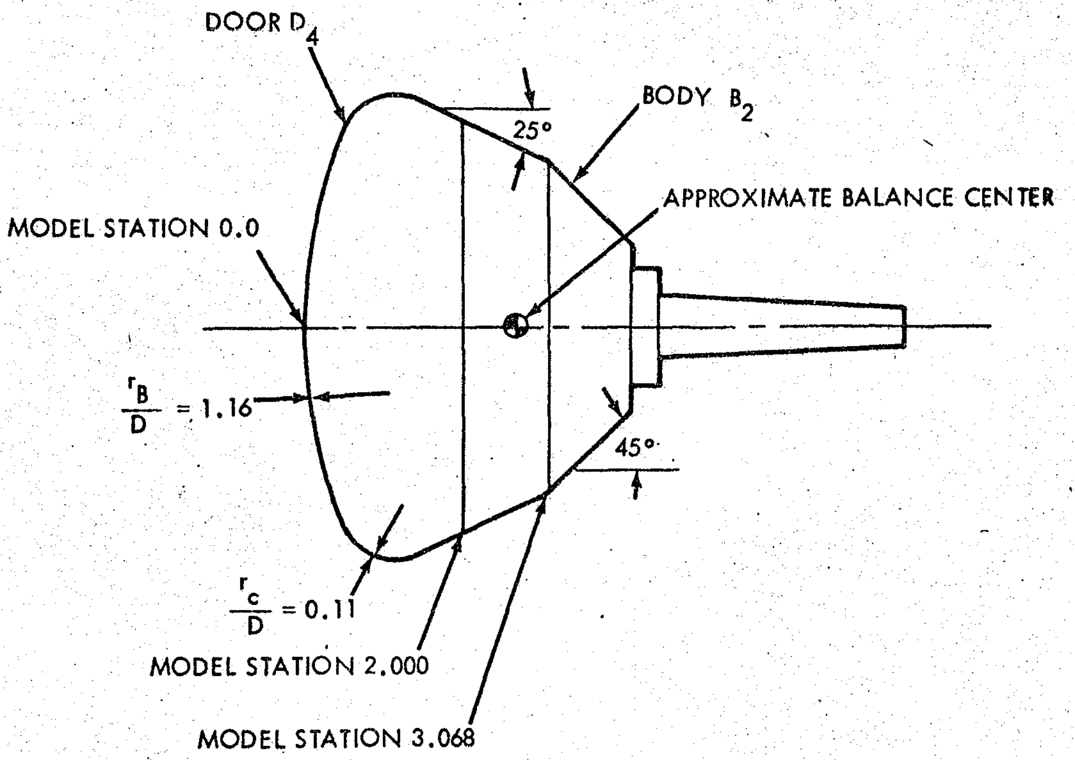

Figure 4.2-1(b). SERV Baseline Descent Configuration - Model OB_2D_4

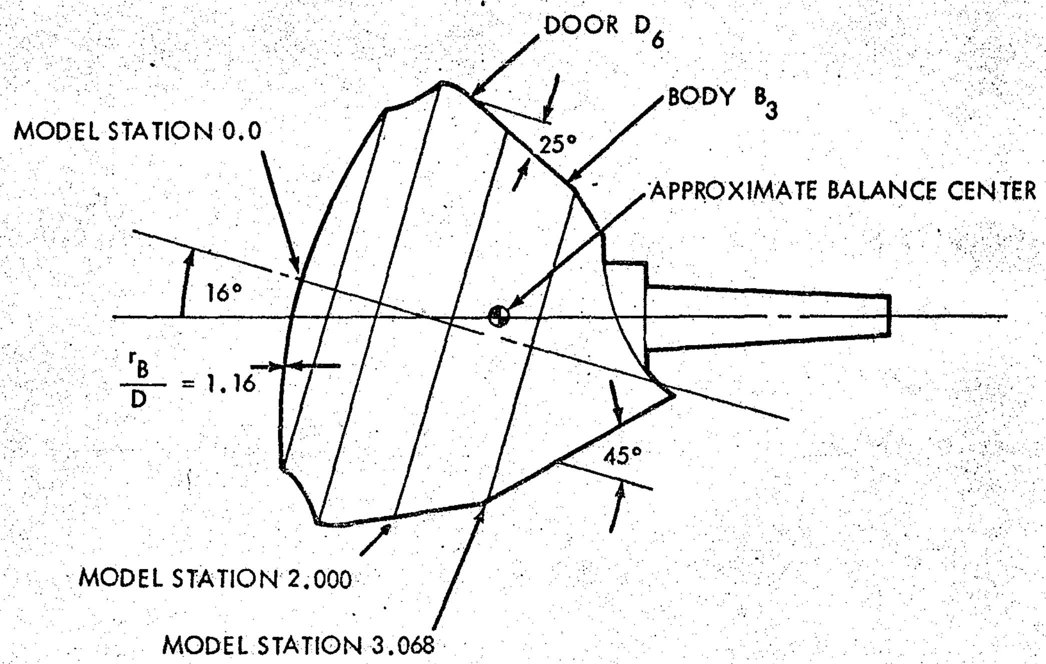

Figure 4.2-1(c). SERV Baseline Descent Configuration - Model OB_3D_6

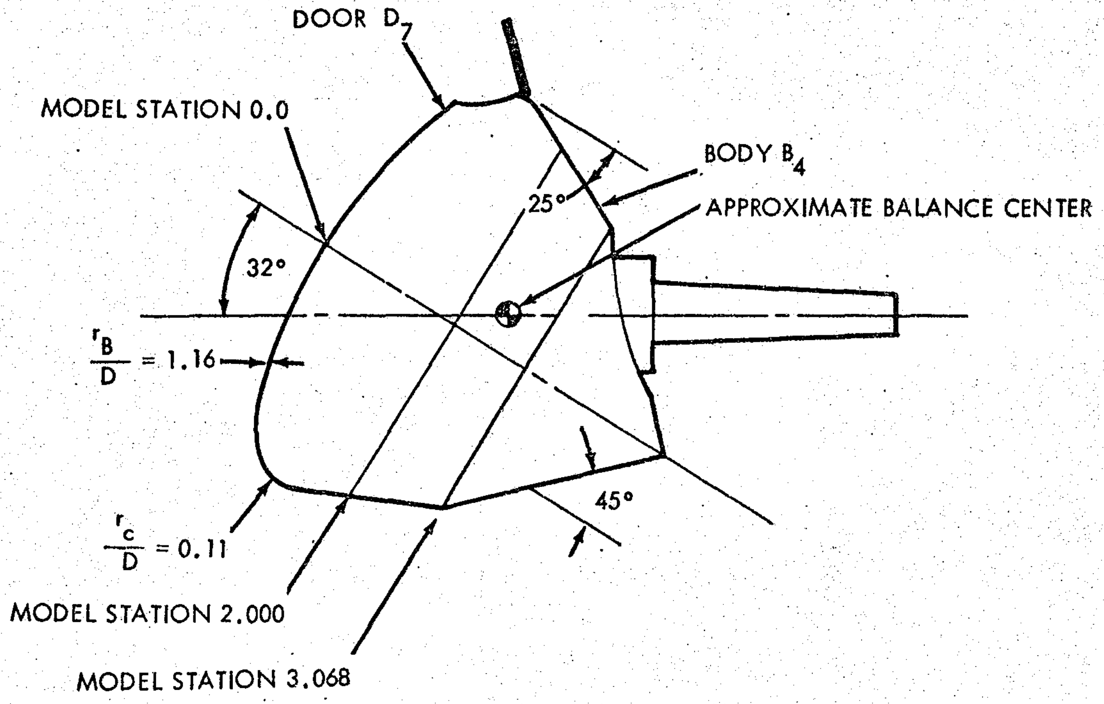

Figure 4.2-1(d). SERV Baseline Descent Configuration with Engine Door Open Model OB_4D_7

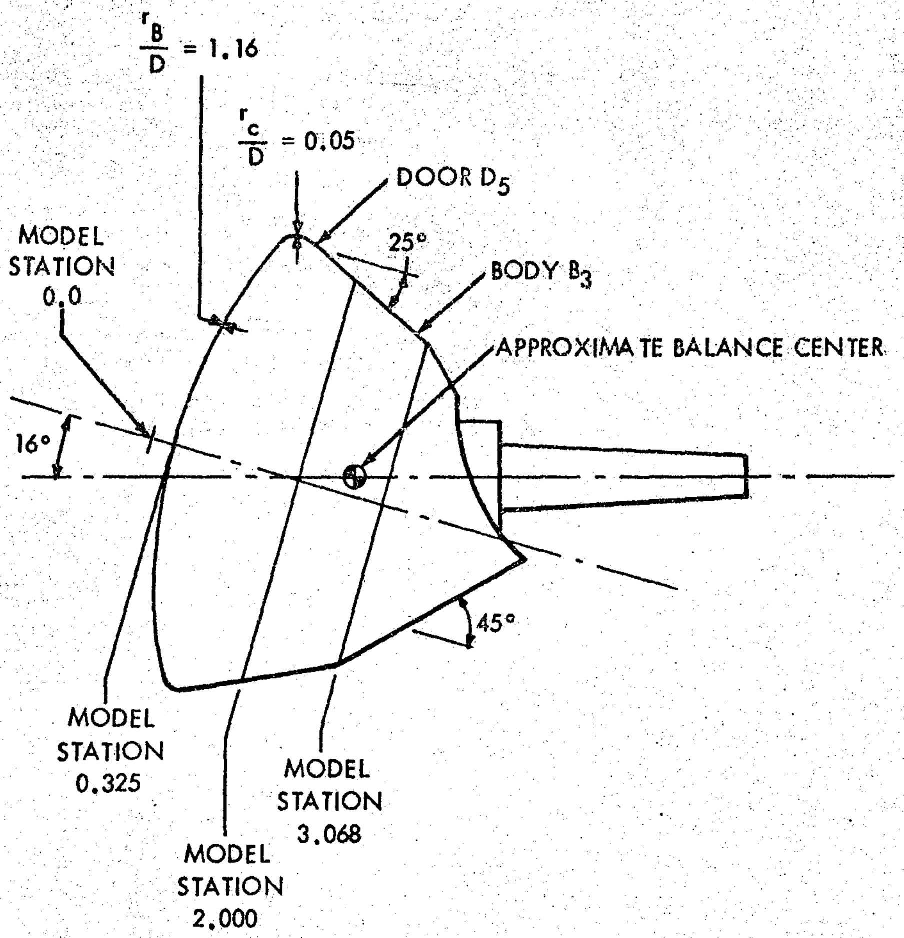

Figure 4.2-1(e). SERV Descent Configuration with $r_c/D = 0.05$ - Model OB_3D_5

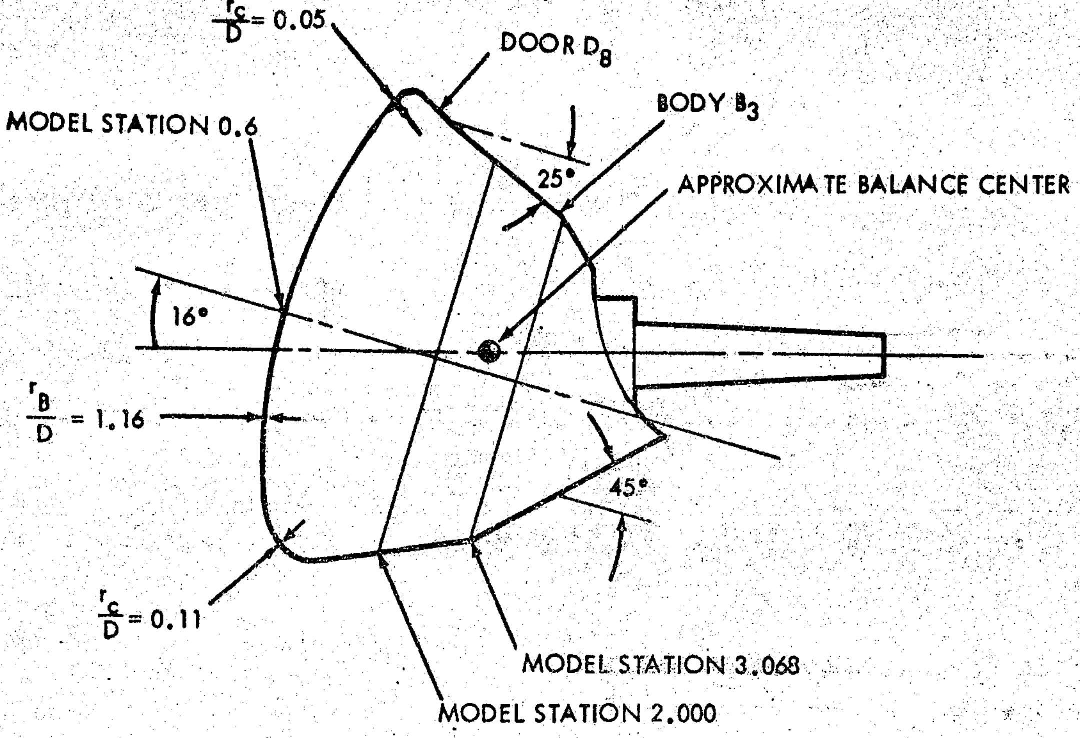

Figure 4.2-1(f). SERV Descent Configuration with Differential Corner Radii - Model OB_3D_8

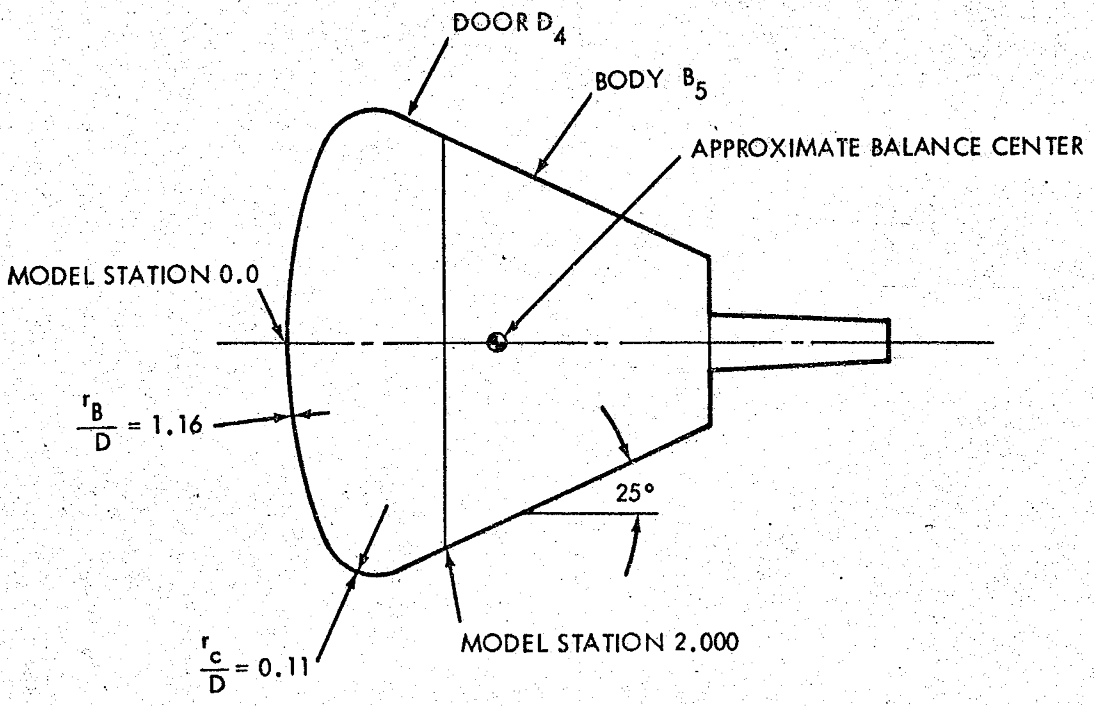

Figure 4.2-1(g). SERV Descent Configuration with Extended After-Body - Model OB_5D_4

The models were approximately 6 inches in maximum diameter. Three heat shield corner radii combinations were tested with two different afterbody configurations. The baseline reentry vehicle was tested with and without engine doors. Stress analysis was performed to verify that the models, force balance, and support system would withstand the maximum anticipated loads with a safety factor of four (4.0) based on the material yield strength.

4.3 TEST PROCEDURE

Wind tunnel installation typical of both test facilities is illustrated in figure 4.3-1. The models were aft mounted utilizing offset stings and canted models to achieve the complete angle-of-attack range. The Langley Research Center UT-22 3-component strain gage balance was used to measure the forces and moments. Base flow interference of the offset stings and low input loads to the balance (capability of 300 lb normal and axial load, and 300 in./lb of moment), resulted in bias errors at small angle of attack near zero load. However, verification in the accuracy of the higher angle-of-attack data allowed the data to be shifted and corrected for these biases within a reasonable tolerance.

Data obtained from the UT-22 balance and pressure transducers were reduced to force, moment and base pressure coefficients as defined in subsection 3.3. Moments measured by the balance were initially referenced to its electrical center, and then transferred to model station 0.0. (See figure 4.2-1.) The transfer distance from the balance moment reference to the reference model stations was measured by hanging weights with the balance installed. In addition to the above coefficients, Schlieren photographs of the shock wave systems were acquired at all conditions of interest.

No significant problems developed during these tests, other than the low angle of attack low load range bias due to the use of the offset sting system. These biases existed only in the subsonic and transonic Mach ranges where base pressures were significantly affected. Above Mach 1.5, these biases tended to dissipate.

4.4 DISCUSSION OF RESULTS

The results of these wind tunnel tests have been presented in detail in references 10 and 11. Aerodynamic characteristics of the SERV baseline descent vehicle were in agreement with previous Apollo test data. The configuration data exhibited sufficient lift-to-drag ratio (L/D) values at angle of attack (approximately 0.3 at $\alpha = -22^{\circ}$, as predicted) and also indicated that the vehicle would have adequate stability margins through transonic and subsonic deceleration flight. Normal force, axial force, pitching moment coefficients, and lift-to-drag ratio (L/D) are presented at representative Mach numbers over the test range in figures 4.4-1 through 4.4-4 for the original baseline descent configuration.

In addition to verifying the basic aerodynamic characteristics of the SERV baseline configuration, specific vehicle geometry details were also studied in these tests. These were the effects on vehicle trim conditions and lift-to-drag ratio caused by:

1) removal of the engine doors

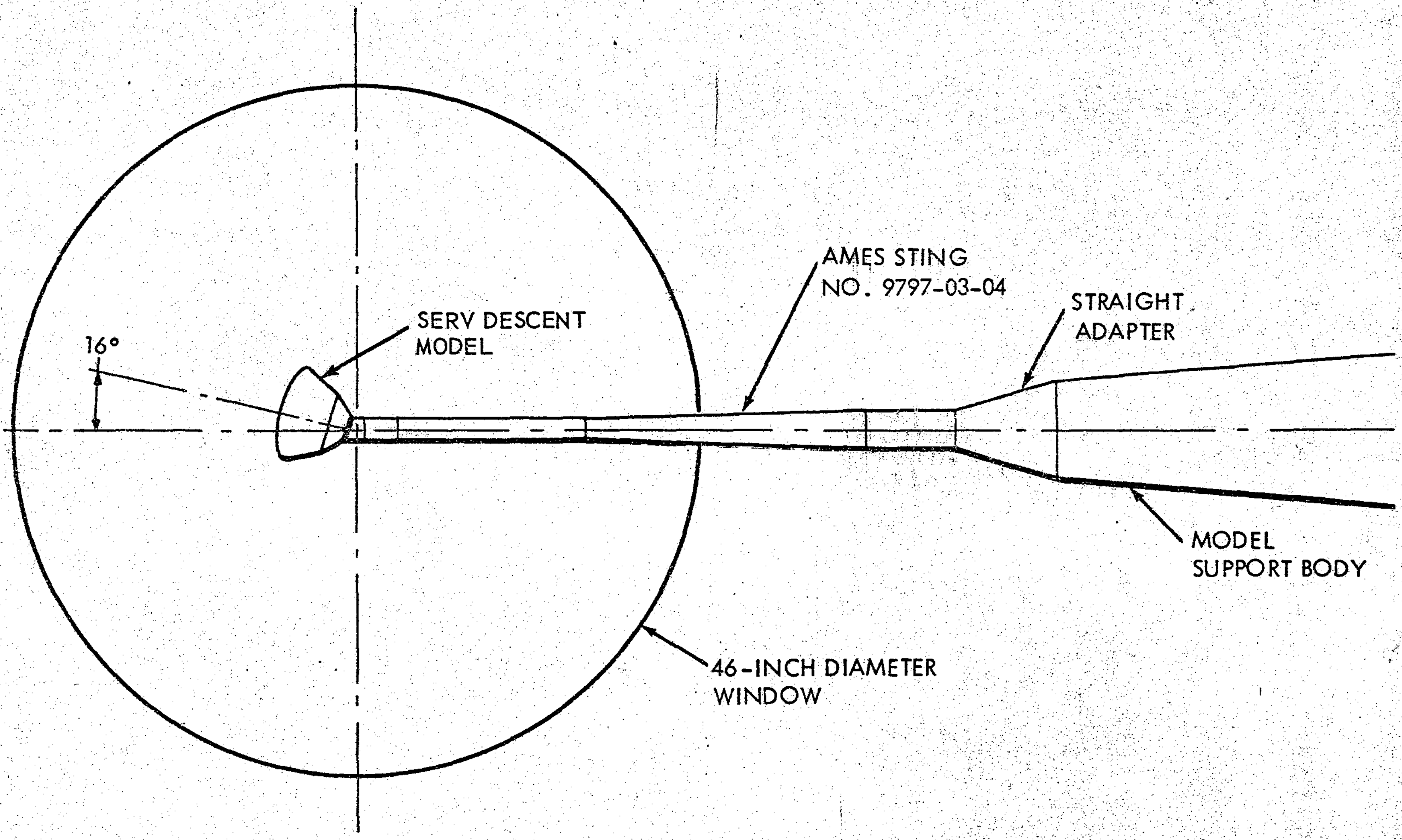

Figure 4.3-1. Ames 6x6 Foot Tunnel Installation

Normal Force Coefficient M= 0.404

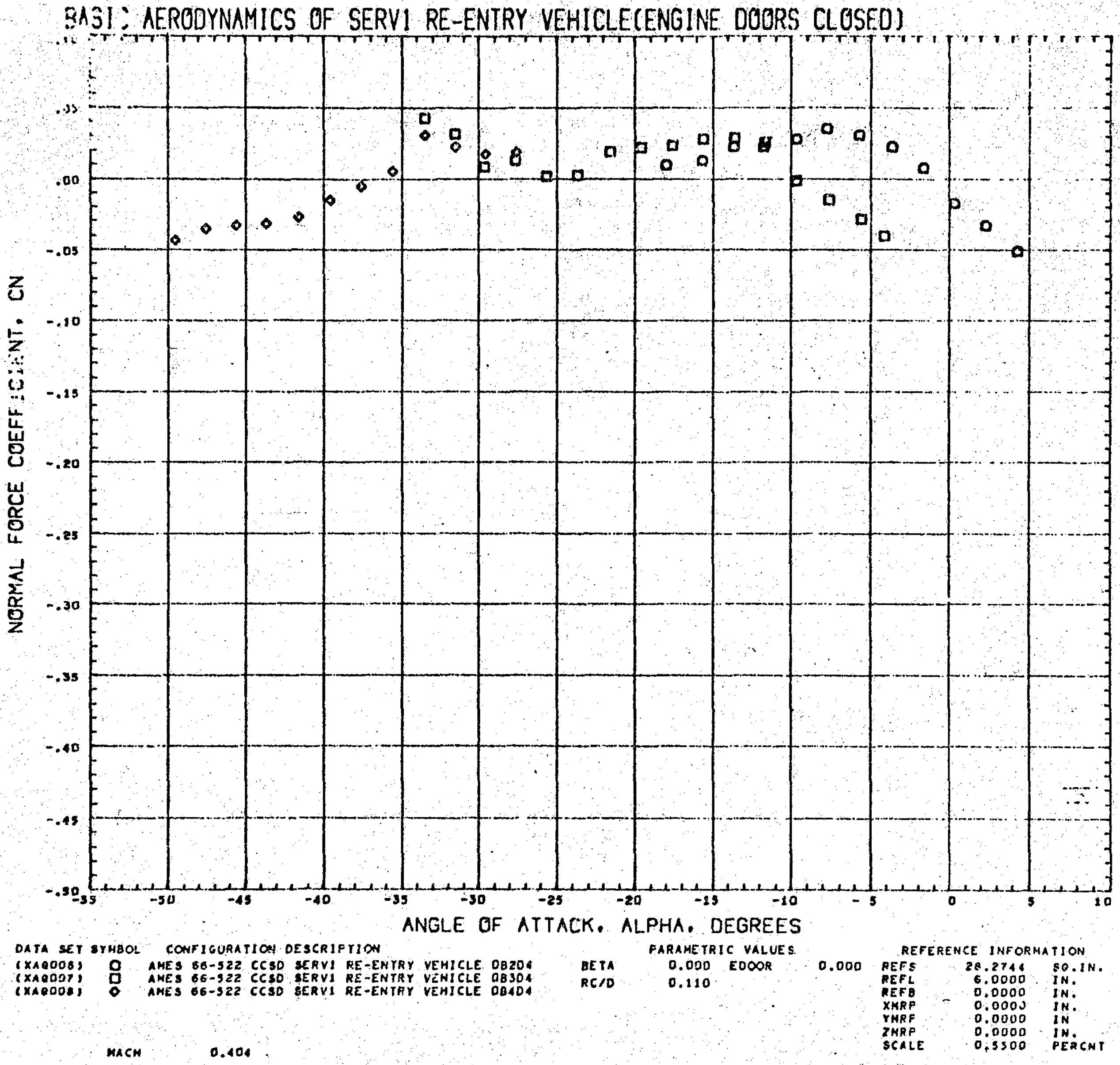

Figure 4.4-1(a).

Normal Force Coefficient M= 0.914

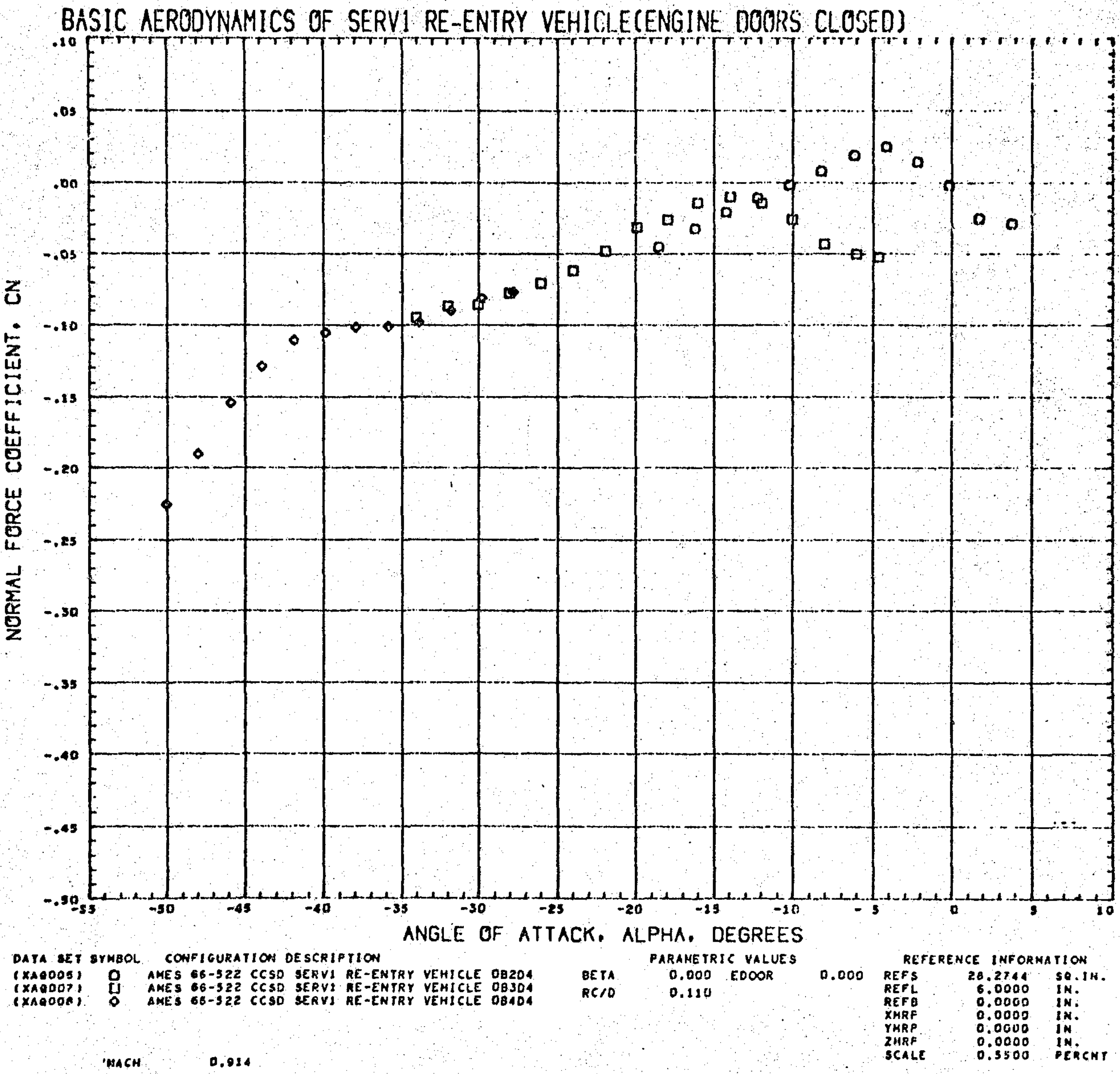

Figure 4.4-1(b).

Normal Force Coefficient M= 1.204

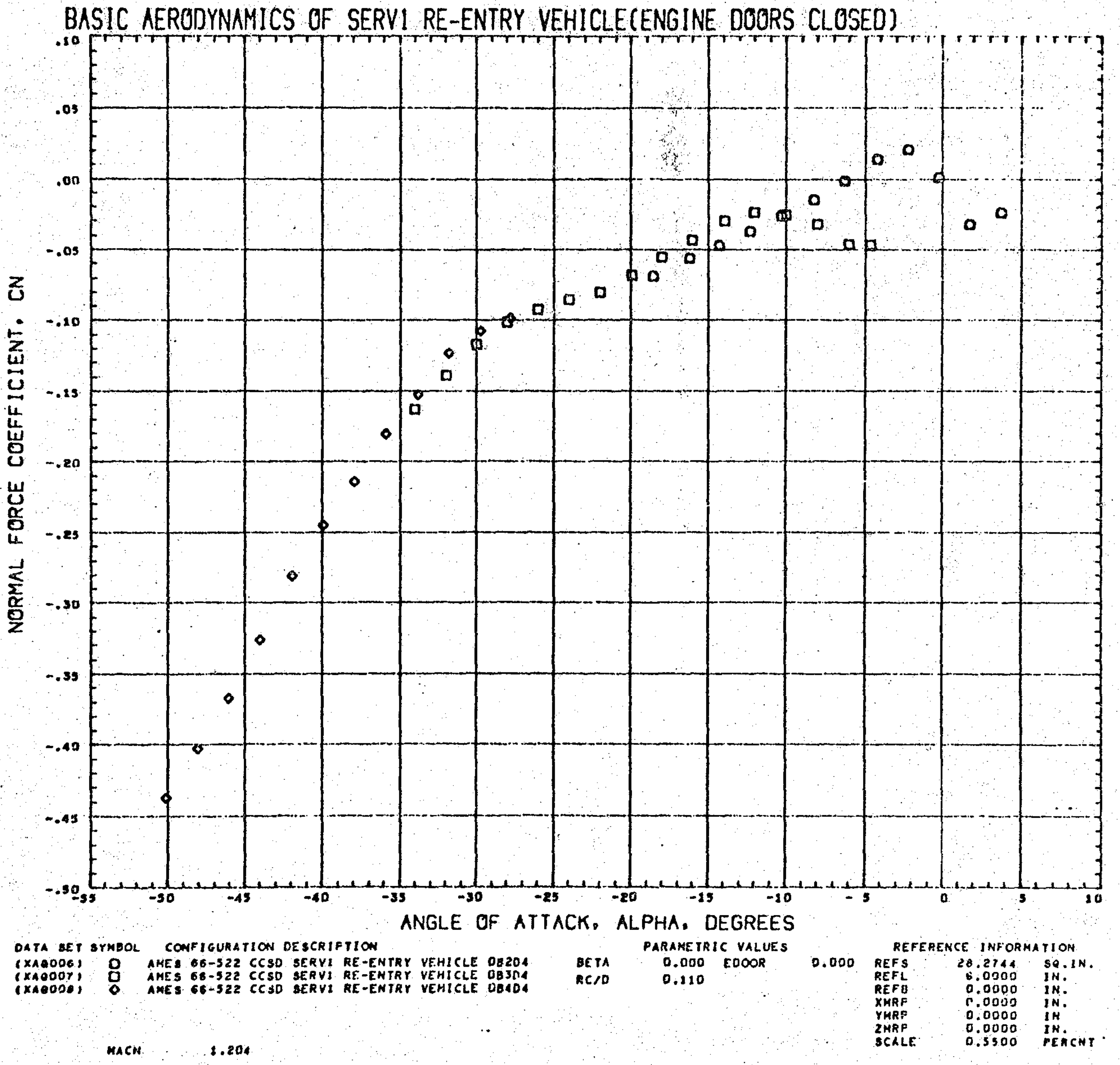

Figure 4.4-1(c).

Normal Force Coefficient M= 1.702

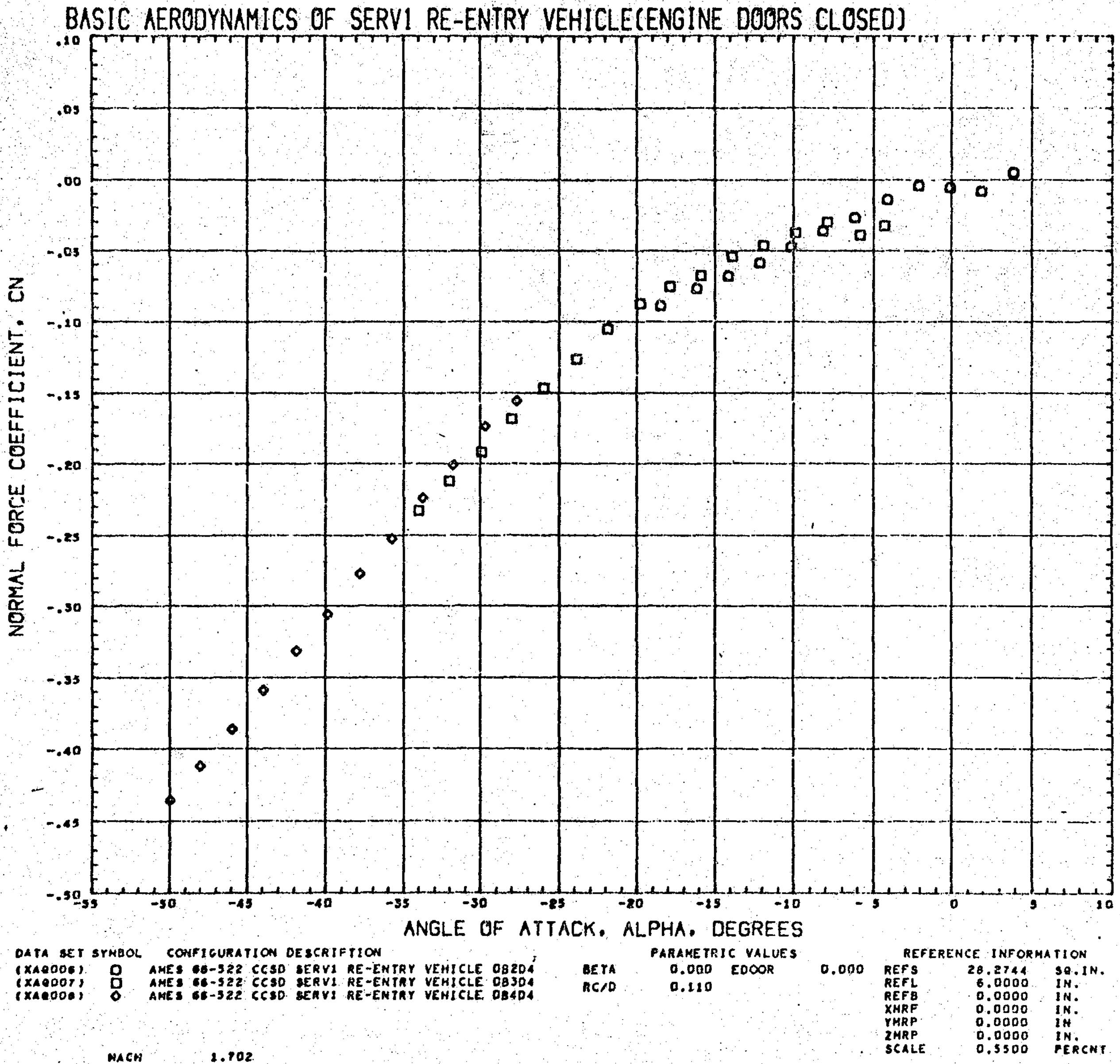

Figure 4.4-1(d).

Normal Force Coefficient M= 2.60

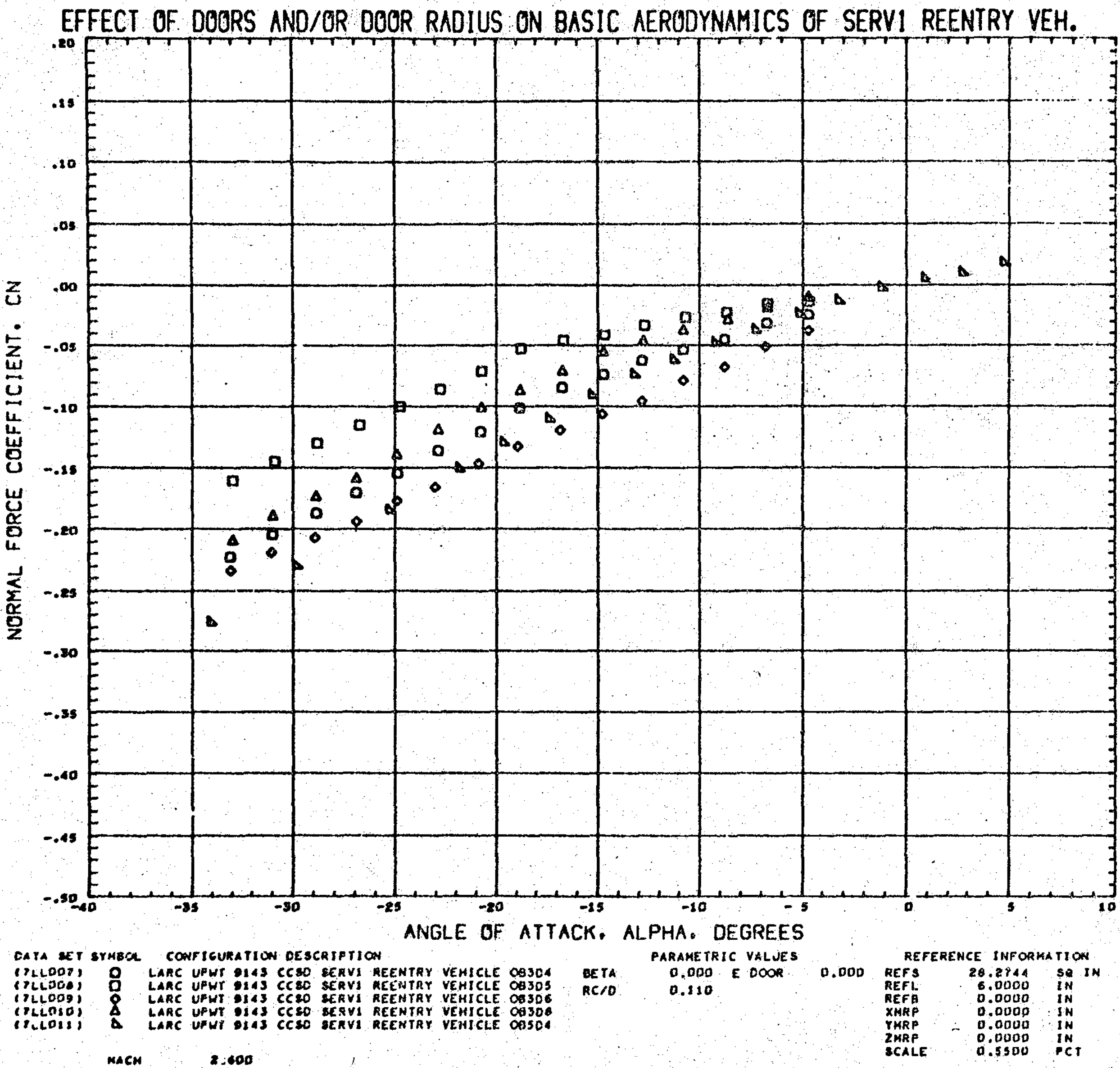

Figure 4.4-1(e).

Normal Force Coefficient M= 3.85

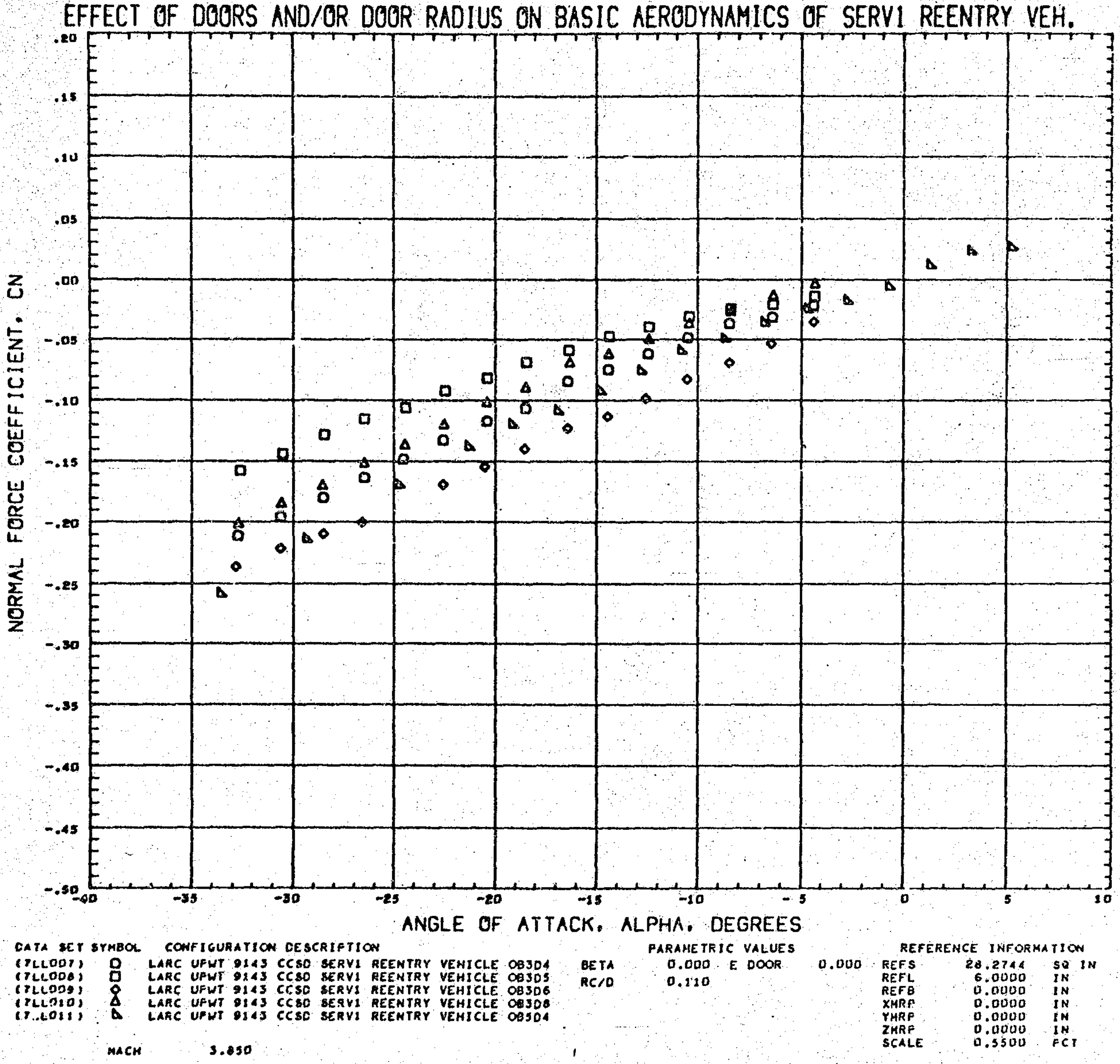

Figure 4.4-1(f).

Normal Force Coefficient M= 4.64

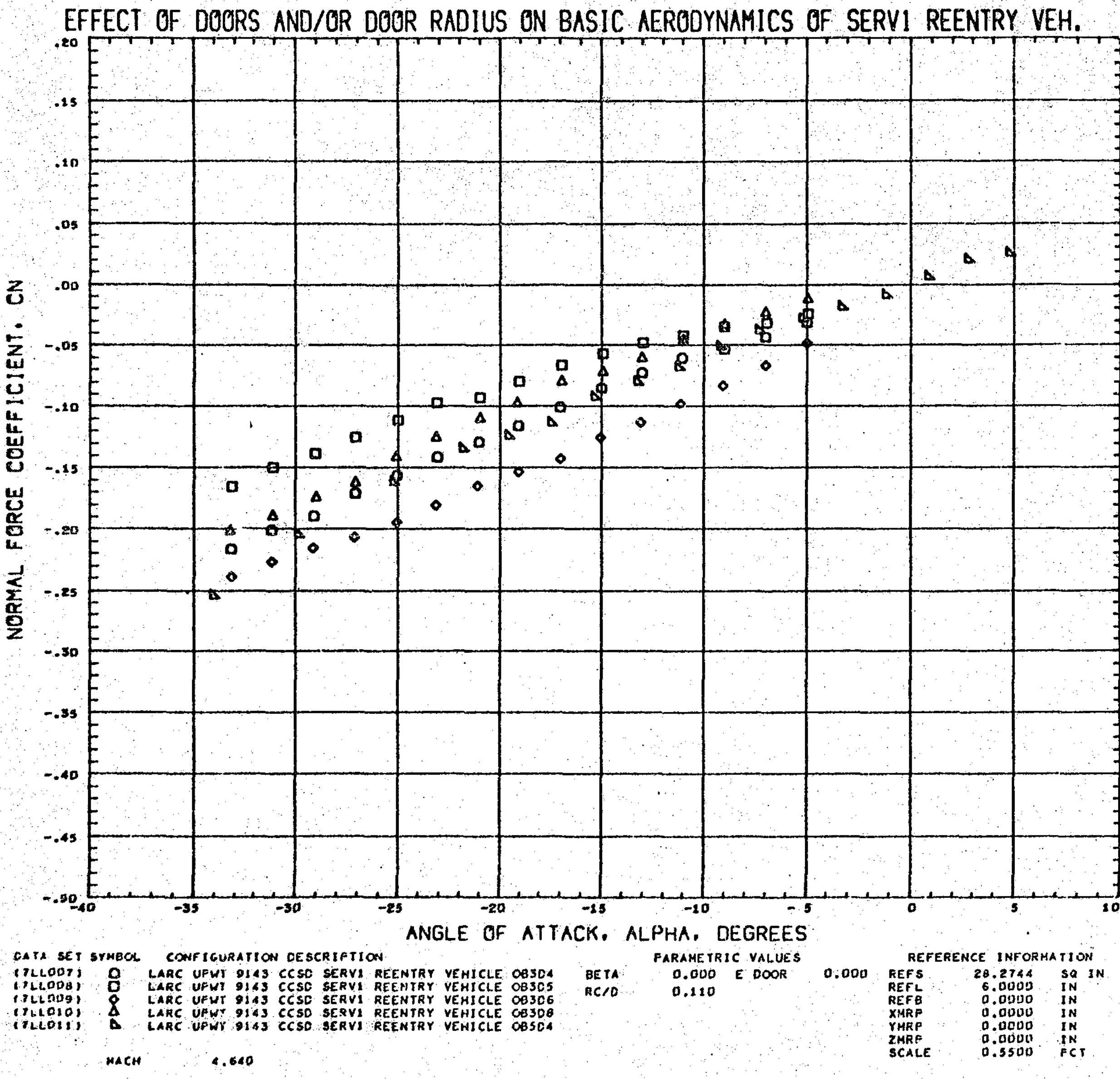

Figure 4.4-1(g).

Pitching Moment Coefficient M= 0.404

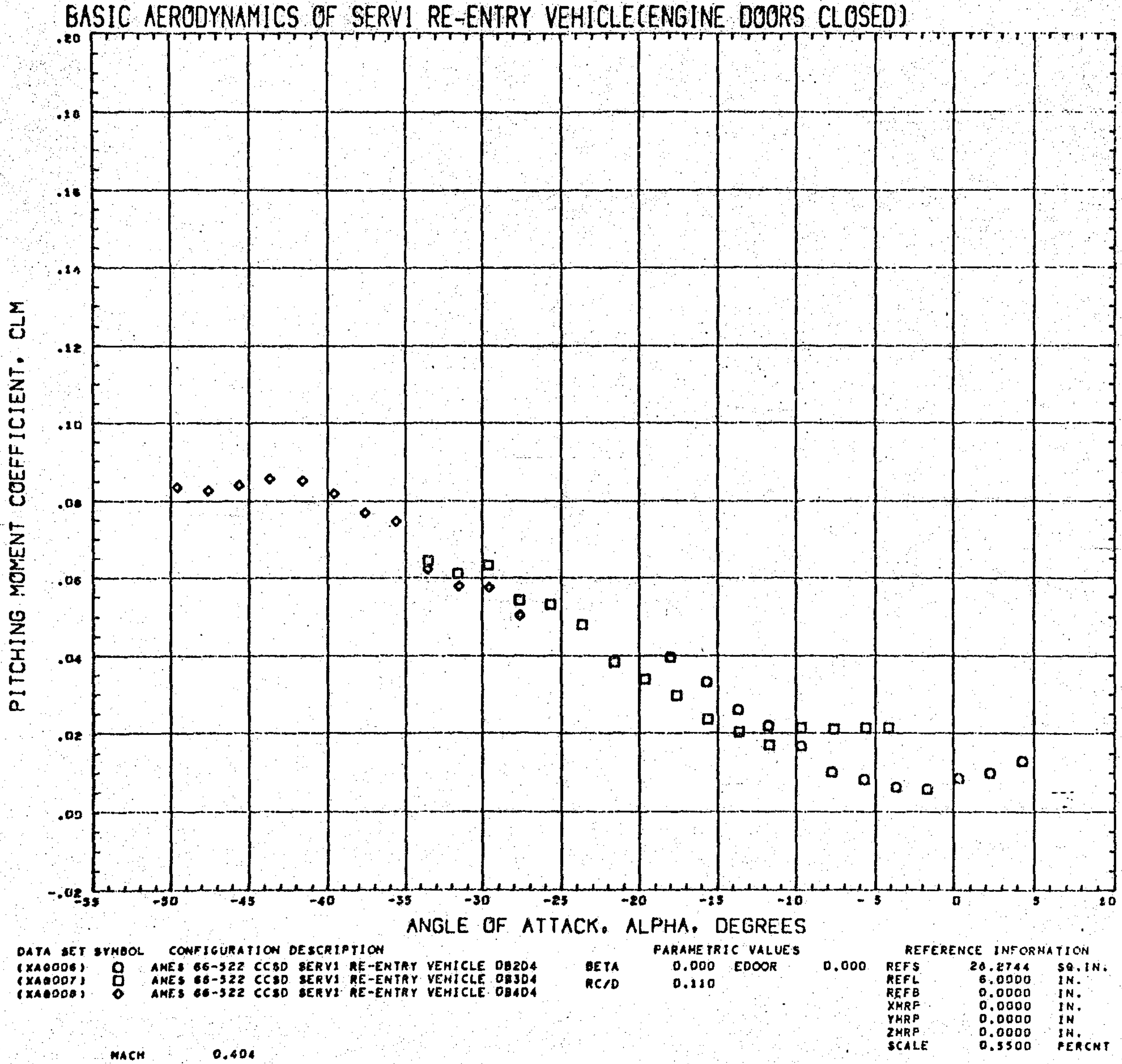

Figure 4.4-2(a).

Pitching Moment Coefficient M= 0.914

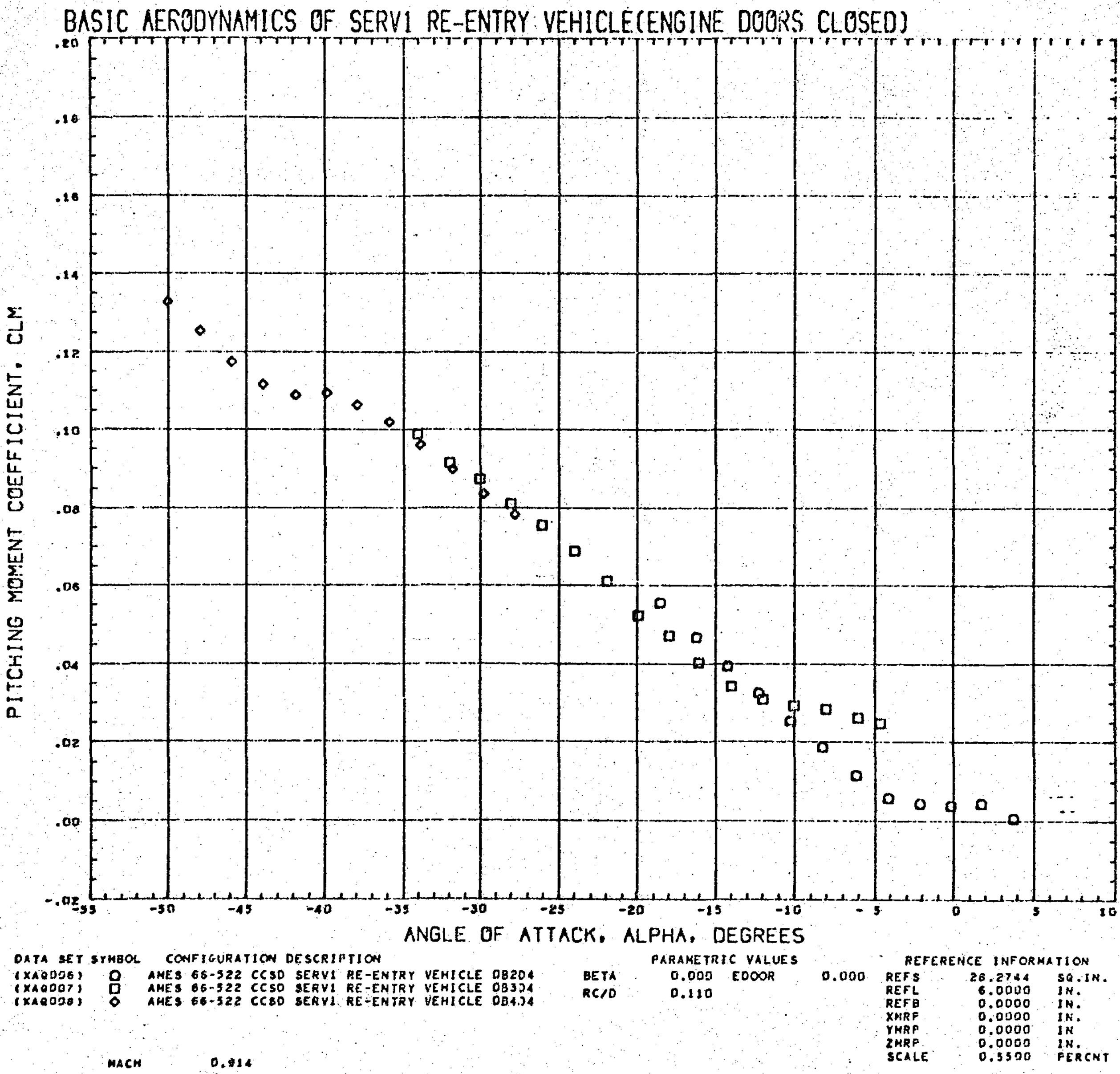

Figure 4.4-2(b).

Pitching Moment Coefficient M= 1.204

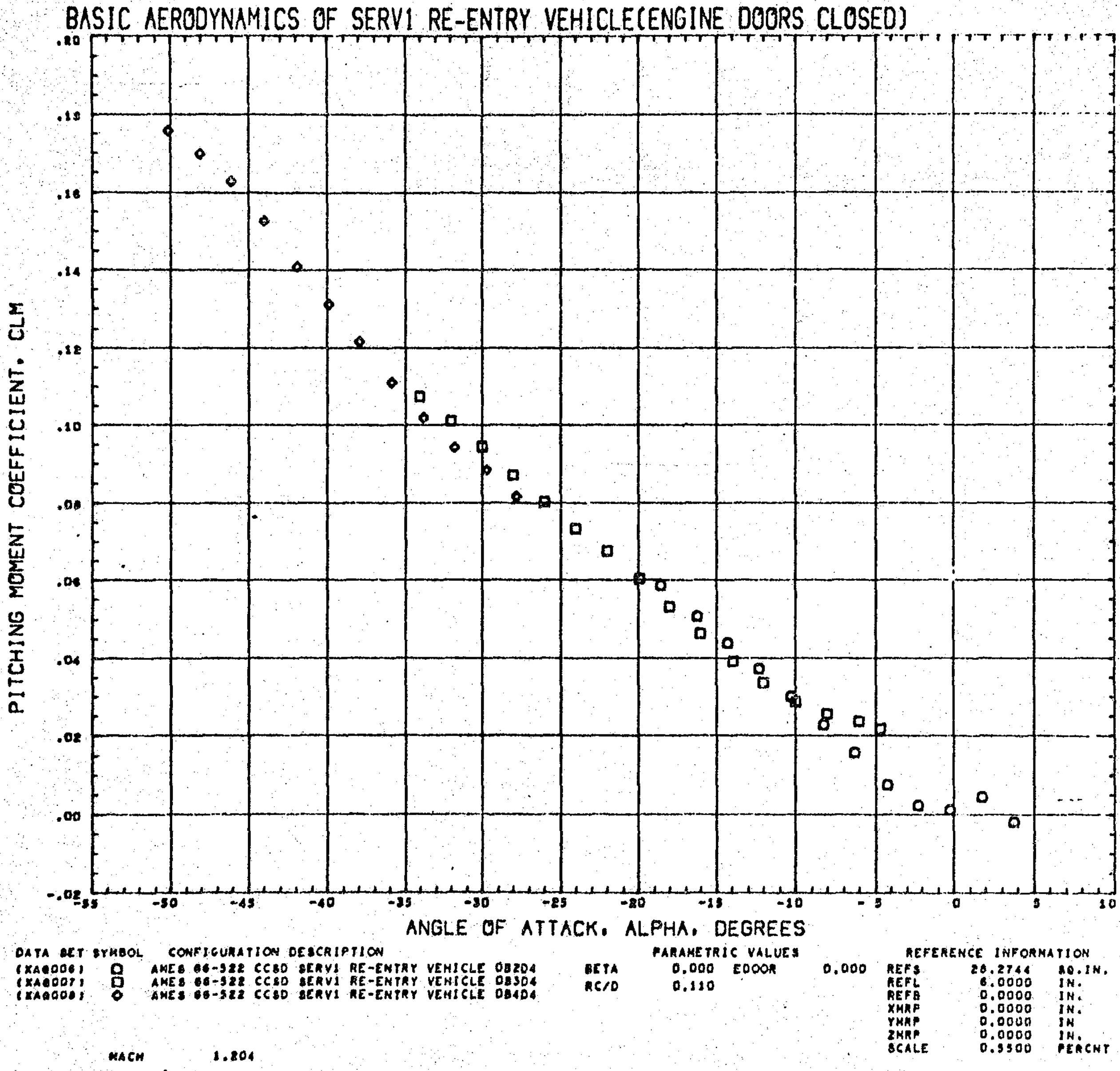

Figure 4.4-2(c).

Pitching Moment Coefficient M==1.702

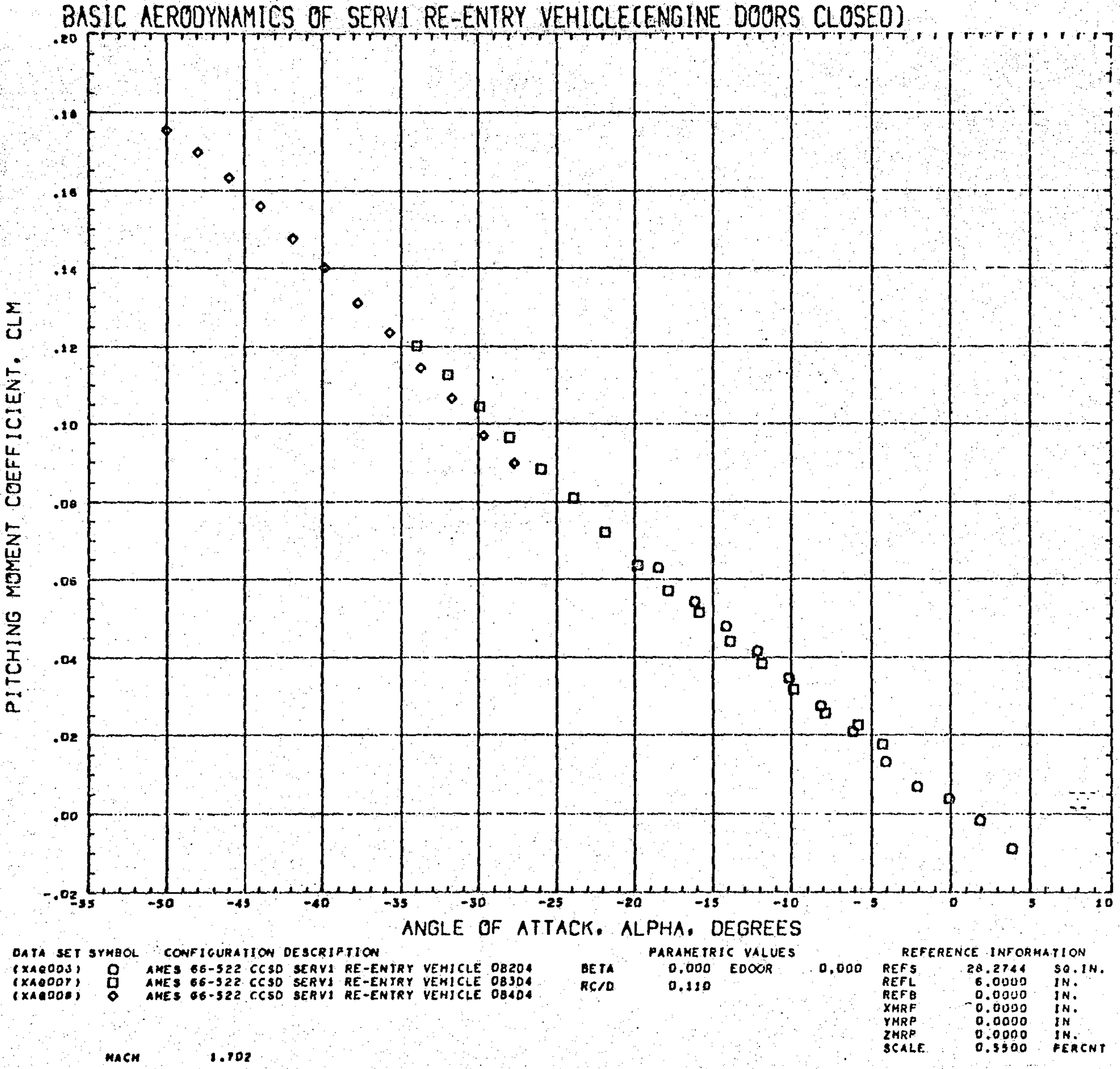

Figure 4.4-2(d)

Pitching Moment Coefficient M= 2.60

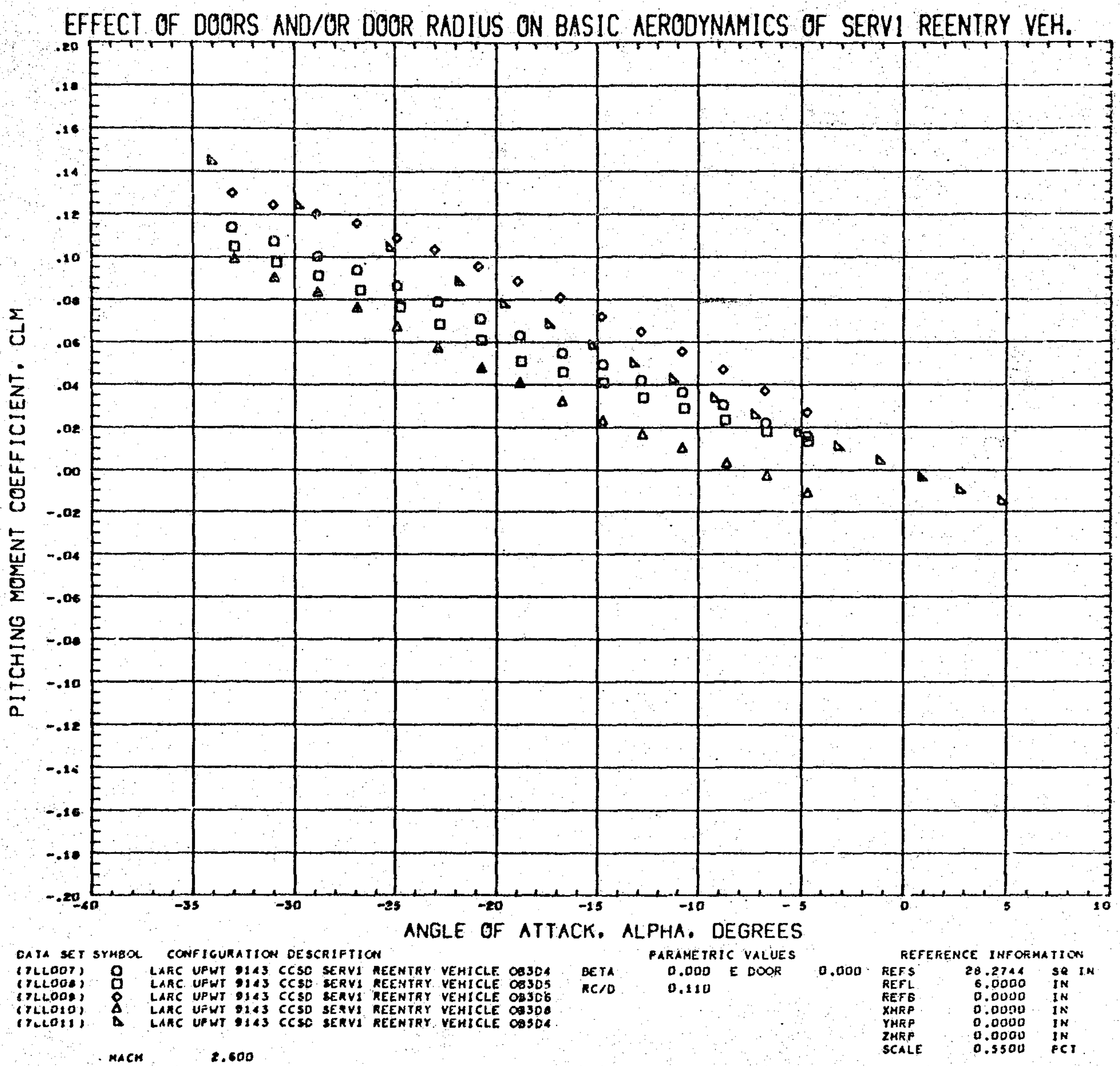

Figure 4.4-2(e).

Pitching Moment Coefficient M= 3.85

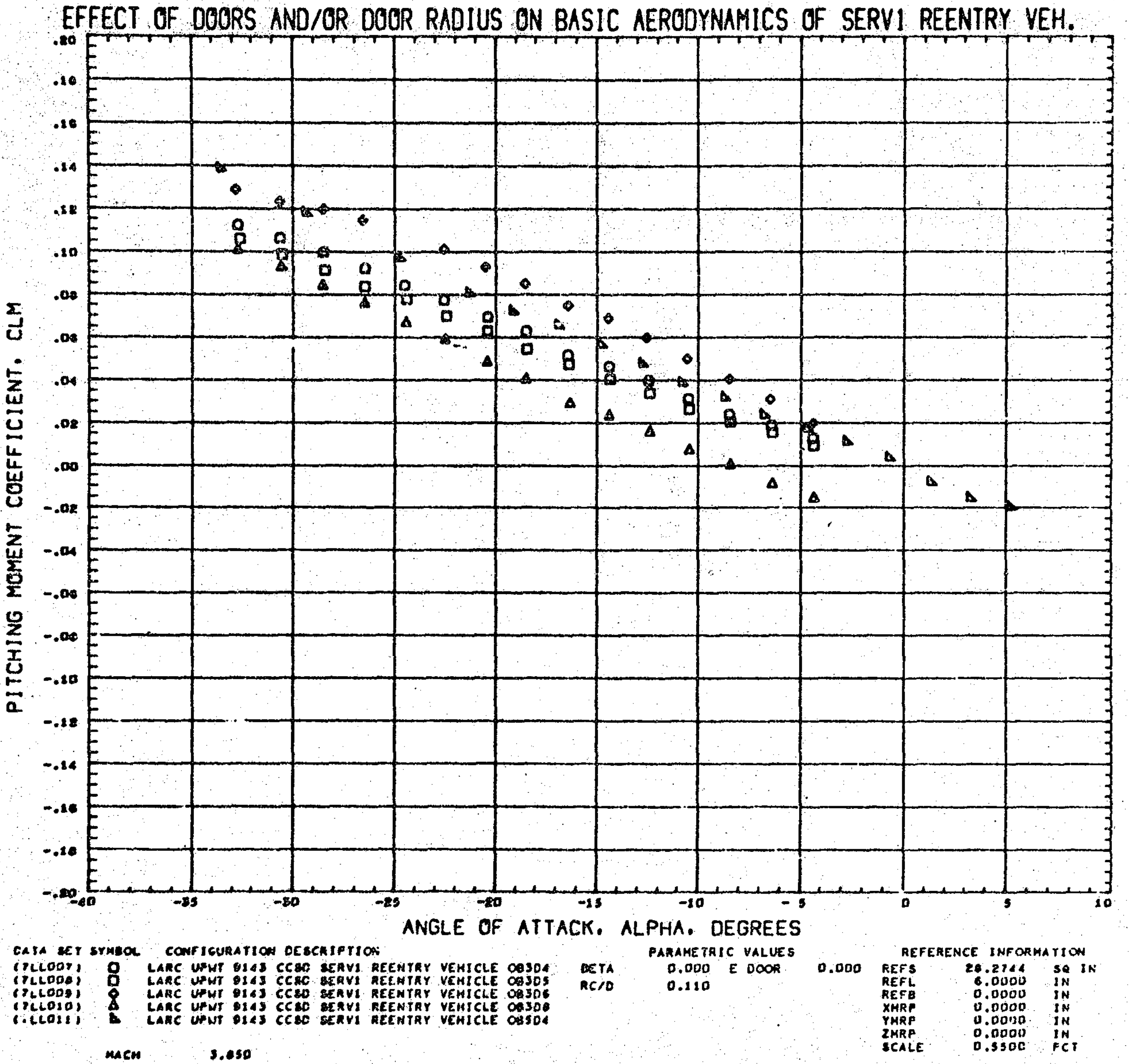

Figure 4.4-2(f).

Pitching Moment Coefficient M= 4.64

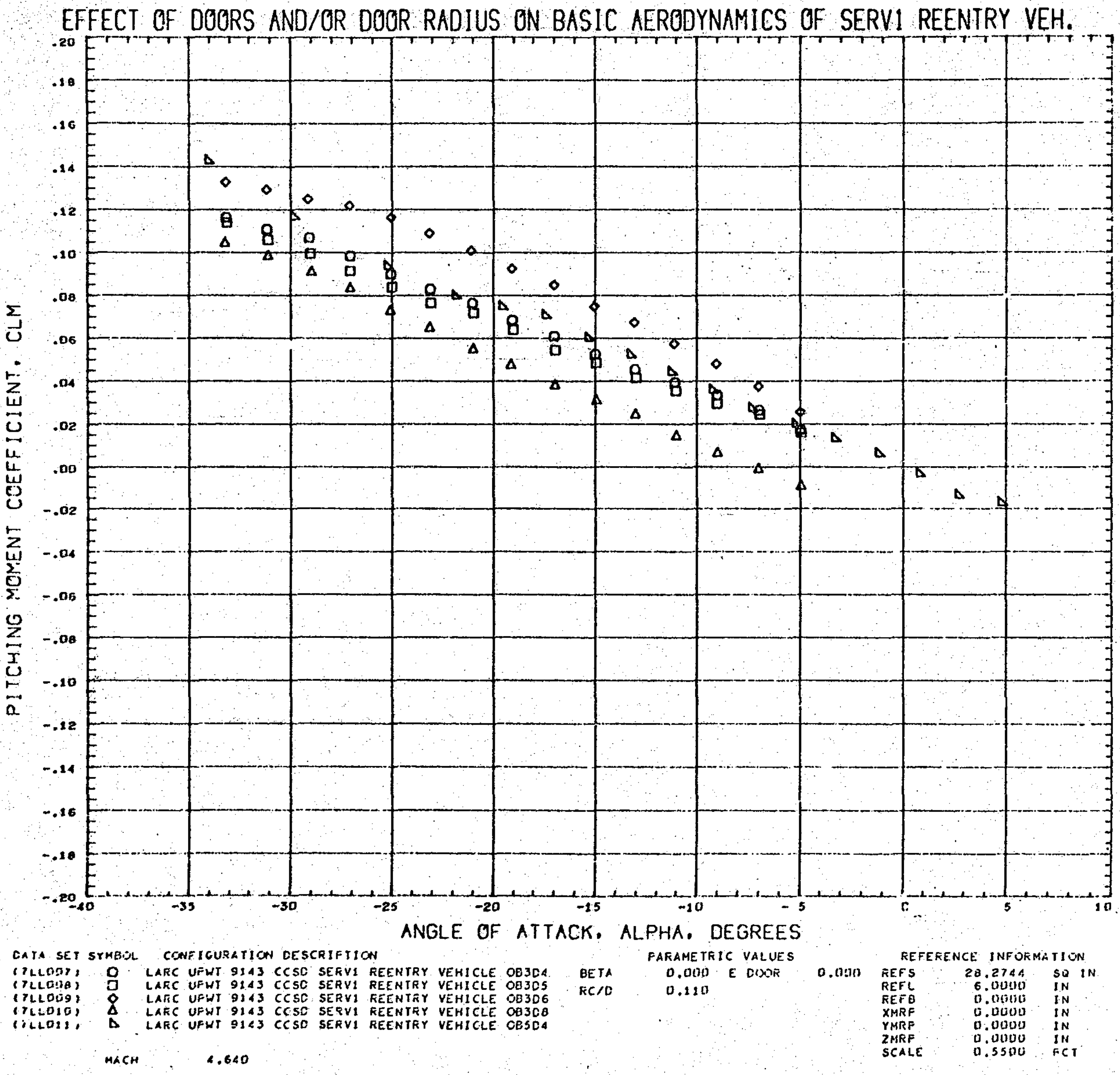

Figure 4.4-2(g).

Axial Force Coefficient M= 0.404

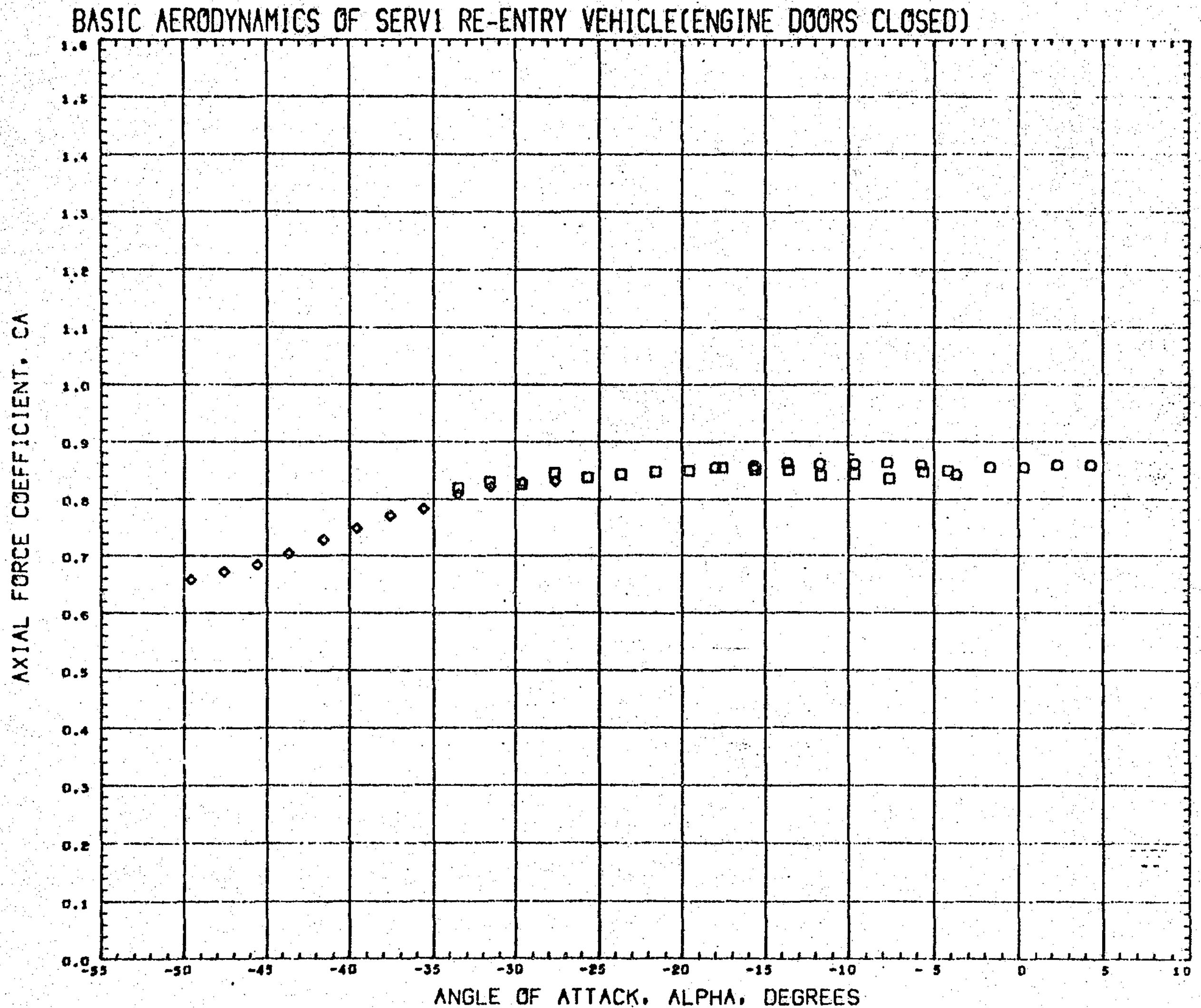

DATA SET	SYMBOL	CONFIGURATION DESCRIPTION
(XA0006)	○	AMES 66-522 CCSD SERV1 RE-ENTRY VEHICLE OB2D4
(XA0007)	□	AMES 66-522 CCSD SERV1 RE-ENTRY VEHICLE OB3D4
(XA0008)	◇	AMES 66-522 CCSD SERV1 RE-ENTRY VEHICLE OB4D4

PARAMETRIC VALUES

BETA	0.000	EDOOR	0.000
RC/D	0.110		

REFERENCE INFORMATION

REFS	28.2744	SQ.IN.
REFL	6.0000	IN.
REFB	0.0000	IN.
XMRP	0.0000	IN.
YMRP	0.0000	IN
ZMRP	0.0000	IN.
SCALE	0.5500	PERCNT

MACH 0.404

Figure 4.4-3(a).

Axial Force Coefficient M= 0.914

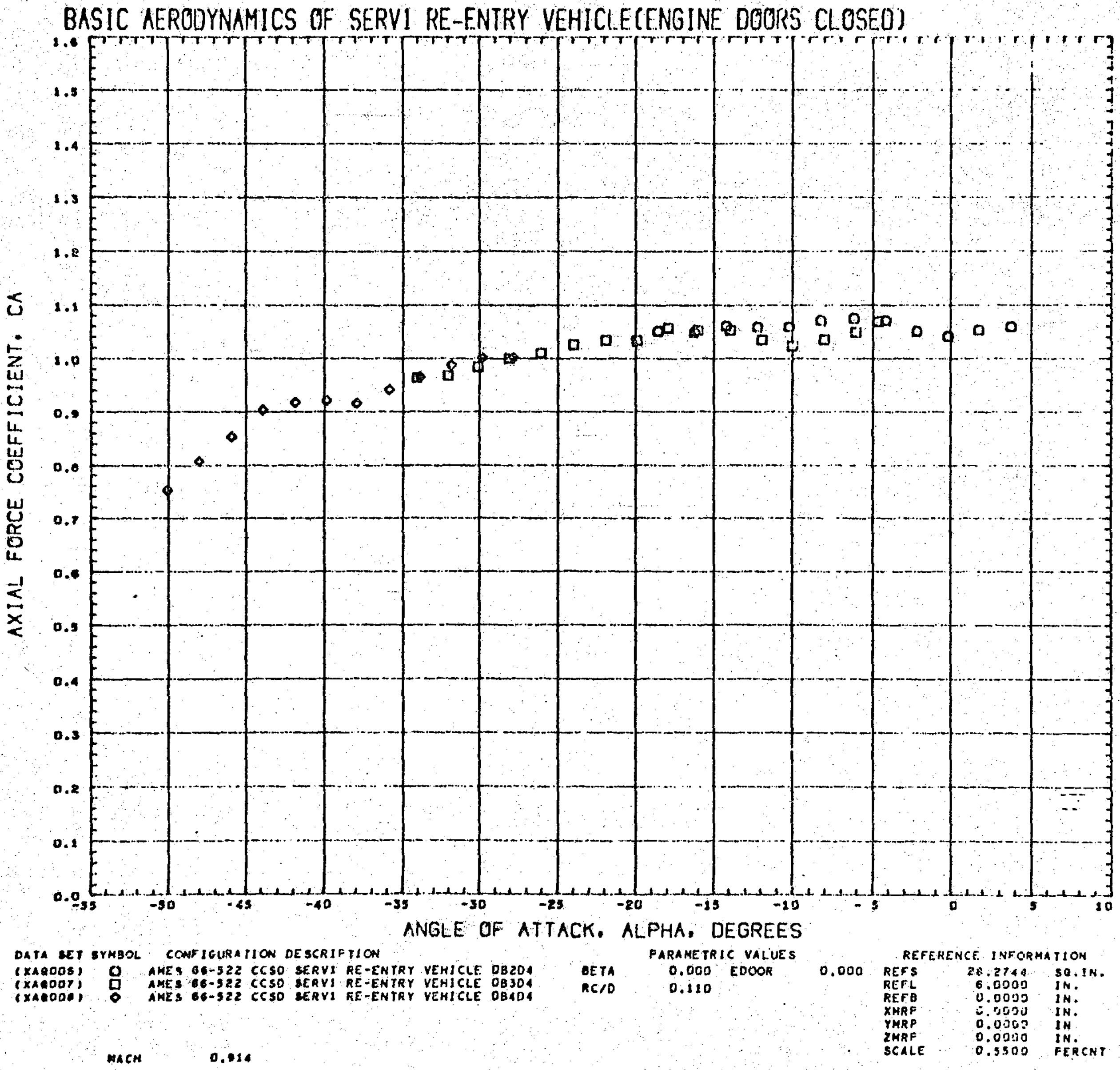

Figure 4.4-3(b)

Axial Force Coefficient M= 1.204

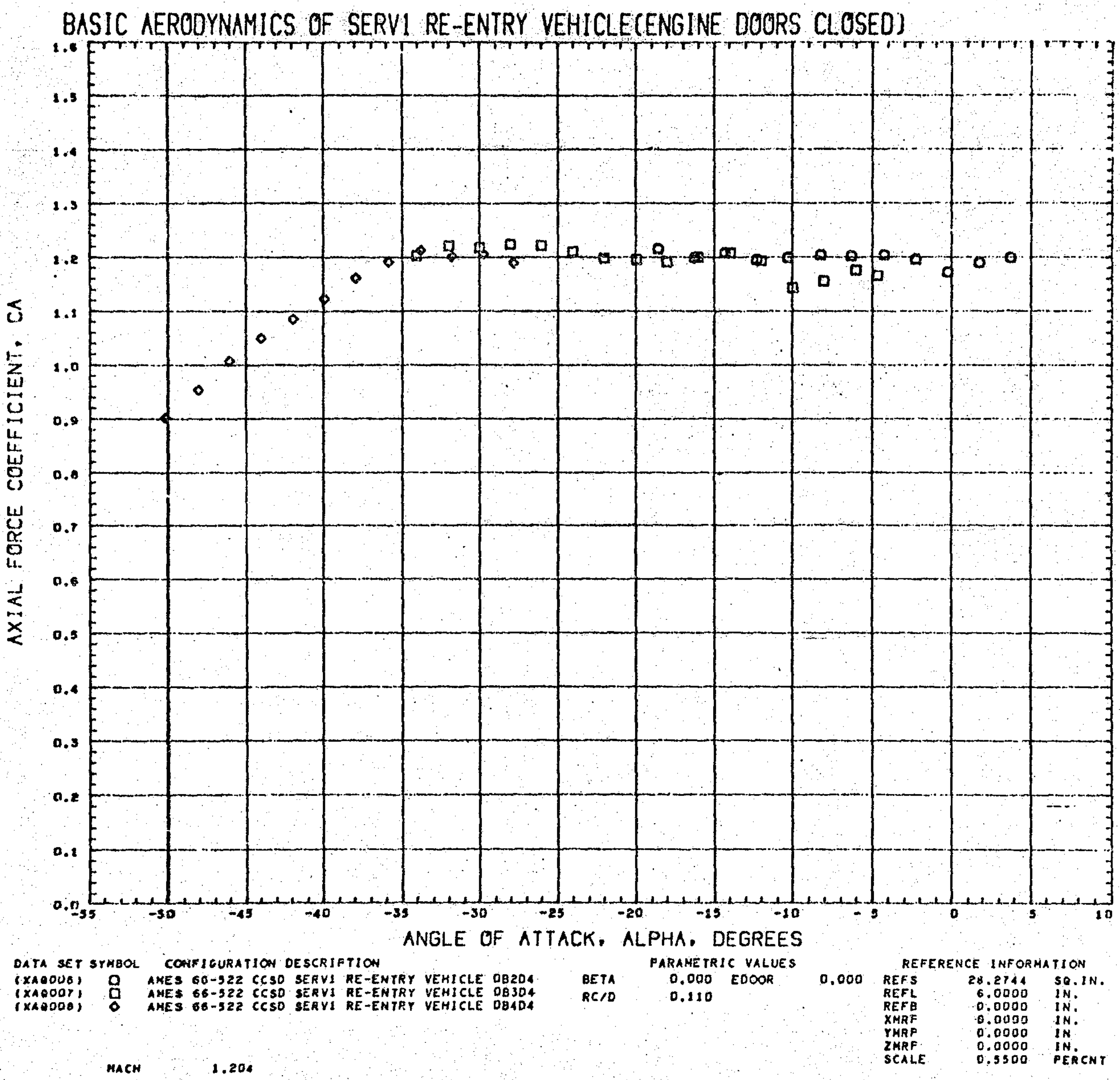

Figure 4.4-3(c).

Axial Force Coefficient M= 1.702

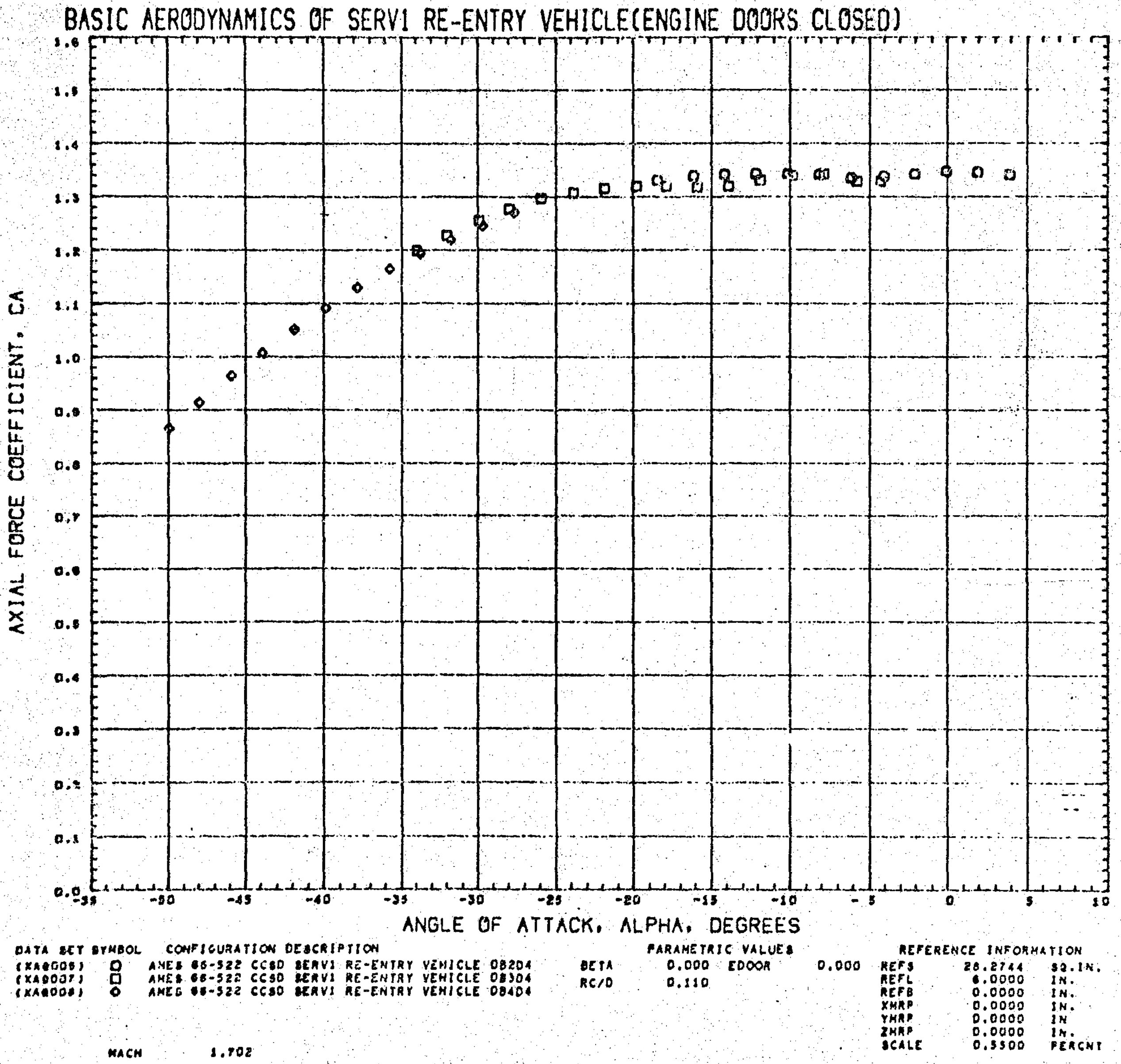

Figure 4.4-3(d).

Axial Force Coefficient M=2.60

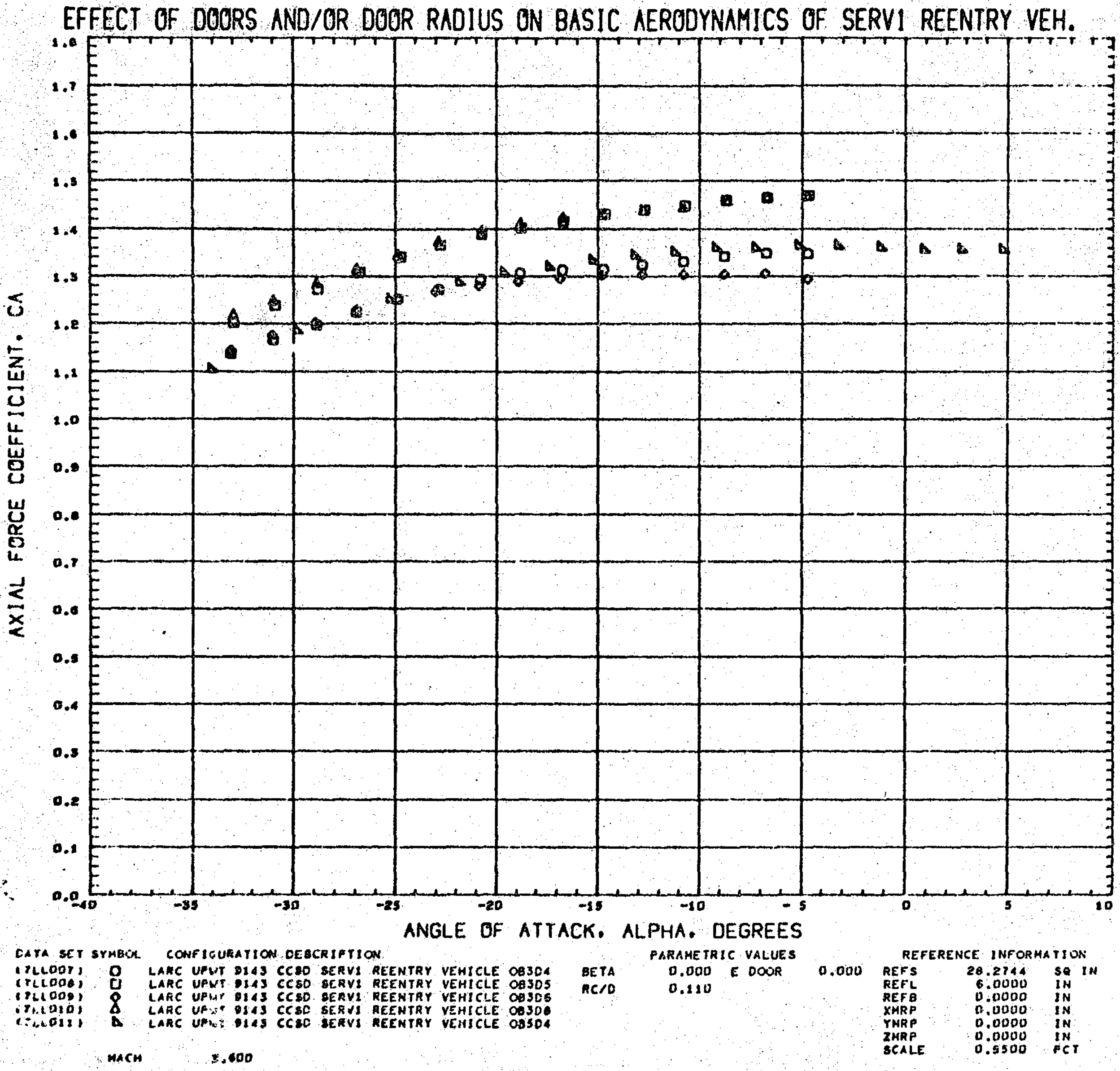

FO.

Figure 4.4-3(e).

Axial Force Coefficient M=3.85

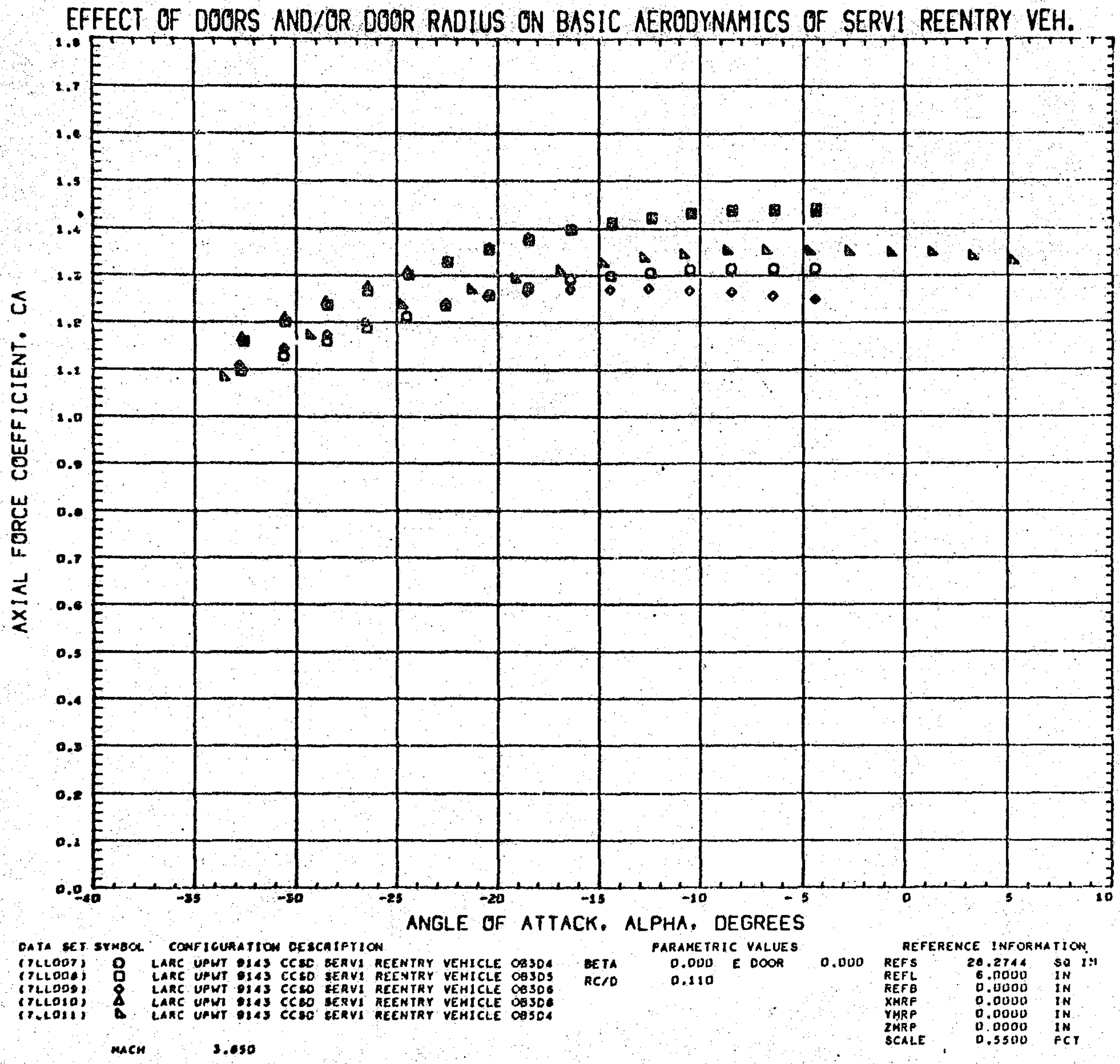

Figure 4.4-3(f).

Axial Force Coefficient M=4.64

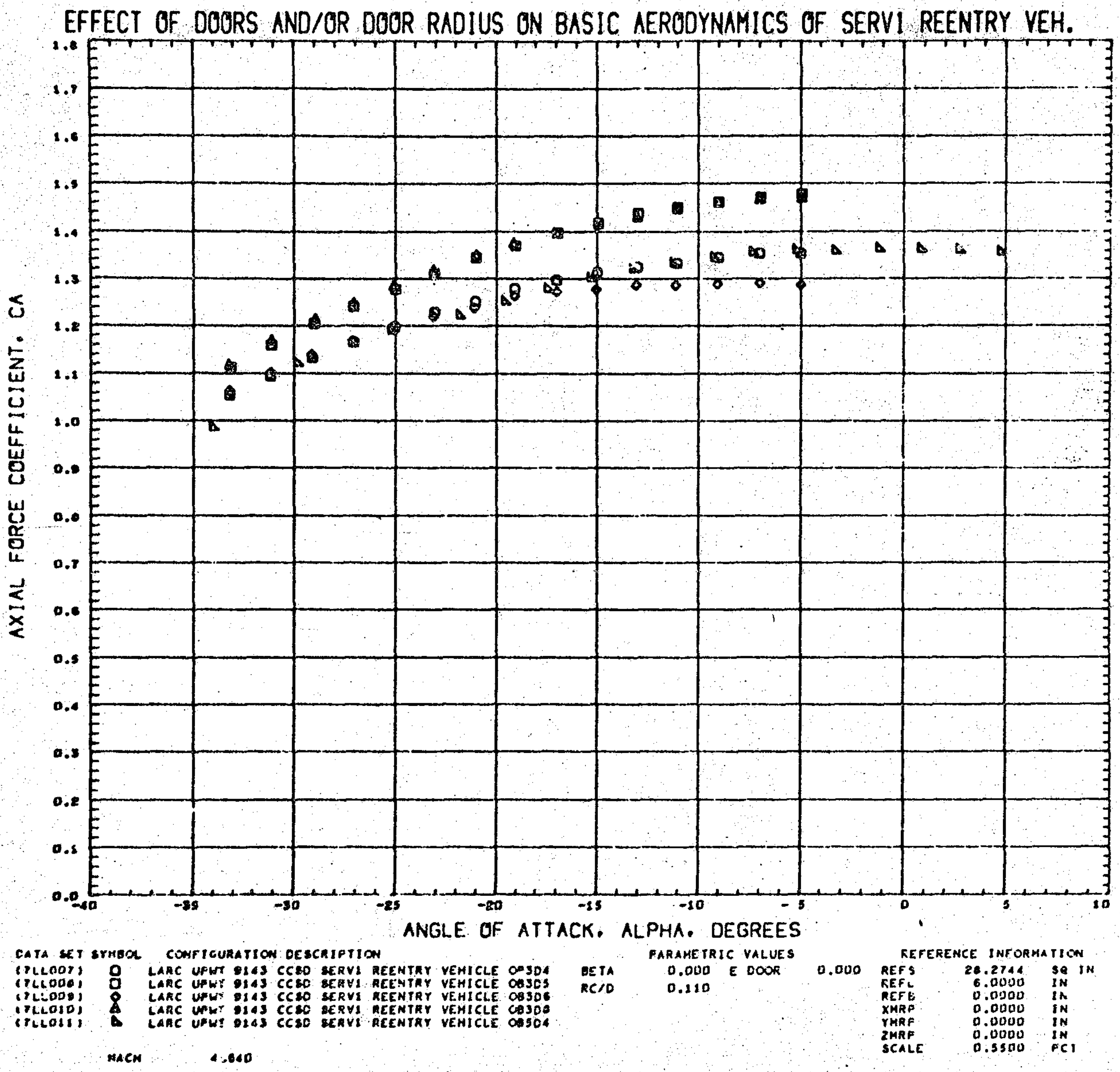

Figure 4.4-3(g).

Lift-to-Drag Ratio M=0.404

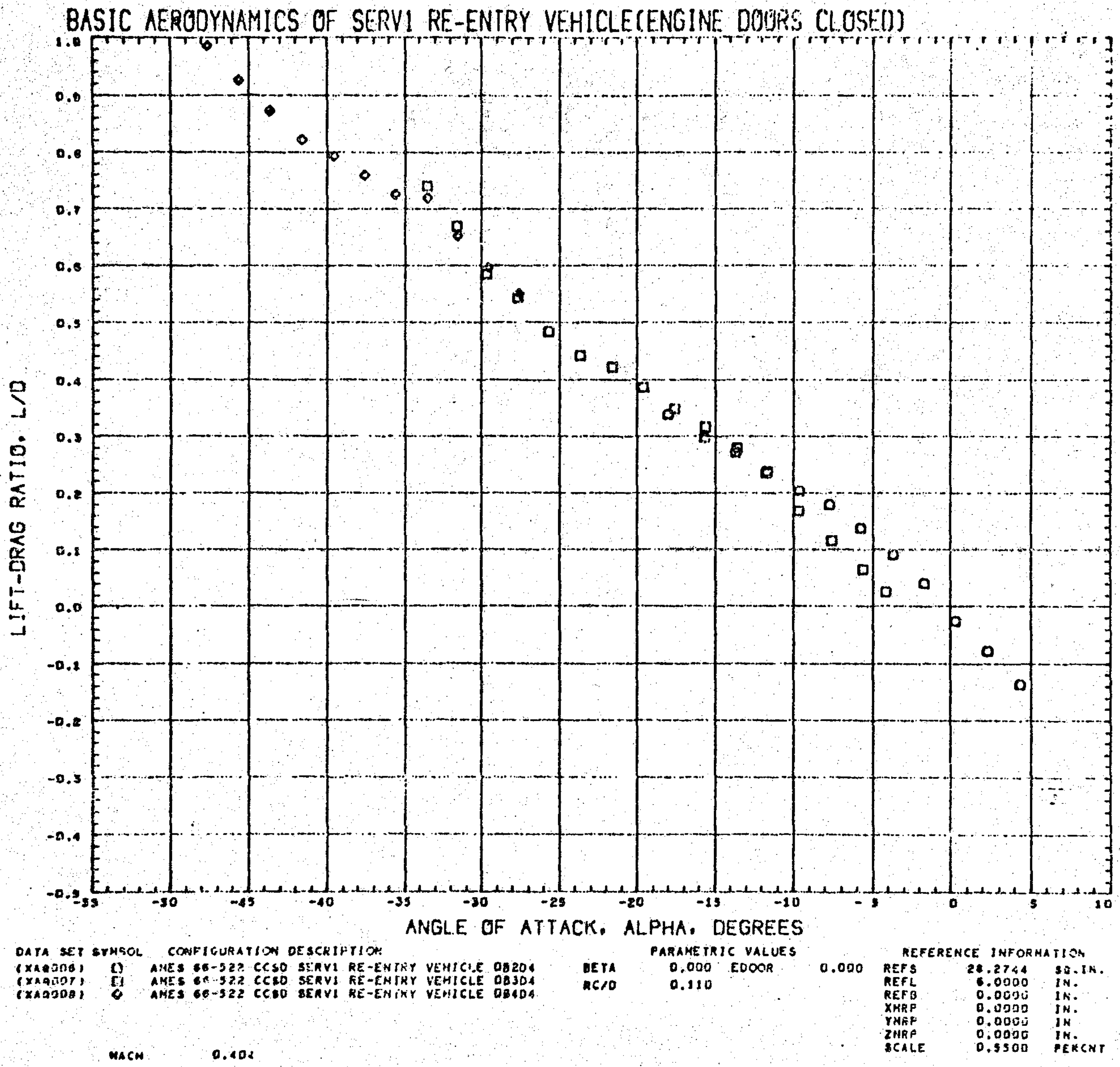

Figure 4.4-4(a).

Lift-to-Drag Ratio M= 0.914

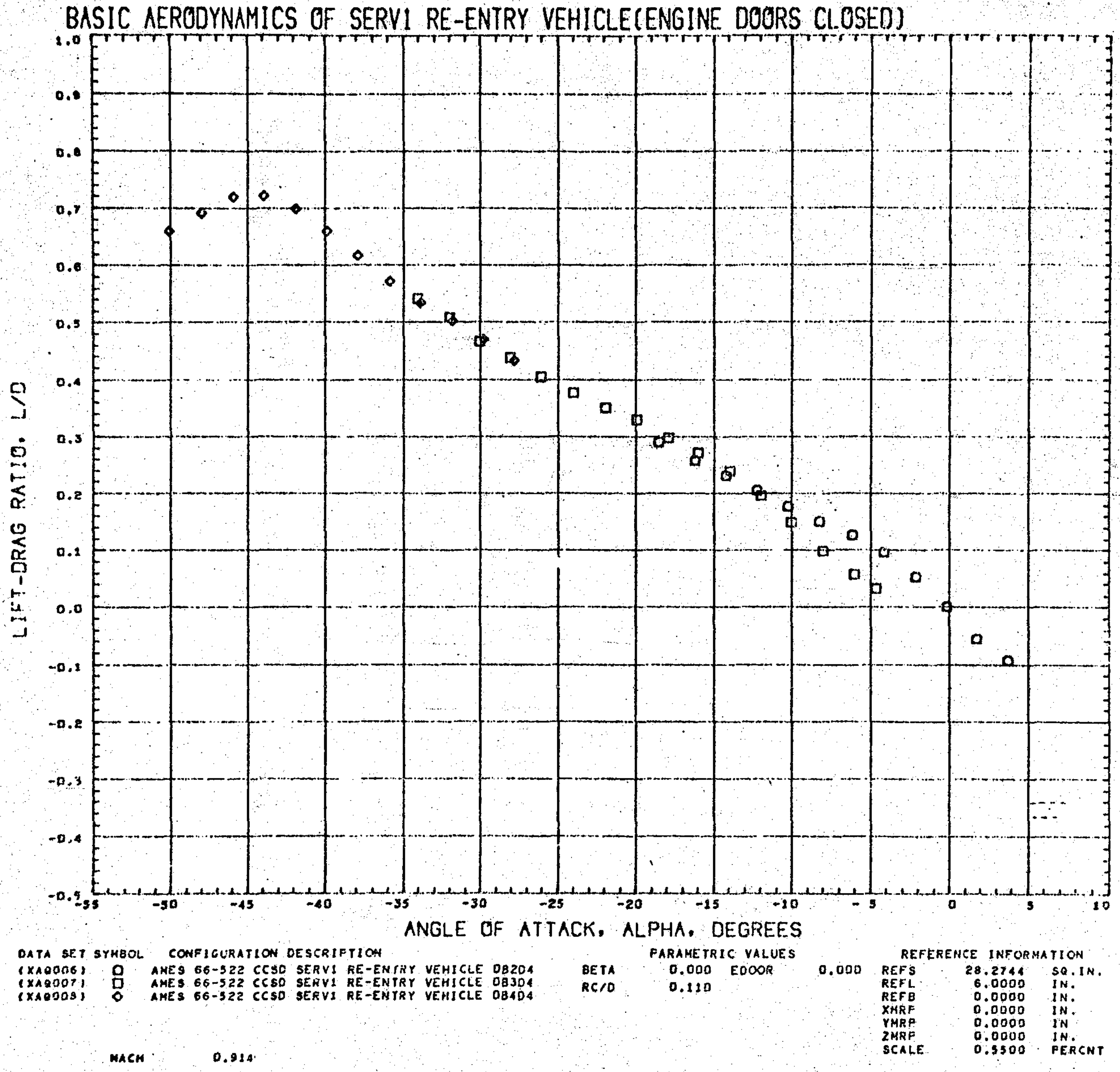

Figure 4.4-4(b).

Lift-to-Drag Ratio M==1.204

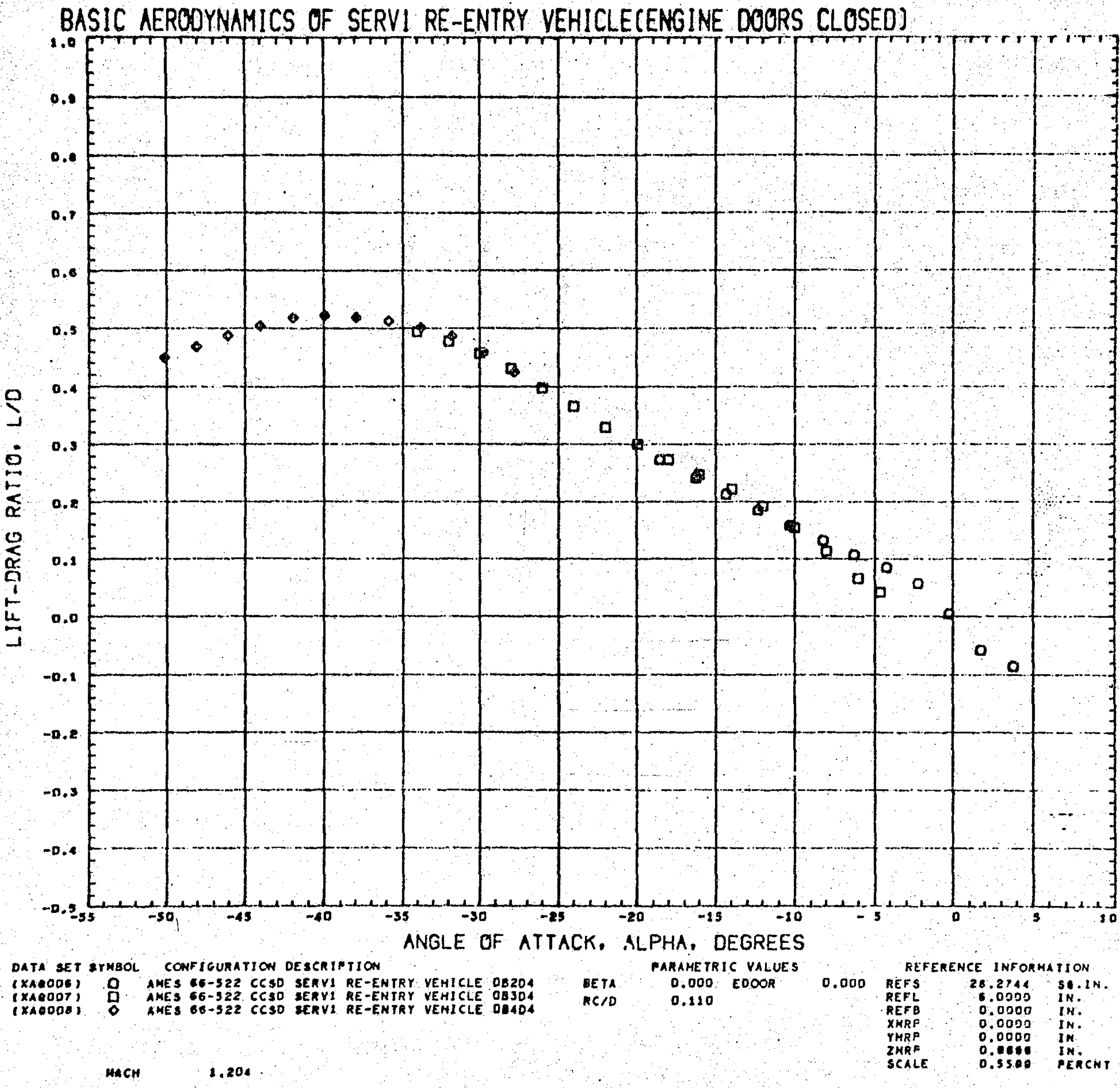

Figure 4.4-4(c).

Lift-to-Drag M=1.702

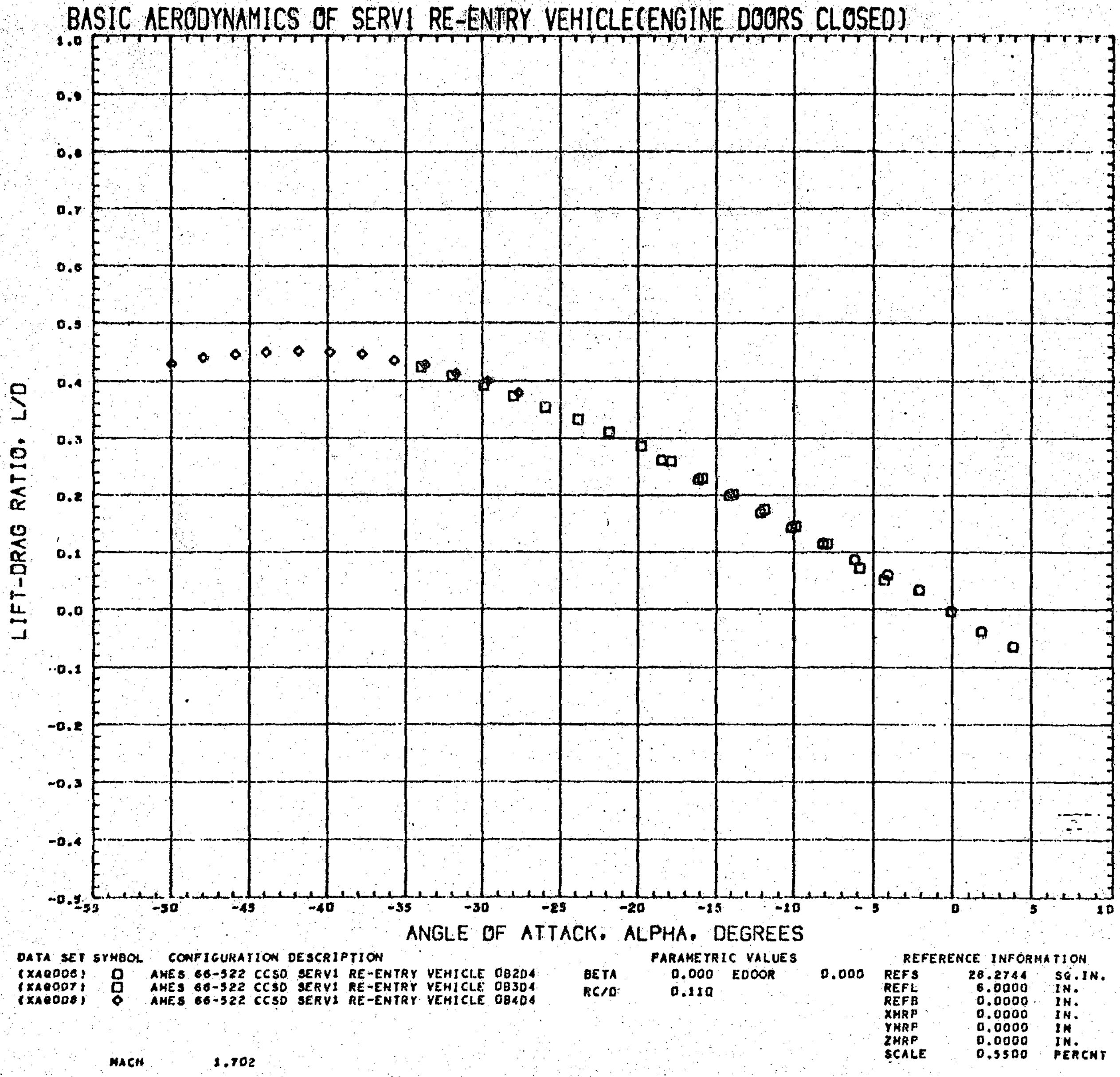

Figure 4.4-4(d).

Lift-to-Drag Ratio M= 2.60

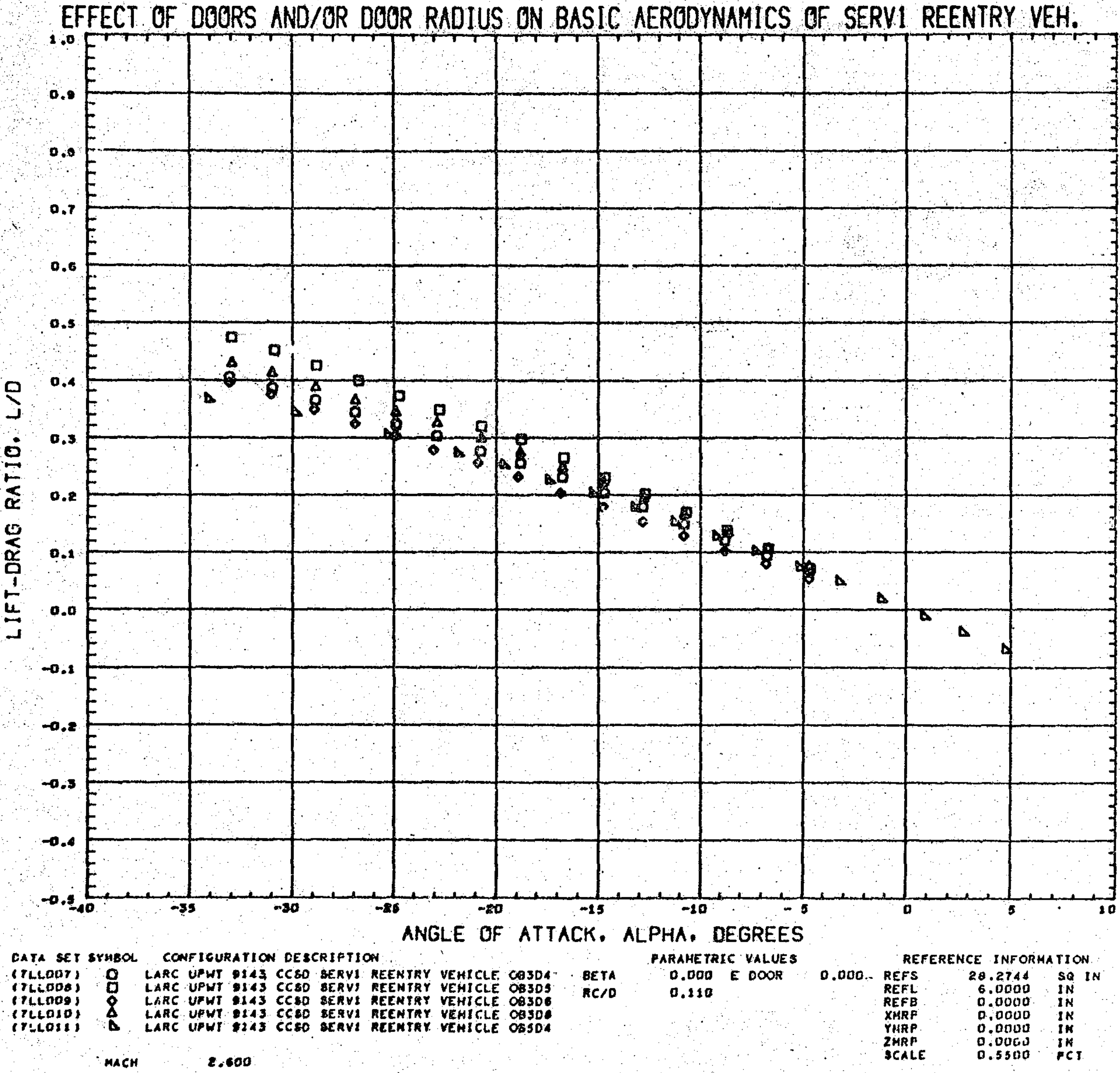

Figure 4.4-4(e).

C-2

Lift to-Drag Ratio M=3.85

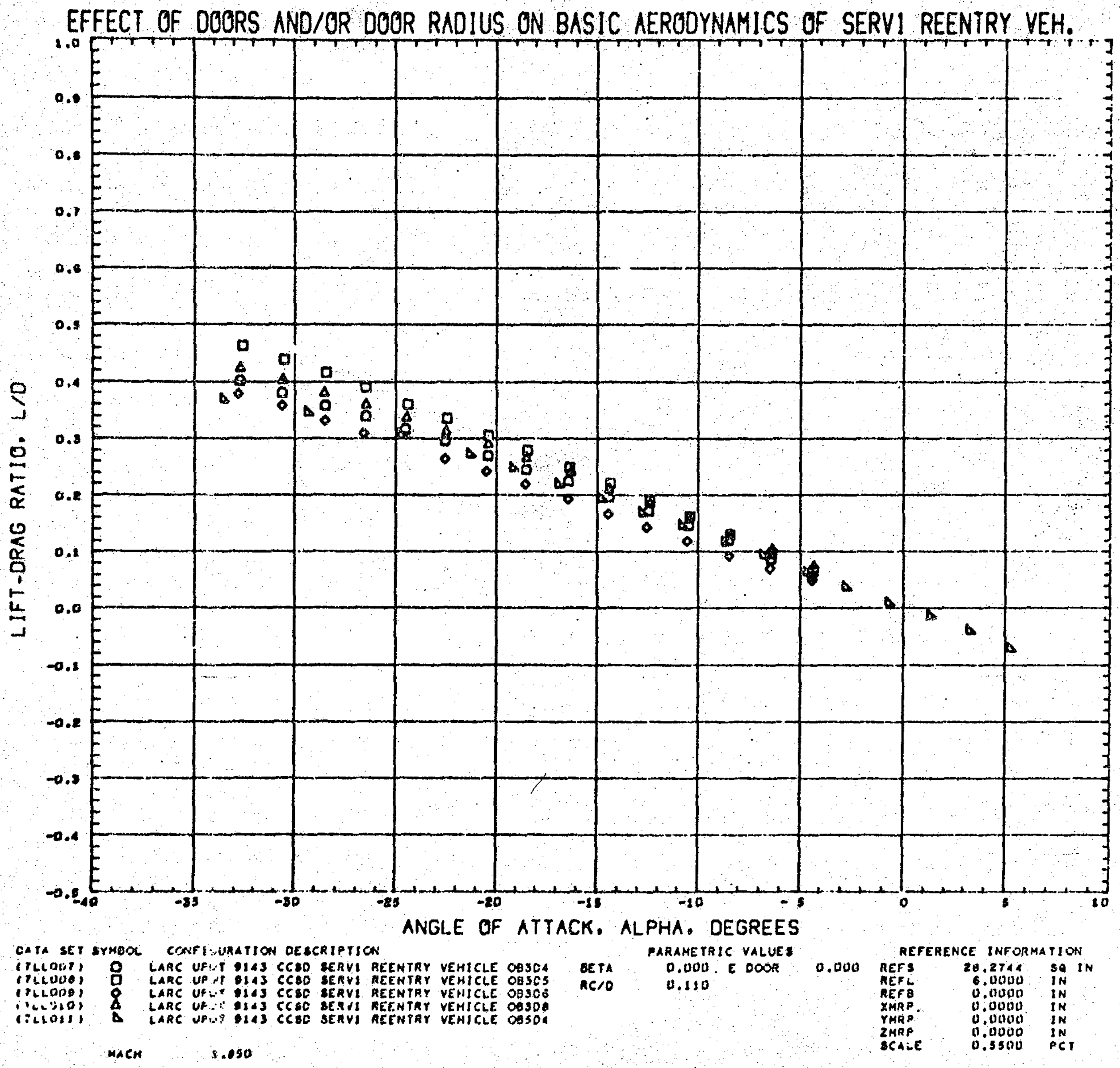

Figure 4.4-4(f).

Lift-to-Drag Ratio M= 4.64

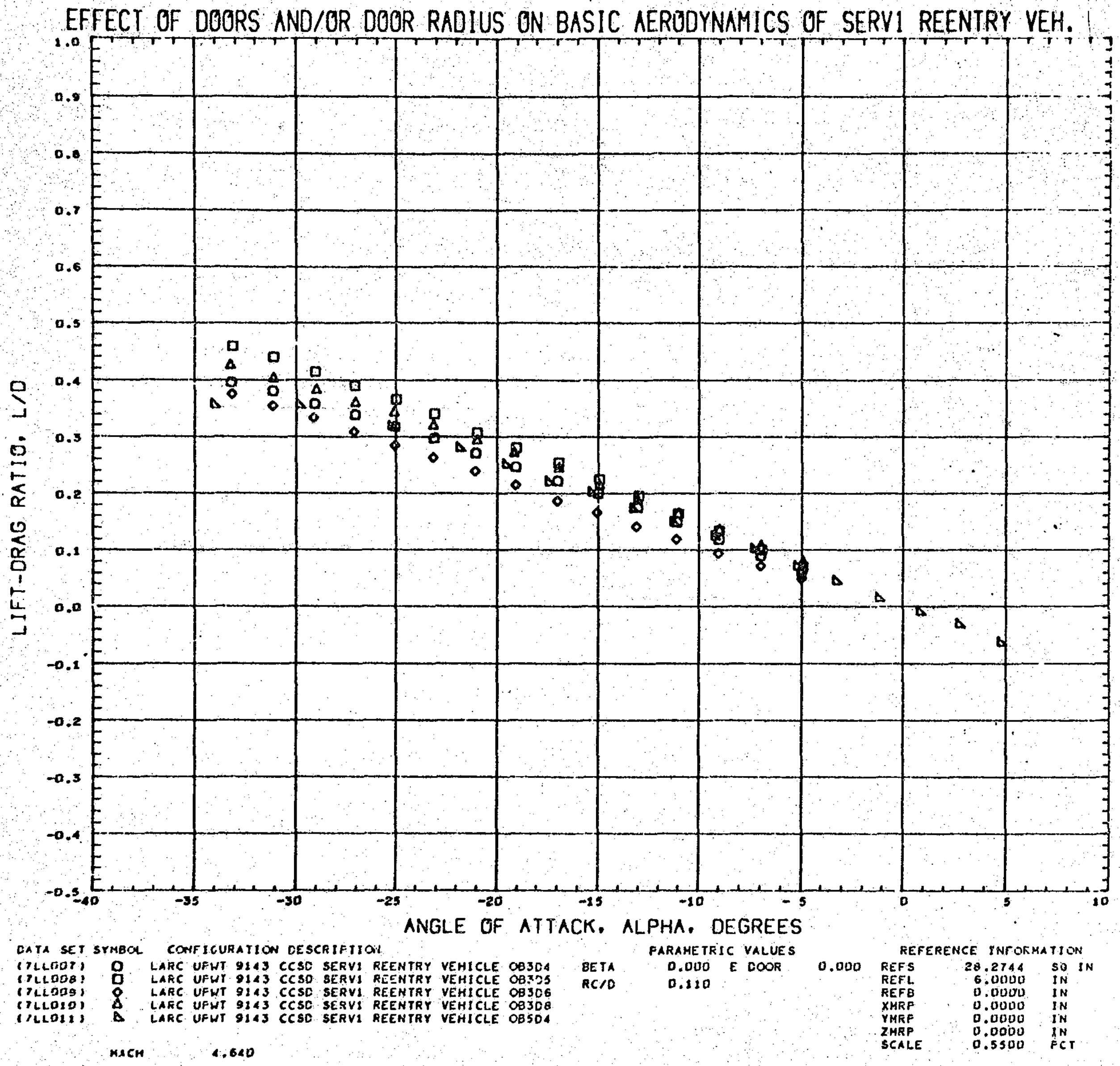

Figure 4.4-4(g).

2) decrease in heat shield corner radius

3) increase in afterbody length

4) different upper and lower heat shield face corner radii

References 10 and 11 give complete graphic presentations and digitized listings of the basic data from these tests with comparisons of the geometric variables noted above. Figures 4.4-5 and 4.4-6 illustrate the general effect of heat shield corner radii and removal of the aerospike engine protection doors.

For comparison purposes, figure 4.4-5 defines the effect of heat shield corner radius at the trim conditions for a vehicle with a typical longitudinal CG located at 0.2459 body diameters from the center of the heat shield face. Variation of trim angle of attack and resultant lift-to-drag ratio with lateral CG offset are given for the various corner radius configurations.

This representative Mach number condition indicates that decreasing the heat shield corner radius from $r/D = 0.11$ to $r/D = 0.05$ does not significantly change the variation in trim angle of attack. However, due to the higher lift-to-drag characteristics at any angle of attack for the smaller corner radius vehicle, it does increase the trim L/D. Removal of the engine doors not only reduces the trim angle of attack, but also produces an even greater decrease in the trim L/D. Finally, leaving the upper heat shield corner radius at $(r/D)_u = 0.11$ and reducing the lower radius to $(r/D)_L = 0.05$, creates an assymetric vehicle which will induce a higher trim angle of attack and resultant lift-to-drag ratio.

To further show the loss in trim angle of attack and L/D by removal of the aerospike engine thermal protection doors, figure 4.4-6 presents the high supersonic test data extrapolated to the hypersonic Mach range by application of appropriate Apollo reference data and hypersonic flow theory (the validity of this procedure is illustrated in more detail in section 2.2 of volume 4.) Trim angle of attack and L/D are shown as a function of lateral and longitudinal CG position. From these trends, it is apparent that even if engine doors could be eliminated as thermal protection, the loss in trim lift-to-drag would be unacceptable. An approximate 1.5-foot additional CG offset would be required to trim this vehicle at the same L/D as the baseline vehicle.

Schlieren photographs of bow shock shapes and flow patterns for the four configurations discussed above are presented in figure 4.4-7. These flow field photographs are all at $M=4.65$ for an angle of attack very near the baseline vehicle nominally required trim angle of attack of $\alpha = 22^{\circ}$.

4.5 CONCLUSIONS

From the SERV descent scale model wind tunnel force tests, the following conclusions can be made.

The SERV baseline descent configuration can be trimmed at a reentry L/D of 0.3 with a CG offset of between 3½ to 4 feet.

NOTE: a) LONGITUDINAL CG LOCATION, X/D = 0.2459
REFERENCED TO VEHICLE STA (O)

b) Z - REFERENCED TO VEHICLE AXIS (FT)

c) $M_\infty = 4.64$

e) ——— 11% HEAT SHIELD CORNER RADIUS
- - - - 5% HEAT SHIELD CORNER RADIUS
— — 11% UPPER, 5% LOWER
HEAT SHIELD CORNER RADIUS
—·— NO DOORS

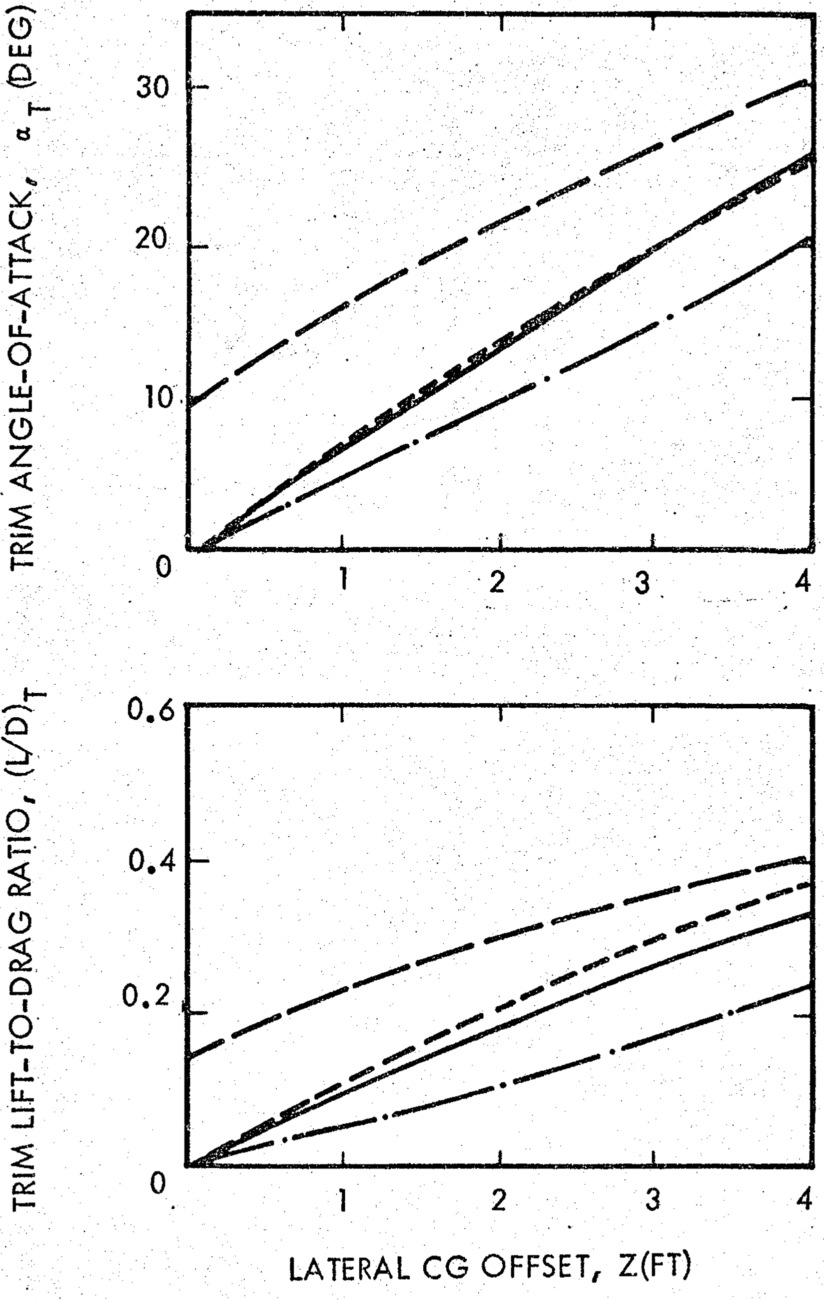

Figure 4.4-5 SERV Task 2 - Decent Vehicle Aerodynamic Trim Characteristics

NOTE:
a) ——— DENOTES DOORS OFF
b) – – – –DENOTES DOORS ON
c) X REFERENCED TO VEHICLE STA. (O) (FT)
d) Z REFERENCED TO VEHICLE AXIS (FT)
e) $M_\infty > 10$

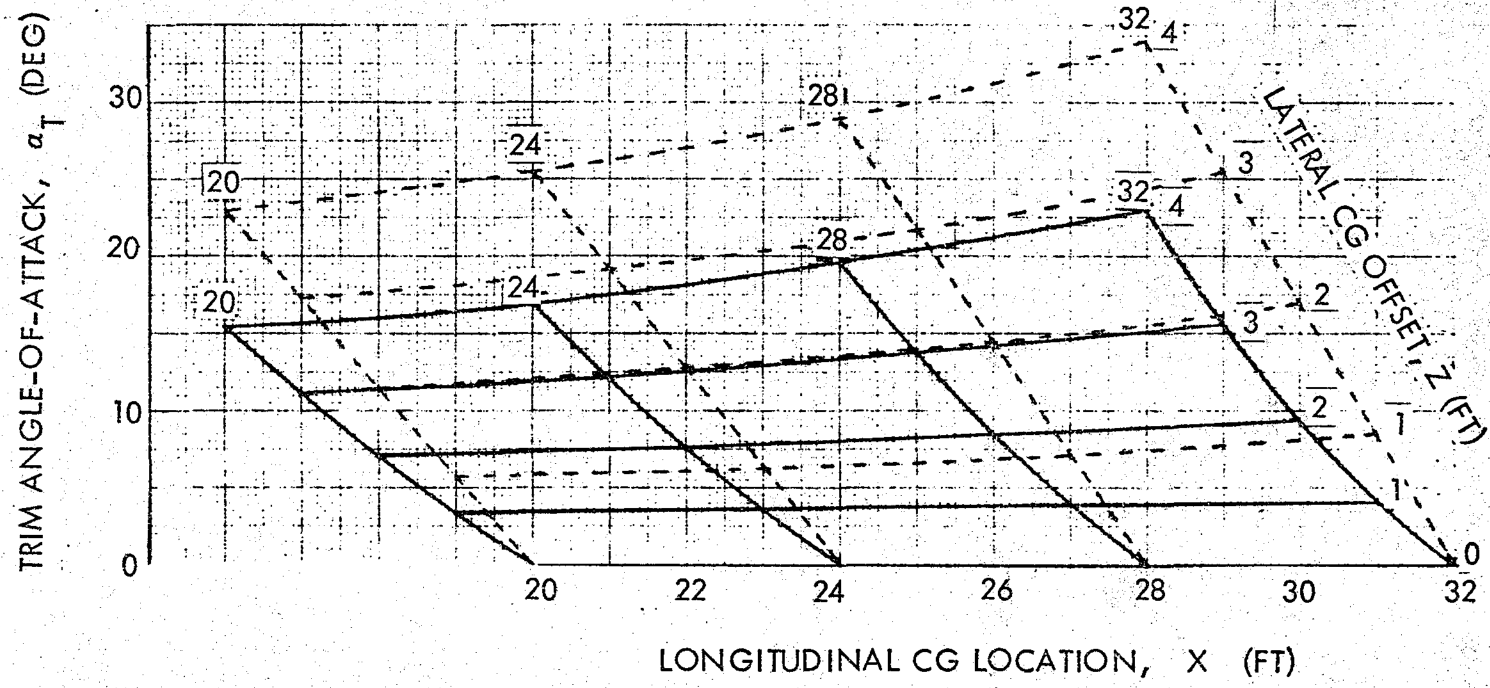

Figure 4.4-6(a). SERV Task 2 - Descent Vehicle Aerodynamic Trim Angle-Of-Attack

NOTE:
a) ——— DENOTES DOORS OFF
b) - - - - DENOTES DOORS ON
c) X REFERENCED TO VEHICLE STA. (O) (FT)
d) Z REFERENCED TO VEHICLE AXIS (FT)
e) $M_\infty > 10$

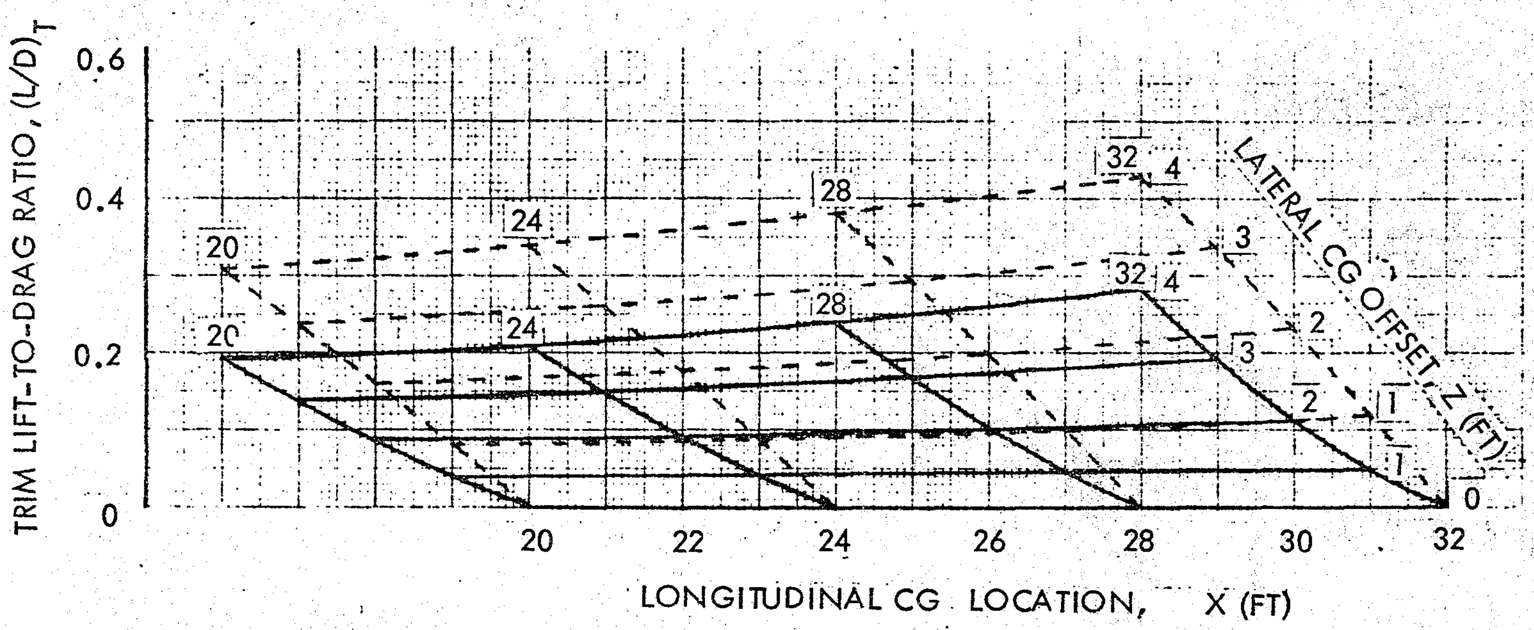

Figure 4.4-6(b). SERV Task 2 - Descent Vehicle Aerodynamic Lift-To-Drag Ratio

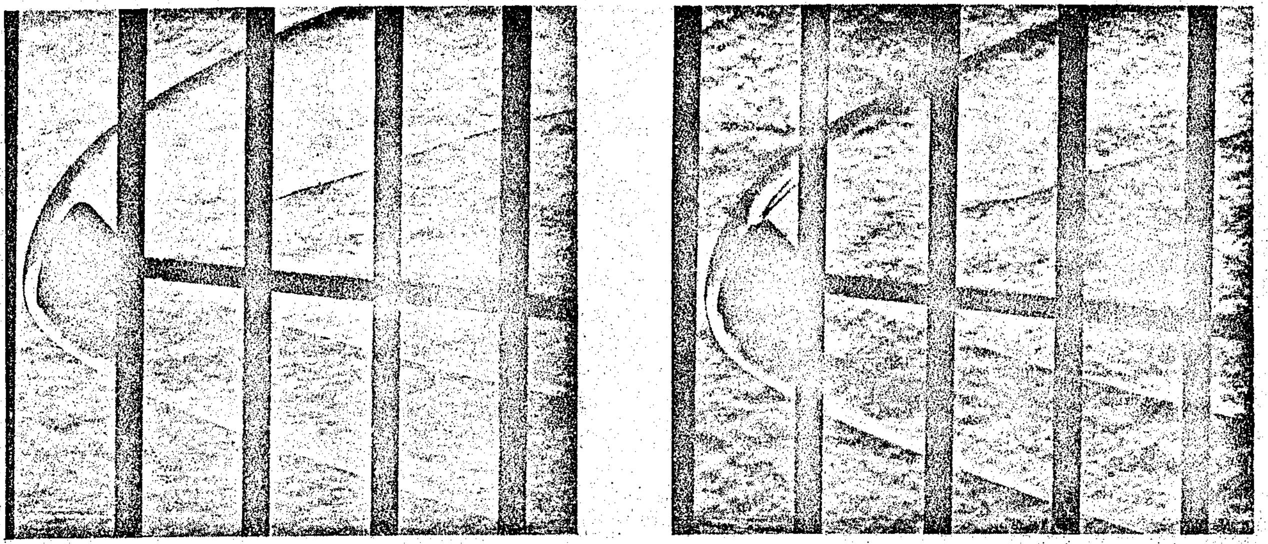

(a) MODEL OB$_3$D$_4$
$M_\infty = 4.64$; $\alpha = 21°$

(b) MODEL OB$_3$D$_6$
$M_\infty = 4.64$; $\alpha \approx 21°$
ENGINE DOORS REMOVED

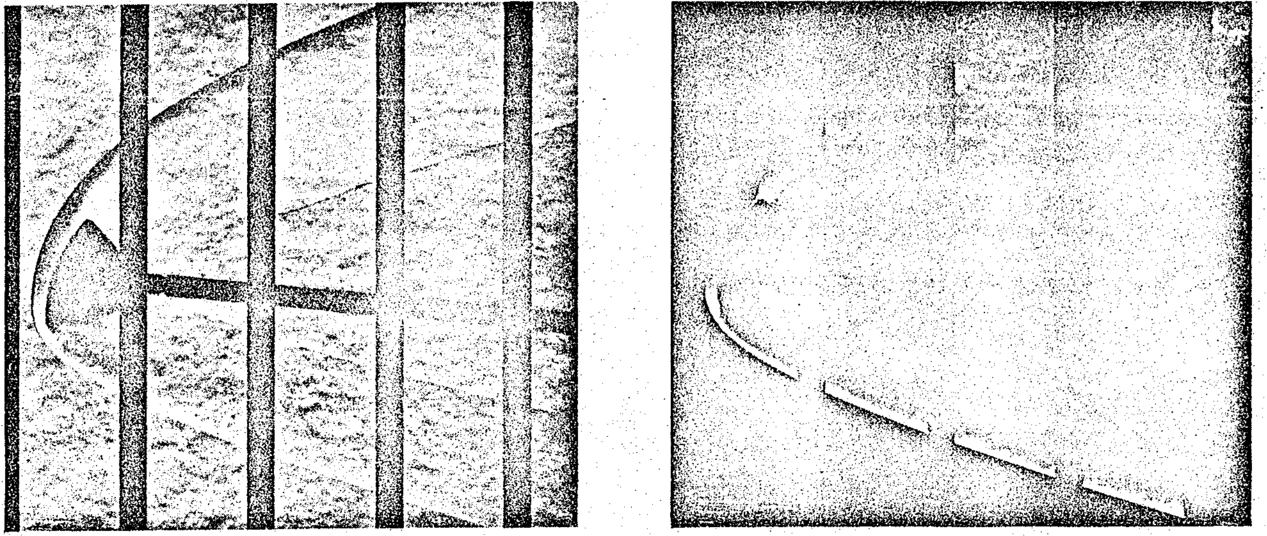

(c) MODEL OB$_3$D$_5$
$M_\infty = 4.64$; $\alpha = 21°$
REDUCED HEAT SHIELD
CORNER RADIUS

(d) MODEL OB$_3$D$_8$
$M_\infty = 4.64$; $\alpha \approx 21°$
DIFFERENTIAL HEAT
SHIELD CORNER

Figure 4.4-7. SERV Baseline Descent Configurations

The SERV baseline descent configuration is adequately stable in a trimmed attitude throughout the reentry and terminal deceleration flight range.

Removal of the aerospike engine protection doors results in too large a decrease in trim lift-to-drag ratio to be feasible.

Reduction in heat shield corner radius tends to increase trim lift-to-drag slightly.

Using a larger corner radius on the top side of the heat shield and a significantly smaller radius on the lower side induces aerodynamic moments which assist in trimming the vehicle at higher L/D for a given CG offset.

REFERENCES

1. Poucher, D.E., Wind Tunnel Test Plan for Pilot Investigation of SERV I Ascent Vehicle, Base Pressures, CCSD TN-AP-70-740, August 1970.

2. Poucher, D.E., Results of the AEDC 1T PWT 0.156% Model Pilot Investigation of SERV I Ascent Vehicle Base Pressures, CCSD TN-AP-70-485, October 1970.

3. Hull, J.J., Wind Tunnel Test Plan for Jet Simulation Testing of A Strut Mounted 2½% Model of the SERV I Launch Vehicle, CCSD TN-AP-479, Volume I, October 1970.

4. Price, Earl A., Jr., Thrust Performance and Pressure Distributions on SERV Launch Vehicle Utilizing An Aerospike Engine at Mach Numbers from 0 to 1.25, AEDC-TR-71-58, April 1971

5. NASA Project SERV Test in the Propulsion Wind Tunnel (16T) On-Line Data, TF 250, PT 1127-B00, ARO, Inc., Arnold Air Force Station, no date.

6. NASA Project SERV Test in the Propulsion Wind Tunnel (16T) Calculated Off-Line Data, TF 250, PT-1127-B00, ARO, Inc., Arnold Air Force Station, no date.

7. NASA Project SERV Test in the Propulsion Wind Tunnel (16T) Graphic Data, TF 250, PT 1127-B00, ARO, Inc., Arnold Air Force Station, no date.

8. Rawls, E.A., Wind Tunnel Test Plan for Investigation of SERV I Ascent and Descent Vehicle Aerodynamic Forces for Mach 0.4 to 2.0, CCSD TN-AP-70-475, September 1970.

9. Rawls, E.A., Wind Tunnel Test Plan for Investigation of SERV I Ascent and Descent Vehicle Aerodynamic Forces for Mach 2.6 to 4.6, CCSD TN-AP-70-471, August 1970.

10. Mellenthin, J. (ARC), Meyer, R.A. (CCSD), Rawls, E.A. (CCSD), Static Aerodynamic Characteristics of the Chrysler Corporation Space Division SERV I Ascent and Reentry Vehicle of Mach Numbers of 0.4 to 2.0, SADSAC Report DMS-DR-1046, SSPD-24, January 1971.

11. Graves, E. (LaRC), Meyer, R.A. (CCSD), Rawls, E.A. (CCSD), Static Aerodynamic Characteristics of the Chrysler Corporation Space Division SERV Ascent and Reentry Vehicle at Mach Numbers of 2.6 to 4.6, SADSAC Report DMS-DR-1068, February 1971.

12. Test Facility Handbook (Eighth Edition), Arnold Engineering Development Center, December 1969.

REFERENCES (Continued)

13. *Characteristics of Six Research Wind Tunnels of the Ames Aeronautical Laboratory*, NACA, 1957.

14. *Manual for Users of the Unitary Plan Wind Tunnel Facilities of the National Advisory Committee for Aeronautics*, 1956.

GOVERNMENT FIELD PRINTING PLANT
[illegible]
NASA - MICHOUD ASSEMBLY FACILITY 1971
NEW ORLEANS, LOUISIANA 70129

APPENDIX A

SERV 2.5 PERCENT SCALE MODEL REPORT

ASR 71-67

SERV 2-1/2% SCALE MODEL
REPORT

PREPARED BY
ADVANCED PROGRAMS

APPROVED BY

H. G. Diem

H. G. Diem
Program Manager
Advanced Technology Programs

Date: 10 March 1971

SCOPE

A feasibility study of a single-stage to orbit reusable vehicle (SERV) is being conducted by the Chrysler Corporation. Integrated into the base of this vehicle is an aerospike-nozzle engine having a diameter of approximately 89 feet. This large diameter allows for a very high nozzle expansion area ratio and therefore high vacuum specific impulse. In addition, the inherent altitude compensation capability of the aerospike-nozzle provides high specific impulse throughout the vehicle trajectory, from sea level to vacuum.

Under a 9 month contract, engine design, performance and operational data were furnished by Rocketdyne for the feasibility evaluation of the SERV concept. Performance data have been generated parametrically with vehicle and engine geometry. A baseline engine geometry was selected on which wind tunnel studies were conducted. The objectives of these tests were to provide data for predicting the effect of the external flow on full size engine performance over the SERV vehicle range of operating conditions. This report presents the results of the model tests, the approach followed for evaluation and scaling of test results to obtain full size SERV engine installed performance, and the full size installed engine performance generated over the range of flight Mach numbers and altitudes of interest for the SERV vehicle.

INTRODUCTION

Aerospike engine specific impulse performance is obtained from the evaluation of: a) combustion and expansion in the combustor; b) expansion in the nozzle and nozzle base, Fig. 1; c) combustion and expansion in the gas-generator turbine systems; and d) friction in the propellant flow circuits. These processes are evaluated in terms of efficiencies which characterize the degree to which ideality is approached in each process. Weighed, summed, and multiplied by ideal specific impulse values, these efficiencies yield the predicted aerospike engine specific impulse.

Extensive cold-flow and hot-firing tests have been conducted to verify the analytical and empirical methods and equations used in the prediction of these efficiencies for conventional aerospike geometries. Because of its high area ratio and short nozzle length the SERV is not considered a conventional geometry. However, except for the expansion process occurring at the base of the nozzle, all efficiencies in the SERV engine are accurately determined using the methods previously developed for conventional aerospikes.

The efficiency of the expansion at the base of the aerospike is characterized by the base pressure, and is incorporated into the nozzle overall thrust coefficient efficiency, C_T. This efficiency evaluates the expansion in the aerospike primary flowfield and in the nozzle base. Initial estimates were made of this efficiency for use in the generation of SERV engine parametric data. A cold-flow program was conducted to improve the reliability of the methods used to obtain C_T estimates in still-air and in slipstream operation.

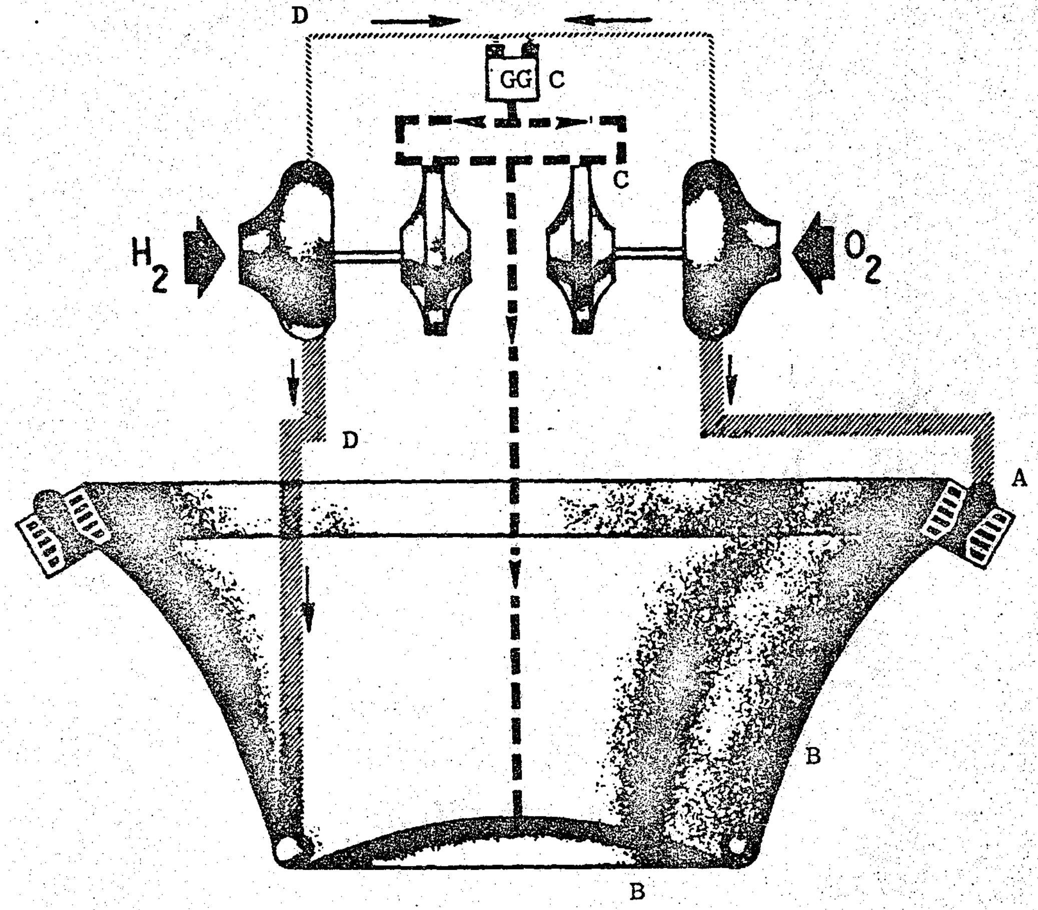

A. Combustor - combustion and gas expansion

B. Nozzle and nozzle base - gas expansion

C. Gas generator and turbines - gas expansion

D. Propellant lines, valves and coolant jacket - fluid friction

<u>NOTE</u>: The SERV baseline engine system uses a separate turbine driven low pressure pump (pre-inducer) in addition to the high pressure pump for both the oxidizer and fuel feed systems rather than the single pumps shown schematically in this figure.

Figure 1. Processes in Aerospike Engine Cycle

The cold-flow test program was run using a scaled model (Fig. 2) of the SERV vehicle, incorporating a high expansion area ratio, short length aerospike engine model. These tests were conducted in still-air and in slipstream, at Rocketdyne's Rocket Nozzle Test Facility (RNTF, and at Arnold Engineering Development Center (AEDC).

The slipstream wind tunnel program simulated low altitude external flow conditions similar to those encountered by the vehicle in flight. These tests were not run at the pressure ratios of an actual trajectory. The data were extrapolated to indicate the effect of the slipstream on high area ratio aerospike engine operation. Previous testing with aerospike nozzles of low area ratio has shown that the integrated effect of slipstream on the complete trajectory is small. Slipstream testing at AEDC has provided information on this aspect for the SERV engine geometry and furnished data used in scaling the slipstream effects.

Still-air testing of the baseline SERV engine geomery is a significant step in the test program since no aerospike of that area ratio (465) and nozzle percent length (5 percent) has been tested previously under cold-flow or hot-firing conditions. Testing under the SERV program provided a basis for the prediction of the basline engine performance and for the parametric engine data. The body of SERV parametric data encompasses a wide range of geometric parameters as indicated in Table 1. The slipstream testing constitutes the basis for correction of these data to slipstream conditions. These tests provide data on the effect of engine operation on vehicle base pressure and therefore vehicle base drag with engine on.

Engine performance estimates have been revised based upon evaluation of test results at RNTF and AEDC facilities. The cold flow program does not provide absolute confirmation of the engine performance, but constitutes the most economic way of determining if the SERV configuration can develop the necessary open-wake base pressure to make concept feasible.

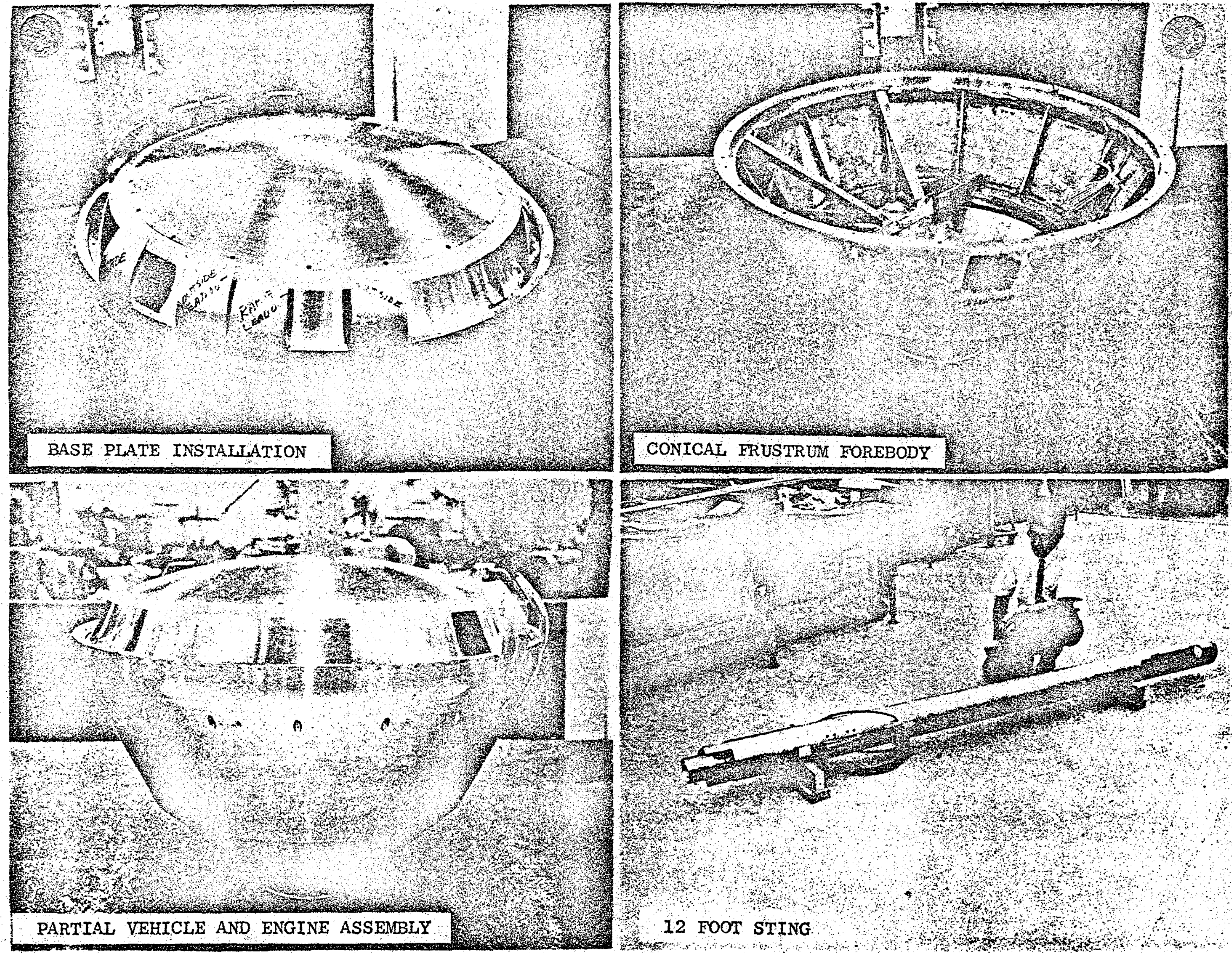

BASE PLATE INSTALLATION

CONICAL FRUSTRUM FOREBODY

PARTIAL VEHICLE AND ENGINE ASSEMBLY

12 FOOT STING

Figure 2. SERV 2.5% SCALE WIND TUNNEL MODEL

TABLE 1

SERV AEROSPIKE PERFORMANCE AND BASE PRESSURE REQUIREMENTS

	Parametric	Baseline Engine
Nozzle Expansion Area Ratio	150 - 1000	465
Nozzle Length, % of Cone	5 - 10	5
Pressure Ratio, % of Design	0.24 - 100	1 - 100
Propellants	LOX/H_2	LOX/H_2

AEROSPIKE PERFORMANCE CORRELATIONS

A large body of data has been generated for the aerospike nozzle under NASA, Air Force, and Rocketdyne sponsorship (Table 2). These data have been used to develop a method of calculation of overall aerospike nozzle performance. This method predicts the primary nozzle contribution and the secondary (base pressure) contribution to overall nozzle performance. The primary contribution is obtained by using the method of characteristics, a longtime proven method. The bulk of the analytical effort has been placed in the development of base pressure calculation methods. Successful theoretical and empirical methods of base pressure prediction were developed for operation at and near design pressure ratio. Past correlations of predicted values and experimental data have shown good results in that pressure ratio range (Fig. 3). As may be noticed from Fig. 3, the base pressure is invariant with pressure ratio in a range of pressure ratios including design pressure ratio. In this range, known as the closed-wake region, ambient pressure is not a variable affecting base pressure. The problem of prediction of base pressure here is therefore greatly simplified. In the range of pressure ratios which includes sea level, the base pressure is affected by the ambient pressure and its theoretical and empirical prediction is more complex. Because of this, overall nozzle performance prediction is made in two distinct ways, one for the closed-wake and one for the open-wake.

CLOSED WAKE OVERALL NOZZLE PERFORMANCE PREDICTION

In the closed-wake the performance of the aerospike engine is obtained from the method of characteristics analysis of the primary and a calculation of the base pressure. From these two analyses the primary and secondary thrusts are computed. The methods used in the calculation of these two contributions are discussed below.

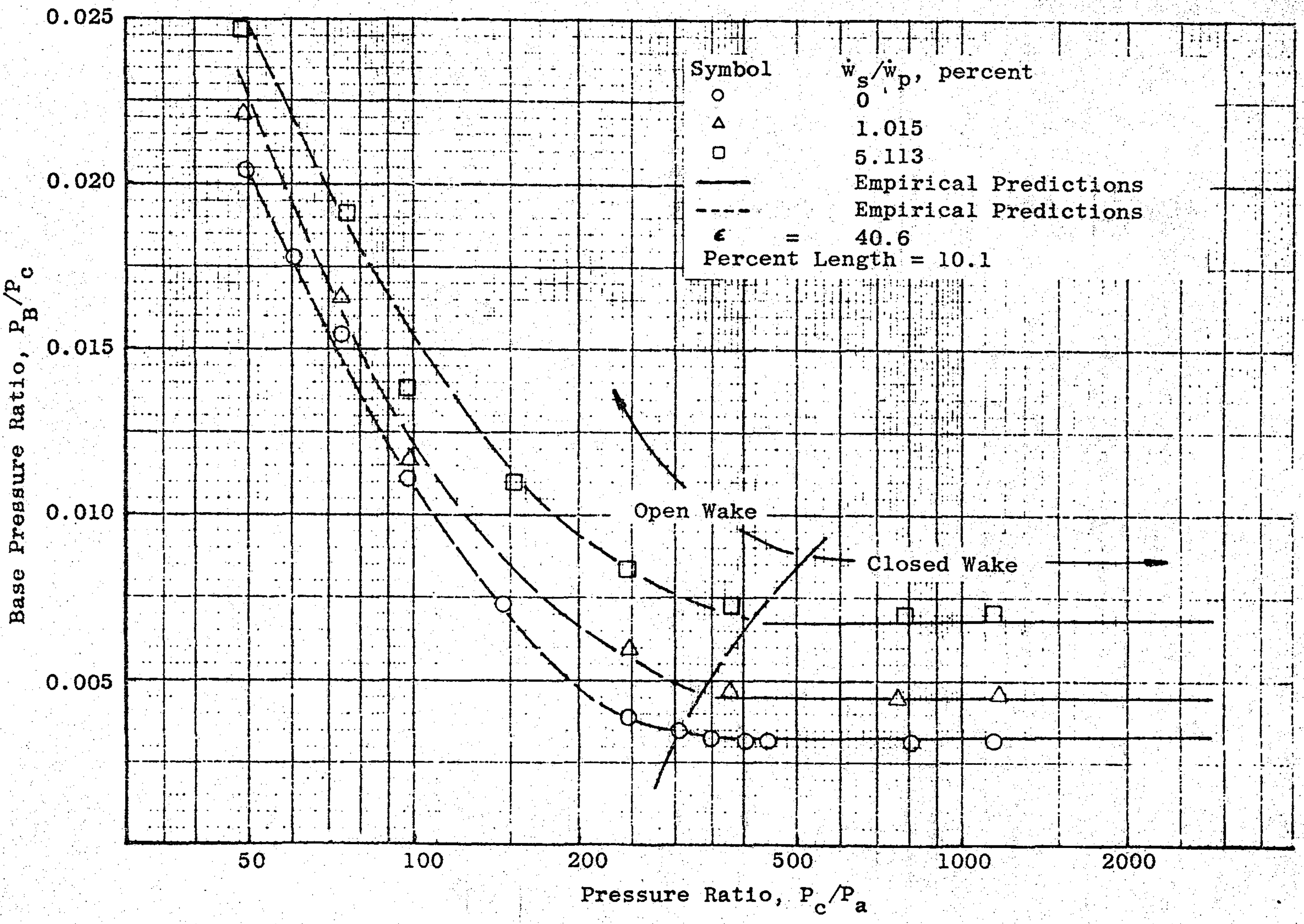

Figure 3. Aerospike Base Pressure Correlation

TABLE 2

AEROSPIKE TESTING RANGE OF EXPERIENCE

	Cold-Flow	Hot-Firing
Nozzle Expansion Area Ratio	8 - 150	8 - 76
Nozzle Length, % of Cone	7 - 30	6 - 20
Pressure Ratio, % of Design	1.3 - 100	3 - 100
Primary Heat Capacity Ratio, γ, or Propellants	1.23, 1.4, 1.67	LOX/RP, LOX/H_2 NTO/50-50, H_2O_2
Number of Tests		
Still-Air	5700	200
Slipstream	123	71

Primary Nozzle Thrust Coefficient, C_{F_P}

This parameter is obtained for any altitude of operation from computerized method of characteristics and boundary layer equations. The methods are very accurate and yield (for a given geometry) nozzle thrust coefficient and nozzle wall pressure values as a function of nozzle length and pressure ratio. This parameter reflects the nozzle expansion efficiency (η_g), the effect of reaction kinetics (η_k), the boundary layer drag (η_d), and other processes such as expansion around baffles (η_b). The various efficiencies combined with the ideal thrust coefficient yield the primary thrust coefficient as shown in the following equation,

$$C_{F_P} = \left[1 + \sum_i (\eta - 1)_i \right] C_{F_{\substack{ideal \\ vac}}}$$

Typical graphs resulting from this type of analysis are shown in Figs. 4 and 5. As can be seen in Fig. 4, the thrust coefficient decreases as pressure ratio (altitude) increases. At high pressure ratios the thrust coefficient becomes constant. This indicates that the nozzle wall pressures are no longer affected by the prevailing ambient pressure. The primary nozzle thrust coefficient presented in Fig. 4 follows the same trends with pressure ratio as the primary intrinsic thrust of the nozzle. The intrinsic thrust of the nozzle. The intrinsic thrust represents the force developed by the engine exclusive of ambient pressure drag.

Closed-Wake Nozzle Base Pressure

The base pressure of aerospike nozzles follows curves with pressure ratio which are similar in behavior to that of the intrinsic nozzle thrust coefficient, Fig. 6. When altitude (pressure ratio) increases the base pressure decreases, as ambient pressure waves transmitted through the

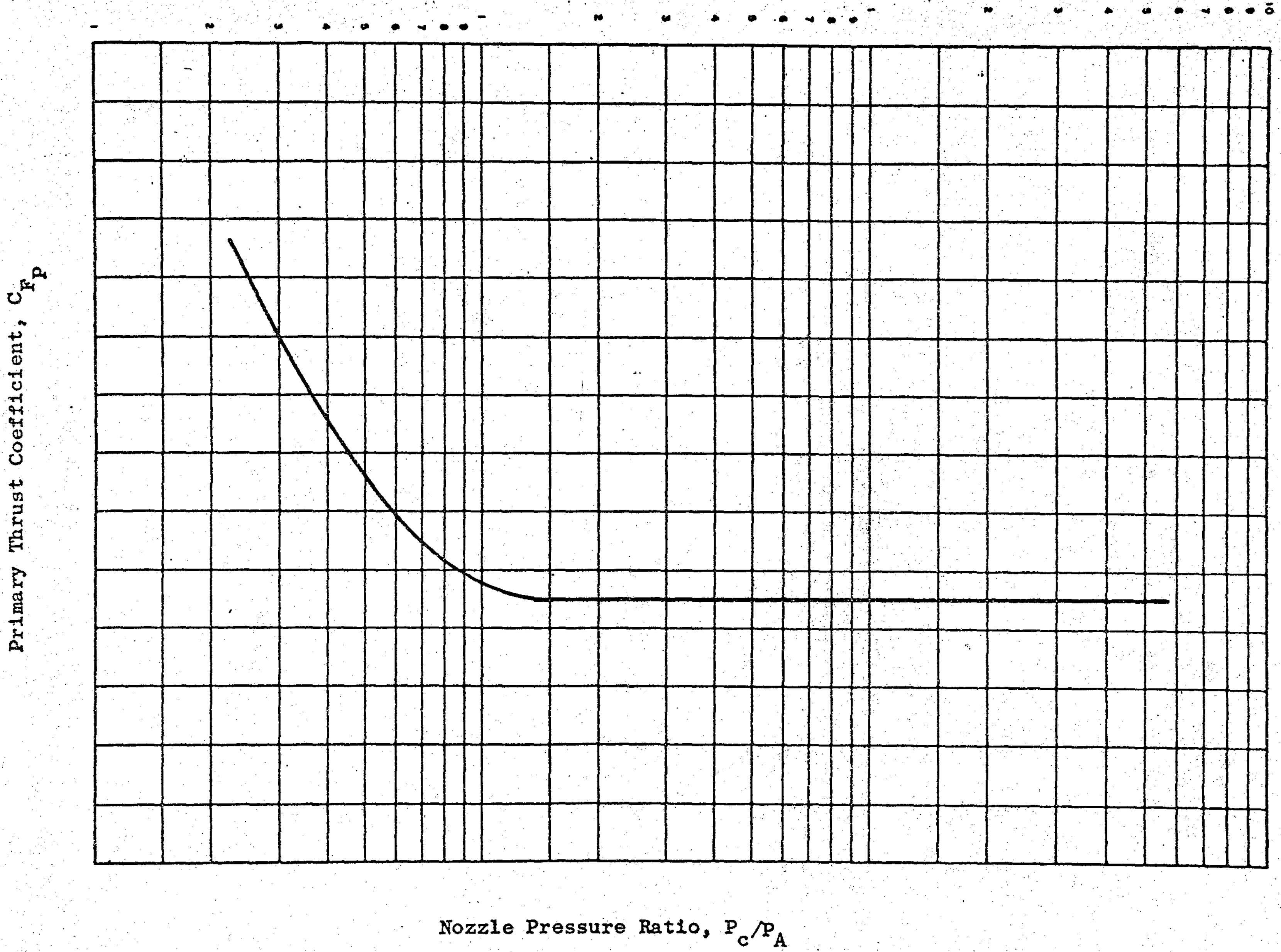

Figure 4. Typical Aerospike Primary Thrust Coefficient vs Pressure Ratio

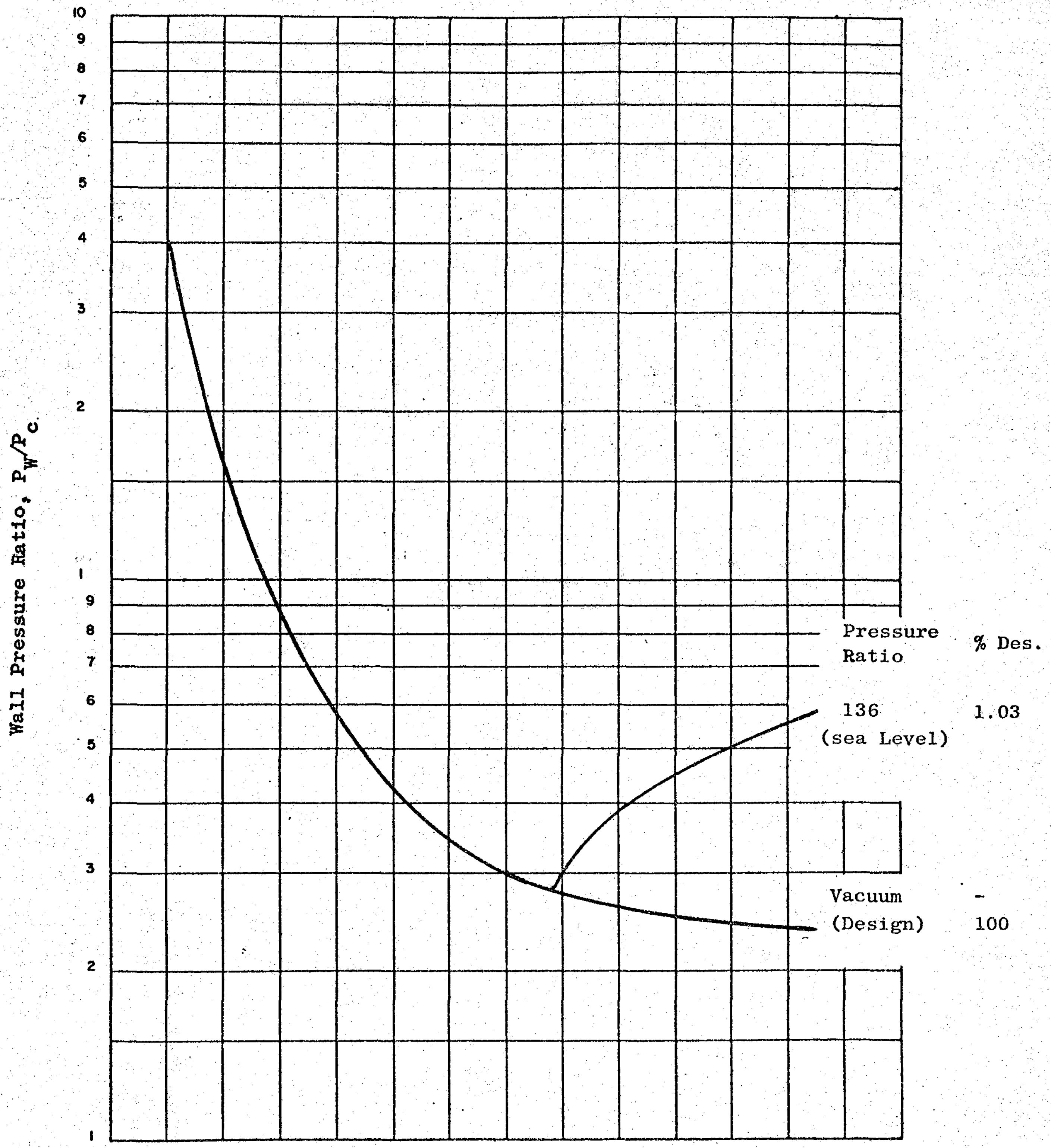

Figure 5. Typical Aerospike Primary Wall Pressure Ratios vs Nozzle Station

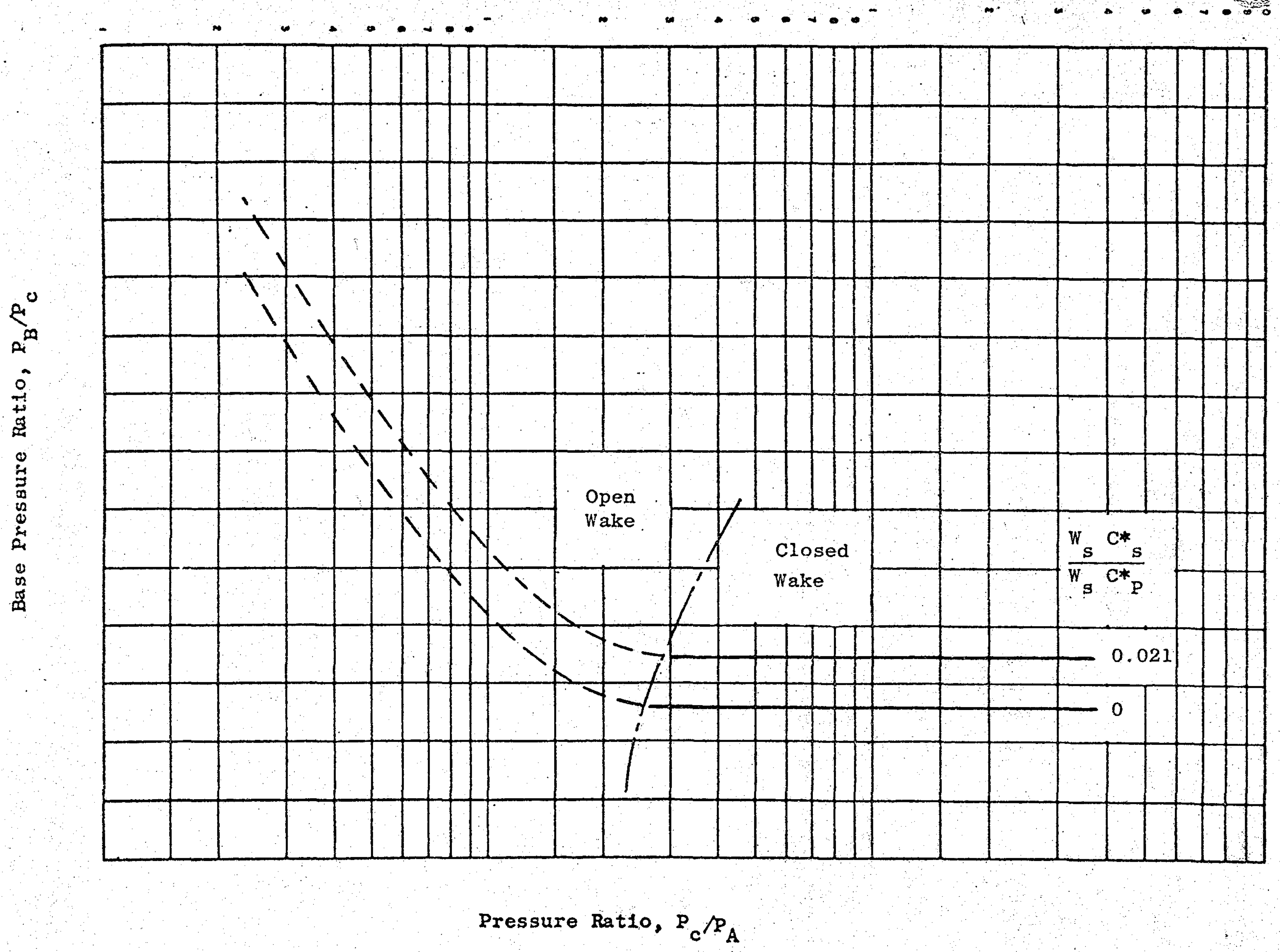

Figure 6. Typical Aerospike Base Pressure Ratios vs Pressure Ratio

primary flowfield affect the base region. An altitude is eventually reached where the ambient pressure does not affect the base. The base pressure remains constant from this point on and the wake is said to be closed.

Two methods are used for prediction of base pressures in the closed-wake regime, a theoretical method, and an empirical method. The empirical method generates only the base pressure. The theoretical method, Appendix A, is more encompassing and generates more information about the flowfield in the base. The results and accuracy of the empirical and theoretical methods are comparable.

For the SERV engine several of the parameters of Table 1 are beyond the range of aerospike test experience. However, the equations were assumed applicable following similar experiences in aerospike programs wherein equations based on the lower expansion area ratio were successfully extended to an area ratio of 150.

Overall Nozzle Performance, C_T

The primary thrust coefficient (C_{F_P}) is combined with the closed-wake base pressure to yield the closed overall nozzle thrust coefficient, referred to as the intrinsic nozzle thrust coefficient,

$$C_{F_{INT}} = C_{F_P} + P_B/P_c \, \epsilon_B \tag{1}$$

A typical intrinsic thrust coefficient curve is shown in Fig. 7. From this parameter, all that is necessary in the closed-wake is to subtract the ambient pressure drag at the altitude in question to obtain the nozzle thrust coefficient. Thus,

$$C_F = C_{F_{INT}} - P_A/P_c \, \epsilon \tag{2}$$

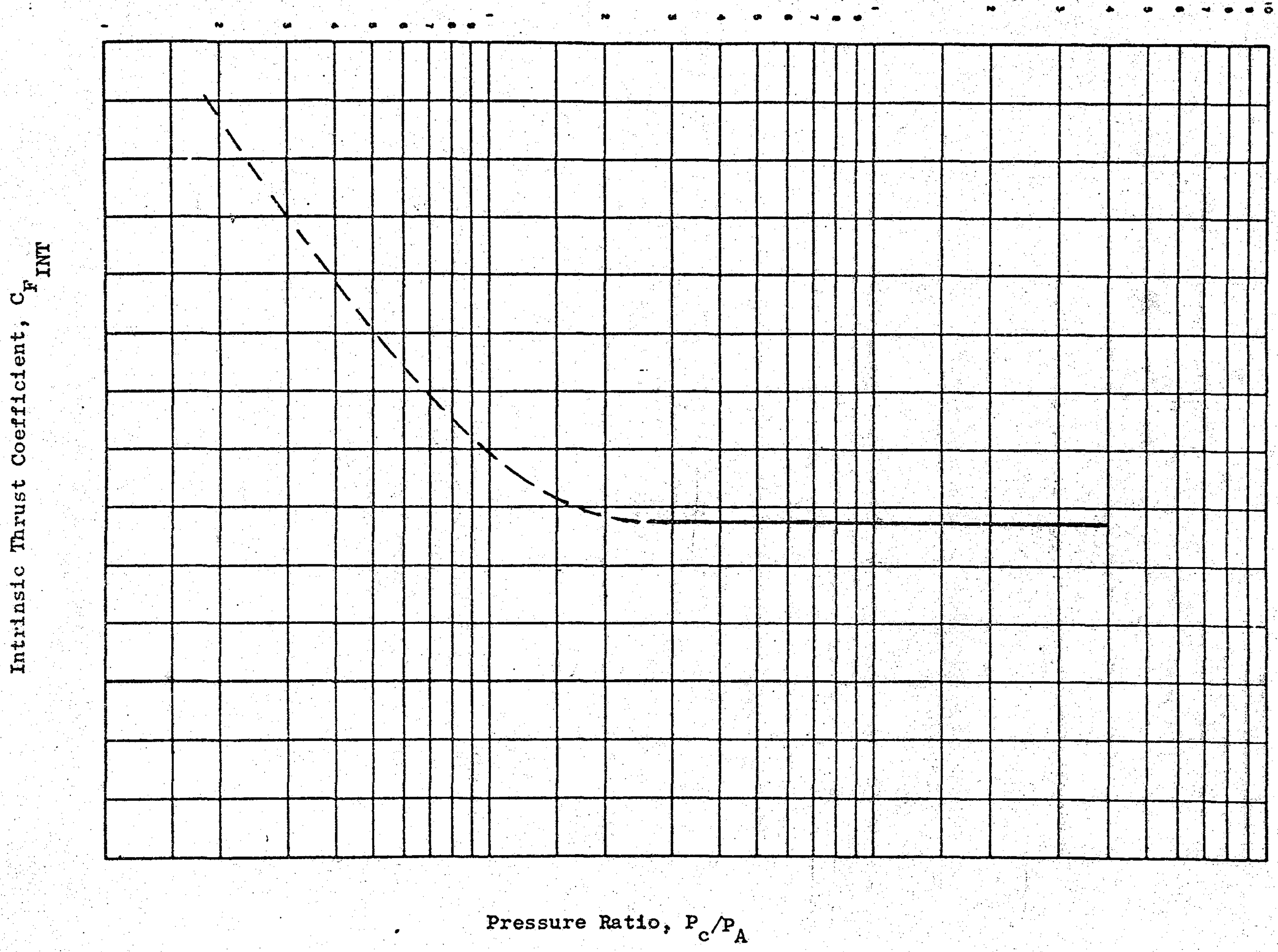

Figure 7. A Typical Aerospike Intrinsic Thrust Coefficient vs Pressure Ratio

The parameters in Eqs. 1 and 2 above, combined with the ideal combustion chamber characteristic velocity (C_i^*) and efficiency (η_c^*), and with the secondary flowrate ratios ($\dot{w}_s/\dot{w}_p$), yield the engine specific impulse,

$$I_s = \frac{C_F \eta_c^* C_i}{g\,(1+\dot{w}_s/\dot{w}_p)} \tag{3}$$

The quotient of nozzle thrust coefficient and the optimum thrust coefficient for that altitude defines the nozzle thrust coefficient efficiency (C_T),

$$C_T = \frac{C_F}{C_{F_{OPT}}} \cdot \frac{1}{(1+\dot{w}_s/\dot{w}_p)} \tag{4}$$

Unlike $C_{F_{INT}}$, C_T varies in the closed-wake region because the ambient drag and the optimum thrust coefficient vary with pressure ratio. A large portion of the C_T curve is generated with knowledge of $C_{F_{INT}}$, P_A and $C_{F_{OPT}}$.

The parameter C_T in Eq. 4 is used for nozzle comparison, nozzle evaluation, and for scaling to hot-firing conditions. An equation for scaling results when C_F from Eq. 4 is substituted into Eq. 3.

OPEN-WAKE OVERALL PERFORMANCE PREDICTION

As in the closed-wake, the open-wake overall nozzle performance coefficient (C_T) is calculated from a primary thrust coefficient contribution and a base pressure contribution. The primary thrust coefficient (C_{F_P}) is accurately established for the open-wake regime using the method of characteristics analysis (Fig. 4). Empirical methods as well as an extension of the closed-wake theoretical method (Appendix B) have been evaluated for prediction of the open-wake base pressure. These methods did not fully characterize the proper trends with nozzle geometrical changes such as expansion area ratio and nozzle length. Because of this, a method has been developed which makes direct use of C_T data generated to date. This method is known as the normalized C_T method.

The Normalized C_T Method

If the C_T data of a given aerospike geometry tested under cold-flow and hot-firing conditions (Fig. 8) is divided by the respective value of C_T at design pressure ratio, and the pressure ratio is divided by the respective design pressure ratio, it is found when the resulting values are plotted together, that the effects of geometry and specific heat ratio are normalized to a considerable degree (Fig. 8). This is especially useful in the open-wake region, for it offers a way of scaling cold-flow to hot-firing performance in the open-wake region. To obtain the performance of a hot-firing engine with cold-flow geometry (using the above technique) one proceeds as follows.

A. Calculate the thrust coefficient efficiency at design pressure ratio (C_{T_d}) per the closed-wake method explained previously.

B. Calculate the normalized pressure ratio (PR/PR_d) at which the hot-firing performance is desired.

C. At this value of (PR/PR_d) read Fig. 8 and obtain $(C_T/C_{T_d})_{N.P.}$

D. Compute C_T for the nozzle in question as

$$C_T = C_{T_d} \left[\frac{C_T}{C_{T_d}}\right]_{N.P.} \tag{5}$$

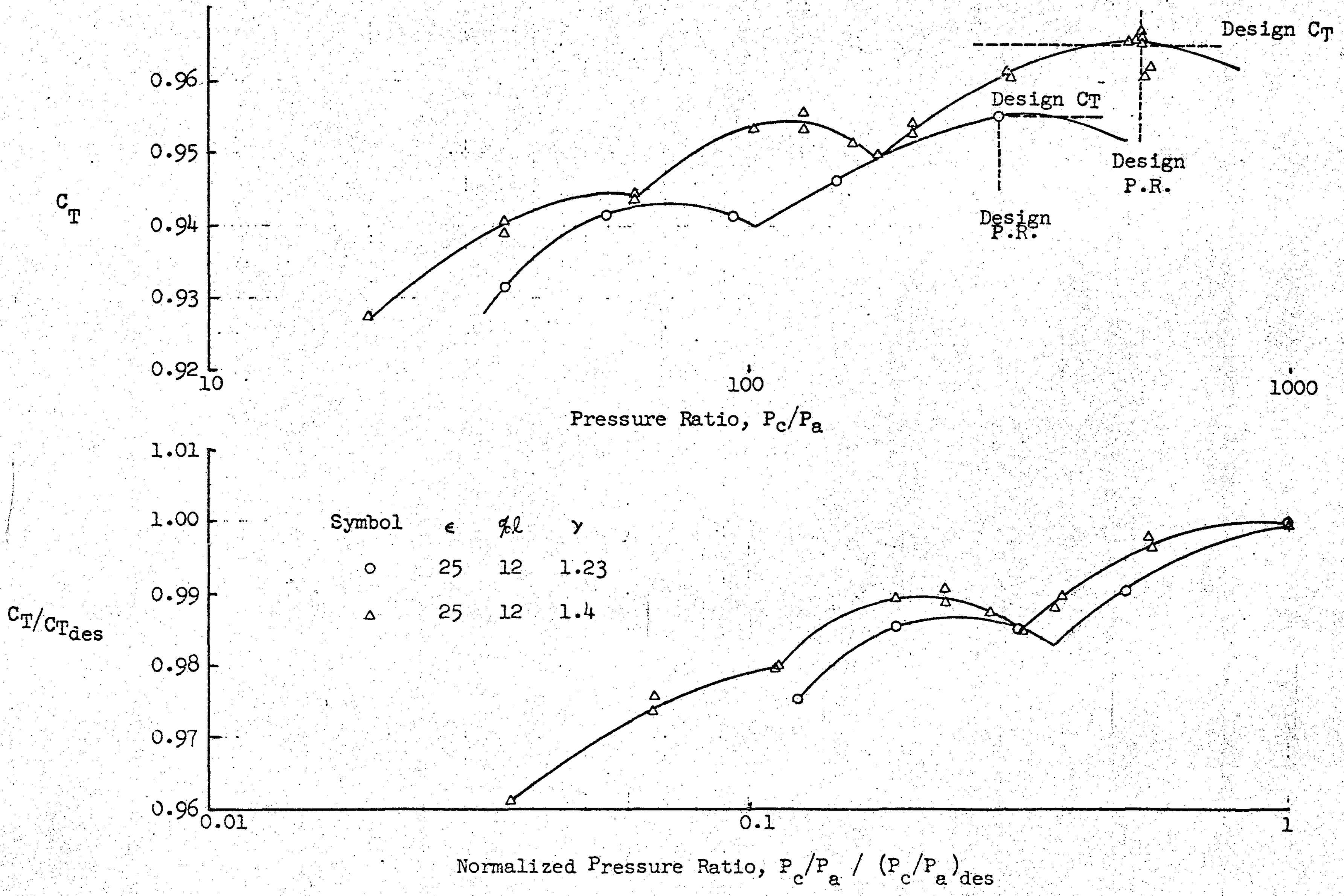

Fig. 8. Comparison of Aerospike C_T Coefficients in Normalized Form

This technique has been used and found to have less uncertainty than the method which relies on calculation of the open-wake base pressure. It also gives the proper trends with the nozzle geometry variations such as expansion area ratio and nozzle length.

There are two ways in which this method is used: 1. Where hot-firing performance is desired for a gometry which has been cold-flow tested, the normalized C_T plot is obtained from the cold-flow data for the exact geometry and used for hot-firing calculations. This approach has the least uncertainty and has been verified in previous tests. 2. Where parametric performance is desired and only a few geometries have been tested, a universal type of normalized C_T is used. This type of plot uses all the data generated to date plotted in the same manner as shown in Fig. 8. This universal plot has a higher uncertainty associated with it, but is suitable for parametric evaluations.

In the SERV program the initial baseline engine performance and the parametric engine data have been generated using the latter method for the open-wake. The baseline engine performance will be updated when the cold-flow model is tested and its "normalized C_T" is obtained.

Open-Wake Base Pressure From Normalized C_T

Once the overall nozzle performance is known for the open-wake condition the base pressure can be calculated indirectly since the primary nozzle thrust coefficient can be calculated using the method of characteristics. Equations 2 and 4 can be combined for this purpose.

RELATIVE IMPORTANCE OF SERV ENGINE BASE PRESSURE

A comparison of the base pressure effects on nozzle performance in the SERV aerospike negine and in a conventional engine is depicted in Fig. 9. Here the thrust coefficient efficiency η_{C_F} has been used. This efficiency is equal to the nozzle thrust coefficient divided by the ideal vacuum thrust coefficient. The gain in performance with small amounts of secondary flow is again greater in the SERV engine than in the conventional aerospike.

At sea level the base pressure contribution becomes more significant in the SERV engine. Its magnitude is comparable to that of the primary contribution.

IMPACT OF SLIPSTREAM

When operating in the slipstream, and during a relatively short interval of time, the vehicle provides an atmosphere unfavorable for efficient expansion of the aerospike engine gases, at the altitude of operation. As a result, the nozzle thrust coefficient (and therefore thrust and specific impulse) is less than would be expected for that altitude. To get the proper appraisal of the situation one must look at the effect as it relates to time.

On a vehicle in flight there are two types of forces in action: a retarding force (drag) caused by the slipstream and vehicle body form (or design), and an accelerating force provided by the engine. The retarding force changes with the vehicle velocity and is practically independent of the type of engine installed in the vehicle base. The accelerating force is the engine intrinsic thrust, characterized by the intrinsic thrust coefficient (Fig. 7). In the absence of adverse slipstream effects, this coefficient would decrease with time along the trajectory as shown in Fig. 10, a replot of Fig. 7 with time as abcissa. The time scale was obtained from a SERV vehicle trajectory.

Figure 9. Effect of Base Pressure on Conventional Aerospike Engine Performance

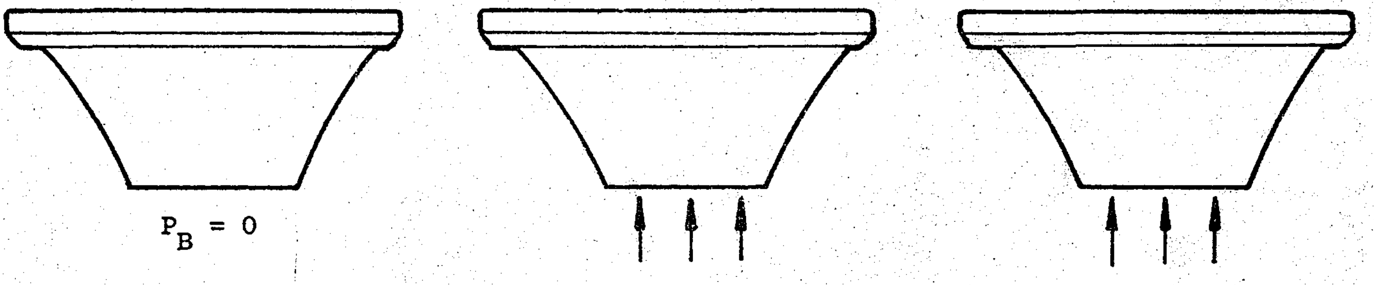

$\dot{W}_S/\dot{W}_P$	-	0.5%	2.4%
η_{C_F} (Vacuum)	0.989	0.996	0.992

Figure 12. Effect of Base Pressure on SERV Aerospike Engine Performance

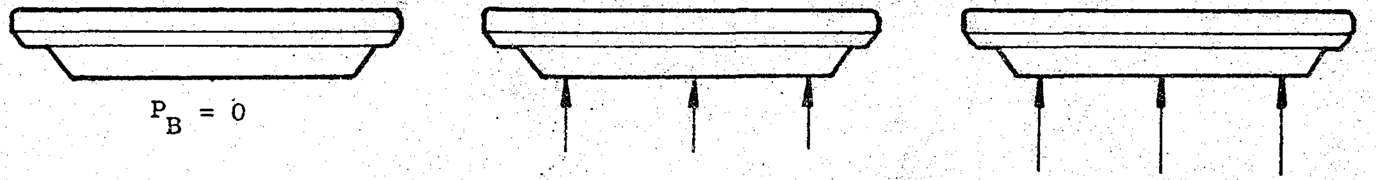

$\dot{W}_S/\dot{W}_P$	-	0.5%	2.95%
η_{C_F} (Vacuum)	0.8672	0.9529	0.9514
η_{C_F} (Sea Level)*	1.1619	2.3477	2.323

* Back pressure (P_a) equal zero

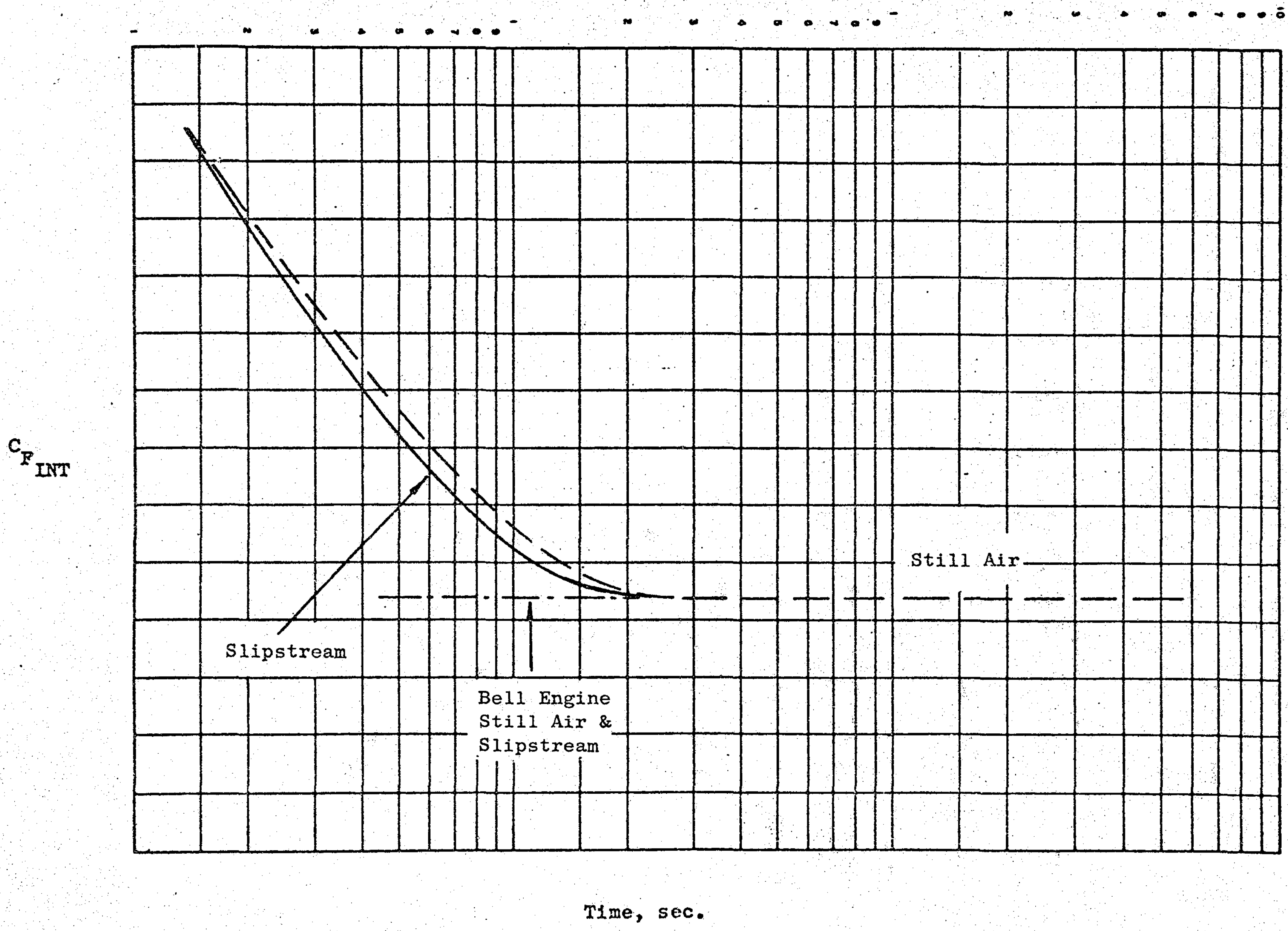

Figure 10. Estimated Effect of Slipstream on SERV Engine Thrust Coefficient as a Function of Time.

Slipstream Effect on Aerospike Thrust Coefficient, $C_{T_{INT}}$

In the presence of slipstream, the engine, installed in the wake of the vehicle, sees an effective ambient pressure. This causes the flow to effectively adjust to a higher altitude so that the intrinsic thrust produced is that which would be experienced at a higher altitude. This means that the intrinsic thrust coefficient would be displaced in time as shown in Fig. 10, an estimate of the effect of slipstream on the SERV engine.

In previous slipstream test programs (Table 2) it was observed that the effect of the pseudo-altitude is the only effect on nozzle performance. That is, expansion of the gases proceeds as if only the altitude had been change, and no extraneous recompressions occur in the nozzle or nozzle base. This was confirmed in two previously conducted slipstream programs. The original data of both programs is shown in Figs. 11a and 12a in terms of nozzle C_T coefficient and base pressure ratios plotted against the altitude pressure ratio P_c/P_∞. When the data is recomputed in terms of the vehicle base pressure ratio and plotted versus P_c/P_{BVEH}, the results indicated in Figs. 11b and 12b were obtained. This shows altitude effects alone have acted upon C_T and the base pressure, so that the vehicle base pressure P_{BVEH} is a correlating parameter for both nozzle efficiency C_T and base pressure ratio (Figs. 11b and 12b). The vehicle base pressure, P_{BVEH} could not, however, be used as a correlating parameter for the SERV engine. The base pressure of the SERV in slipstream corresponded to a still air value at an ambient pressure somewhere between P_{BVEH} and P_∞. These results are discussed in the Slipstream Model Test Results section.

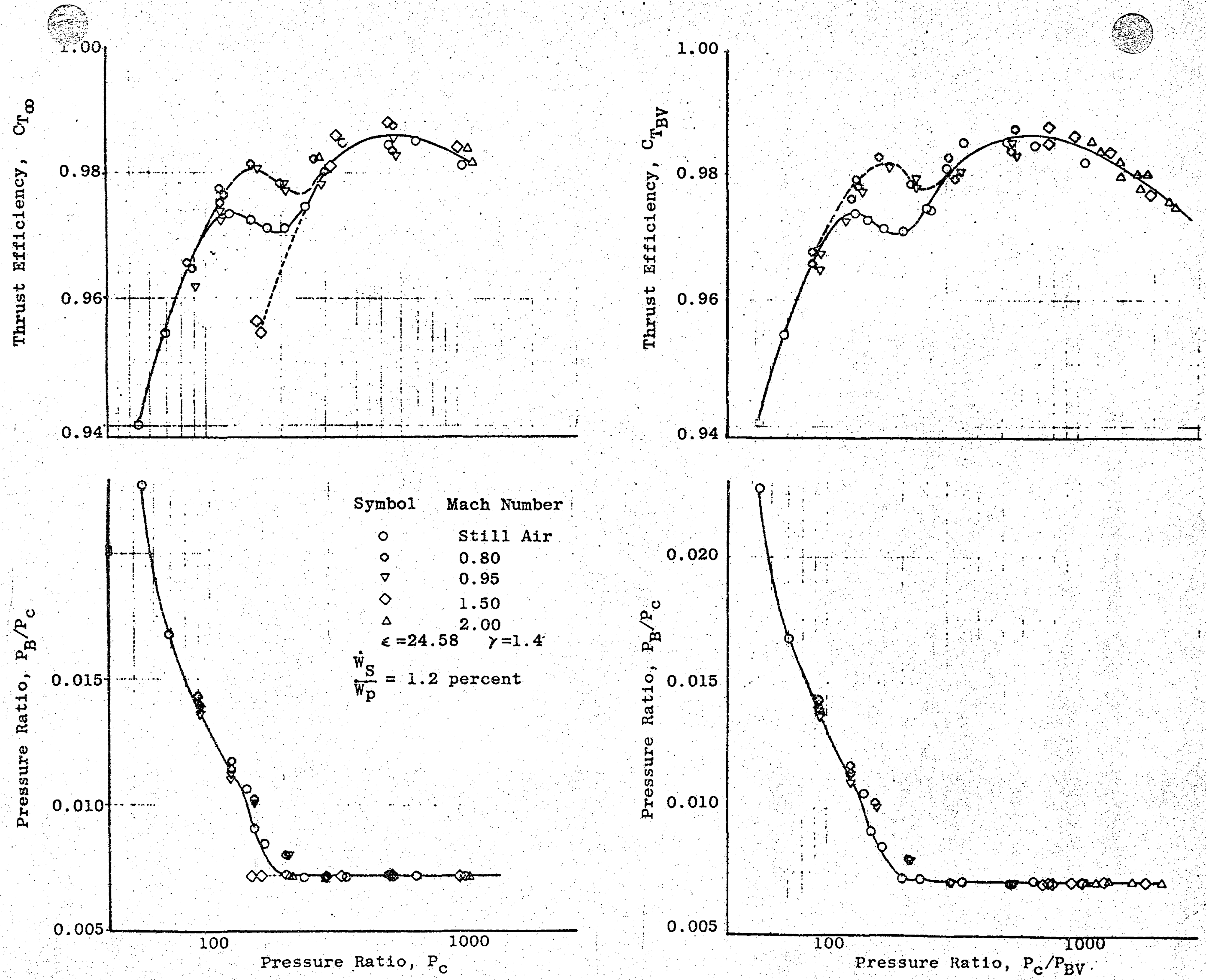

Figure 11. Aerospike Cold Flow Slipstream Test Program, Data Correlation

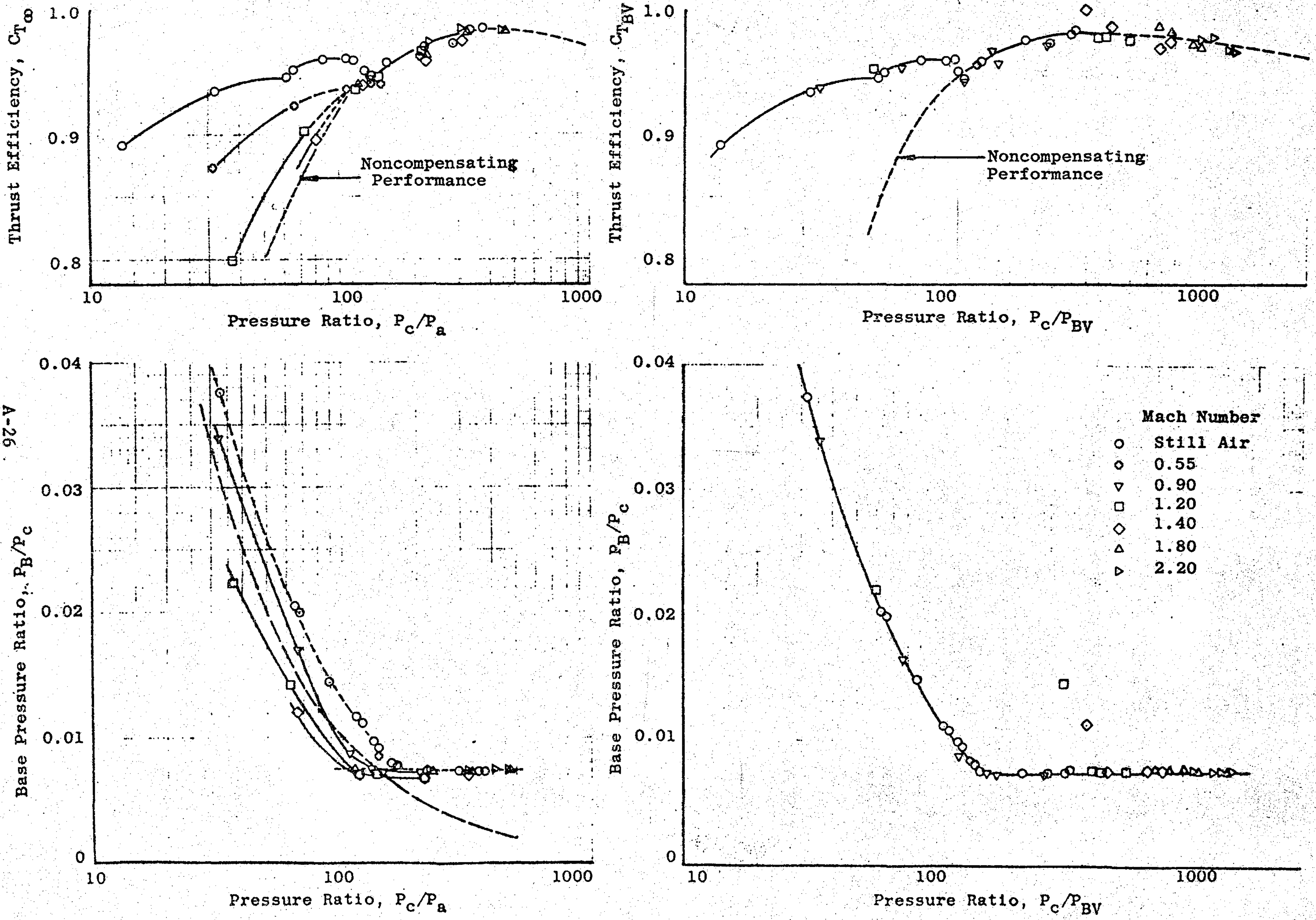

Figure 12. Aerospike Hot Firing Slipstream Test Program, Data Correlation

SERV COLD-FLOW TEST MODEL

The SERV cold-flow test model (Fig. 1) has a diameter of 27 inches at the base and a length of 20 inches. It has a double cone forebody and a semi-spherical reentry type heat shield base. The model is attached to a cylindrical forebody of approximately 126 inches in length. A strut attached to the cylindrical forebody supported the model during tests at AEDC.

The SERV vehicle model incorporates a scaled model of the SERV aerospike engine. The engine model has been designed for air operation at a chamber pressure of 400 psia. With a mass flow approaching 11 pounds per second, the model develops approximately 730 lb of thrust with a thrust coefficient of approximately 1.6. Placed at a diameter of approximately 26 inches the throat annulus has a width of approximately 0.014 inches. This latter dimension was an important factor in the selection of the model size. The more critical model geometric parameters are summarized in Table 3.

MODEL SCALING

Complete simulation of aerospike engine C_T performance and base pressures is achieved when geometry, specific heat ratio (γ), and boundary layer conditions are matched between engine and model. Matching of geometry and specific heat ratio ensures identical dimensionless primary inviscid flowfield properties (exit Mach number, design pressure ratio, and exit flow angles). Equal boundary layer conditions ensure equal dimensionless primary nozzle friction loss and base pressure ratios. When all three conditions are satisfied nozzle thrust coefficient efficiencies (C_T) of model and engine are identical (except for kinetic and gas relaxation effects).

Numerous aerospike test programs have indicated that nozzle geometry (characterized by nozzle area ratio, percent length, and nozzle contour) is the key parameter in the correlation of nozzle C_T performance. Relying on this experimental evidence, the SERV engine was scaled geometrically from

TABLE 3

SERV ENGINE MODEL GEOMETRIC PARAMETERS

	AS DESIGNED	AS BUILT	AS TESTED
Exit Diameter, in.	25.8392	25.84	
Throat Diameter, in.	1.2016	1.230	
Throat Gap, in.	0.0139	0.0147	
Throat Area, Geometric	1.136	1.237	
Throat Area, Aerodynmaic	1.02	1.20	1.266
Expansion Area Ratio	465	440	417
Base Area Ratio	368.8	348	
Nozzle Length, %	5	5	

from the SERV baseline engine. Nozzle expansion area ratio and nozzle percent length were preserved. The nozzle contours are different. This results in a different base area ratio between engine and model.

MODEL NOZZLE CONTOUR DESIGN

A truncated isentropic spike contour is the basic geometry from which the final SERV nozzle contour is obtained. In this basic geometry the expansion of the gases centers about a point on the nozzle throat resulting in external expansion of the gases. For the SERV configuration a two-dimensional double wall section replaces a section of the basic isentropic spike contour near the throat. The resulting geometry expands the gases internally in the double wall section and externally in the truncated isentropic spike section. Careful matching of the two sections is made to retain the same external flowfield as the basic truncated isentropic nozzle contour. This insures equal nozzle performance of the SERV and the truncated isentropic spike geometries.

The model nozzle contour design resulting from geometry scaling alone is presented in Fig. 13 . Since the specific heat ratio of the model test medium is 1.4 and that of the SERV engine combustion gases have an effective value of 1.16, the nozzle contours differ slightly.

SERV MODEL OVERALL DESIGN

The SERV model was designed by Chrysler with close coordination with Rocketdyne. The following discussion on the overall SERV model design and drawings are taken from a Chrysler document (Ref. 2 , revised where applicable.

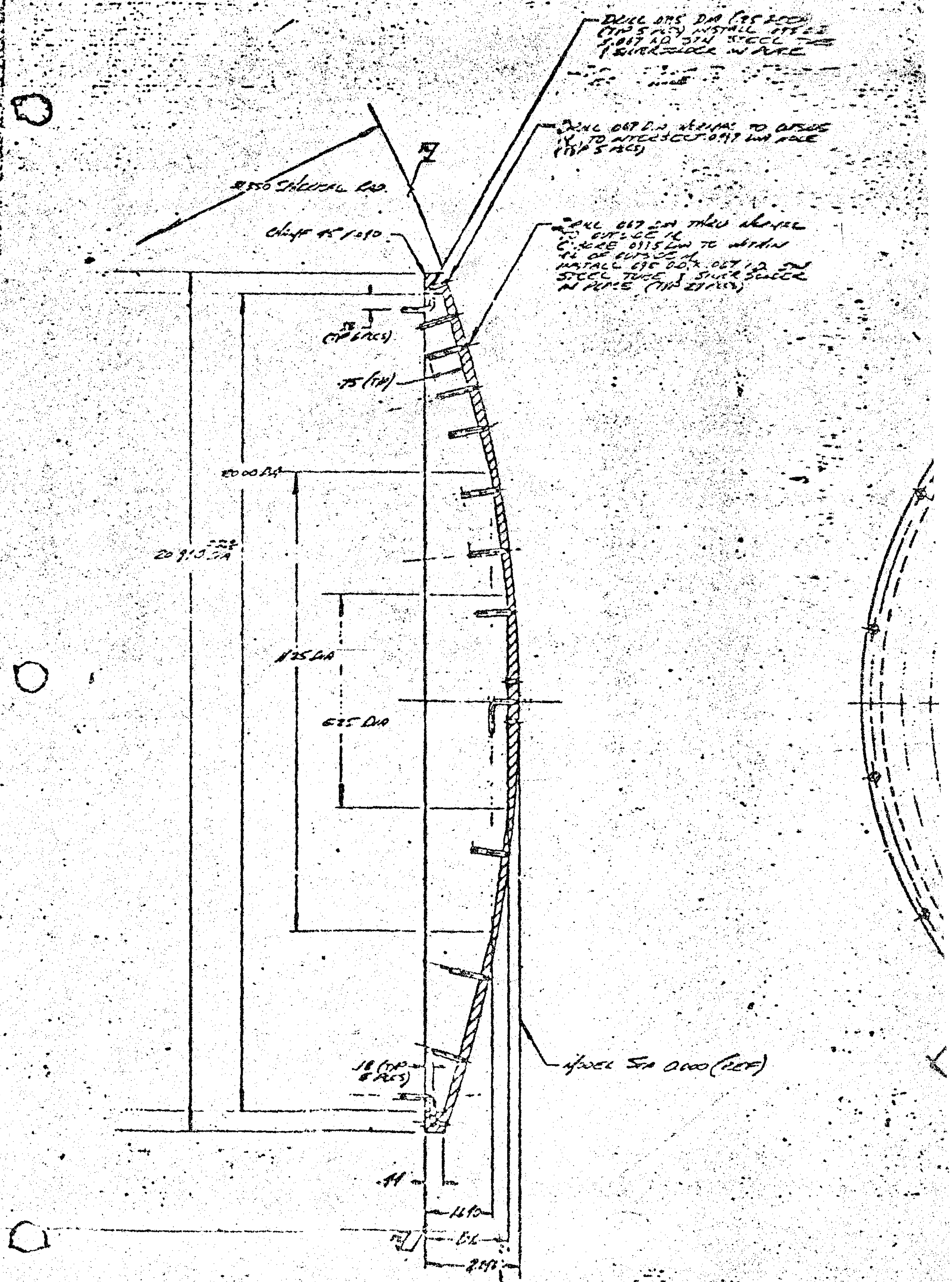
DRILL .095 DIA (.25 DEEP) (TYP 5 PLCS) INSTALL .095 O.D. X .067 I.D. 304 STEEL TUBE & SILVER SOLDER IN PLACE
DRILL .067 DIA [illegible] TO [illegible] TO INTERSECT .0937 DIA HOLE (TYP 5 PLCS)
DRILL .067 DIA THRU [illegible] TO OUTSIDE [illegible] .0135 [illegible] TO WITHIN [illegible] OF OUTSIDE [illegible] INSTALL .095 O.D. X .067 I.D. 304 STEEL TUBE & SILVER SOLDER IN PLACE (TYP 27 PLCS)
2.550 SPHERICAL RAD.
CHAMF 45° X .030
.38 (TYP 6 PLCS)
.75 (TYP)
20.00 DIA
20.915 DIA
11.25 DIA
6.25 DIA
.18 (TYP 8 PLCS)
MODEL STA 0.000 (REF)
.44
1.410
1.56
2.55

SEC. J-J

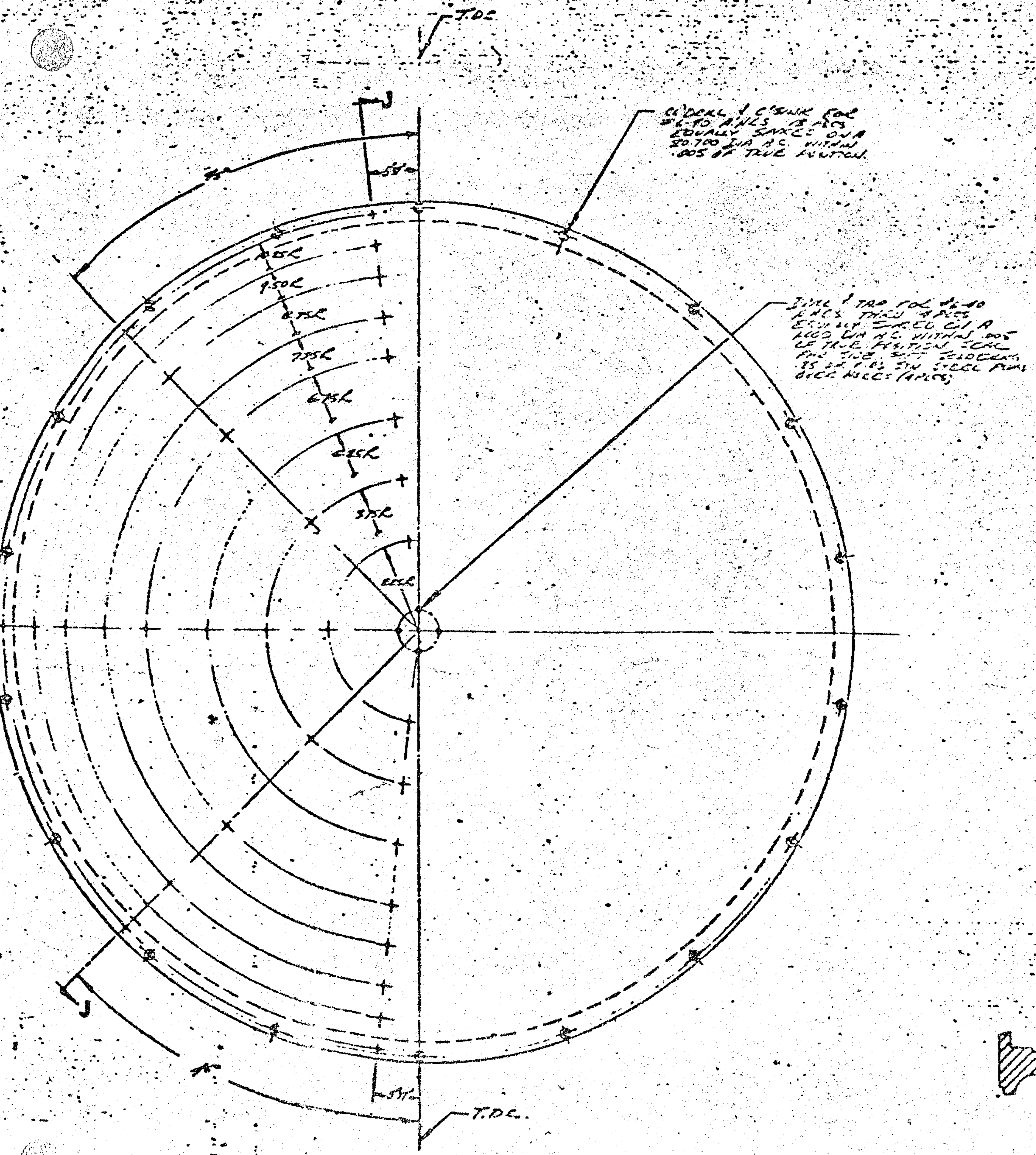

DOME & CAGE PLATE 1K20
MAT'L 321 STN STEEL

DETAIL J
(TYP ...)
(SEE ...)

TABLE I	
TAP NO.	ATTACH LOC
1	E
2	E
3	H
4	H
5	H
6	H
7	H
8	H
9	G
10	G
11	G
12	G
13	G
14	G
15	G
16	G
17	F
18	F
21	J
25	J

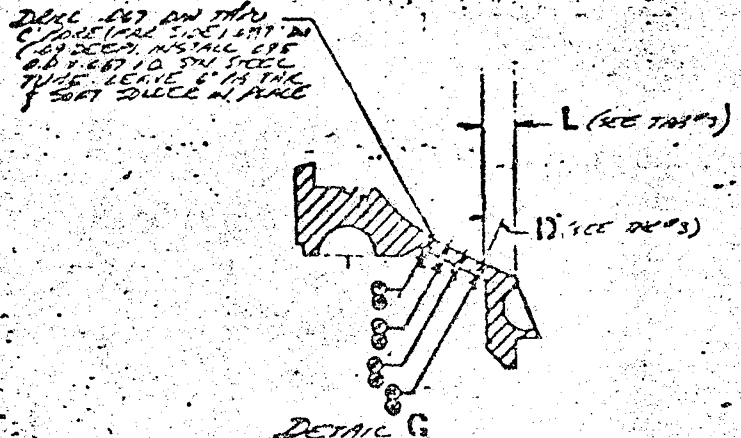

DETAIL G

NOTE: STATIC TAPS ARE SHOWN ON ONE PLANE FOR SIMPLICITY SEE TAB #'S FOR RADIAL LOCATION.

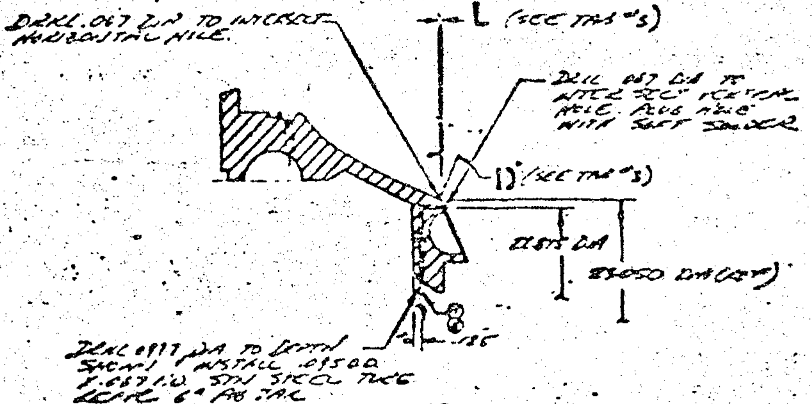

DETAIL F
(TYP 2 PLCS)
(SEE TAB #'S FOR RADIAL LOCATION)

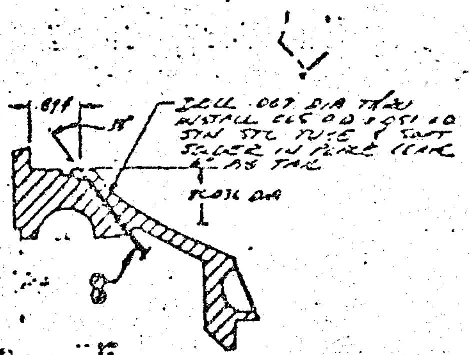

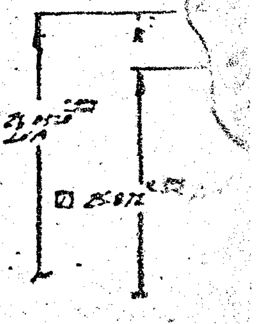

DETAIL E
(TYP 2 PLCS)
(SEE TAB #'S FOR RADIAL LOCATION)

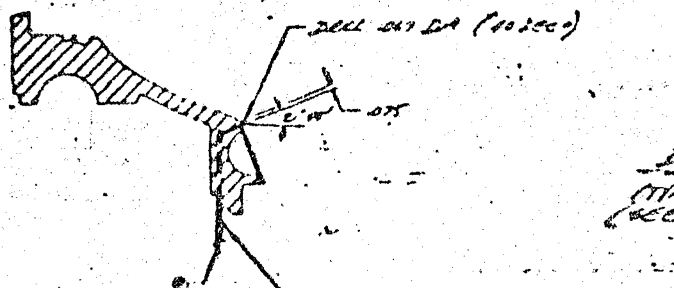

DETAIL J
(TYP 2 PLCS)
(SEE TAB #'S FOR RADIAL LOCATION)

TABLE #3

[illegible]	θ	L	D
E	90°	—	—
E	[illegible]	—	—
H	[illegible]	[illegible]	[illegible]
H	[illegible]	2.010	[illegible]
H	[illegible]	1.960	36°
H	[illegible]	1.960	36°
H	[illegible]	1.720	34°
H	[illegible]	1.720	34°
G	[illegible]	1.380	29°
G	[illegible]	1.380	29°
G	[illegible]	1.120	28°
G	[illegible]	1.120	28°
G	[illegible]	.850	26°
G	[illegible]	.850	26°
G	[illegible]	.560	24°
G	[illegible]	.560	24°
F	[illegible]	.067	22°
F	[illegible]	.067	[illegible]
J	[illegible]	—	—
J	[illegible]	—	—

TABLE #2

X	Y
[illegible]	[illegible]
[illegible]	[illegible]
[illegible]	[illegible]
[illegible]	[illegible]
[illegible]	[illegible]
[illegible]	[illegible]
[illegible]	[illegible]
[illegible]	[illegible]
[illegible]	[illegible]
[illegible]	[illegible]
[illegible]	[illegible]
[illegible]	[illegible]
[illegible]	[illegible]
[illegible]	[illegible]
[illegible]	[illegible]
[illegible]	[illegible]
[illegible]	[illegible]
[illegible]	[illegible]
[illegible]	[illegible]
[illegible]	[illegible]
[illegible]	[illegible]
[illegible]	[illegible]
[illegible]	[illegible]
[illegible]	[illegible]
[illegible]	[illegible]
[illegible]	[illegible]

CONTINUED

TABLE #2

X	Y
[illegible]	[illegible]
[illegible]	[illegible]
[illegible]	[illegible]
[illegible]	[illegible]
[illegible]	[illegible]
[illegible]	[illegible]
[illegible]	[illegible]
[illegible]	[illegible]
[illegible]	[illegible]
[illegible]	[illegible]
[illegible]	[illegible]
[illegible]	[illegible]
[illegible]	[illegible]
[illegible]	[illegible]
[illegible]	[illegible]
[illegible]	[illegible]
[illegible]	[illegible]
[illegible]	[illegible]
[illegible]	[illegible]
[illegible]	[illegible]
[illegible]	[illegible]
[illegible]	[illegible]
[illegible]	[illegible]
[illegible]	[illegible]
[illegible]	[illegible]

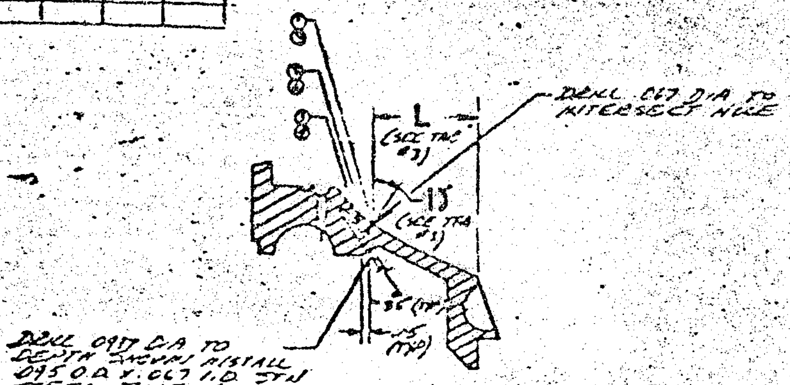

DETAIL H

NOTE: STATIC TAPS ARE SHOWN ON ONE PLANE FOR SIMPLICITY. SEE TAB #3 FOR RADIAL LOCATION

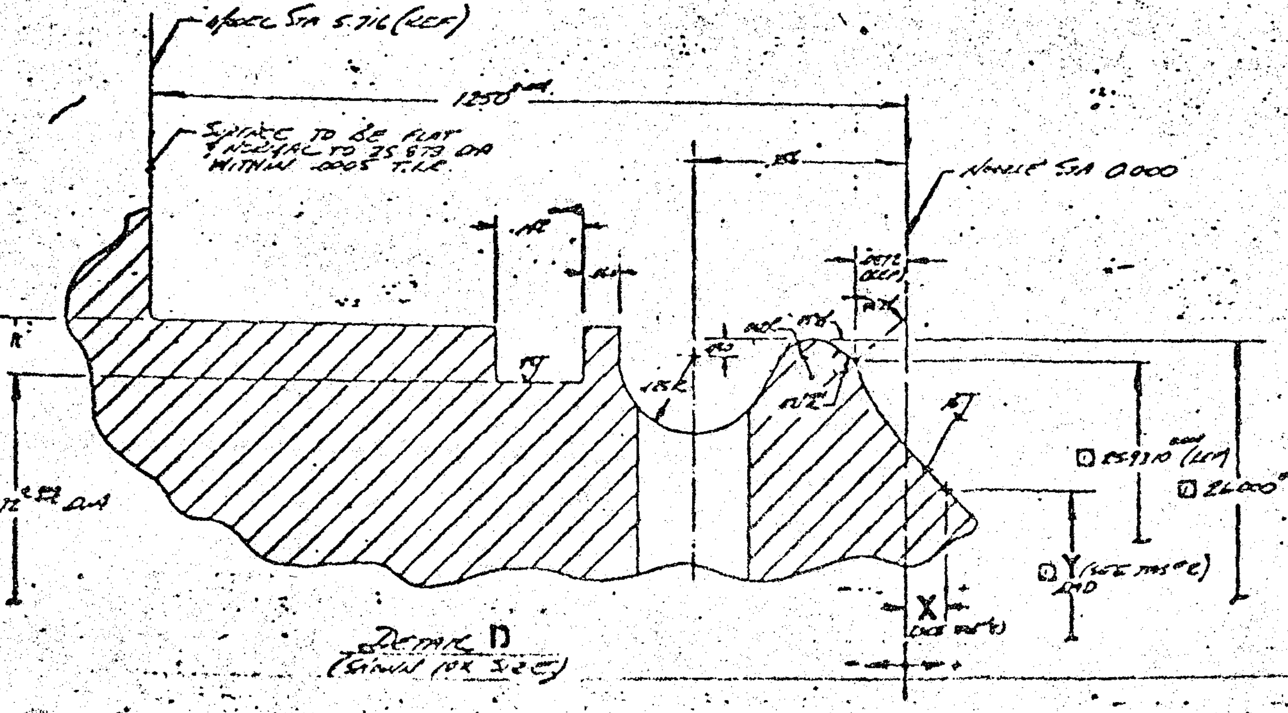

DETAIL D
(SHOWN 10X SIZE)

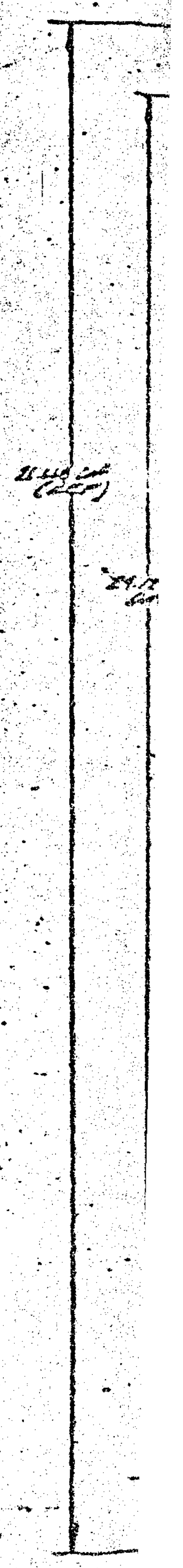

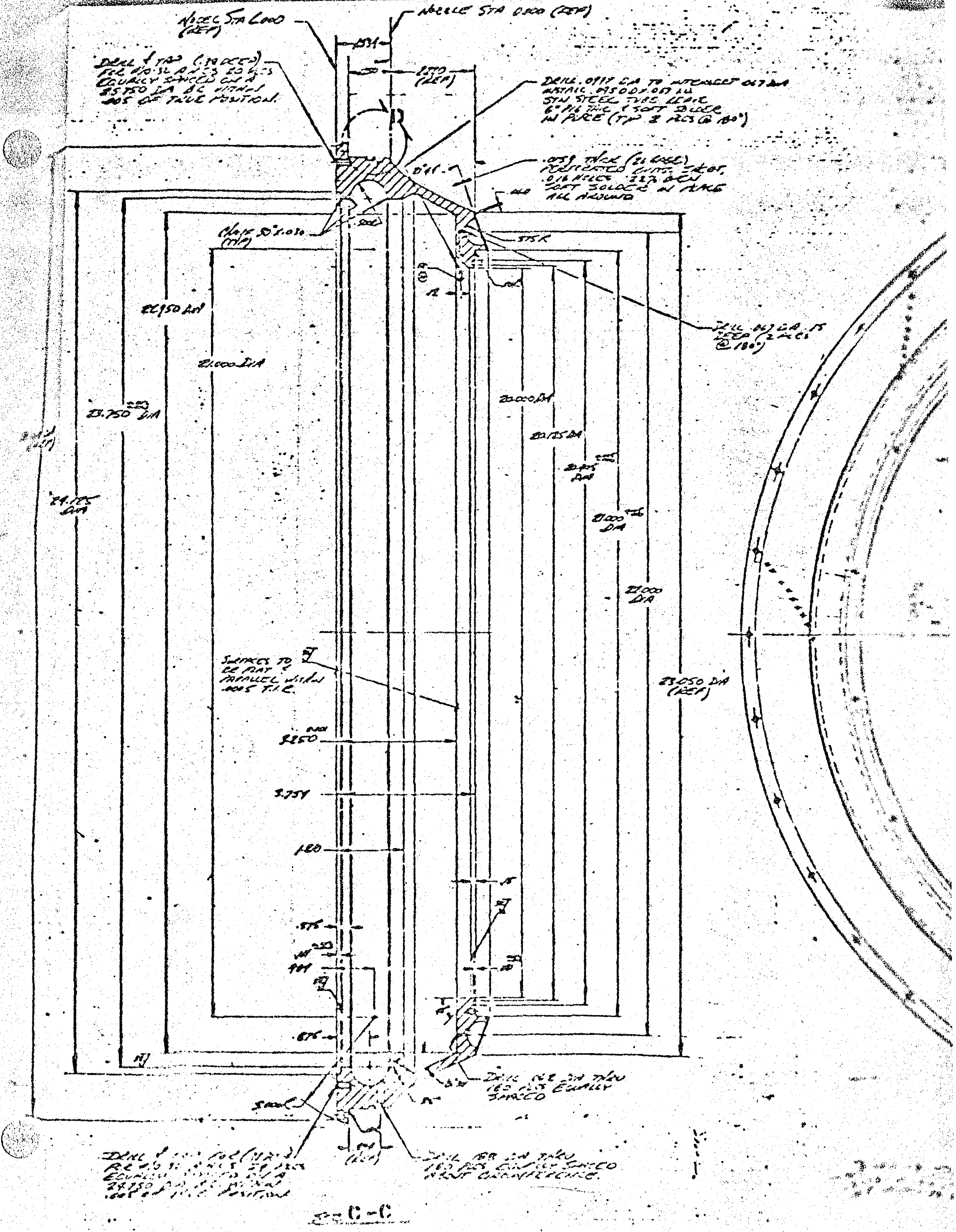
NOZZLE STA 1.000 (REF)
NOZZLE STA 0.000 (REF)
.031
.270 (REF)
DRILL & TAP (.30 DEEP) FOR NO. 32 ... 20 PCS EQUALLY SPACED ON A 25.750 DIA BC WITHIN .005 OF TRUE POSITION.
DRILL .0917 DIA TO INTERSECT .067 DIA DETAIL .095 OD X .067 ID STN STEEL TUBE LEAVE 6" PIG TAIL & SOFT SOLDER IN PLACE (TYP 2 PCS @ 180°)
.059 THICK (26 GAGE) PERFORATED WITH ... .016 HOLES ... SOFT SOLDER IN PLACE ALL AROUND
CHAM 30° X .030 (TYP)
.375 R
22.950 DIA
21.000 DIA
23.750 DIA
24.125 DIA
DRILL .043 DIA .15 DEEP (2 PCS @ 180°)
20.000 DIA
20.125 DIA
20.875 DIA
21.000 DIA
22.000 DIA
23.050 DIA (REF)
SURFACES TO BE FLAT & PARALLEL WITHIN .005 T.I.R.
3.250
3.759
.180
.375
.494
.875
DRILL .062 DIA THRU 160 PCS EQUALLY SPACED
DRILL .188 DIA THRU 160 PCS EQUALLY SPACED ABOUT CIRCUMFERENCE.
DRILL & TAP FOR ... 24 PCS EQUALLY SPACED ON A 24.750 DIA BC WITHIN .005 OF TRUE POSITION

C-C

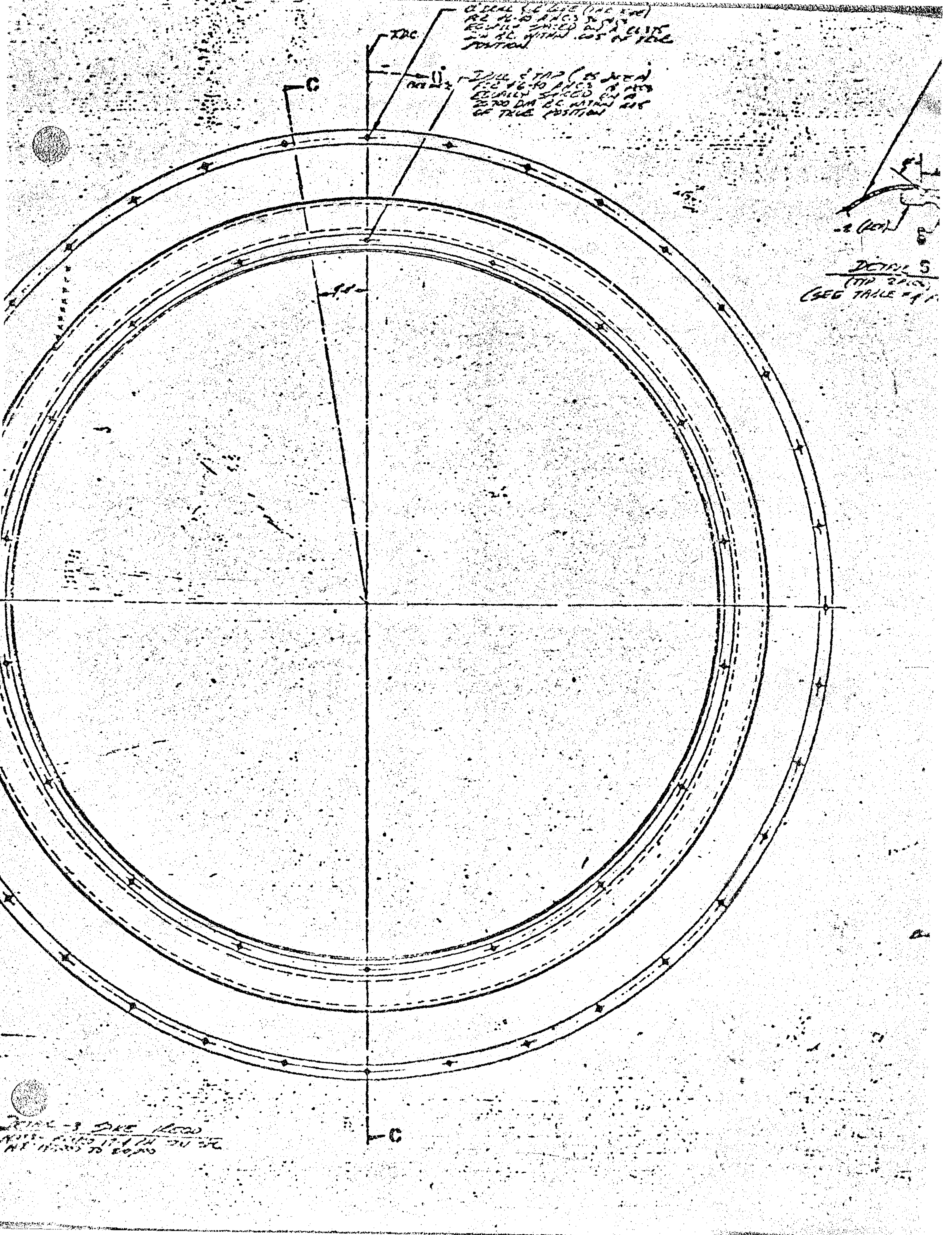
TYP.
C
C
[illegible] B.C. [illegible] HOLES [illegible] EQUALLY SPACED ON A [illegible] B.C. WITHIN .005 OF TRUE POSITION
DRILL & TAP [illegible] 46-10 HOLES [illegible] EQUALLY SPACED ON A 23.00 DIA B.C. WITHIN .015 OF TRUE POSITION
9.8°
-2 (REF)
DETAIL 5
(TYP 2 PLCS)
(SEE TABLE #1
[illegible] -3 [illegible]
[illegible]

LOCATION OF [illegible]

TABLE #1		
HOLE NO	N	[illegible]
23	[illegible]	[illegible]
24	[illegible]	[illegible]
25	[illegible]	[illegible]
26	[illegible]	[illegible]
27	[illegible]	[illegible]
28	[illegible]	[illegible]
29	[illegible]	[illegible]
30	[illegible]	[illegible]

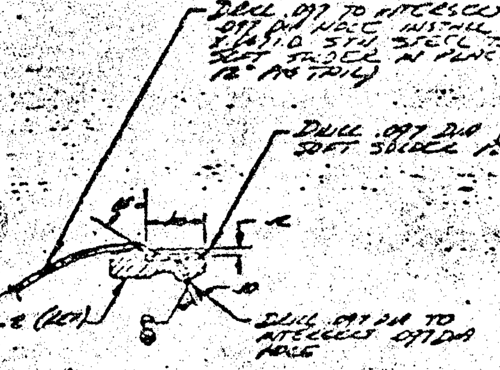
DRILL .097 TO INTERSECT WITH .097 DIA HOLE INSTALL .075 O.D. X .047 I.D. STN STEEL TUBE & SOFT SOLDER IN PLACE (LEAVE 12" AS TAIL)

DRILL .097 DIA (1.00 DEEP) SOFT SOLDER PLUG IN PLACE

DRILL .097 DIA TO INTERSECT .097 DIA HOLE

DETAIL S
(TYP 2 PLCS)
(SEE TABLE #1 FOR RADIAL LOCATION)

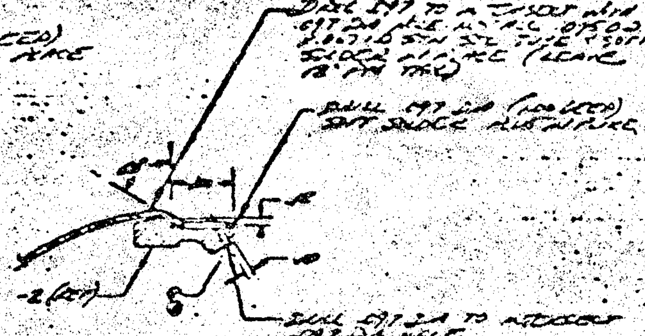
DRILL .097 TO INTERSECT WITH .097 DIA HOLE INSTALL .075 O.D. X .047 I.D. STN STL TUBE & SOFT SOLDER IN PLACE (LEAVE 12" AS TAIL)

DRILL .097 DIA (1.00 DEEP) SOFT SOLDER PLUG IN PLACE

DRILL .097 DIA TO INTERSECT .097 DIA HOLE

DETAIL R
(TYP 2 PLCS)
(SEE TABLE #1 FOR RADIAL LOCATION)

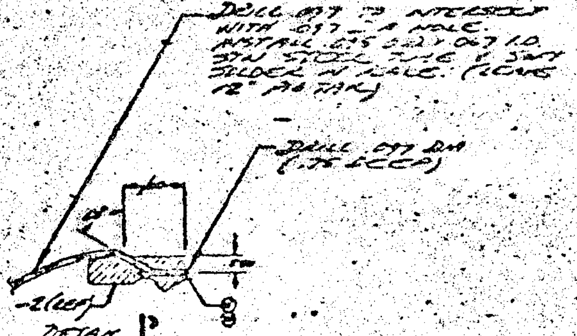
DRILL .097 TO INTERSECT WITH .097 DIA HOLE. INSTALL .075 O.D. X .047 I.D. STN STEEL TUBE & SOFT SOLDER IN PLACE. (LEAVE 12" AS TAIL)

DRILL .097 DIA (.75 DEEP)

DETAIL P
(TYP 2 PLCS)
(SEE TABLE #1 FOR RADIAL LOCATION)

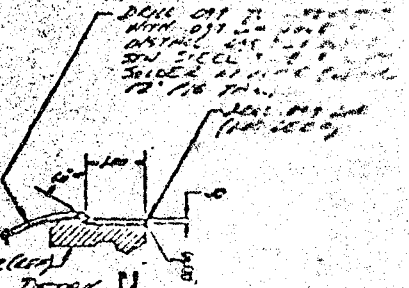
DRILL .097 TO INTERSECT WITH .097 [illegible] INSTALL [illegible] STN STEEL [illegible] SOLDER [illegible] 12" AS TAIL

DRILL .097 DIA (1.00 DEEP)

DETAIL N
(TYP 2 PLCS)
(SEE TABLE #1 FOR RADIAL LOCATION)

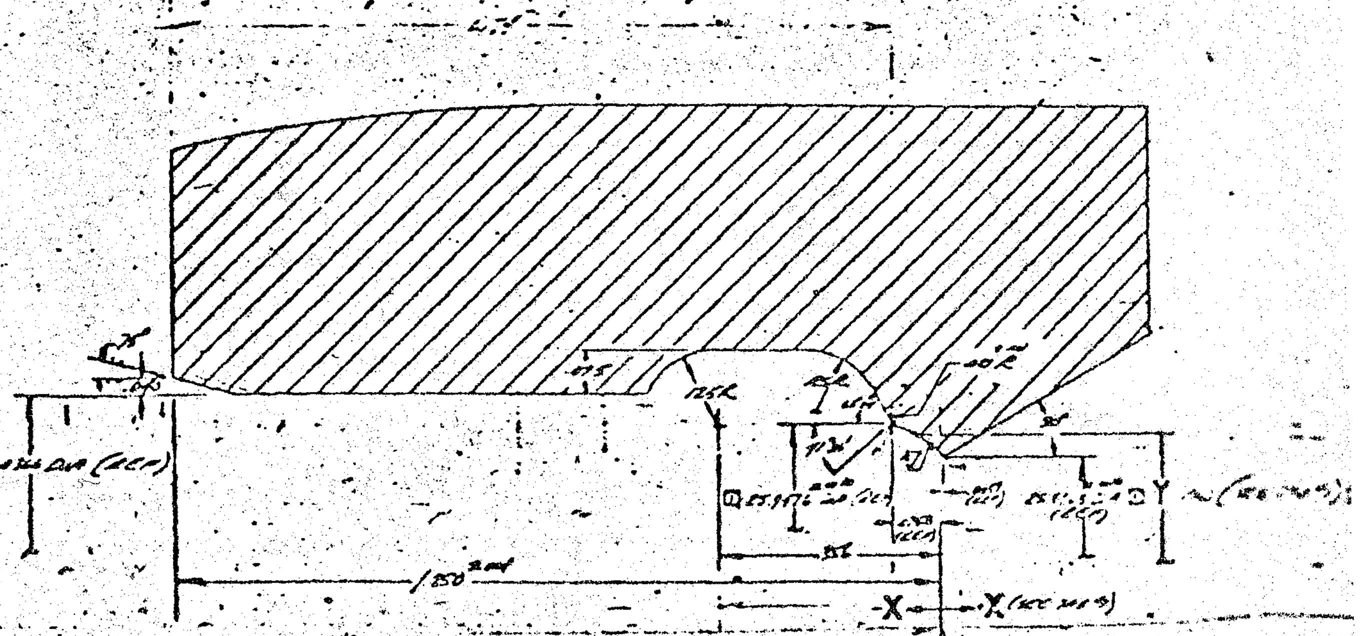

DETAIL A
(SHOWN 1/4 SIZE)

TABLE #1	
X	Y
-.4768	12.9778
-.4767	12.9777
-.4766	12.9776
-.4765	12.9775
-.4764	12.9774
-.4763	12.9773
-.4762	12.9772
-.4761	12.9771
-.4760	12.9770
-.4758	[illegible]
-.4756	[illegible]
-.4741	[illegible]
-.4737	[illegible]
-.4730	[illegible]
-.4725	[illegible]
-.4696	[illegible]
-.4686	[illegible]
-.4675	[illegible]
-.4661	[illegible]
-.4649	[illegible]
-.4628	[illegible]
-.4587	[illegible]
-.4565	[illegible]
-.4499	[illegible]
[illegible]	[illegible]
[illegible]	[illegible]
-.4312	[illegible]
[illegible]	[illegible]
-.4122	[illegible]
-.4051	[illegible]

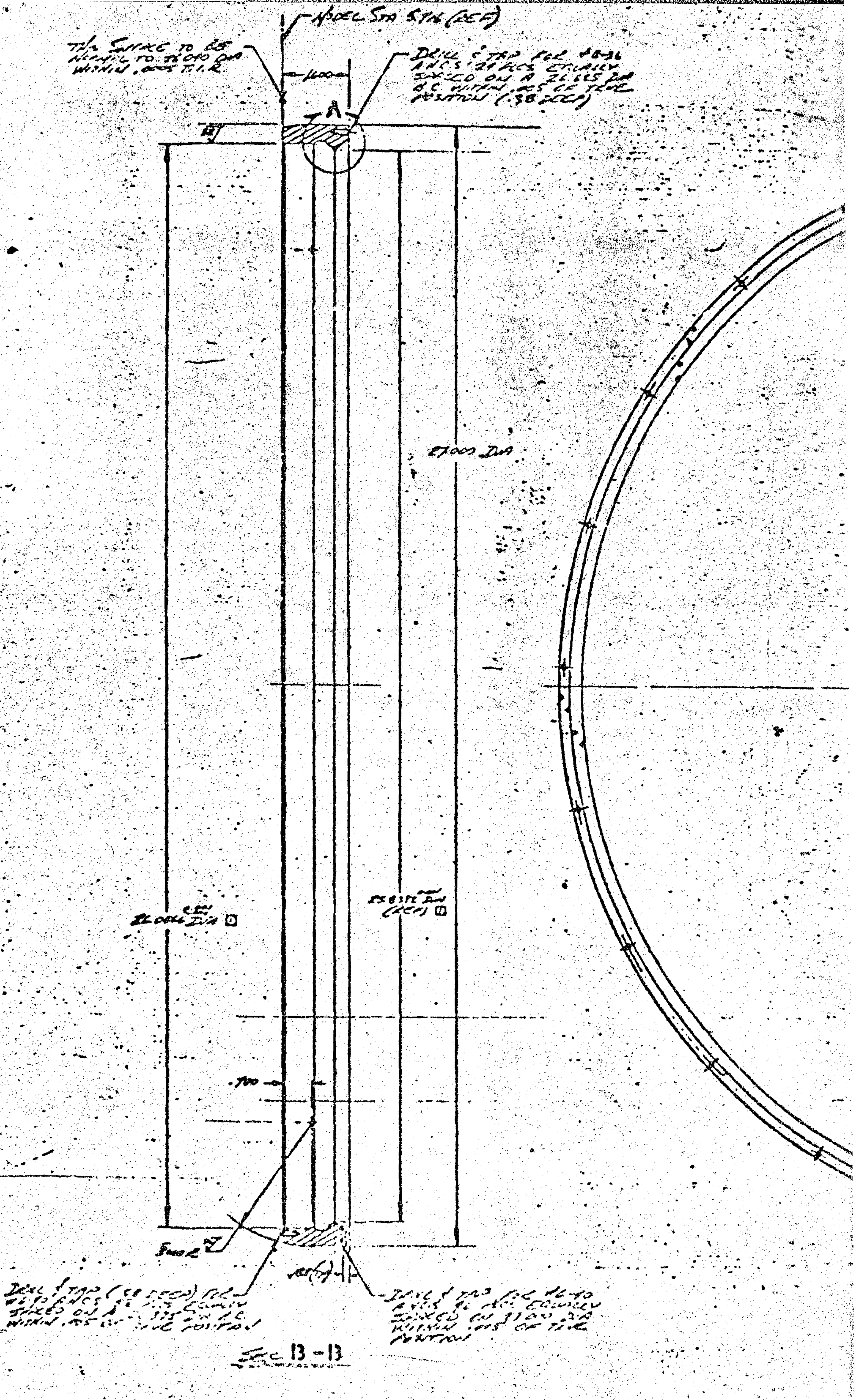

SEC B-B

(location)

(REF) □

(REF)

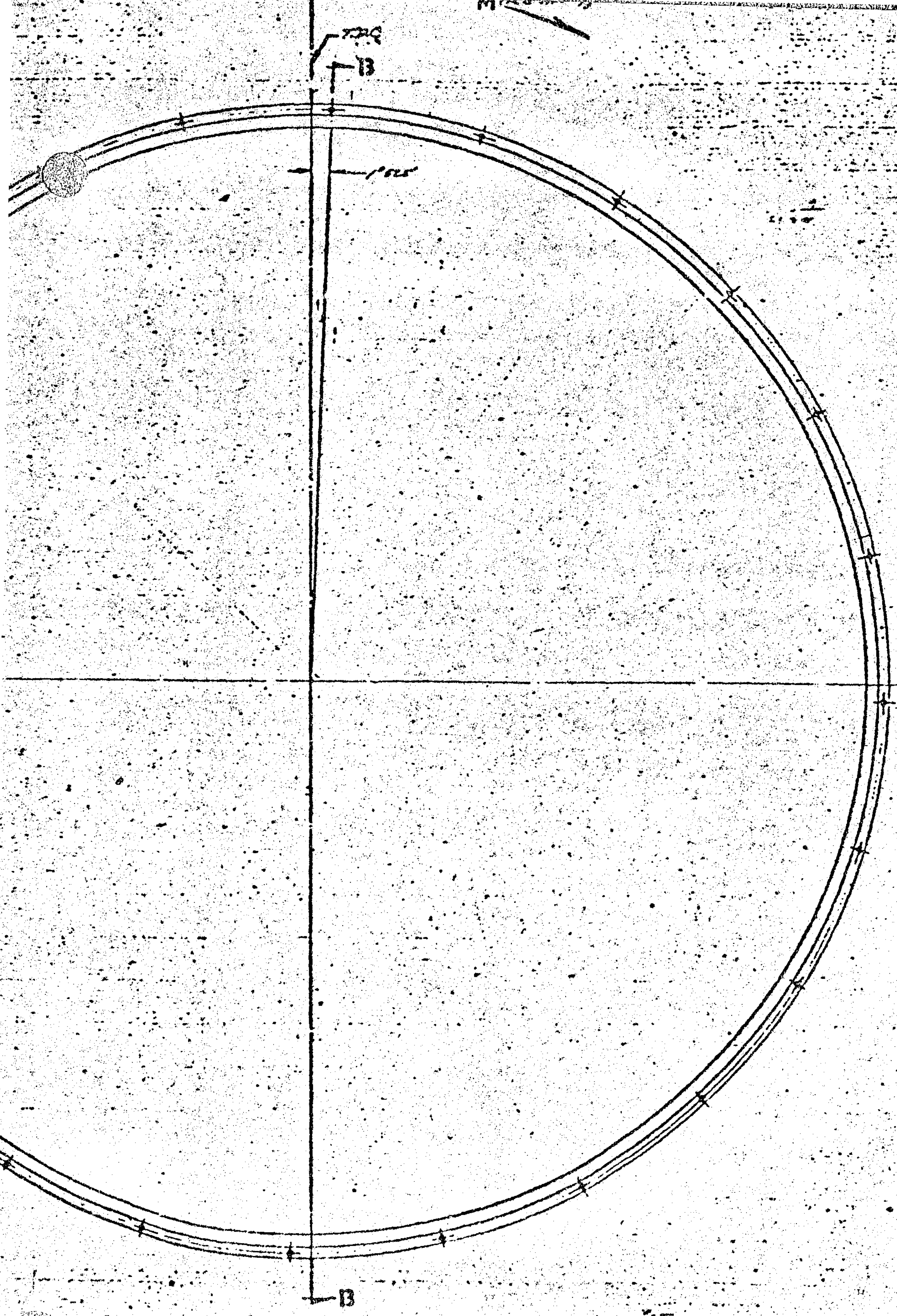

DETAIL - [illegible]

[illegible]

NOTES: [illegible]

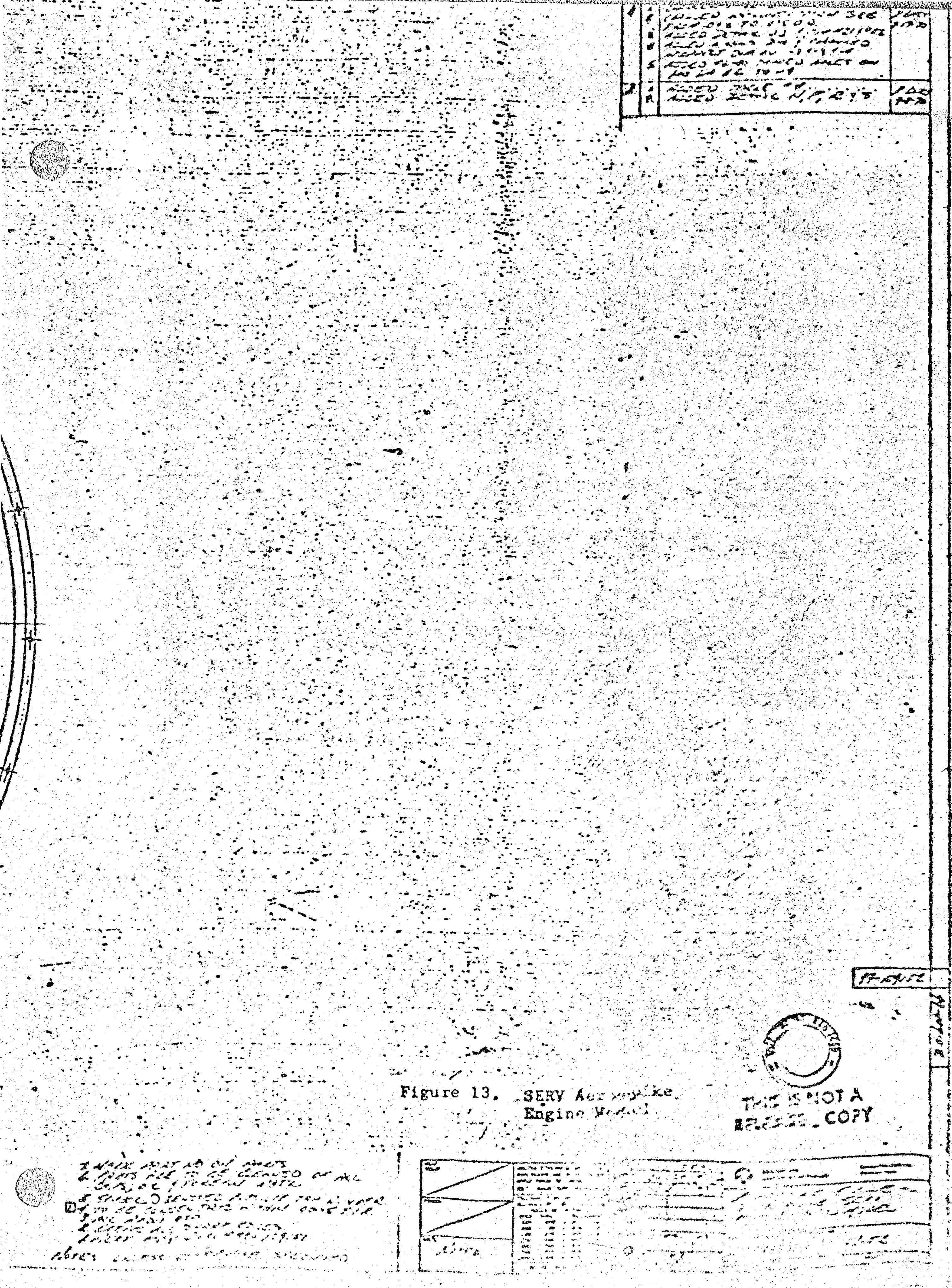

Figure 13. SERV Aerospike Engine Model

The test model is a 2.5 percent scale, stainless steel replica of the aft portion of the SERV Launch Vehicle. It has a diameter of 27 inches at the base and is approximately 20 inches in length. The model has a double cone forebody consisting of 45 deg and 25 deg half angle conical frustrums and a semi-spherical reentry type heat shield base. The model will be mounted on a strut supported cylincrical forebody that is 6.68 inches in diameter and 126 inches in length. A drawing of the model geometry is shown in Fig. 13.

The model has a scaled 5 percent length aerospike engine incorporated in the base and is designed to determine axial force, engine performance and body static pressure distribution during cold-flow jet simulation testing. The model engine combustion chamber, nozzle, and nozzle contour have been designed for air operation, at a chamber pressure of 400 psia and at mass flows of 11 pounds per second. Internal ducting is provided in the model to bleed off approximately 2.1 percent of the engine mass flow from the air manifold to the turbine exhaust annulus located in the base just inboard of the aerospike ramp.

The air manifold which feeds the aerospike engine is the main model support structure. This manifold consists of a center barrel, three rows of radial tubes, a ring flange, and a set of flexures at the forward end. The center barrel mates with the model sting at a socket joint and is secured with a Marman clamp. Two rows of 10 thin-walled radial tubes are brazed to the center barrel and to the outer ring flange. These tubes duct air from the center barrel to the engine and provide radial support for the model. A third row of 10 radial tubes are brazed to the center barrel and to the aft section of the ring flange to duct air to the turbine exhaust annulus. An orifice place is provided in the center barrel to meter the turbine exhaust mass flow.

An axial ring flexure is secured to the foreward end of the center barrel and provides radial support and roll restraint for the model. Model axial restraint is provided by a 1000-pound load cell mounted between universal flexures and secured between the center barrel and the model thrust structure.

The aerospike ramp, including the inboard combustion chamber, inboard nozzle surface, and turbine exhaust manifold is secured to the ring flange with socket heat cap screws. The outboard combustion chamber and exit nozzle surface mates with the ramp section in a slip joint and is secured with socket heat cap screws which will allow exact spacing of the nozzle throat gap. O-ring seals are provided at all joints.

The model base plate is attached to the aerospike ramp at a flange type joint. The base plate provides access to the model for final assembly and connection of model instrumentation. The plate also has provisions for an alternate turbine exhaust dump location.

One set of engine reentry protection doors is provided with the model. These doors are fabricated as split rings for ease of handling and installation on the model. The doors are attached to the outboard nozzle ring with socket head cap screws.

The first forebody section consists of the 25 deg frustrum, and is attached to the air manifold ring flange at the aft end and to the ring flexure at the foreward end at flange joints. This section also includes the model thrust structure and transmits model axial forces to the load cell.

The second model forebody section consists of the 45 deg frustrum and is attached to the first forebody section at a flange joint. This section provides access for connection of model instrumentation.

The cylindrical section supporting the model has a thick wall center tube which supports the model and ducts the high pressure air to the engine manifold. Spacer bars are welded to the outside of the center tube and support a removable sheet metal cylindrical fairing which provides access channels for routing instrumentation from the model and simulates the outside diameter of one of the SERV payload configurations. The forward end of the cylinder is closed with a 15 deg half angle cone.

A modified double wedge strut extends from the support tube to the tunnel floor (Fig. 14) for slipstream testing. This strut has a chord of 30 inches, a thickness of 2.75 inches. The center portion of the strut provides the structural support and houses four inlet air tubes. The leading and trailing edges of the strut are removable for routing instrumentations. Spacers will be provided for placement between the strut and the tunnel floor so that ± 10 deg angle of attack may be achieved.

An installation drawing of the model for still-air testing at the Rocketdyne RNTF is shown in Fig. 15.

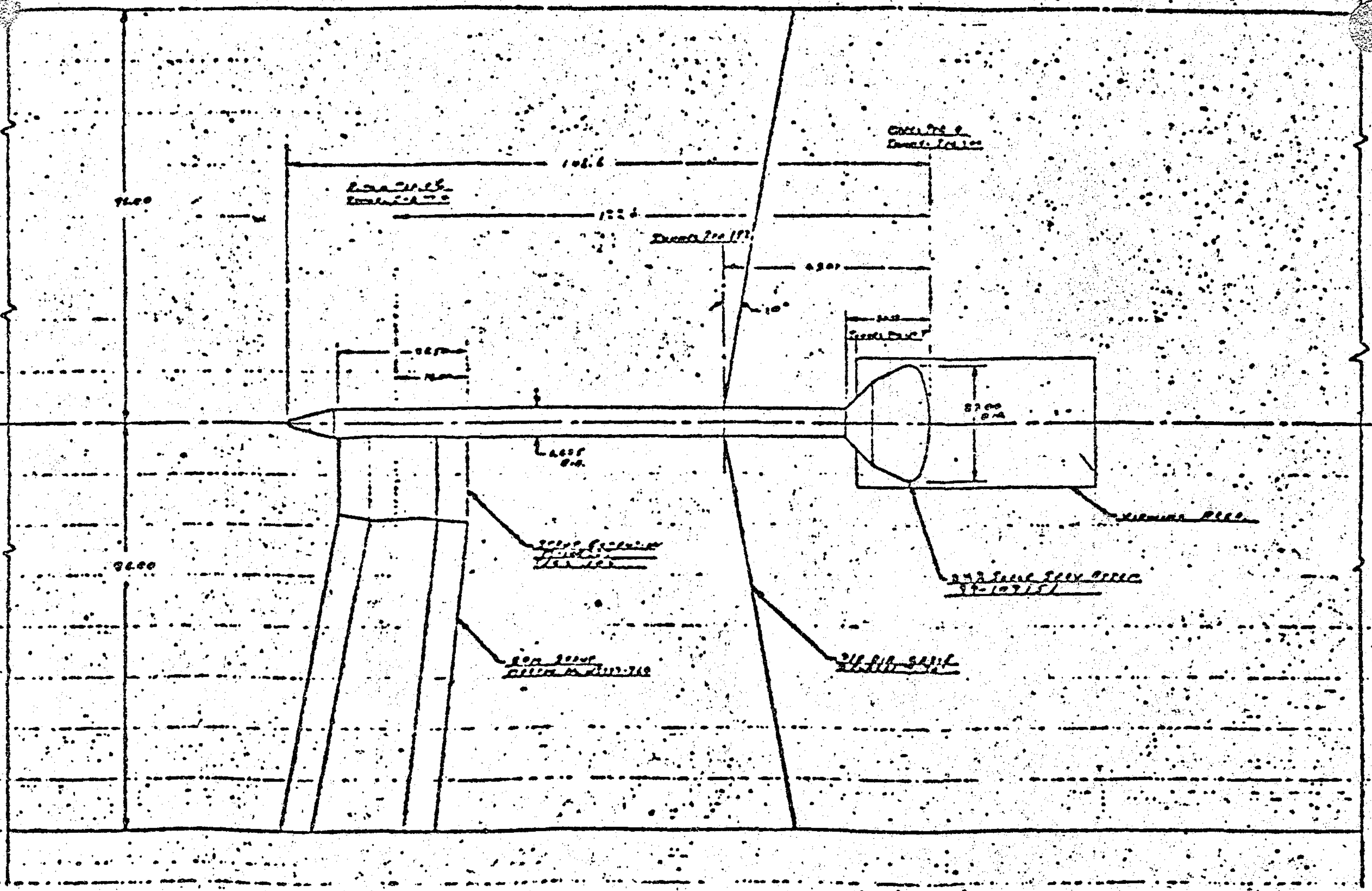

Figure 14. SERV Aerospike Engine Model, AEDC Installation

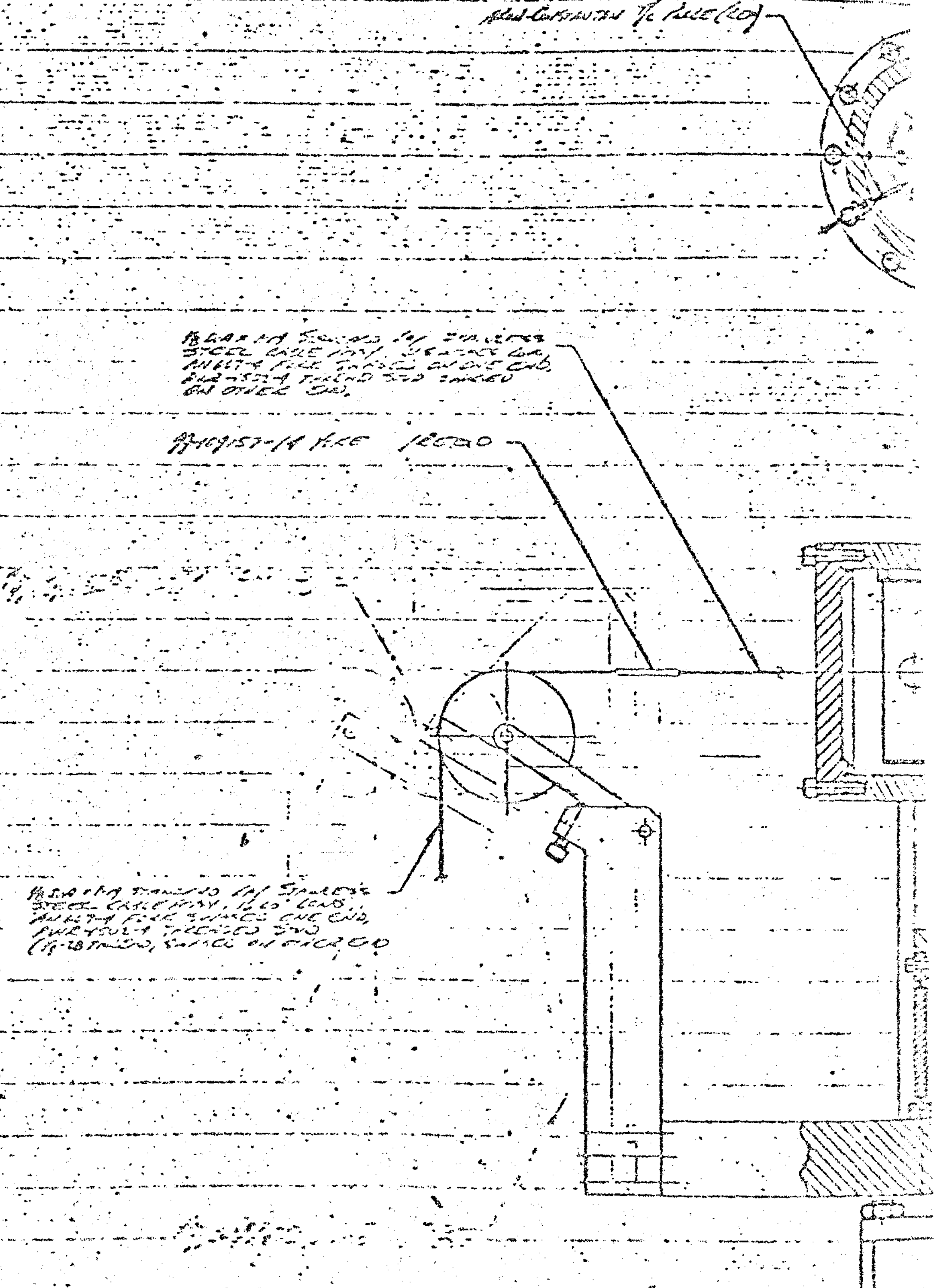
Add Countersunk ½ Hole (10)
Bearing Stand (1) Stainless Steel Cable Assy, having fine thread on one end, thread and swaged on other end.
Adjustable Pulley (1)
Bearing Stand (1) Stainless Steel Cable Assy, 1/8 60° lead, having fine thread one end, threaded stud (¼-28 thread), swaged on other end

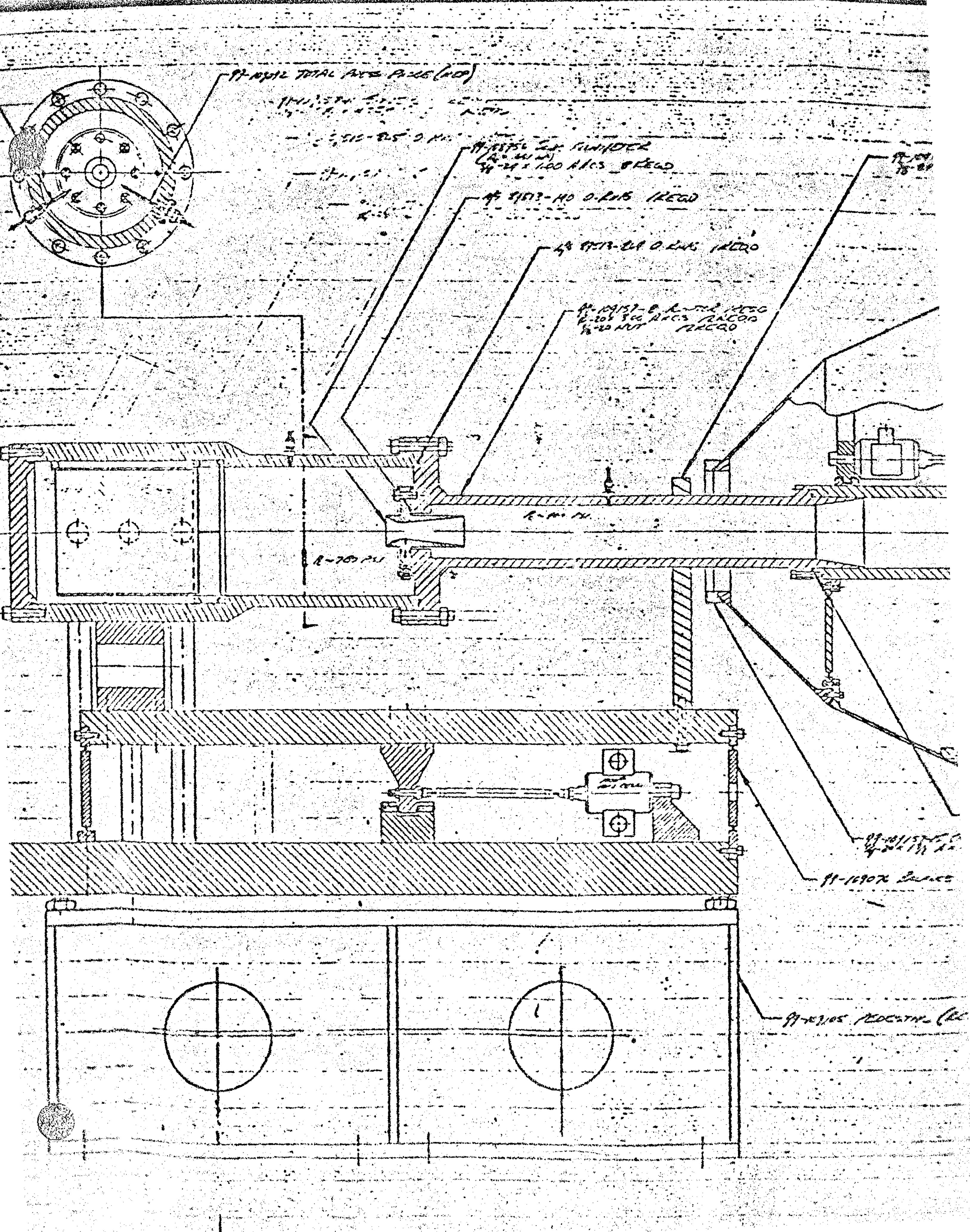
97-10912 TOTAL AXIS PLATE (NOP)
.512-.825 D. ...
97-18756 ... ADAPTER
(R-... ...)
3/4-24 x 1.00 ... 8 REQD
#8 91513-140 O-RING 1 REQD
#8 91513-248 O-RING 1 REQD
97-10157-8 ... 1 REQD
8-20 3/4 ... 1 REQD
5/8-20 NUT 1 REQD
R-700 PSI
97-10115
97-16907 BRACE
97-12105 MOUNTING (RE

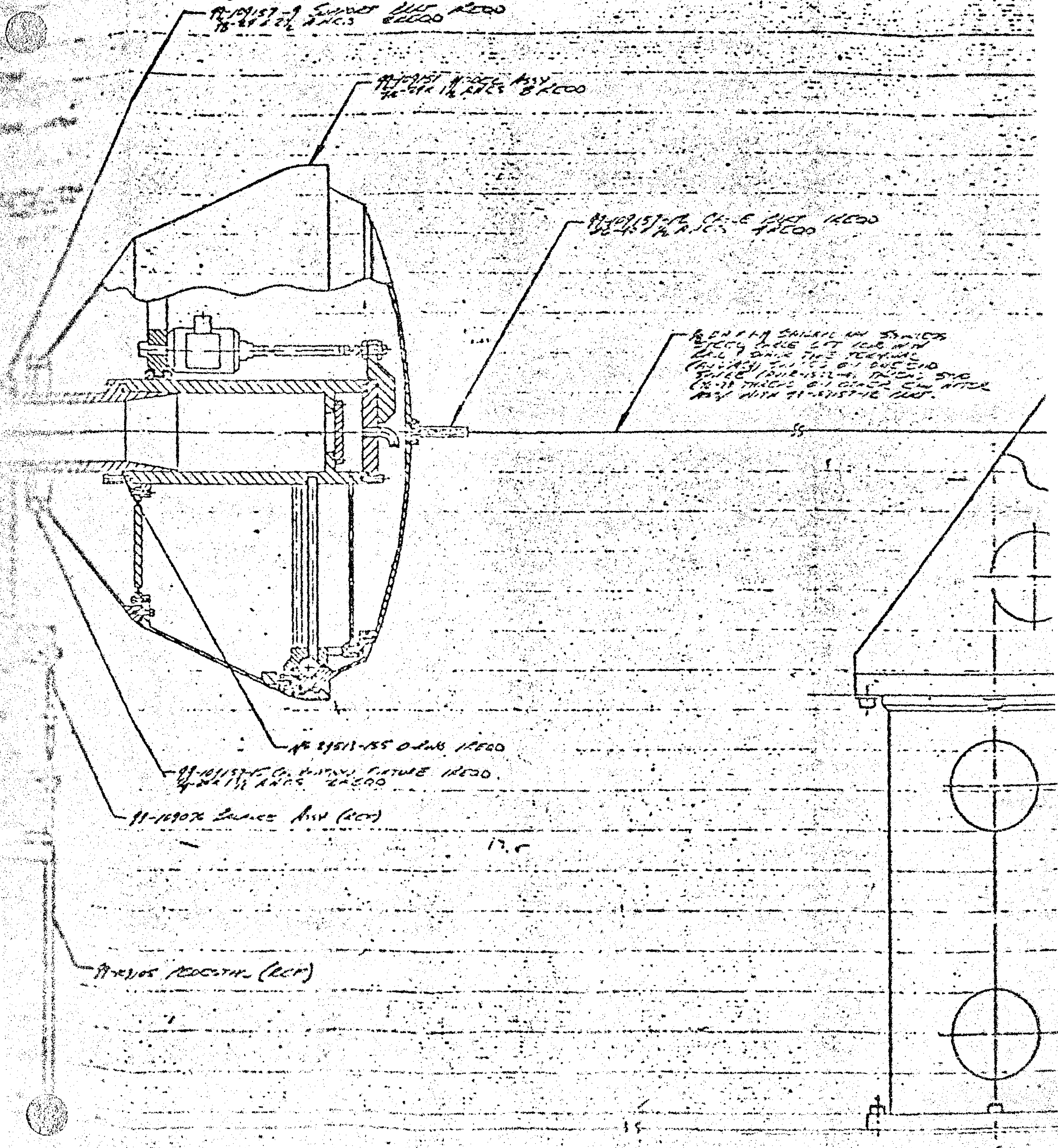
11-10157-9 SUPPORT ... REQD
11-10157 ... ASSY ... REQD
11-10157-12 ... REQD
MS 29513-155 O-RING 1 REQD
11-10157-... FIXTURE 1 REQD
11-16907 ... ASSY (REF)
11-...05 PEDESTAL (REF)
SS
17.6

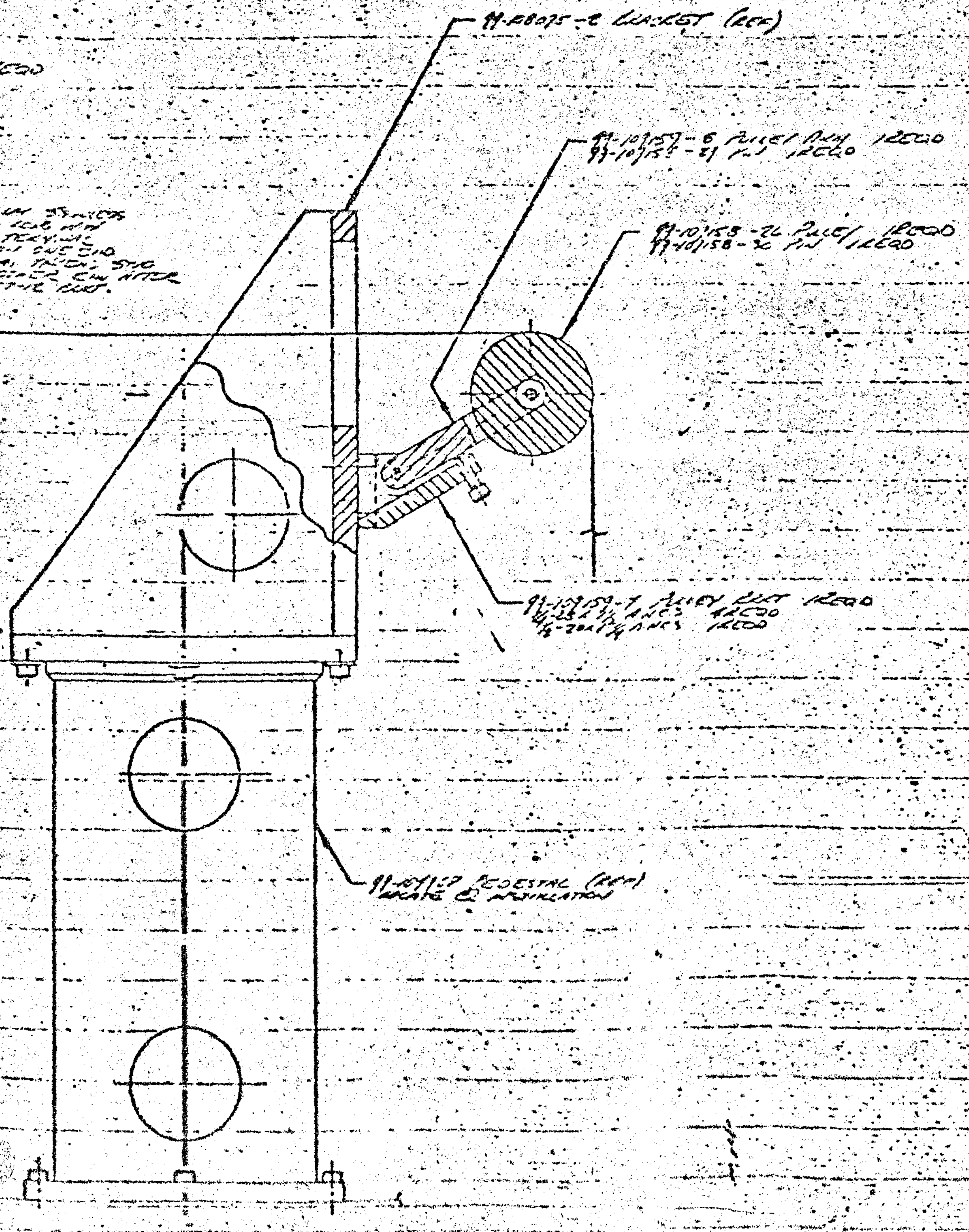
11-R8075-2 BRACKET (REF)
11-10157-6 PULLEY ARM 1REQD
93-10158-21 PIN 1REQD
11-10158-26 PULLEY 1REQD
11-40158-30 PIN 1REQD
93-10159-7 PULLEY BKT 1REQD
1/4-28 x 1/2 ANCS 4REQD
1/2-20 x 1 1/4 ANCS 1REQD
11-10150 PEDESTAL (REF)
LOCATE @ INSTALLATION
REQD
REQD
SS

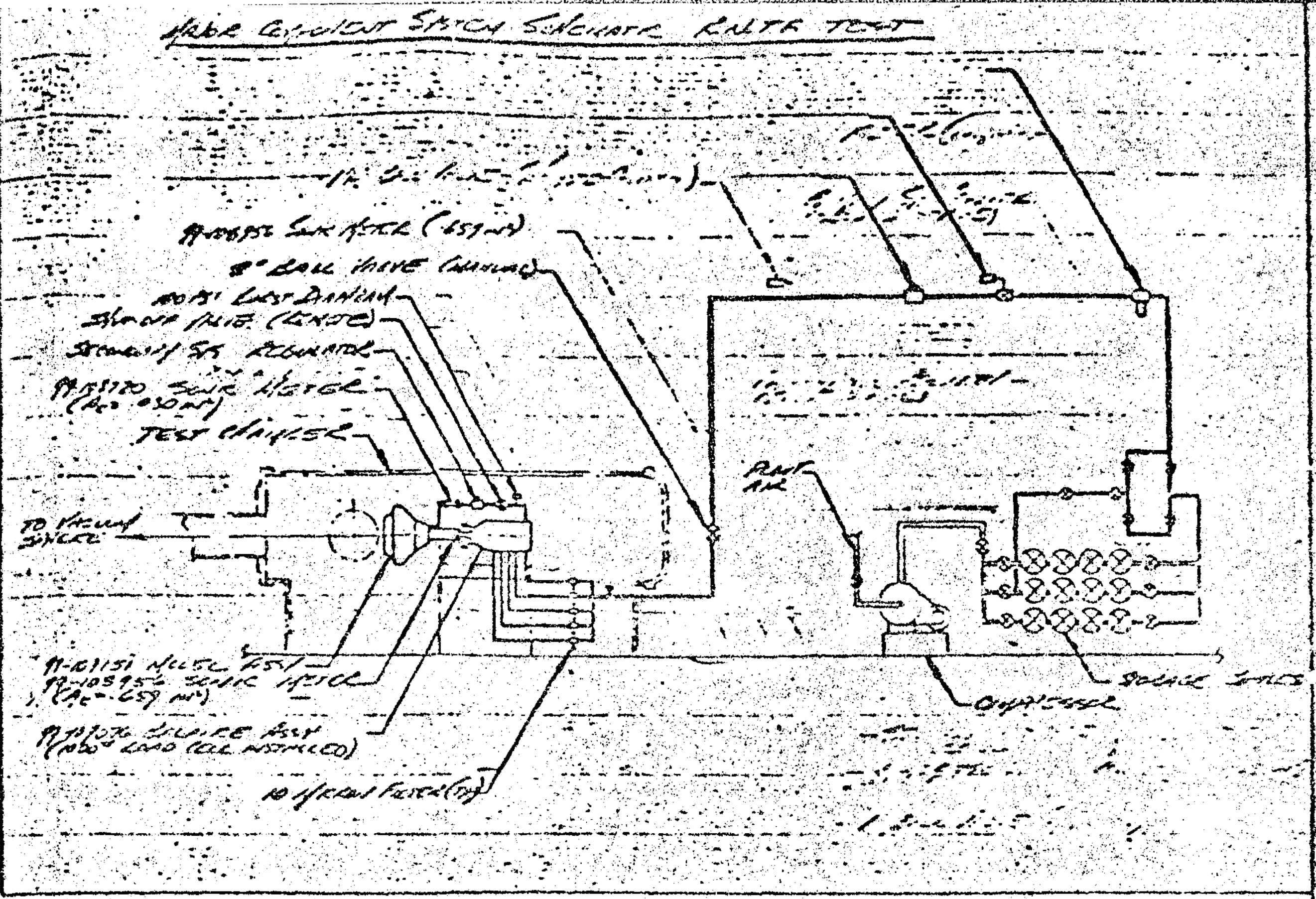

Figure 15. SERV Aerospike Engine Model, RNTF Installation

THIS IS NOT A RELEASE COPY

41

PRECEDING PAGE BLANK NOT FILMED

ENGINE PERFORMANCE REVIEW

BASELINE ENGINE PERFORMANCE

A complete description of the SERV baseline engine design, engine balance, and component efficiency parameters is shown in Table 4. The data in the table traces the development of the initial baseline engine to its present geometry. In this table values are furnished for the various process efficiencies whose combined effect determine the engine specific impulse. System geometry and flowrates as well as temperature and pressure schedules are presented in the table. The performance shown is the nominal engine performance based on the nominal efficiencies shown in the table.

ENGINE REBALANCE

Since the initial baseline engine performance estimate was prepared (Ref. 3), studies have been conducted to provide a 10:1 throttling capability in the SERV engine, to evaluate the turbomachinery efficiency values, to refine the nozzle contour and the respective nozzle divergency and drag efficiencies, and the fuel heat gain in the jacket cooling process. As a result of these refinements, an increase in baseline performance can be predicted. A reduction in turbine flow requirements for the engine was also indicated. The reduction in secondary flow results in part of the increased engine I_s.

These studies indicated that turbine flow requirements could be reduced to 0.0264. To provide throttling of the engine to 10 percent of its nominal thrust, the oxidizer injector pressure drop had to be increased to 2000 psia to insure proper combustion in the chamber.

The increased pressure drop required an oxidizer pump discharge of 4320 psia. This additional requirement on the turbomachinery was met by increasing the turbine flow ratio (τ) to 0.0295.

TABLE 4
SERV BASELINE ENGINE DESIGN DATA

	INITIAL BASELINE ENGINE	INITIAL BASELINE WITH 10:1 THROTTLING	CURRENT GEOMETRY WITH 10:1 THROTTLING
CONFIGURATION			
ENGINE DIAMETER, IN.	1049	1049	1065
COMBUSTOR	SINGLE	SINGLE	SINGLE
CYCLE	GAS GENERATOR	GAS GENERATOR	GAS GENERATOR
TURBINE ARRANGEMENT	PARALLEL	PARALLEL	PARALLEL
ENGINE			
SEA LEVEL THRUST, LB	5.4×10^6	5.4×10^6	5.4×10^6
SEA LEVEL SPECIFIC IMPULSE, SEC	344.6	347.1	346.7
VACUUM THRUST, LB	7.29×10^6	7.286×10^6	7.31×10^6
VACUUM SPECIFIC IMPULSE, SEC	465.3	468.3	469.5
MIXTURE RATIO, O/F	6.0	6.0	6.0
OXIDIZER FLOWRATE, LB/SEC	13,432	13,335	13,349
FUEL FLOWRATE, LB/SEC	2,239	2,222	2,225
EFFICIENCY AT VACUUM	0.9421* (0.9555**)	0.9456* (0.9618**)	0.9466* (0.9633**)
COMBUSTOR			
MIXTURE RATIO, O/F	6.64	6.51	6.51
CHAMBER PRESSURE, PSIA	2000	2000	2000
OXIDIZER FLOWRATE, LB/SEC	13,141	13,099	13,113
FUEL FLOWRATE, LB/SEC	1,979	2,012	2,014
FUEL INJECTION TEMPERATURE, R	474	474	474
CHARACTERISTIC VELOCITY, FT/SEC	7509	7549	7551
COMBUSTION EFFICIENCY (REF. TO INJECTION CONDITIONS	0.995	0.995	0.995

* REFERENCED TO PROPELLANT INJECTION CONDITIONS

** REFERENCED TO PROPELLANT TANK CONDITIONS

TABLE 4
SERV BASELINE ENGINE DESIGN DATA (Continued)

	INITIAL BASELINE ENGINE	INITIAL BASELINE WITH 10:1 THROTTLING	CURRENT GEOMETRY WITH 10:1 THROTTLING
PRIMARY NOZZLE			
AREA RATIO	465	462.8	482.9
NOZZLE THRUST COEFFICIENT	1.881	1.878	1.887
DIVERGENCE EFFICIENCY	0.9086	0.909	0.9126
DRAG EFFICIENCY	0.9865	0.9866	0.9865
KINETICS EFFICIENCY	0.999	0.9996	0.9996
BAFFLE EFFICIENCY	0.999	0.999	0.999
BASE			
SECONDARY FLOW RATIO, $\dot{W}_S/\dot{W}_P$	0.0364	0.0295	0.0295
SECONDARY CHARACTERISTIC VELOCITY, FT/SEC	5500	5500	5500
BASE PRESSURE AT VACUUM, PSIA	1.10	1.048	0.991
GAS GENERATOR			
MIXTURE RATIO, O/F	1.12	1.12	1.12
OXIDIZER FLOWRATE, LB/SEC	290.8	235.5	235.8
FUEL FLOWRATE, LB/SEC	259.6	210.3	210.5
TEMPERATURE, R	1960	1960	1960
SPECIFIC HEAT, BTU/LB-R	1.8	1.8	1.8
GAMMA	1.348	1.348	1.348
MOLECULAR WEIGHT	4.272	4.272	4.272
CHARACTERISTIC VELOCITY, FT/SEC	7045	7045	7045

TABLE 4
SERV BASELINE ENGINE DESIGN DATA (Continued)

	INITIAL BASELINE ENGINE		INITIAL BASELINE WITH 10:1 THROTTLING		CURRENT GEOMETRY WITH 10:1 THROTTLING	
GEOMETRY						
ENGINE DIAMETER, IN.	1049.04		1049.04		1064.5	
NOZZLE EXIT DIAMETER, IN.	1022.05		1022.05		1044.7	
THROAT CENTERLINE DIAMETER, IN.	1028.4		1028.4		1051.04	
BASE AREA RATIO	337.64		337.64		346.7	
BASE DIAMETER, IN.	870.94		873		885.3	
NOZZLE PERCENT LENGTH	5.0		5.0		5.265	
NOZZLE LENGTH, IN.	90.94		90.93		97.97	
COMBUSTOR THROAT AREA, IN.	1764.4		1772.8		1775.2	
COMBUSTOR THROAT GAP, IN.	0.5904**		0.5932**		0.5812**	
	OXIDIZER	FUEL	OXIDIZER	FUEL	OXIDIZER	FUEL
PRESSURE SCHEDULE						
CHAMBER PRESSURE, PSIA	2000		2000		2000	
INJECTOR END PRESSURE, PSIA	2030		2030		2030	
△P INJECTOR, PSI	500	200	2000	200	2000	200
△P COOLING JACKET, PSI	---	700	---	700	---	700
△P LINES, VALVES, MANIFOLDS, PSI	290	120	290	120	290	120
GG SOURCE PRESSURE, PSIA	2820	3050	2820	3050	2820	3050
TURBINE INLET PRESSURE, PSIA	900	900	825	900	825	900
TURBINE EXIT PRESSURE - STATIC, PSIA	60	60	60	60	60	60

* BASED ON 12 FEET NPSH FOR OXIDIZER, 0 FEET FOR FUEL

** REFERENCED TO PROPELLANT TANK CONDITIONS

TABLE 4

SERV BASELINE ENGINE DESIGN DATA (Continued)

	INITIAL BASELINE ENGINE		INITIAL BASELINE WITH 10:1 THROTTLING		CURRENT GEOMETRY WITH 10:1 THROTTLING	
	OXIDIZER LOW PRESSURE/ HIGH PRESSURE	FUEL LOW PRESSURE/ HIGH PRESSURE	OXIDIZER LOW PRESSURE/ HIGH PRESSURE	FUEL LOW PRESSURE/ HIGH PRESSURE	OXIDIZER LOW PRESSURE/ HIGH PRESSURE	FUEL LOW PRESSURE/ HIGH PRESSURE
PUMPS						
INLET PRESSURE, PSIA	*20.7/321	*14.7/222	*20.7/321	*14.7/222	*20.7/321	*14.7/222
INLET TEMPERATURE, R	*163/164	*36.5/39.5	*163/164	*36.5/39.5	*163/164	*36.5/39.5
HORSEPOWER, HP	1650/12600	3050/43000	2800/18300	3050/43000	2800/18300	3050/43000
DISCHARGE PRESSURE, PSIA	321/2820	222/3050	544/4320	222/3050	544/4320	222/3050
SPEED, RPM	4760/21700	13400/22700	7040/21700	13400/22700	7040/21700	13400/22700
EFFICIENCY	0.80/0.81	0.80/0.77	0.80/0.81	0.80/0.77	0.80/0.81	0.80/0.77
TURBINES						
INLET TEMPERATURE, R	1110/1960	1050/1960	1110/1960	1050/1960	1110/1960	1050/1960
DISCHARGE TEMPERATURE, R	980/1110	980/1050	980/1110	980/1050	980/1110	980/1050
PRESSURE RATIO	1.65/9.0	1.3/1125	1.88/8.0	1.3/11.25	1.88/8.0	1.3/11.25
EFFICIENCY	0.395/0.45	0.62/0.53	0.50/0.70	0.70/0.74	0.50/0.70	0.70/0.74
FLOWRATE, LB/SEC	12.2/13.0	28.2/34.7	12.6	25	12.6	25

Since the sea level thrust and baseline engine diameter are kept constant, the above changes in turbomachinery efficiencies and turbine flow requirements have led to improved baseline engine performance. These improvements and the associated geometry changes are reflected in Table 5.

TABLE 5

BASELINE ENGINE REBALANCE

Case No.	τ	I_{s_v}	$I_{s_{SL}}$	ϵ	Engine Description
6-A	.0364	465.3	344.6	465	Initial Baseline
6-B	.0264	468.7	347.6	461.1	Improved Process Efficiencies
6-1	.0295	468.3	347.1	462.8	10:1 Throttling Capability

BASELINE ENGINE NOZZLE REDESIGN

Structural studies have been conducted recently which resulted in the incorporation of the engine thrust ring with existing vehicle structural elements. This action resulted in a weight savings. It also allowed for the nozzle throat to be placed at a larger diameter and at a position closer to the propellant tanks. Two changes in engine geometry resulted from the above alterations: the nozzle expansion area ratio increased as well as the nozzle length. Both of these changes have led to improved engine performance as shown in Table 6.

TABLE 6

BASELINE ENGINE NOZZLE REDESIGN

Case No.	τ	I_{s_v}	$I_{s_{SL}}$	ϵ	Length	Engine Description
6-A	.0364	465.3	344.6	465	90.94	Initial Baseline
6-2	.0295	469.5	346.7	482.9	97.96	Larger Engine Diameter

The above studies and a redesign of the secondary flow exhaust manifold have resolved the interference problem encountered in the original baseline engine with the turbofan engines.

BASELINE ENGINE PERFORMANCE PARAMETERS

In this section the engine performance parameters necessary for correlation with cold-flow nozzle data are compiled. In Table 7 the nozzle efficiencies and base pressure data are presented at three pressure ratios of interest.

TABLE 7

SERV BASELINE ENGINE NOZZLE PERFORMANCE PARAMETERS

Nozzle Expansion Area Ratio, $\epsilon = 465$

	Sea Level	Design Altitude	Vacuum
Pressure Ratio	136.09	10,303.4	∞
Percent of Design Pressure Ratio	1.321	100	∞
Primary Nozzle Thrust Coefficient Efficiency			
Nozzle Overall Thrust Coefficient Efficiency	0.856	0.9464	0.9468
Nozzle Normalized Thrust Coefficient Efficiency	0.9045	1.0	--
Nozzle Base Pressure, psia	14.48	1.10	1.10
Nozzle Exit Wall Pressure, psia			
Ambient Pressure, psia	14.7	0.1941	0

SERV MODEL STILL AIR PERFORMANCE CALCULATIONS

The "as designed" geometry of the SERV cold-flow model was used to determine the expected still air nozzle primary performance (C_{F_p}), nozzle C_T performance, the nozzle wall pressure, and the nozzle base pressures. The model was designed with an area ratio of 465. Cold flow blowdowns of the assembled nozzle at chamber pressure of 400 psia indicate that the model area ratio as tested was 417.

NOZZLE PRIMARY THRUST COEFFICIENT

The nozzle primary thrust coefficient was obtained from a method of characteristics analysis of the primary flowfield. It was calculated for pressure ratios from simulated sea level (450) to vacuum. Results are shown in Fig. 16. Recompression of the nozzle can be seen to end at a pressure ratio of 440 as indicated by the constancy of the primary thrust coefficient.

NOZZLE THRUST COEFFICIENT EFFICIENCY, C_T

Equations 1 through 4 were used for the calculation of the closed-wake C_T performance shown in Fig. 17. The drag thrust coefficient loss ΔC_{F_d} was obtained from a boundary layer analysis of the model. The base pressures were calculated using the closed-wake empirical equations. Performance is shown for the case of no secondary flow and for the turbine flow conditions of the baseline engine ($W_s C_s^* / W_p C_p^* = 0.021$).

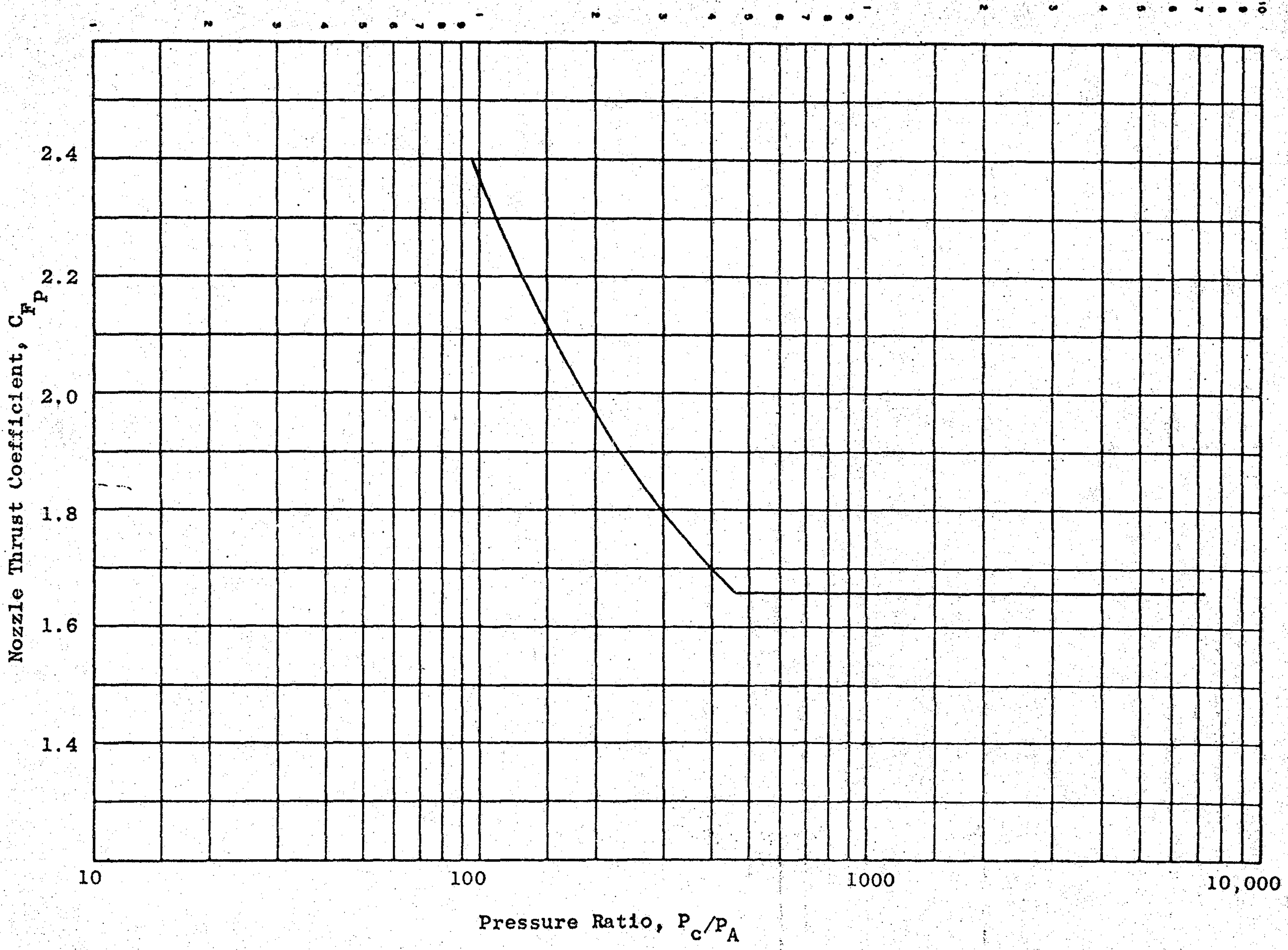

Figure 16. SERV Cold-Flow Model Primary Thrust Coefficient vs Pressure Ratio.

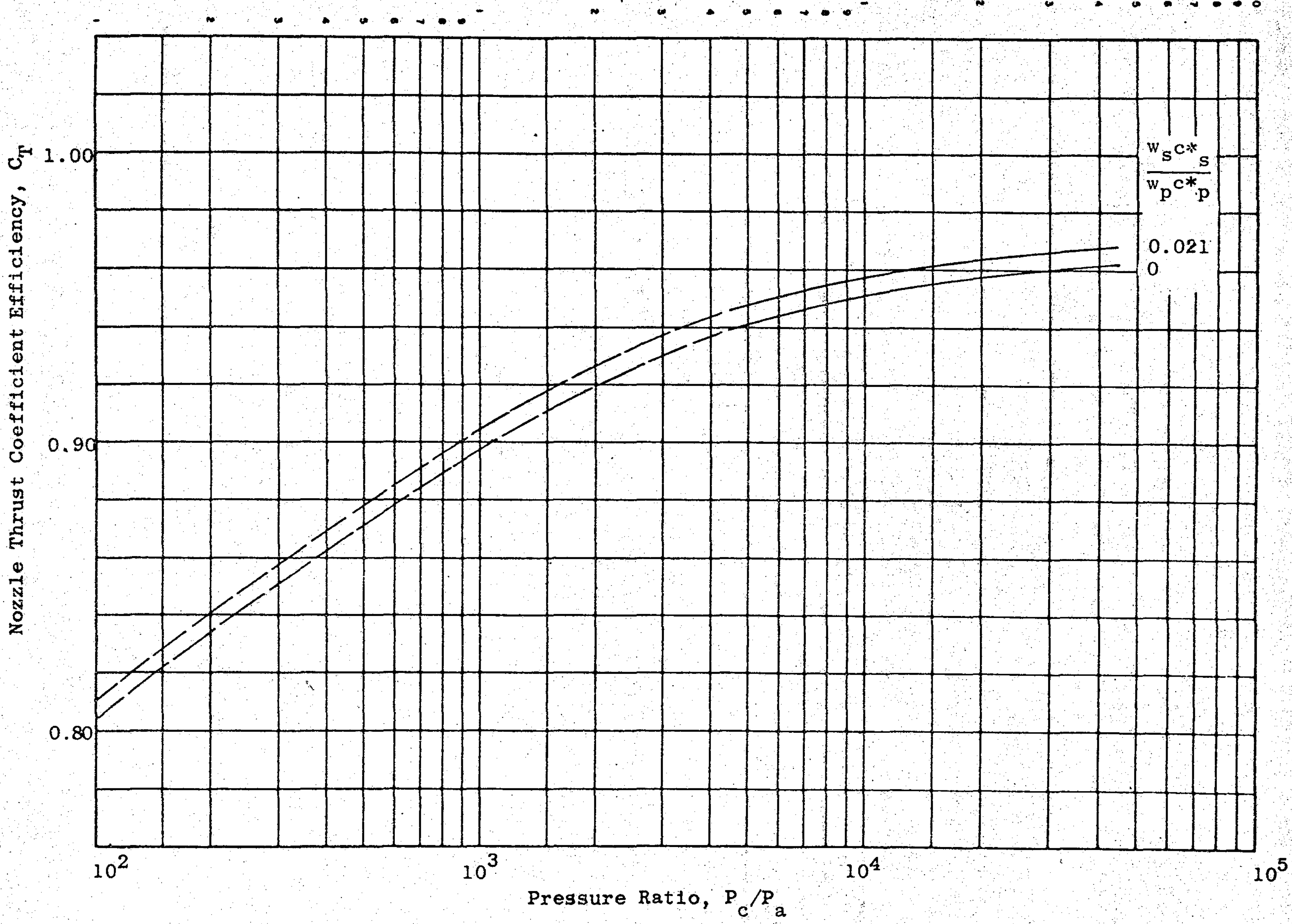

Figure 17. SERV Cold Flow Model Thrust Coefficient Efficiency vs Pressure Ratio

NOZZLE WALL PRESSURE RATIOS

The nozzle wall pressure ratios, one of the outputs of the method of characteristics analysis of the nozzle, are shown in Fig. 18. Two pressure ratios are shown; vacuum, for which there is no recompression, and sea level (simulated) for which strong recompression is felt on the nozzle walls. The wall pressure ratios (P_w/P_c) are plotted against the dimensionless datance (X/R_T) from the nozzle throat. Pressure taps at selected locations on the model nozzle wall were used to verify the calculated values.

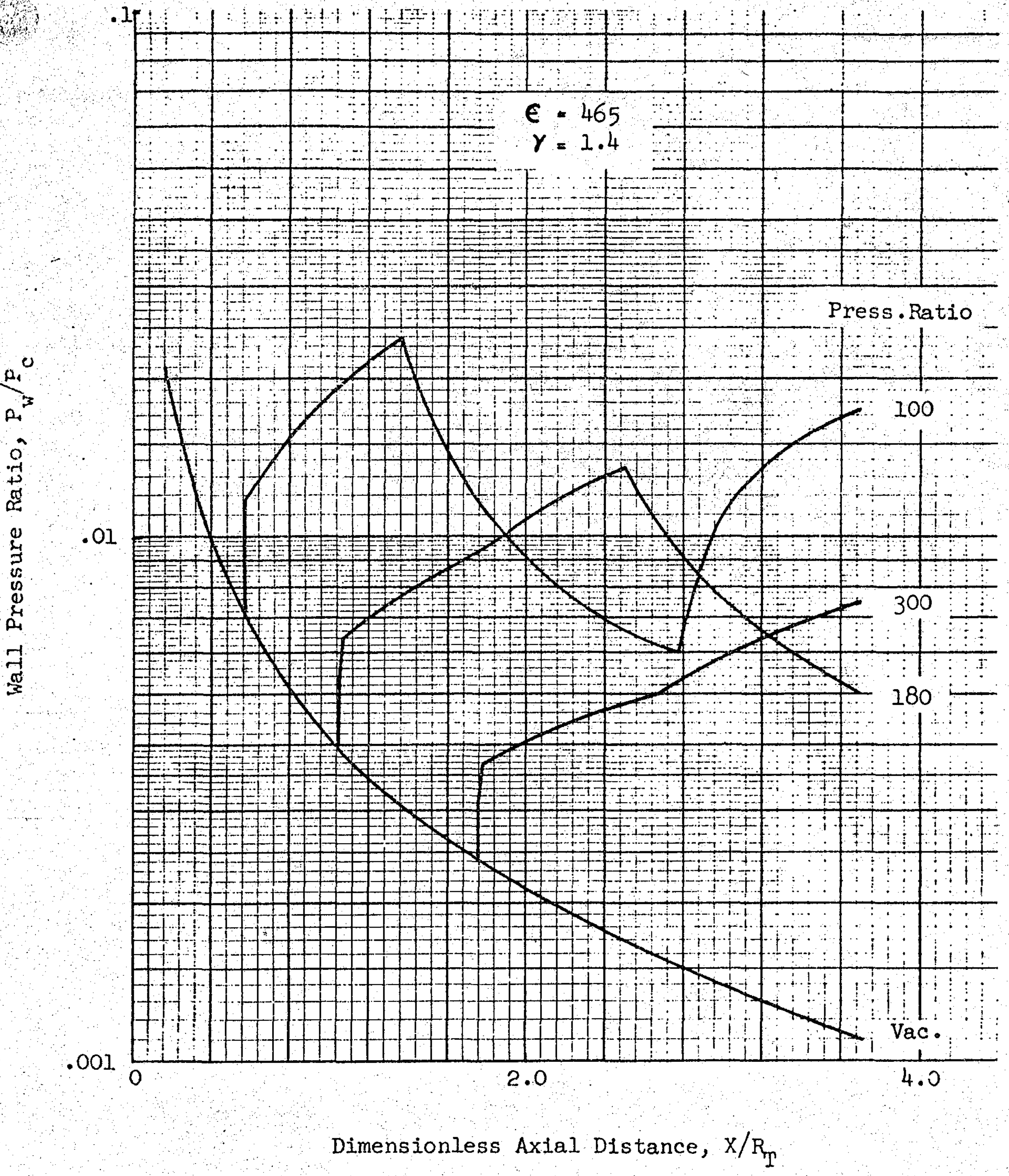

Fig. 18. SERV Cold Flow Model Wall Pressure Ratios Vs. Nozzle Station

MEASURED MODEL PERFORMANCE

When the slipstream model test program was originally formulated, it was recognized that the engine thrust would not be directly measured during the slipstream runs, but could be isolated from the force balance measurements of thrust-plus-vehicle-drag, using engine-off and engine-on runs at identical slipstream conditions. The test procedure was designed to provide pairs of runs consisting of an engine-on case followed by an engine-off case at as nearly the same slipstream Mach number and total pressure as was practically obtainable. The difference in force balance readings between each pair of runs would then be the engine thrust, plus the force due to the change in vehicle drag due to the engine, plus error forces due to changes in run conditions between the engine-on case and corresponding engine-off case, as well as any shift in the force balance zero due to pressure and temperature induced loads caused by the engine gas supply flowing in the model. The model was designed to minimize the zero shift, and this effect was assumed to be negligible in planning the test program. In monitoring the on-line data during the testing, it was found that internal stresses, apparently produced by a temperature difference between the model and the nozzle supply air, caused force balance loads that would be an important factor in interpreting the test results.

From the results of a pair of runs, an engine-on case followed by an engine-off case at the same slipstream conditions, the engine thrust can be obtained.

The force balance load, FAC, opposes the net force on the model (Fig. 19).

$$\mathrm{FAC} = F_{\mathrm{model}}$$

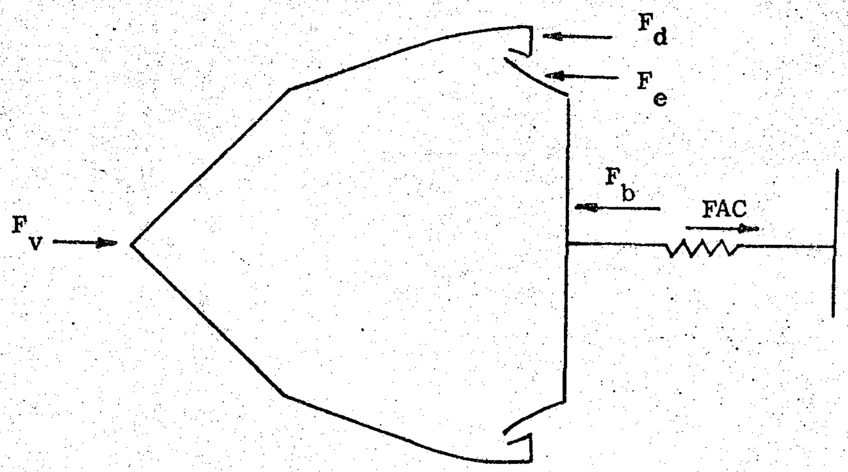

Figure 19. Definition of Force Terms

For engine-on operation,

$$FAC = F_e + F_d - F_v$$

where F_e is the engine thrust, F_d is the force on the cowl and doors (the part of the vehicle base not occupied by the engine), and F_v is the drag force of the vehicle forebody.

For the engine-off case ($F_e = 0$),

$$FAC_o = F_{d_o} - F_{v_o} - F_{b_o}$$

where F_{b_o} is the engine-off force on the part of the vehicle base occupied by the engine.

Assuming that the engine does not affect F_v, i.e., $F_v = F_{v_o}$, F_e can be obtained,

$$F_e = (FAC - FAC_o) - (F_d - F_{d_o}) + F_{b_o}$$

In this development the engine thrust, F_e, is referenced to vacuum, rather than the local ambient pressure as is usually the case. F_e is termed the intrinsic thrust of the engine.

The forces F_d, F_{d_o} and F_{b_o} are relatively small compared to the force balance readings, therefore, the accuracy of the engine thrust values is strongly dependent on the accuracy of the force balance readings, for both the engine-on and engine-off cases. As a check on the engine-off force data, a series of engine-off high dynamic pressure runs were made at slipstream Mach numbers of .6, .8, .9, 1.1 and 1.25 to obtain drag/dynamic pressure, D_q, which should be constant with varying q. Having q for the engine-on/engine-off pair of runs, the engine-off drag could be computed using D/q from the high q runs. The high q data provided a source of engine-off force results that avoided the uncertainty associated with the internal loading of the force cell, since the model was in thermal equilibrium during the high q runs. Drag forces from the D/q data were in general felt to be more accurate than the engine-off force reading taken immediately after the engine-on run. The D/q forces were used in the data reduction procedure finally selected.

Having determined that the originally selected method of obtaining performance from the test data could introduce considerable error, an alternative method was used to check the sensitivity of the final results to the method used. It was observed that for chamber pressure/cowl pressure (P_c/PBV) of more than 400, the nozzle wall pressures were independent of slipstream Mach number and P_c/P_∞. Figure 20 compares experimental and theoretical wall pressures. The experimental pressures are higher than the predicted values due to the lower area ratio of the model, $\epsilon = 417$, compared to $\epsilon = 465$ used for the predictions. The theoretical results indicated that the wall pressure should be constant for $P_c/\text{PBV} > 450$. For P_c/PBV greater than 400, the intrinsic thrust of the nozzle, excluding the nozzle base, $F_{p_{int}}$, is therefore constant. If the value of $F_{p_{int}}$ were know, the nozzle thrust at various slipstream conditions could be obtained without using the force balance outputs, either for engine-on or engine-off, since

$$F_{e_\infty} = F_{p_{int}} + \text{PBE} \times A_b - P_\infty A_e$$

where

PBE is the integrated average base pressure

P_∞ is the freestream ambient static pressure

A_b is the base area

A_e is the area of the vehicle base occupied by the engine

In this case the accuracy of the results is independent of the force readings for a given case, but is dependent on a pressure integration.

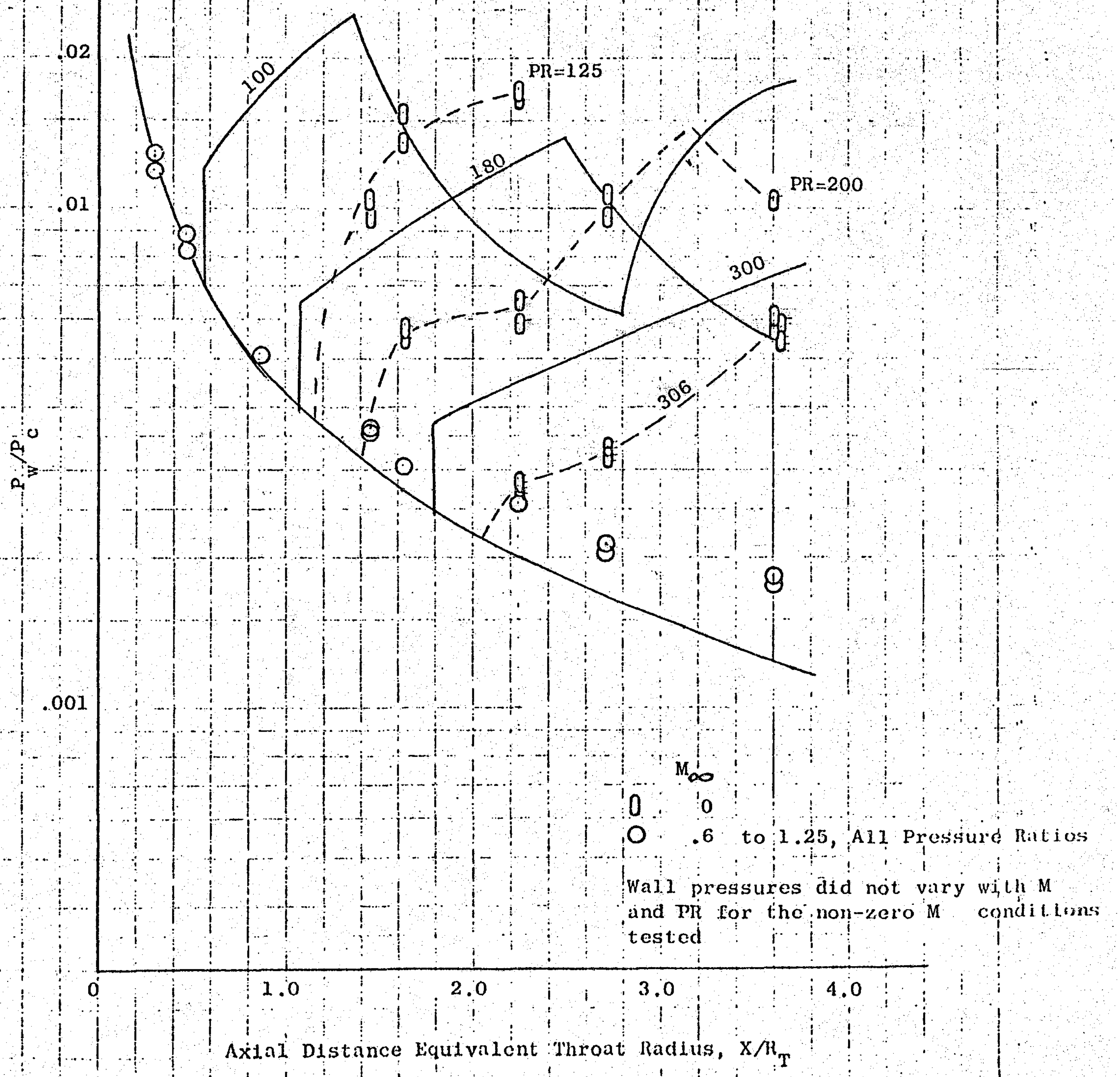

Wall Pressures - Doors Off

ϵ = 465 For Theoretical Values

γ = 1.4

Wall pressures did not vary with M and PR for the non-zero M conditions tested

Figure 20

$F_{p_{int}}$ was obtained from the force balance outputs for many cases and an average value of 865 lbs was selected. Using experimental data,

$$F_{p_{int}} = (FAC - FAC_o) - (PBD - PBDO) \times A_d - PBE \times A_b + PBVO \times A_e$$

where

FAC_o is the force balance reading, engine-off

PBD is the integrated average pressure on the vehicle base outside of the area occupied by the engine

PBDO is the PBD for engine-off

PBVO is the integrated average pressure on the vehicle base area occupied by the engine

A_b is the area of the engine base

A_e is the area of the engine

A_d is the vehicle base area minus area of the engine

Figure 21 shows model nozzle efficiency for the doors-off configuration, referenced to freestream ambient pressure, P_∞, base on $F_{p_{int}} = 865$ lbs. The efficiency, C_{T_∞}, is defined as

$$C_{T_\infty} = \frac{F_\infty}{F_{ideal}}$$

where

$$F_\infty = F_{p_{int}} + PBE \times A_b - P_\infty \times A_e$$

and

F_{ideal} is the thrust that would be obtained by a one-dimensional frictionless, equilibrium expansion from the nozzle stagnation conditions to the freestream ambient static pressure.

Figure 22 shows C_{T_∞} for the model based on force balance readings. The engine-off forces were based on the high dynamic pressure D/q data in cases where the force balance and high q results varied.

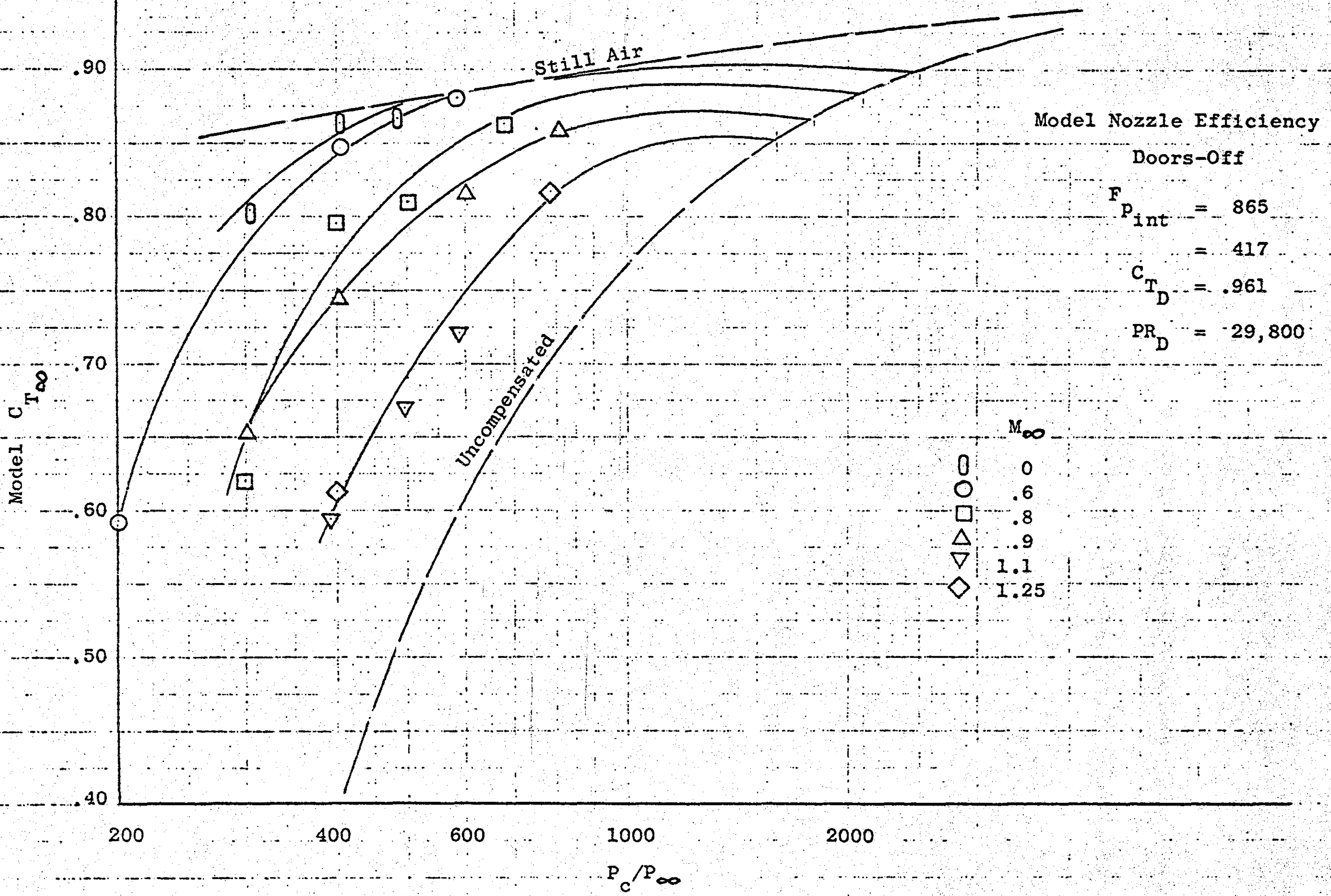
Still Air
Uncompensated
Model Nozzle Efficiency
Doors-Off
$F_{P_{int}}$ = 865
= 417
C_{T_D} = .961
PR_D = 29,800
M_∞
0
.6
.8
.9
1.1
1.25
Model C_{T_∞}
.90
.80
.70
.60
.50
.40
200
400
600
1000
2000
P_c/P_∞

Figure 21

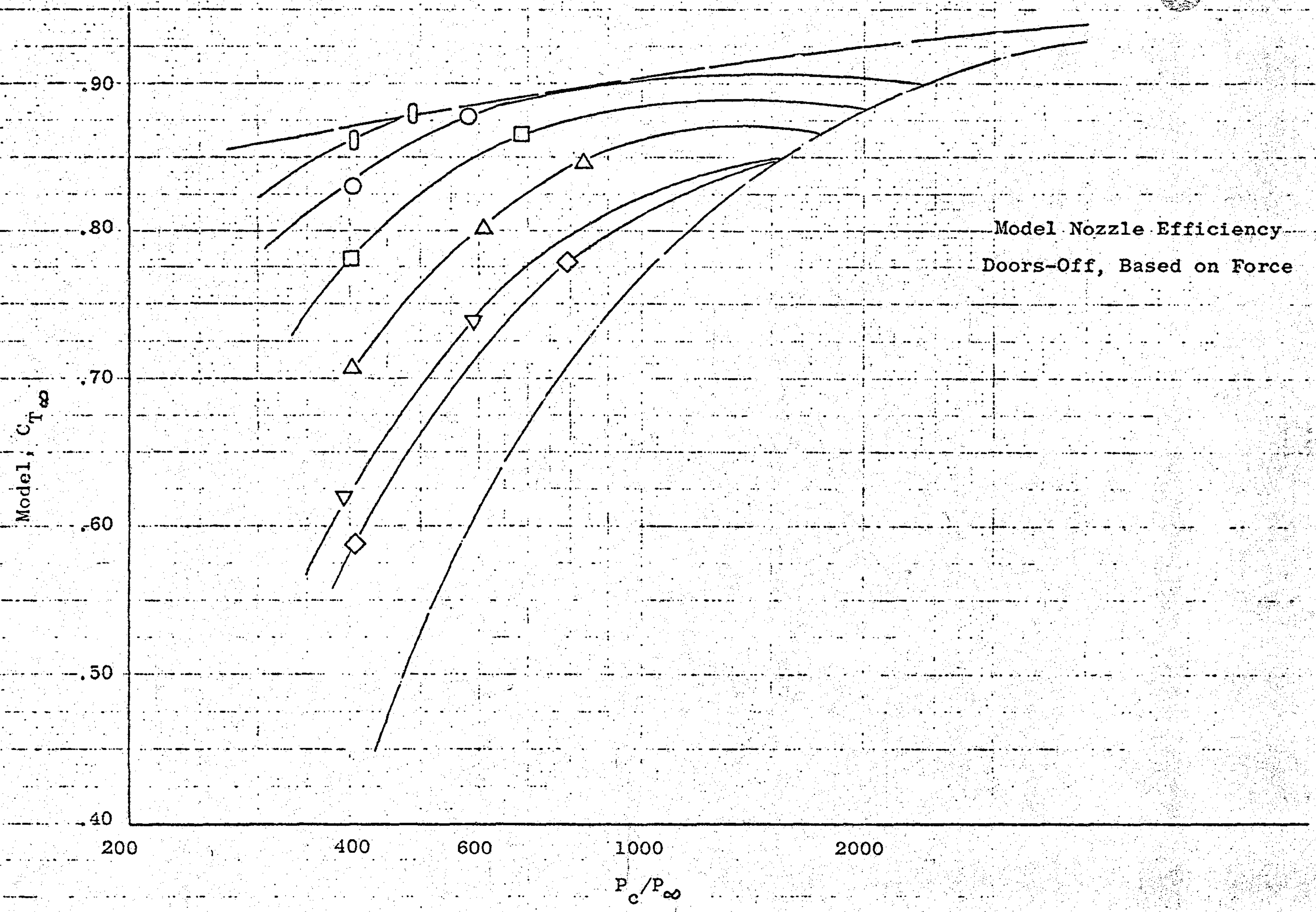
Model Nozzle Efficiency
Doors-Off, Based on Force
Model, $C_{T\infty}$
.90
.80
.70
.60
.50
.40
200
400
600
1000
2000
P_c/P_∞

Figure 22

EXTRAPOLATION OF PERFORMANCE TO HIGHER PRESSURE RATIOS

The SERV model expansion area ratio was 417 as tested. A one-dimensional isentropic expansion of air to an expansion ratio of 417 gives an exit pressure/total pressure of $.336 \times 10^{-4}$. The design pressure ratio, PR_D, is the chamber pressure to ambient pressure ratio where the exit pressure equals ambient pressure, which in this case is $1/.336 \times 10^{-4} = 29800$. For the full scale O_2/H_2 engine with an expansion ratio of 483, PR_D=11000. Model performance can best be scaled to hot firing performance by using the normalized performance method described in an earlier section. This method states that if $\frac{PR}{PR_{D\ \mathrm{Model}}} = \frac{PR}{PR_{D\ \mathrm{Full}}}$, then $\frac{C_T}{C_{T_{D\ \mathrm{Model}}}} = \frac{C_T}{C_{T_{D\ \mathrm{Full}}}}$, where C_{T_D} is the nozzle efficiency at the design pressure ratio. For a typical SERV trajectory, M_∞ = 0, .06, .8, .9, 1.1 and 1.25 occurred at P_c/P_∞ = 135, 260, 390, 480, 740 and 1000 respectively. The equivalent model pressure ratios are $P_c/P_{\infty\ \mathrm{Full}} \times \frac{PR_{D\ \mathrm{Model}}}{PR_{D\ \mathrm{Full}}}$, which are 365, 700, 1050, 1300, 2000 and 2700.

The test conditions run for the model fall short of the required pressure ratios for all flight Mach numbers except $M_\infty = 0$. The model data must therefore be extrapolated to determine performance at the equivalent trajectory pressure ratios. The extrapolation could be reduced to an interpolation by anchoring a high pressure ratio point on each M_∞ curve. The high pressure ratio points used were the computed points at which the performance departed from the theoretical uncompensated performance curve for each slipstream Mach number.

The exhaust plume outer boundary of an aerospike nozzle adjusts to the pressure on the vehicle base pressure just outside the engine, PBV, as shown in Fig. 23. The influence of the outer jet boundary (OJB) is felt along the first characteristic line from the OJB. For $P_c/PBV = PR_D$ this

Figure 23

SLIPSTREAM INTERACTION WITH NOZZLE EXHAUST JET

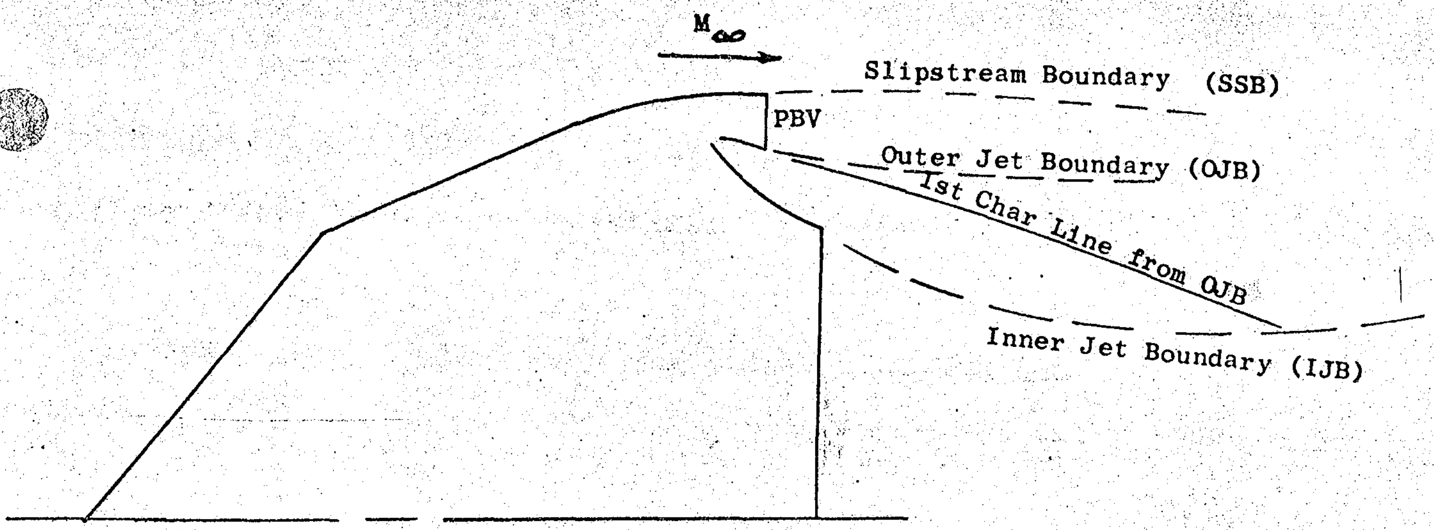

a. Slipstream, $P_c/PBV \cong$ Design Pressure Ratio

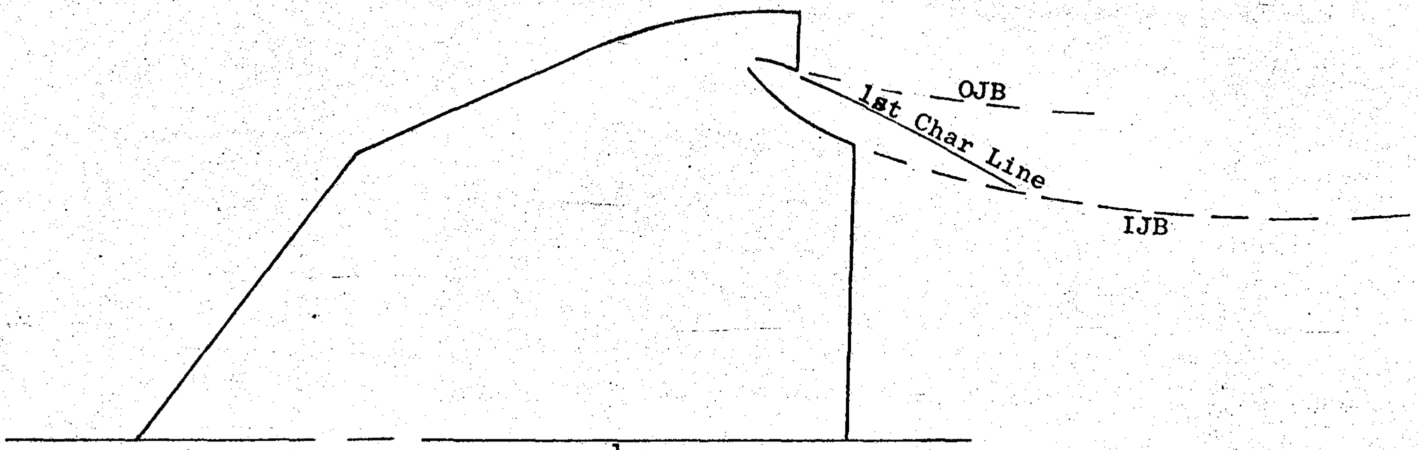

b. Still Air, $PBV = P_\infty$, $P_c/PBV < \frac{1}{3}$ Design Pressure Ratio

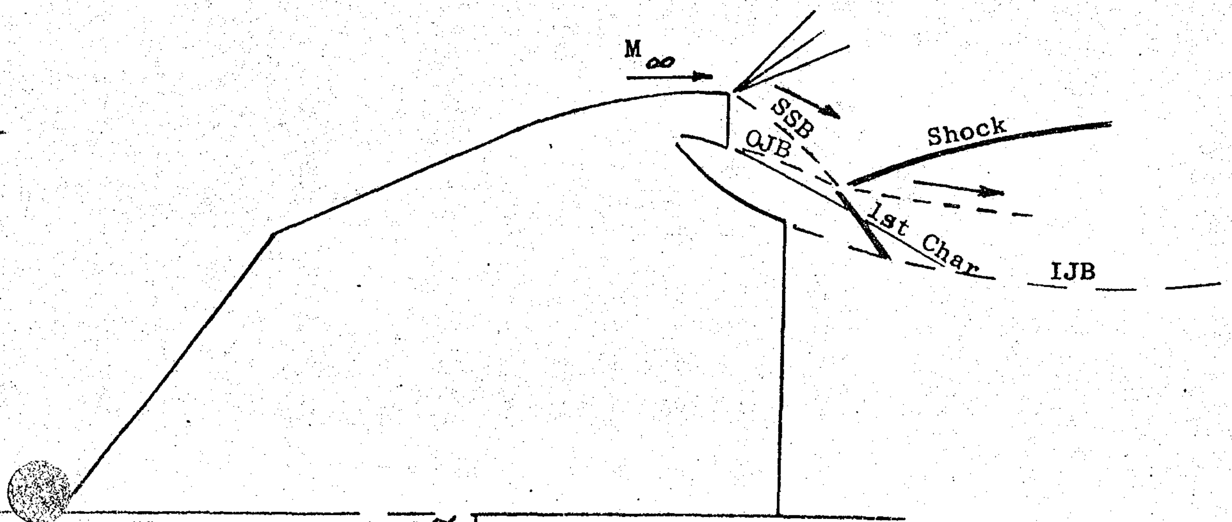

c. Slipstream, $P_c/PBV \cong \frac{1}{2}$ Design Pressure Ratio, Shock Intersects IJB Close Enough to Engine Base to Influence Base Pressure line passes well downstream of that part of the inner jet boundary (IJB) that determines the engine base pressure and base pressure is independent of PBV in this range. In still air, the first characteristic line from the OJB intersects the IJB close enough to the nozzle to influence (raise) the engine base pressure when $P_c/PBV \cong \frac{1}{3} PR_D$. For slipstream with a blunt vehicle base, the vehicle slipstream intersects the OJB causing a shock which influences base pressure at P_c/PBV considerably greater than the $\frac{1}{3} PR_D$ which holds for still air.

Considering the performance of an aerospike nozzle as ambient pressure is increased at constant P_c, C_T follows the uncompensated curve until the shock from the intersection between the slipstream and the engine jet causes the base pressure to begin to rise. The point at which the performance curve for a given slipstream Mach number intersects the uncompensated performance curve is the point at which the base pressure starts to increase above the vacuum value. Figure 24 shows the measured nozzle base pressure extrapolated to intersect the theoretical closed wake base pressure for zero bleed. Based on these results, the $M_\infty = .6, .8, .9, 1.1$ and 1.25 performance intersects the uncompensated curve at $P_c/P_\infty = 2600, 2200, 1800, 1700$ and 1700 respectively. The points anchor the high pressure ratio end of the slipstream performance curves. A curve of C_T faired through the test data and intersecting the uncompensated curve at the appropriate point was used to estimate performance at high pressure ratios as shown in Fig. 21.

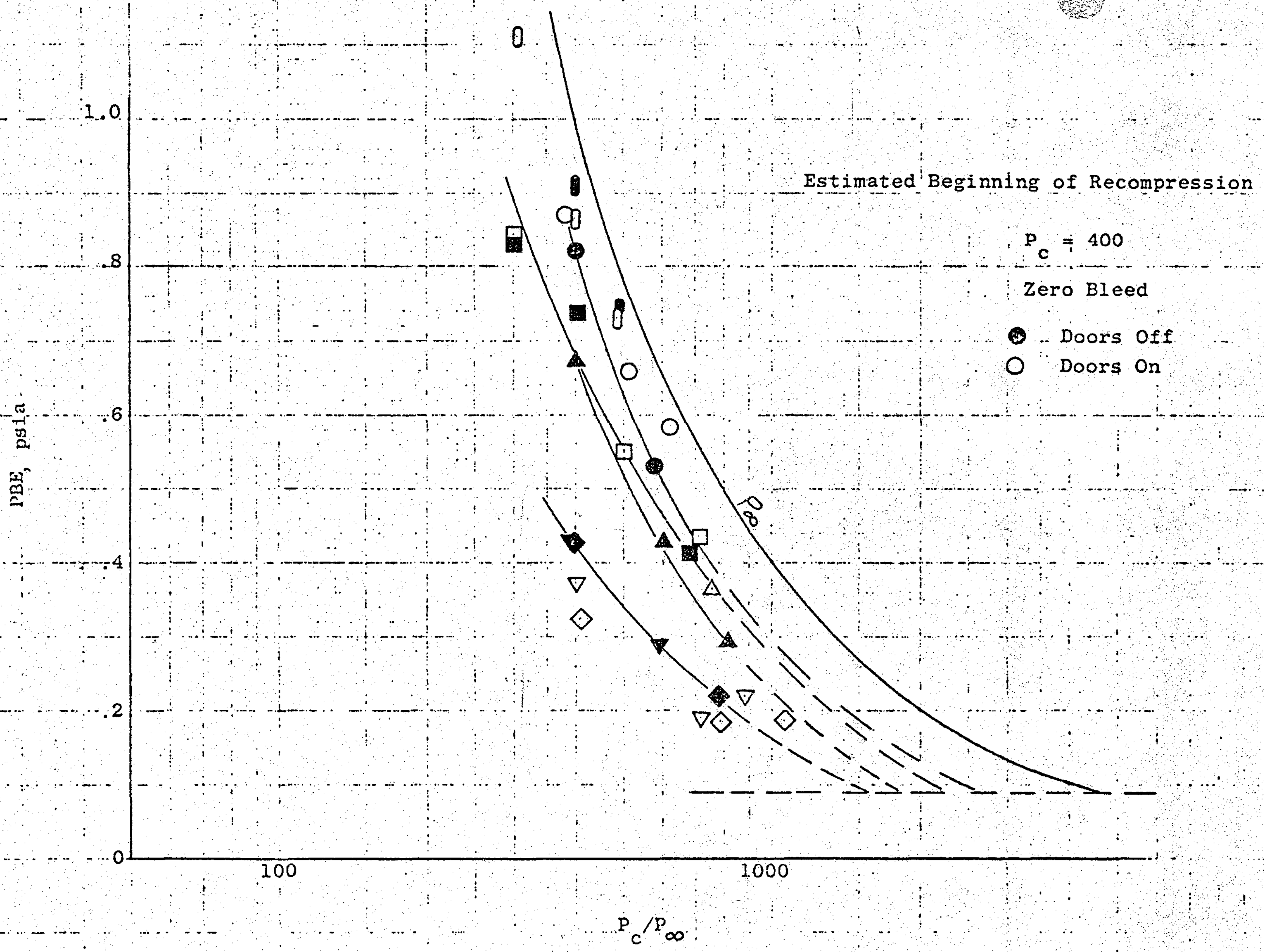
Estimated Beginning of Recompression
$P_c = 400$
Zero Bleed
● Doors Off
○ Doors On
PBE, psia
1.0
.8
.6
.4
.2
0
100
1000
P_c/P_∞
P_∞

Figure 24

INSTALLED PERFORMANCE

Figure 25 shows nozzle efficiencies with the vehicle with doors on and off. The effect of the doors on the nozzle is complex. For some pressure ratio/Mach number cases, the doors cause a reduced PBV which reduces nozzle base pressure, and therefore reduces nozzle efficiency. For other conditions, the nozzle jet impinges on the doors, constraining the nozzle expansion thereby increasing base pressure. Referring to Fig. 24, at $M_\infty = 9$ and PR = 800, PBE = .36 with doors and .30 without. In this case the doors increase PBE, and from Fig. 25 it can be seen that for these conditions the doors-on C_{T_∞} is 2 percent more than the doors-off performance. Similarly, at $M_\infty = 1.25$ and PR = 800, PBE is .18 with doors on and .22 with doors off, in which case the doors-off C_{T_∞} is 2 percent higher than for doors-off.

The installed performance of the engine is defined as (nozzle thrust plus the change in vehicle drag due to the engine exhaust)/ideal thrust

$$C_{T_I} = \frac{F_\infty + (PBD - PBDO)\ A_d}{F_{ideal}}$$

or

$$C_{T_I} = C_{T_\infty} + \Delta C_{T_D}$$

where

$$\Delta C_{T_D} = \frac{(PBD - PBDO)\ A_d}{F_{ideal}}$$

Figure 26 shows ΔC_{T_D} for the slipstream tests with both doors-on and doors-off. The large effect of the doors on vehicle performance is best seen in these results. For slipstream operation ΔC_{T_D} with doors-on is

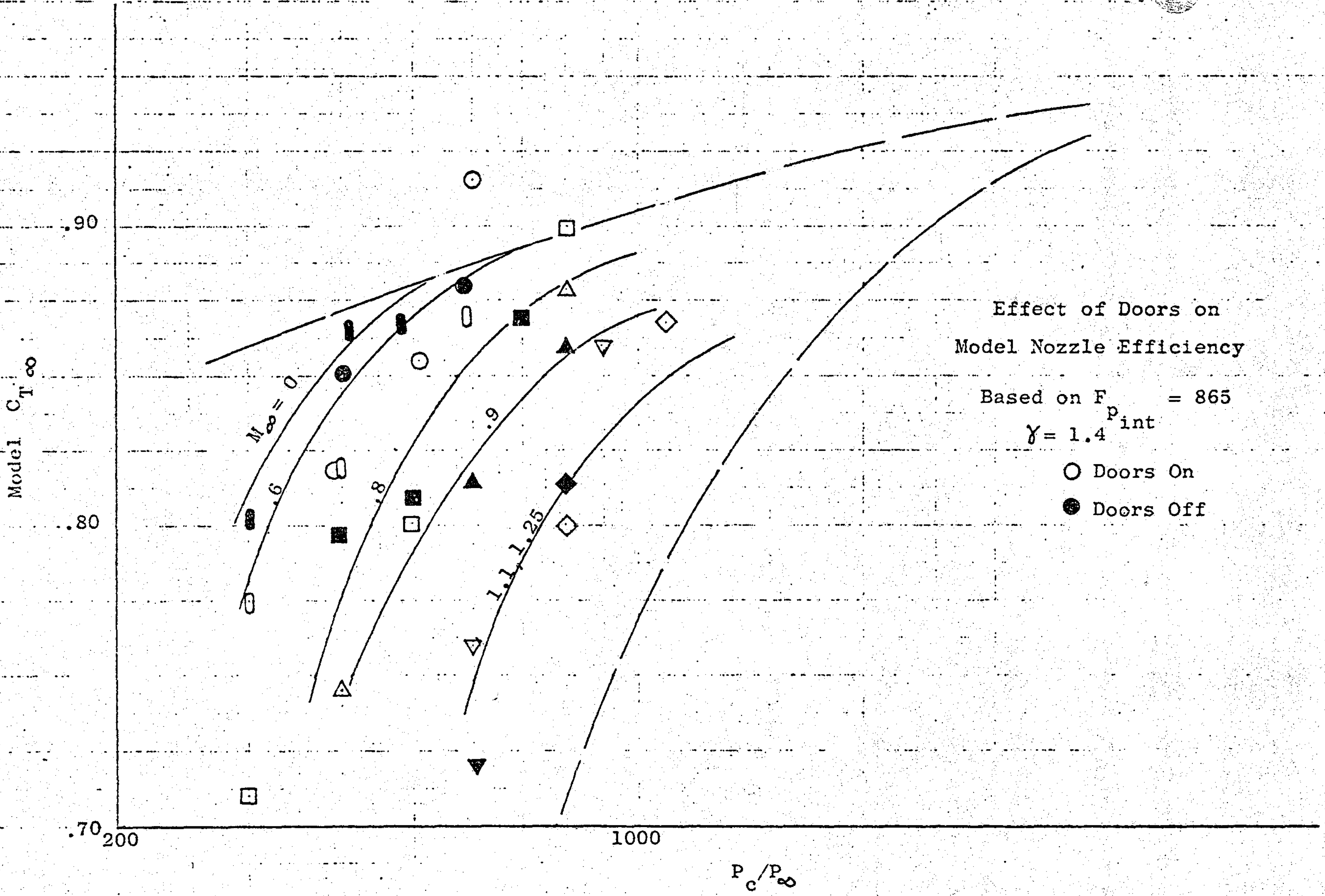
Effect of Doors on
Model Nozzle Efficiency
Based on $F_{p_{int}} = 865$
$\gamma = 1.4$
○ Doors On
● Doors Off
Model $C_{T\infty}$
.90
.80
.70
200
1000
P_c/P_∞
$M_\infty = 0$
.6
.8
.9
1.1, 1.25

Figure 25

Increase in Vehicle Drag Due to Engin

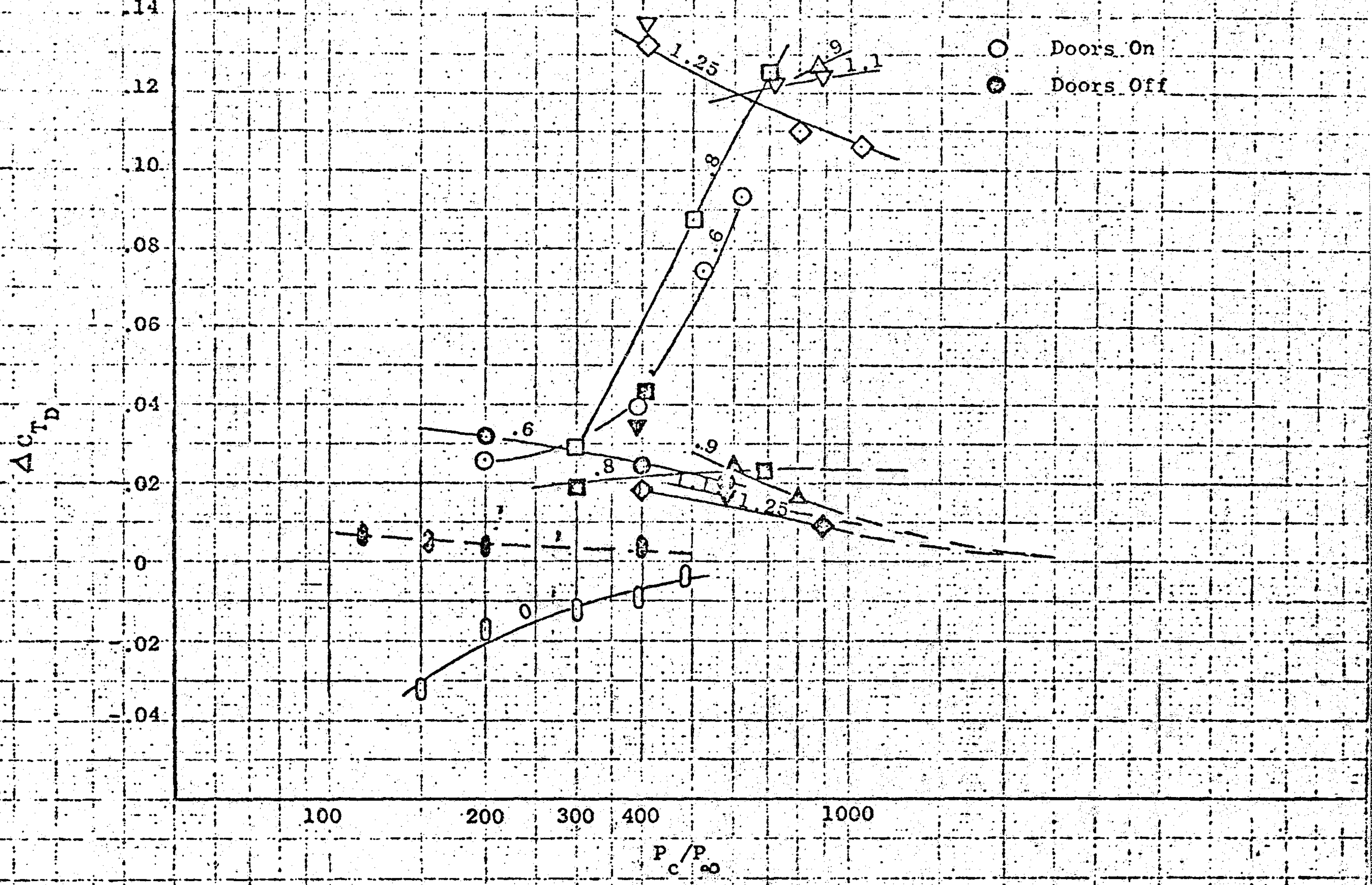

Figure 26

10 to 13 percent while ΔC_{T_D} without doors is 0 to 2 percent for the pressure ratios of interest. The large effect of the doors on vehicle drag at high pressure ratios is apparently due to impingement of the expanding engine jet on the inside of the doors. The high pressure impingement region inside the doors has a relatively large projected area normal to the engine centerline, and is opposed by a relatively low pressure outside the doors over the same projected area. Figure 27 shows the measured static pressures inside and outside the doors for the conditions tested. Figure 28 compares installed performance for doors-on and doors-off. At high pressure ratios installed performance, increases of 5 to 10 percent were obtained by removing the doors. These performance gains were relative to the tested doors position which was clearly a poor configuration, due to the exhaust impingement that occurred at high pressure ratios for this doors position. Performance approaching the doors-off values should be obtained if the doors are swung out to avoid impingement and a vent is provided to increase PBV relative to P_∞. The doors-off performance is representative of the performance expected from a configuration resulting from a doors optimization program.

The doors-off model ΔC_{T_D} values shown in Fig. 26 are strongly dependent (approximately 1 to 1) on the vehicle cowl area, A_d, which is proportionally much greater than the corresponding area on the full scale vehicle. The over-size cowl area was required for the model to maintain the throat deflection within allowable limits. For an optimized full scale vehicle ΔC_{T_D} would approach zero, therefore in this way doors-off C_{T_I} values are conservative.

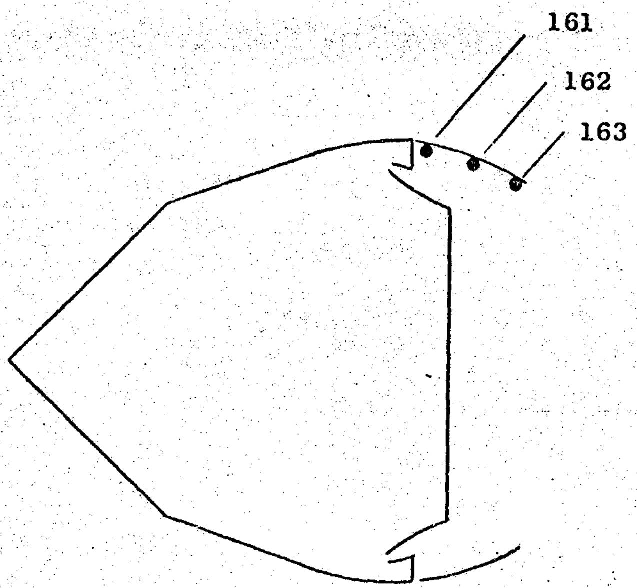

M_∞	PR	Tap No.	P/P_∞
.9	400	161	.16
		162	1.02
		163	1.64
1.25	400	161	.16
		162	1.08
		163	1.54
.9	700	161	.26
		162	1.88
		163	3.04
1.25	800	161	.26
		162	1.92
		163	3.12

Figure 27. Static Pressure Distribution on Inside of Doors

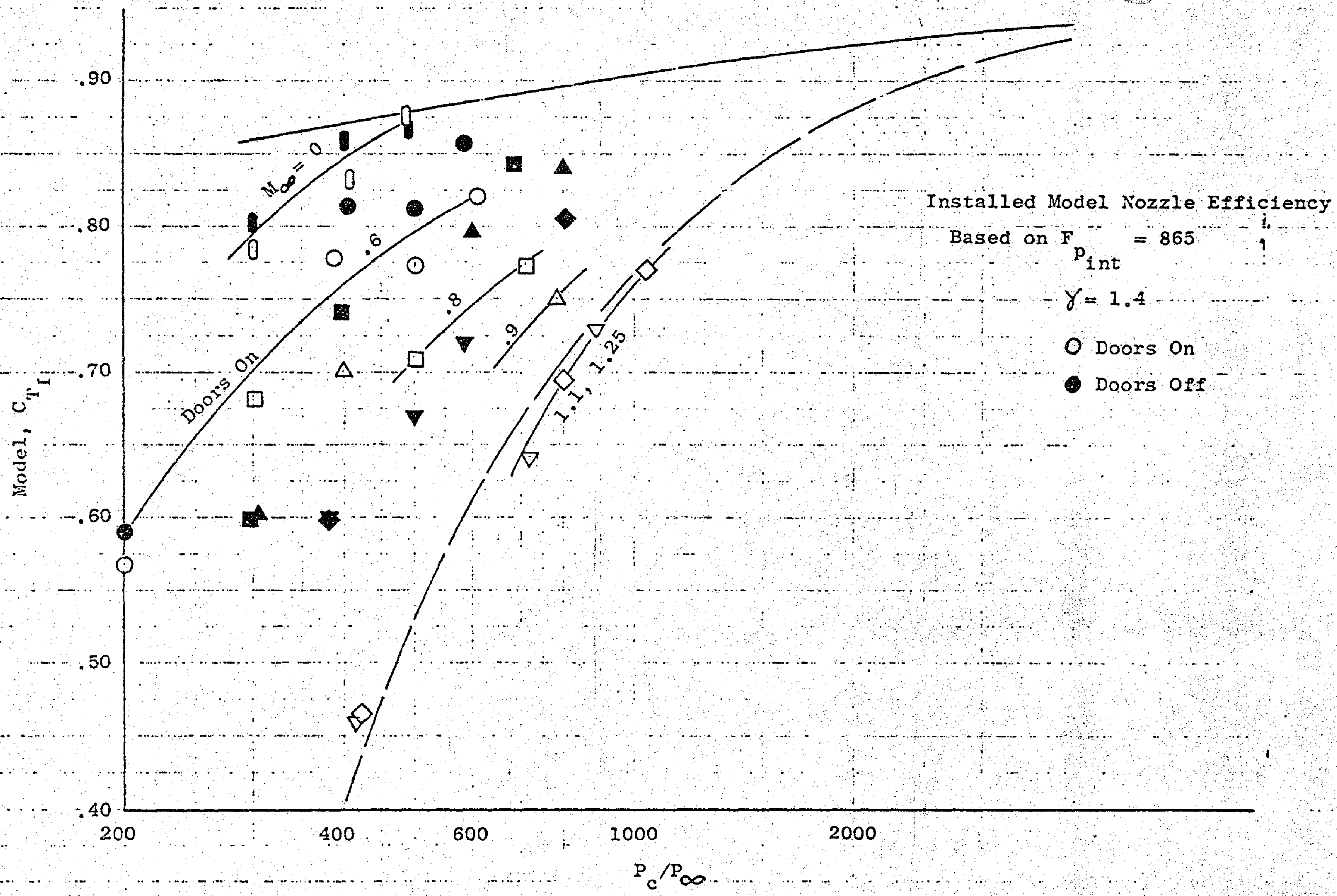
Installed Model Nozzle Efficiency
Based on $F_{p_{int}} = 865$
$\gamma = 1.4$
○ Doors On
● Doors Off
$M_\infty = 0$
.6
.8
.9
1.1, 1.25
Doors On
Model, C_{T_I}
.90
.80
.70
.60
.50
.40
200
400
600
1000
2000
P_c/P_∞

Figure 28

PERFORMANCE SCALED TO FULL SCALE

Model performance was scaled to predict the installed performance of the full scale engine over the range of conditions that might occur for SERV missions. The scaling procedure used was the normalized efficiency method discussed previously. The full scale performance at some combination of M and pressure ratio was obtained by extrapolating the cold flow C_{T_∞} curve (e.g., Fig. 21) at that M_∞ value to the pressure ratio where

$$PR_M = PR_{Full} \frac{PR_{D_M}}{PR_{D_{Full}}}$$

The model C_{T_∞} value was then adjusted to account for the effect of the engine on vehicle drag at the proper pressure ratio and M_∞ (using Fig. 26)

$$C_{T_I} = C_T + \Delta C_{T_D}$$

This gives the installed model nozzle performance. To obtain C_{T_I} for the firing engine conditions, first C_{T_∞} for the full scale nozzle was computed from

$$C_{T_\infty \, Full} = C_{T_\infty \, Model} \frac{C_{T_{D \, Full}}}{C_{T_{D \, Model}}}$$

Then assuming that $\Delta C_{T_{D \, Full}} \cong \Delta C_{T_{D \, Model}}$, $C_{T_{I \, Full}}$ was obtained at any M_∞ and PR/PR_D using

$$C_{T_{I \, Full}} = C_{T_\infty \, Full} + \Delta C_{T_{D \, Model}}$$

where $\Delta C_{T_{D \, Model}} = \Delta C_{T \, Full}$ at the same M_∞ and PR/PR_D. Figure 29 shows

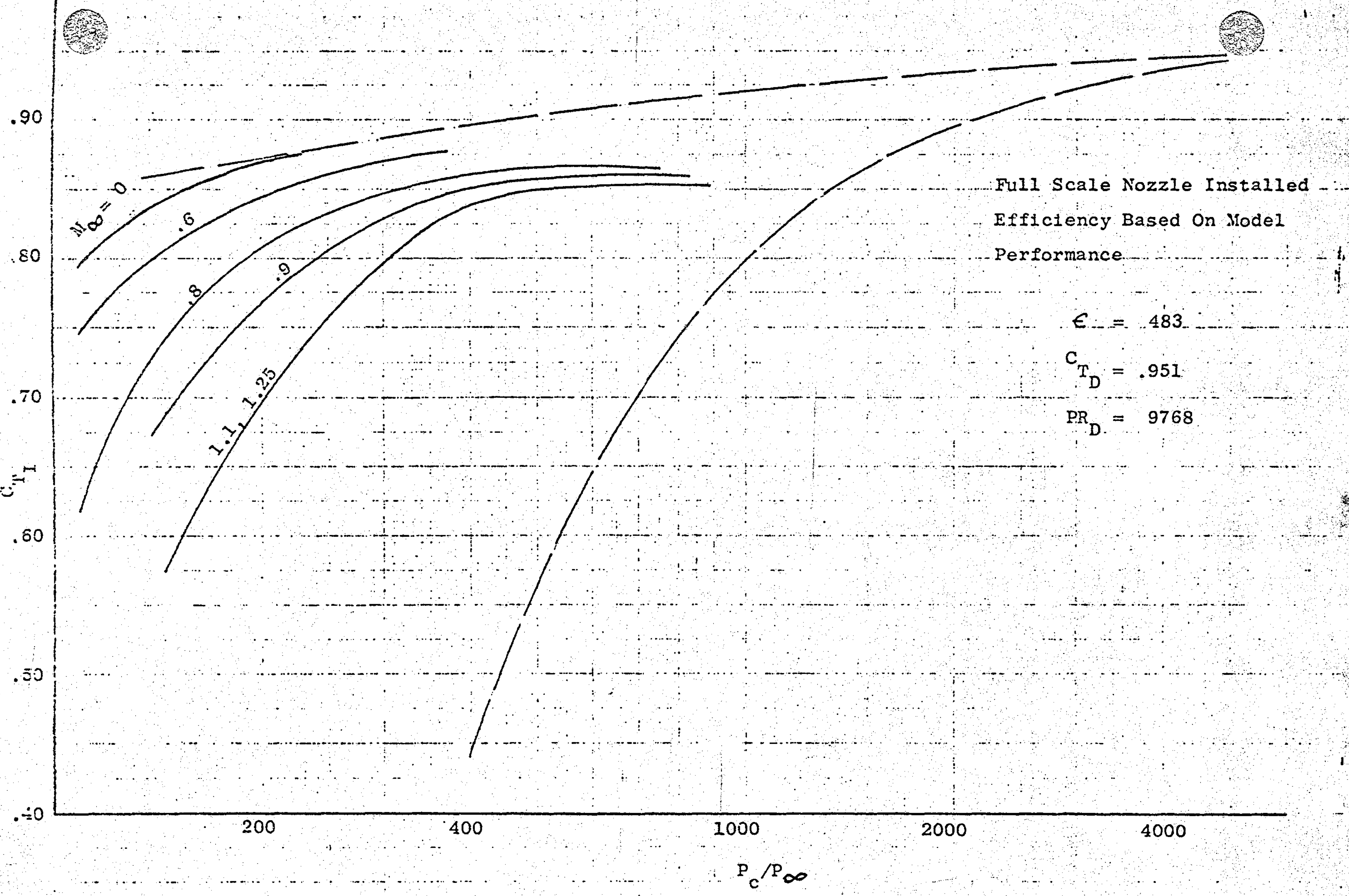
Full Scale Nozzle Installed
Efficiency Based On Model
Performance
ε = .483
C_{T_D} = .951
PR_D = 9768
M_∞ = 0
.6
.8
.9
1.1, 1.25
C_{T_I}
.90
.80
.70
.60
.50
.40
200
400
1000
2000
4000
P_c/P_∞

Figure 29

C_{T_I} for full scale conditions was based on the model results using $F_{p_{int}}$ = 865 lbs. The O_2/H_2 uncompensated curve is not near the scaled uncompensated air curve, therefore under hot firing conditions performance is expected to continue in a smooth curve to the O_2/H_2 uncompensated curve.

Figure 30 is the best available prediction of installed specific impulse performance of the ϵ = 483 O_2/H_2 SERV engine over the range of altitudes of interest for each of the flight Mach numbers tested. Figure 31 shows the installed performance (I_s) over a typical SERV trajectory using the performance curves from Fig. 30.

The results presented in Figs. 30 and 31 are applicable to a specific full scale nozzle area ratio, in this case 483. The model performance can be used to predict performance for other full scale area ratios having the hot firing design pressure ratio and design C_{T_∞} for the case in mind. Figure 32 shows the model C_{T_∞} data normalized by C_{T_D} and plotted against the normalized pressure ratio, PR/PR_D. Having C_{T_D} and PR_D for any area ratio near the model ϵ (465),

$$C_{T_\infty}\text{ Full at }PR/PR_D = \left.\frac{C_{T_\infty}}{C_{T_D}}\right|_{\text{Model at }PR/PR_D} \times C_{T_D}\text{ Full}$$

and as before

$$C_{T_I}\text{ Full at }PR/PR_D = C_{T_\infty}\text{ Full at }PR/PR_D + \Delta C_{T_D}\text{ Model at }PR/PR_D$$

Final results are not sensitive to the assumption that $\Delta C_{T_{D\,\text{Model}}} = \Delta C_{T_{D\,\text{Full}}}$ at the same normalized pressure ratio since the magnitude of ΔC_{T_D} is relatively small. In some cases it may be more accurate to scale model C_{T_I} directly rather than scale C_{T_∞} then add ΔC_{T_D}. Neither method is exact however.

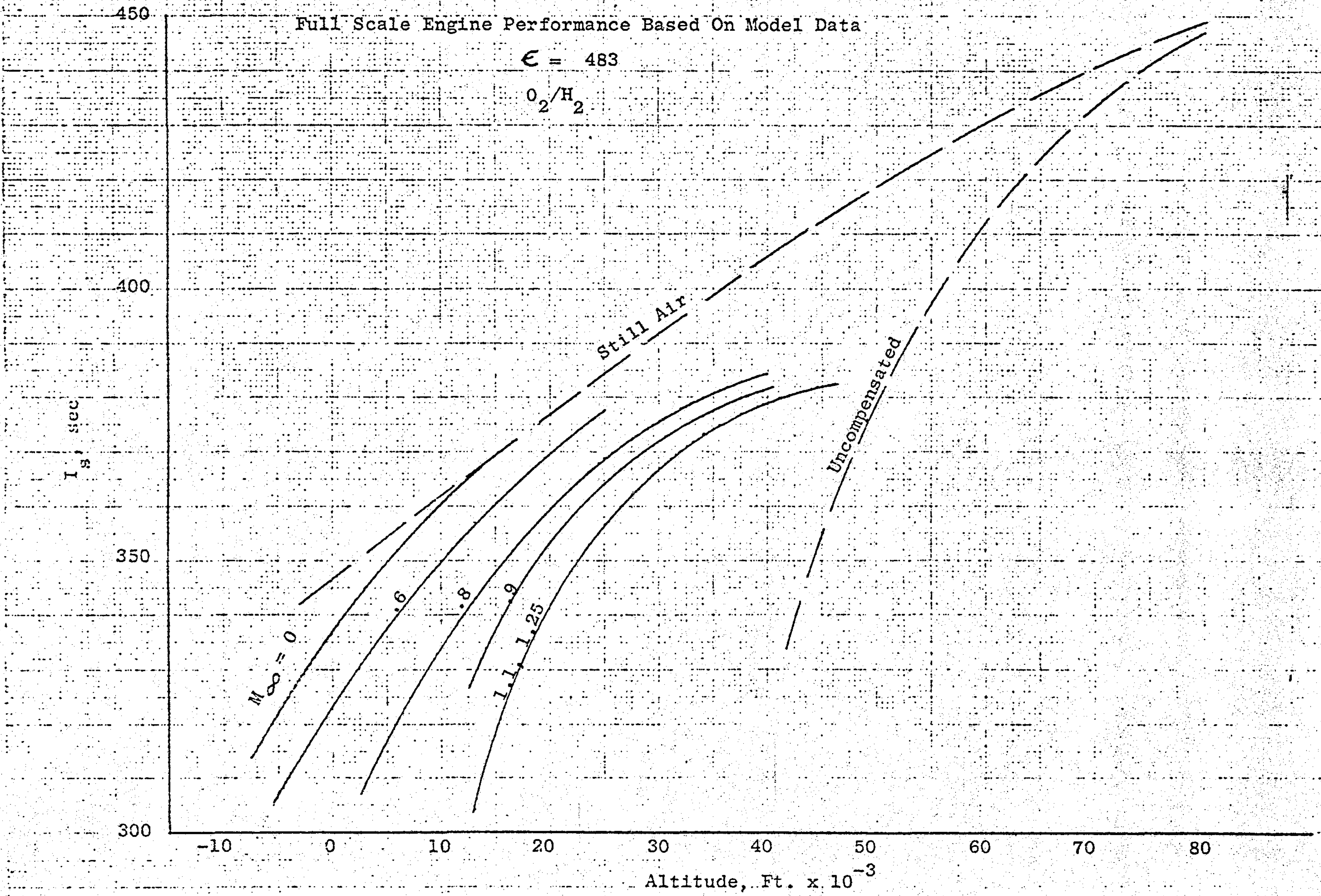
Full Scale Engine Performance Based On Model Data
ϵ = 483
O_2/H_2
I_s, sec
450
400
350
300
-10
0
10
20
30
40
50
60
70
80
Altitude, Ft. x 10^{-3}
Still Air
Uncompensated
$M_\infty = 0$
.6
.8
.9
1.1, 1.25

Figure 30

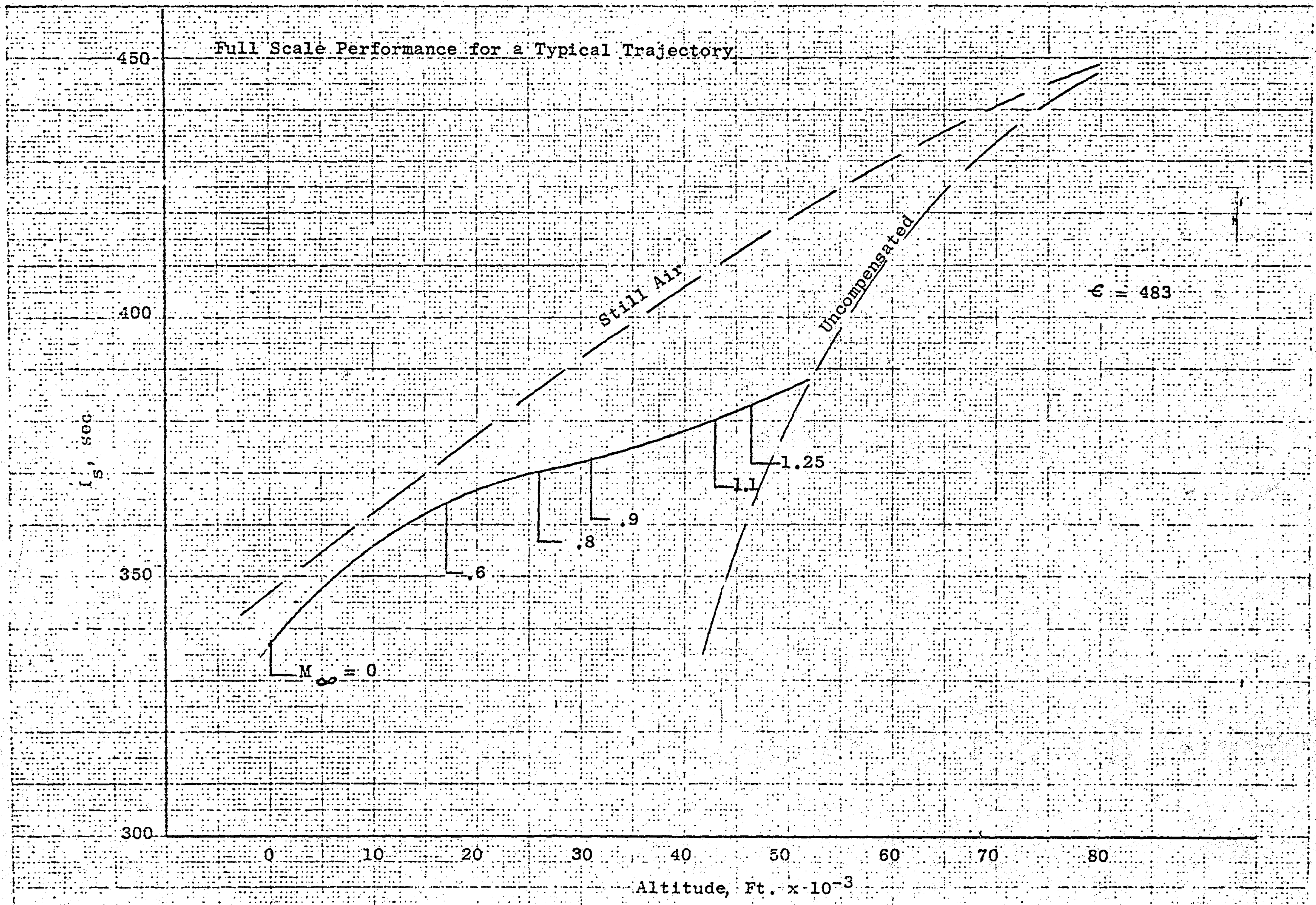
Full Scale Performance for a Typical Trajectory
450
400
350
300
I_s, sec
Still Air
Uncompensated
ε = 483
M∞ = 0
.6
.8
.9
1.1
1.25
0
10
20
30
40
50
60
70
80
Altitude, Ft. x 10^-3

Figure 31

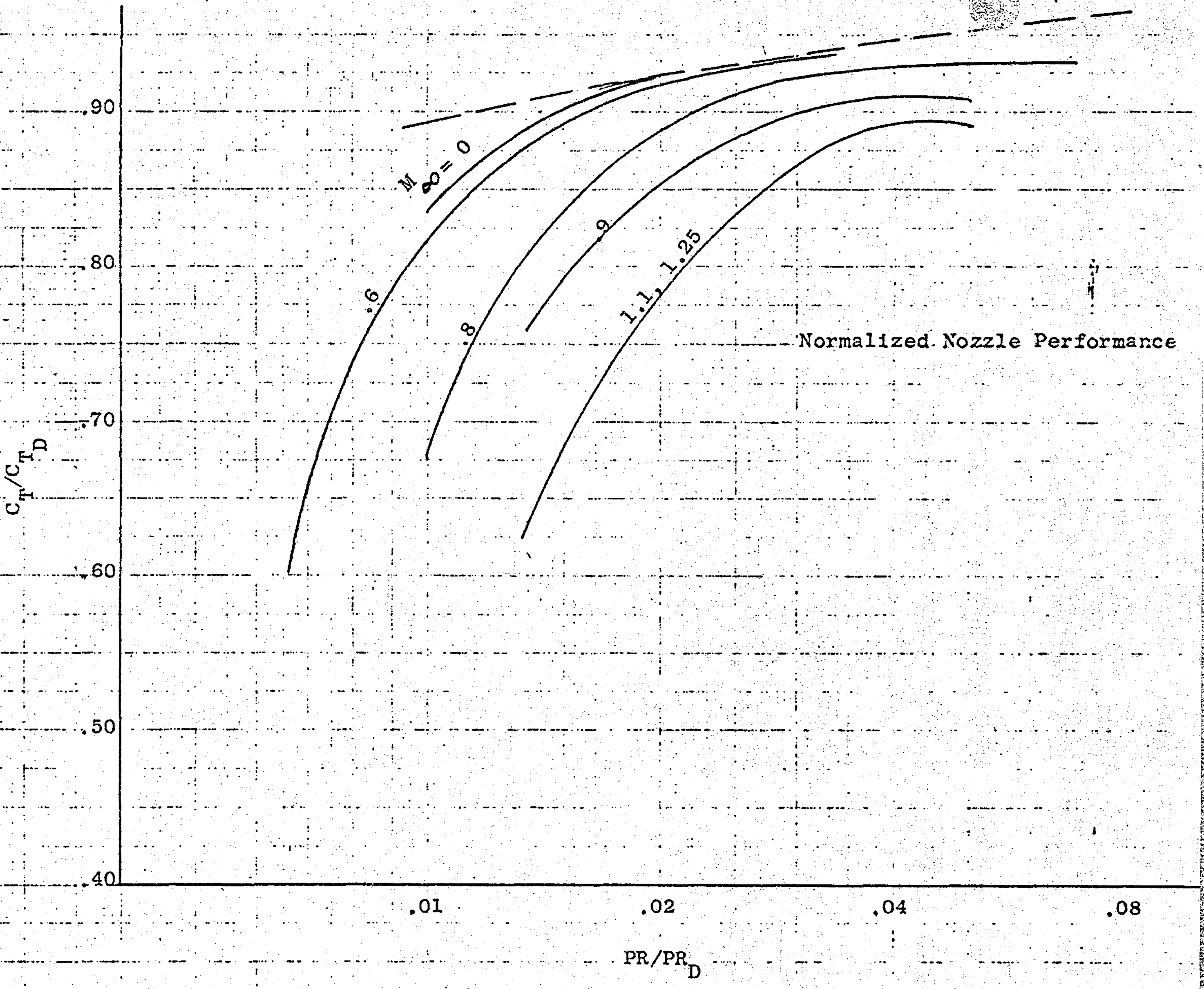

Normalized Nozzle Performance

Figure 32

REFERENCES

1. AEDC 1T SERV Model Data, dated 9-1-70, Released by Chrysler Corp., Space Division, 9-4-70.
2. A Plan for Jet Simulation Testing of Strut Mounted 2-1/2% Scale Model of the SERV Launch Vehicle, Chrysler Corp., Space Division.
3. ASR 70-325, Preliminary SERV Engine Performance Review, 31 August 1970, Rocketdyne a Division of North American Rockwell.
4. R-6273, Interim Report, Aerodynamic Nozzle Study, Vol. III - Slipstream Studies (NAS 8-2654), July 31, 1965, Rocketdyne a Division or North American Rockwell.
5. AFRPL-TR-67-246-Vol II, Final Report, Advanced Aerodynamic Spike Configurations, Vol II - Hot Firing and Performance in Slipstream Investigations, September 1967, Rocketdyne a Division or North American Rockwell.

ADDENDUM TO ROCKETDYNE REPORT ASR-71-67

Page 50.

The lower area ratio of the model resulted in the test geometry being slightly different from the design configuration. This was due mainly to manufacturing tolerances.

Page 52.

In earlier slipstream model tests it was found that nozzle efficiencies, C_T, at different slipstream Mach numbers mapped into a single curve when plotted against Pc/PBV. These tests were run using models with much lower expansion area ratios, tested at much higher fractions of design pressure ratios than was used for the SERV model. Fig A shows the ratio of engine base pressures to vehicle cowl pressures for SERV. At the low fractions of design pressure ratios tested, the slipstream affected the engine base pressure downstream of the region of influence of PBV. The correlation to PBV cannot be made in the SERV case.

Fig. B summarizes the model base pressures measured during the slipstream test program normalized by the pressure on the engine base in slipstream with the engine off. For flight Mach numbers of .8 or above, the interaction of the engine exhaust with the vehicle slipstream produced a low PBV value which in turn produced a low value of PBE compared to the pressure on the same region with engine off. The increase in engine base pressure with the addition of base bleed, ω_s, is shown.

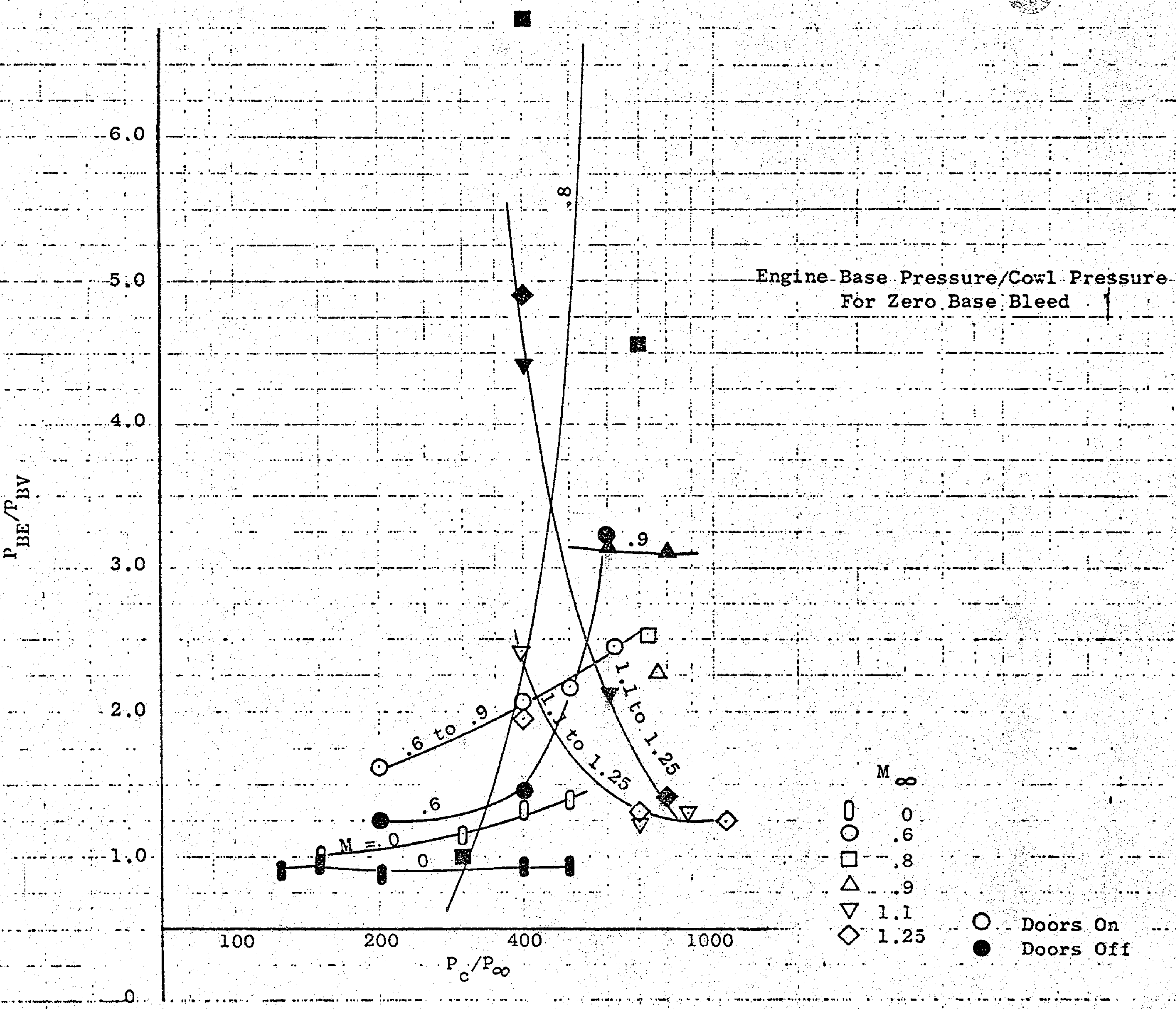
Engine Base Pressure/Cowl Pressure
For Zero Base Bleed
P_{BE}/P_{BV}
6.0
5.0
4.0
3.0
2.0
1.0
0
100
200
400
1000
P_c/P_∞
.8
.9
.6 to .9
1.1 to 1.25
1.1 to 1.25
.6
M = 0
0
M_∞
0
.6
.8
.9
1.1
1.25
○ Doors On
● Doors Off

FIGURE A

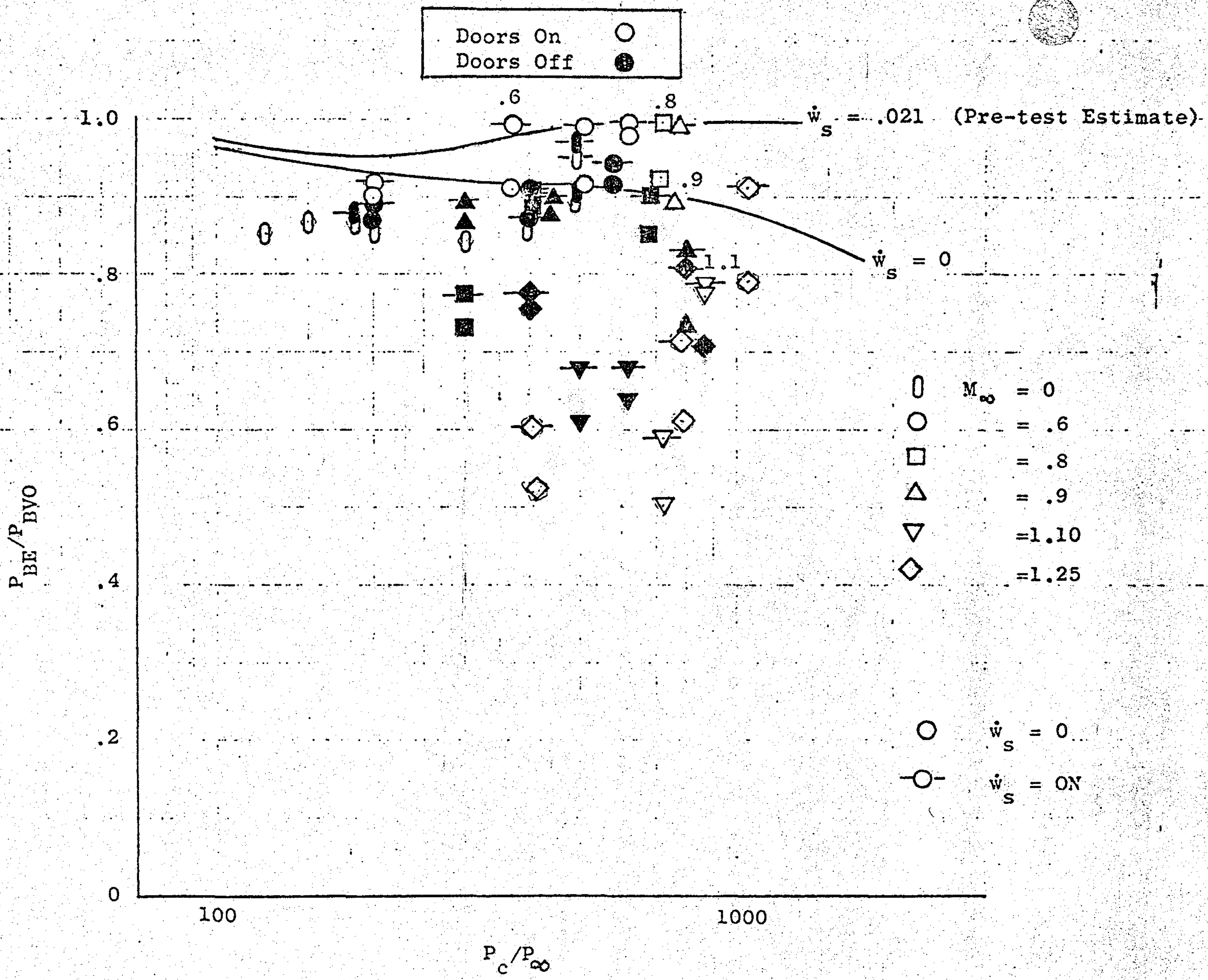

Measured Engine Base Pressure/Pressure at Engine Base with Engine Off
From Model Slipstream Tests

FIGURE B

APPENDIX A

BASE PRESSURE THEORY

Rocketdyne became interested in the base flow problem because of the necessity of calculating the base pressure to complete the thrust calculations for the aerospike nozzle. In this nozzle, high-pressure gas is exhausted from an annular-type combustion chamber with low-pressure turbine exhaust gas introduced through a base region (Fig. A-1). Part of the thrust contribution normally attributed to a full-length nozzle is obtained by the pressure of the secondary gases acting over the base region and, therefore, calculation of base pressure is an important part of overall performance evaluation. Because the centerbody is truncated, the primary flow separates from the end of the nozzle and encloses a near-wake region aft of the base. The turbine exhaust gas bled into the base region tends to keep the recirculating hot gases off of the base surface. In addition, the introduction of base bleed gives rise to higher base pressures.

For the purpose of analysis, the base pressure problem was conveniently divided into two regimes: zero- and small-bleed, and large-bleed. In the former regime, the near wake is characterized by a recirculating flow pattern, whereas, in the latter regime, the bleed rate is sufficient to suppress the reverse-flow component. It has been found that the inner free jet boundary has the general shape shown in Fig. A-1 . This shape differs from the usual free jet boundary shape for flow over cylinders because the expansion waves from the flow expanding at the outer lip intersect the inner jet boundary and cause it to be concave upward. Because of this inner jet boundary shape, it was found that, for the "large-bleed" regime, the flow through the central core was much like the flow through a converging-diverging nozzle with choking occurring at minimum area. In the case of flow over a cylinder, this type of flow configuration will not exist because the constant pressure free jet boundary tends to curve into the axis of symmetry, so that a minimum area cannot occur. Therefore, only the small-bleed theory will be applicable for flow over cylinders.

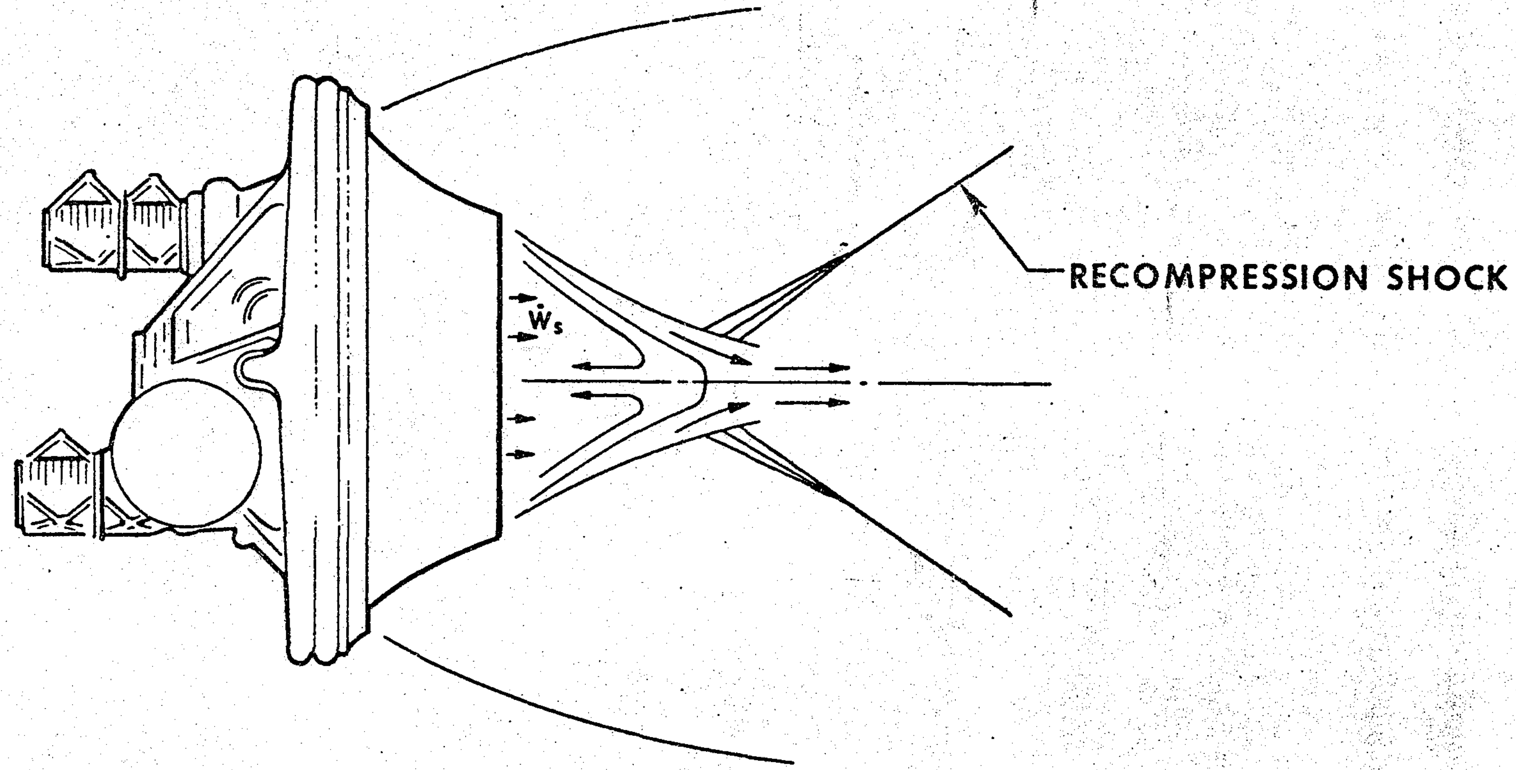

Figure A-1. Flow Field of the Aerospike Nozzle

It should be mentioned that the terms small-bleed and large-bleed were introduced to define the flow configurations for the case in which recirculation is present and the case in which recirculation does not occur. Therefore, the small-bleed theory might actually be used on flow fields in which substantial amounts of base bleed are introduced. The details of this theory are presented below.

KORST TWO-DIMENSIONAL MODEL

For the zero- and small-bleed case, the Korst two-dimensional model (Ref. A-1) has been taken as a starting point. In its original form, this model considers a supersonic primary flow field expanding isentropically into a lower pressure base region (Fig. A-2). The thickness of the boundary layer before separation is assumed to be negligible. Most of this flow field is inviscid, but there exists a turbulent shear layer in which mixing occurs between the primary flow and the recirculating fluid near the base. The width of this mixing zone is proportional to its length. Two important streamlines in the shear layer are defined by continuity. The jet boundary streamline originates at the point of flow separation, and divides primary flow from base flow. The discriminating streamline separates the fluid which passes through the wake from that which recirculates back to the base. Any bleed introduced into the base region is bounded by these two streamlines. With no bleed, the two are identical.

The static pressure is assumed to be constant from the initial expansion until the recompression region is reached. At that point, the inviscid flow, which has been converging toward the axis of symmetry, is turned parallel to the axis with an accompanying pressure rise. This pressure gradient is imposed on the turbulent shear layer, causing deceleration and, for the slower elements, a reversal of flow back into the base region. The discriminating streamline stagnates in the adverse pressure gradient. All higher velocity elements penetrate the recompression region and escape into the far wake; all those possessing lower velocity are turned back.

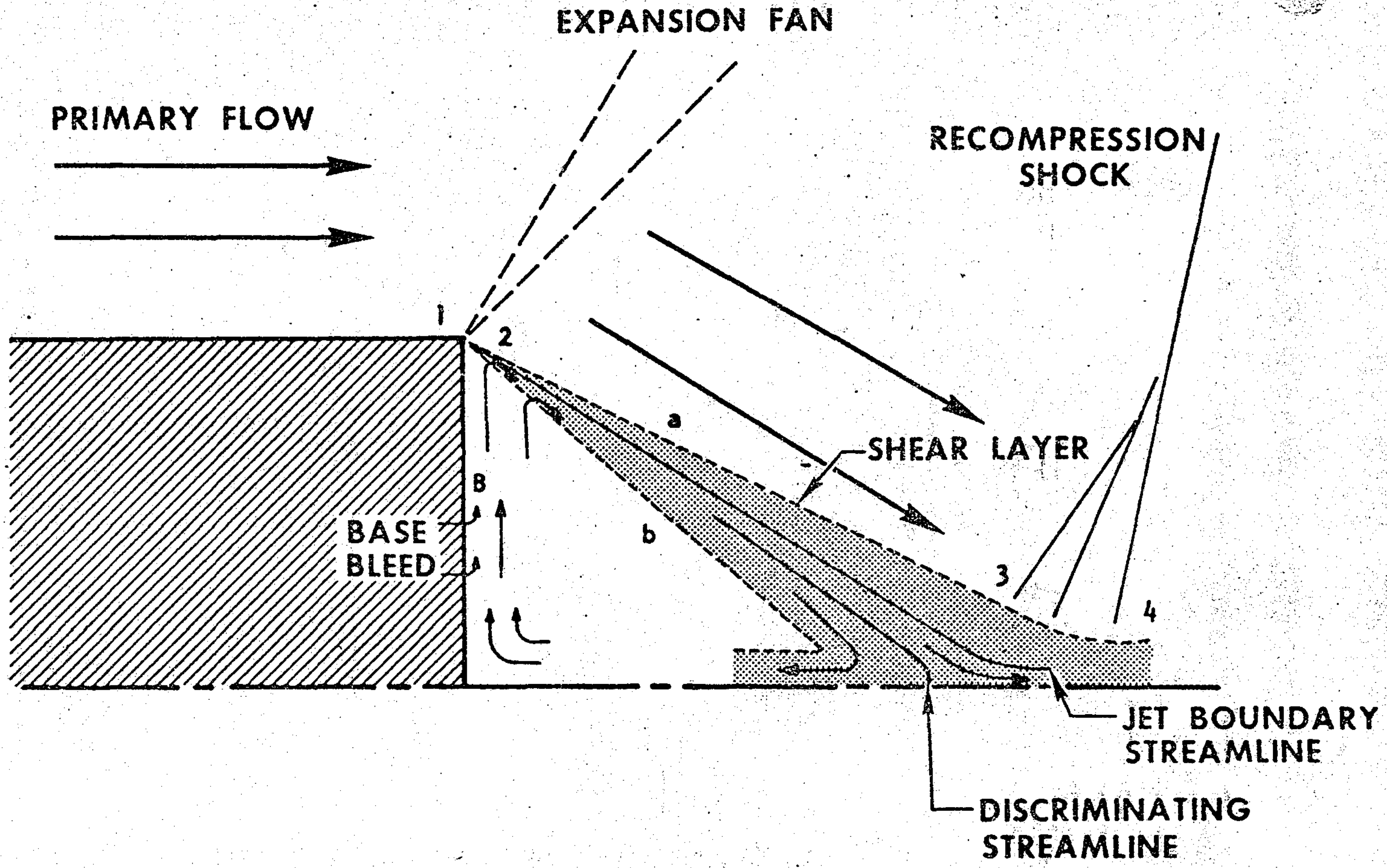

Figure A-2. Korst Base-Flow Model

On the basis of simplified shear layer flow equations, Korst arrived at an error-function similarity velocity profile, in terms of a dimensionless length coordinate, η, and a dimensionless velocity, φ, normalized with respect to the velocity along the corresponding inviscid jet boundary.**

$$\varphi = \frac{1}{2}(1 + \text{erf}\ \eta) \qquad \text{(A-1)}$$

where

$$\varphi = \frac{u}{u_{2a}} \qquad \text{(A-2)}$$

and

$$\eta = \frac{\sigma y}{x} \qquad \text{(A-3)}$$

The turbulent spreading parameter, σ, is a measure of the linear rate of growth of the shear layer with length. The values for σ suggested by Channapragada (Ref. A-2) have been used in the present analysis.

This velocity profile is superimposed on the corresponding inviscid jet boundary (that boundary which would exist in the absence of a viscous shear layer, Fig. A-3). An intrinsic coordinate system (x, y) is set up within the shear layer. The x-axis originates at the point of inception of the shear layer and coincides with the midpoint of the velocity profile ($\varphi = 0.5$). To fix the location of the velocity profile in space, a reference coordinate system (X, Y) is defined in which the X-axis is coincident with the corresponding inviscid jet boundary. The displacement, y_m, between the X-axes of the intrinsic and reference coordinate systems is determined by a momentum balance between the point of separation and the downstream location of the velocity profile. If the slight angle between the X-axes is ignored in computing the abscissa then the relationship between the two coordinate systems is given by:

$$X = \simeq x \qquad \text{(A-4)}$$

$$Y = y - y_m \qquad \text{(A-5)}$$

**Refer to Fig. A-2 for subscript notations

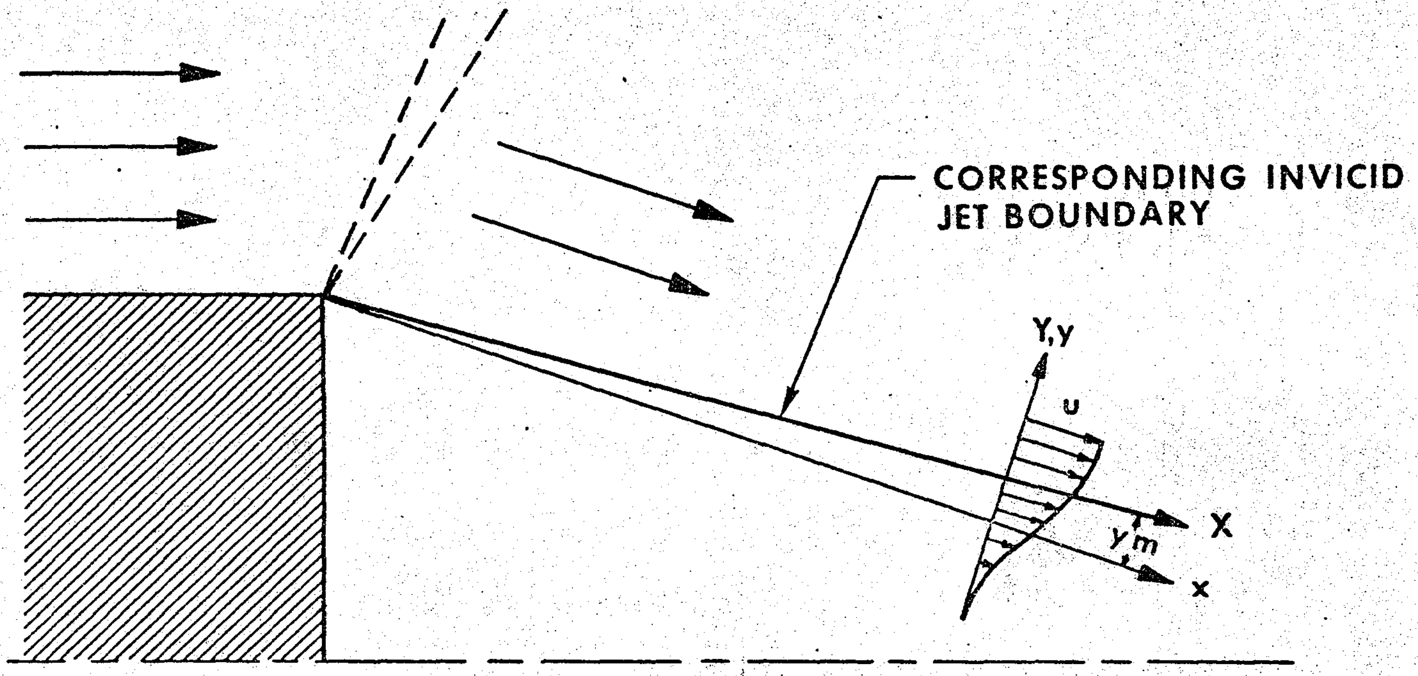

Figure A-3. Orientation of Shear Layer Velocity Profile

APPLICATION TO AXISYMMETRIC GEOMETRY

For application of the Korst flow model to axisymmetric geometry, consideration must be given to the distortion in shape of the annular stream tubes as they approach the axis. In the absence of longitudinal density and velocity gradients, the cross-sectional area of an annular stream tube would be constant. Therefore, as the mean radius of the shear layer decreased, the width of the individual stream tubes would increase, and there would be an accompanying distortion of the overall velocity profile.

In Fig. A-4, a hypothetical step-function profile is used to illustrate the effect. At location A-A, each stream tube of the profile has the same annular flow area. At section B-B, the areas are unchanged, but it can be seen that the total radial width of the profile, as well as the relative widths of the two stream tubes, are quite different.

In the present method, it is assumed that the normal shear layer spreading rate observed in two-dimensional flow and the radial distortion effect are additive. That is, if axisymmetric effects were reduced by moving the actual shear layer out to a position of large constant radius, the velocity profile and geometric dimensions would approach those of a two-dimensional configuration. To quantify this concept, a hypothetical shear layer is considered, having the same origin as the actual shear layer, and characterized by the same spreading parameter (Fig. A-5). The jet boundary streamline, which originates at the separation point, remains at a distance R_o from the axis. It is assumed that the thickness of the shear layer is sufficiently small compared to R_o so that the two-dimensional error-function profile is applicable. Under the foregoing assumptions, the mass flow between any two streamlines in the hypothetical shear layer is equal to the corresponding flow in the actual shear layer. In addition, the radial position of any streamline in the actual shear layer, as a function of x, can be determined from its position in the hypothetical shear layer by use of the fact that stream-tube flow areas are equal.

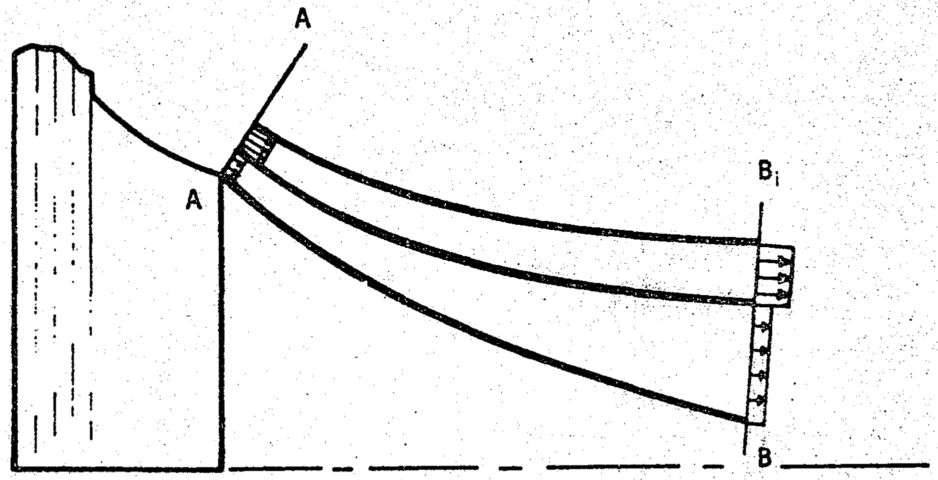

Figure A-4. Distortion of Axisymmetric Profile

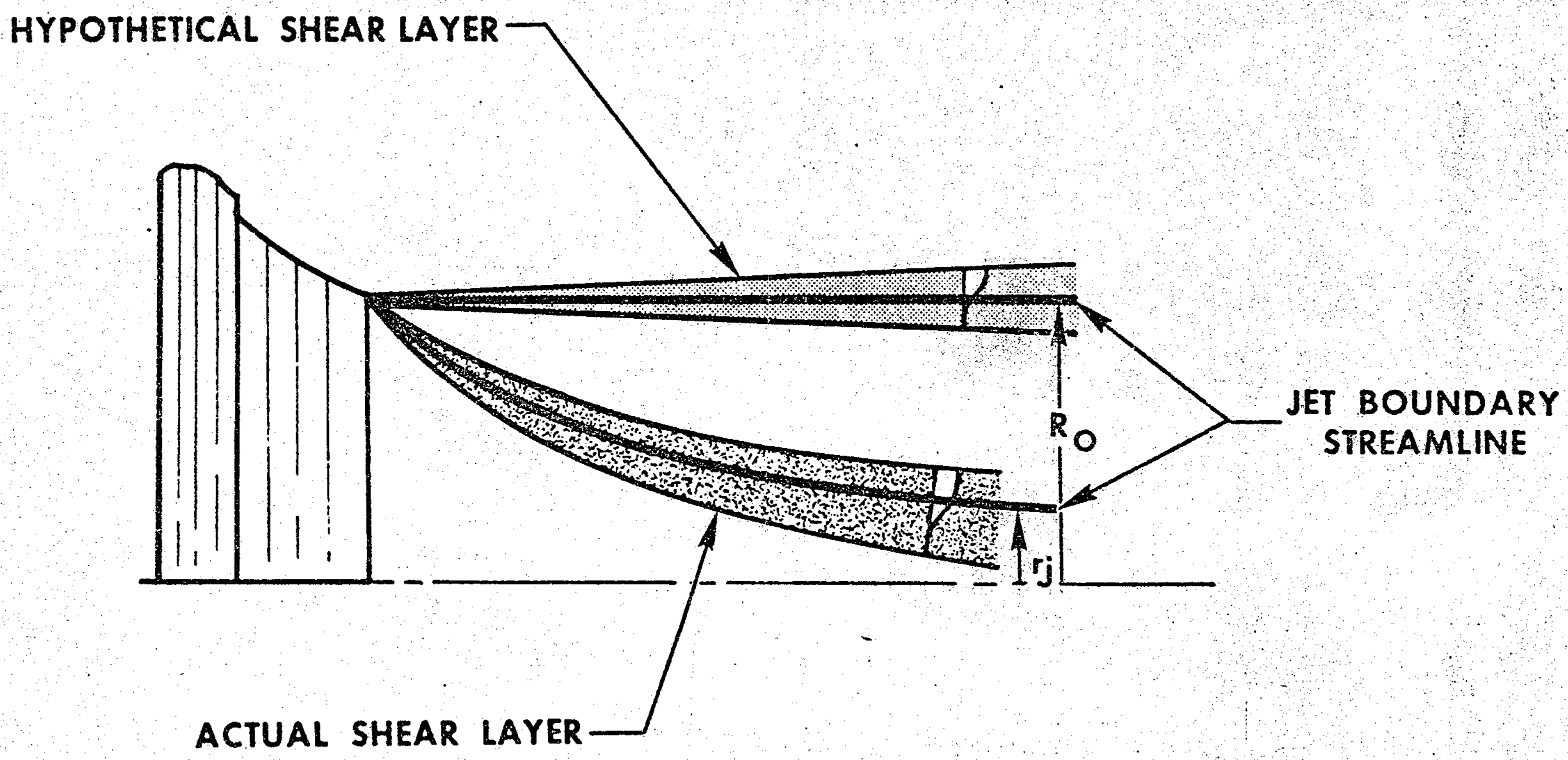

Figure A-5. Hypothetical Shear Layer Concept

The hypothetical shear layer concept, combined with the two-dimensional Korst model leads to the following relationships in the viscous region, assuming a negligible boundary layer on the solid surface at the separation corner. A momentum balance between the point of flow separation and some point downstream in the hypothetical shear layer (Fig. A-6) is given by:

$$2\pi \int_{0}^{\bar{Y}_R^*} \rho_{2a} \, u_{2a}^2 \, \bar{r}^* \, d\bar{Y}^* \Bigg|_{\bar{x}^* = 0} = 2\pi \int_{-\infty}^{\bar{Y}_R^*} \rho \, u^2 \bar{r}^* d\bar{Y}^* \Bigg|_{\bar{x}^* = \bar{x}^*} \qquad \text{(A-6)}$$

where $\bar{Y}_R^*$ represents an asymptotic streamline that is essentially in the inviscid flow field having velocity $u = u_{2a}$ and density $\rho = \rho_{2a}$. The bar over the quantities indicates no initial boundary layer, and the starred quantities refer to the hypothetical shear layer.

By use of Eq. A-5, and the following information: at $\bar{x}^* = 0$, $\bar{r}^* = R_o + \bar{Y}^*$ and at $\bar{x}^* = \bar{x}^*$, $\bar{r}^* = R_o - \bar{y}_j^* + \bar{y}^*$, Eq. A-6 can be transformed to:

$$\int_{0}^{\bar{Y}_r^*} \rho_{2a} \, u_{2a}^2 \, (R_o + \bar{Y}^*) \, d\bar{Y}^* = \int_{-\infty}^{\bar{Y}_R^* + \bar{y}_m^*} \rho \, u^2 \, (R_o - \bar{y}_j^* + \bar{y}^*) \, d\bar{y}^* \qquad \text{(A-7)}$$

Multiplication of both sides by $\dfrac{\sigma^2}{\bar{x}^{*2} \, \rho_{2a}^2 \, u_{2a}^2}$ yields:

$$\int_{0}^{\frac{\sigma \bar{Y}_R^*}{\bar{x}^*}} \left(\frac{\sigma R_o}{\bar{x}^*} + \frac{\sigma \bar{Y}^*}{\bar{x}^*} \right) d \left(\frac{\sigma \bar{Y}^*}{\bar{x}^*} \right)$$

$$= \int_{-\infty}^{\frac{\sigma \bar{Y}_R^*}{\bar{x}^*} + \frac{\sigma \bar{y}_m^*}{\bar{x}^*}} \frac{\rho}{\rho_{2a}} \left(\frac{u}{u_{2a}} \right)^2 \left(\frac{\sigma R_o}{\bar{x}^*} - \frac{\sigma \bar{y}_j^*}{\bar{x}^*} + \frac{\sigma \bar{y}^*}{\bar{x}^*} \right) d \left(\frac{\sigma \bar{y}^*}{\bar{x}^*} \right) \qquad \text{(A-8)}$$

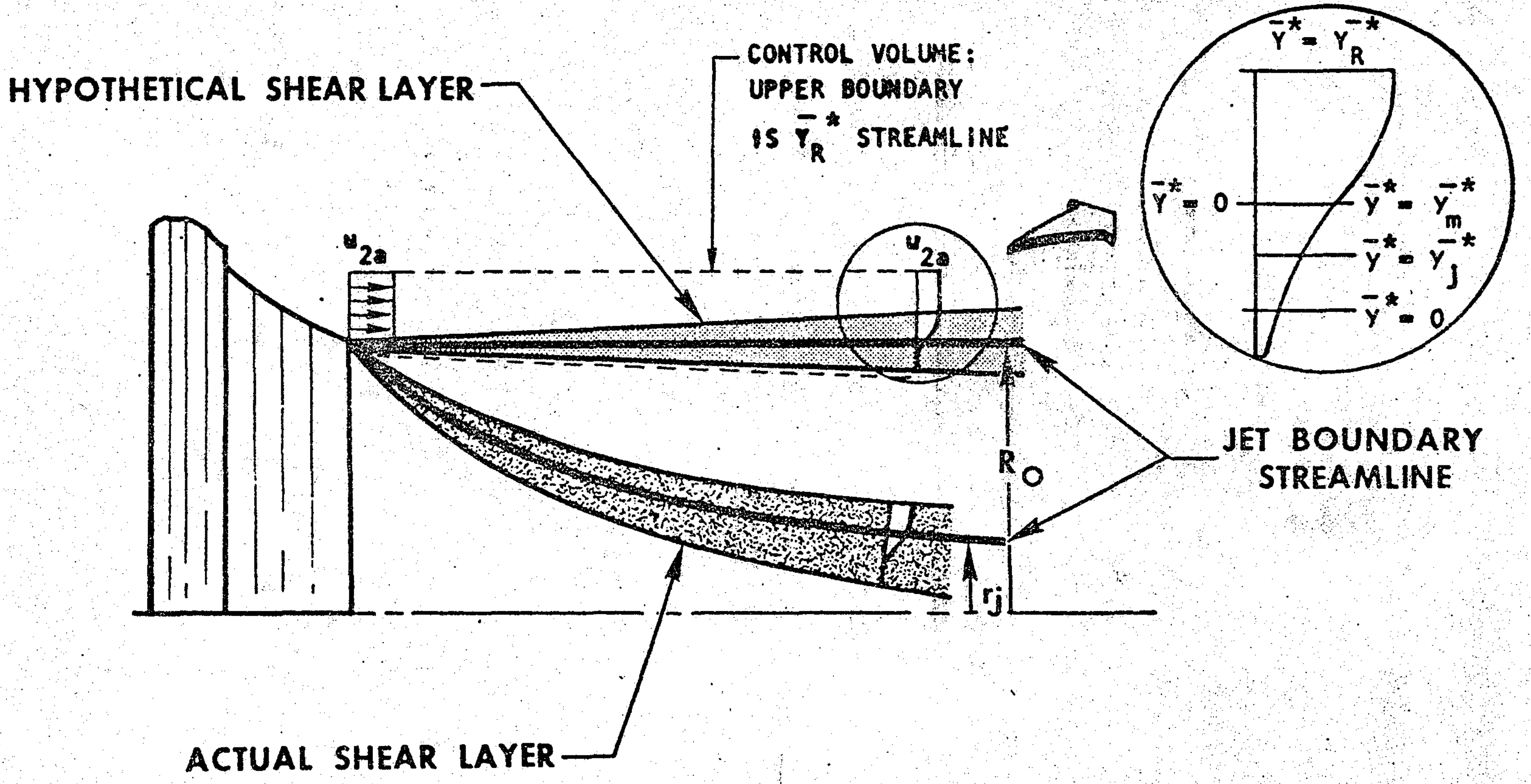

Figure A-6. Control Volume for Shear Layer Momentum Balance

For constant pressure and stagnation temperature:

$$\frac{\rho}{\rho_{2a}} = \frac{1 - C_{2a}{}^{2}}{1 - C_{2a}{}^{2}\left(\frac{u}{u_{2a}}\right)^{2}} \qquad \text{(A-9)}$$

where C_{2a} is the Crocco number of the free stream. Application of Eq. A-2, A-3, and A-9 to Eq. A-8 yields:

$$\int_{0}^{\bar{\eta}^{*}_{Y_R}} (\bar{\eta}^{*}_{R_o} + \bar{\eta}^{*}_{Y})\, d\,(\bar{\eta}^{*}_{Y}) = (1 - C_{2a}{}^{2}) \int_{-\infty}^{\bar{\eta}^{*}_{Y_R}} \frac{\varphi^{2}}{1 - C_{2a}{}^{2}\varphi^{2}} \left(\bar{\eta}^{*}_{R_o} - \bar{\eta}^{*}_{j} + \bar{\eta}^{*}\right) d\bar{\eta}^{*}$$

$$+ \int_{\bar{\eta}^{*}_{Y_R}}^{(\bar{\eta}^{*}_{Y_R} + \bar{\eta}^{*}_{m})} \left(\bar{\eta}^{*}_{R_o} - \bar{\eta}^{*}_{j} + \bar{\eta}^{*}\right) d\bar{\eta}^{*} \qquad \text{(A-10)}$$

where

$$\bar{\eta}^{*}_{Y} = \frac{\sigma\, \bar{Y}^{*}}{\bar{x}^{*}}$$

$$\bar{\eta}^{*}_{Y_R} = \frac{\sigma\, \bar{Y}^{*}_{R}}{\bar{x}^{*}}$$

$$\bar{\eta}^{*}_{R_o} = \frac{\sigma\, R_o}{\bar{x}^{*}}$$

and

$$\varphi \cong 1.00 \text{ for } \bar{\eta}^{*} \geq \bar{\eta}^{*}_{R}$$

Integration of Eq. A-10 leads to:

$$\bar{\eta}^*_{R_o}\,\bar{\eta}^*_{Y_R} + \frac{\bar{\eta}^{*2}_{Y_R}}{2} - \bar{\eta}^*_m\left(\bar{\eta}^*_{R_o} + \bar{\eta}^*_{Y_R} - \bar{\eta}^*_j\right) - \frac{\bar{\eta}^{*2}_m}{2}$$

$$= \left(1 - C_{2a}^{\,2}\right)\left[\left(\bar{\eta}^*_{R_o} - \bar{\eta}^*_j\right)\int_{-\infty}^{\bar{\eta}^*_{Y_R}} \frac{\varphi^2\, d\bar{\eta}^*}{1 - C_{2a}^{\,2}\varphi^2} + \int_{-\infty}^{\bar{\eta}^*_{Y_R}} \frac{\varphi^2\, \bar{\eta}^*\, d\bar{\eta}^*}{1 - C_{2a}^{\,2}\varphi^2}\right] \qquad \text{(A-11)}$$

Similarly, the continuity equation is written for the fluid above the jet boundary streamline:

$$2\pi \int_0^{\bar{Y}^*_R} \rho_{2a}\, u_{2a}\, \bar{r}^*\, d\bar{Y}^* \Bigg|_{\bar{x}^* = 0} = 2\pi \int_{\bar{Y}^*_j}^{\bar{Y}^*_R} \rho\, u\, \bar{r}^*\, d\bar{Y}^* \Bigg|_{\bar{x}^* = \bar{x}^*} \qquad \text{(A-12)}$$

Operations analogous to these used on the momentum equation give the following result:

$$\bar{\eta}^*_{R_o}\,\bar{\eta}^*_{Y_R} + \frac{\bar{\eta}^{*2}_{Y_R}}{2} - \bar{\eta}^*_m\left(\bar{\eta}^*_{R_o} + \bar{\eta}^*_{Y_R} - \bar{\eta}^*_j\right) - \frac{\bar{\eta}^{*2}_m}{2}$$

$$= \left(1 - C_{2a}^{\,2}\right)\left[\left(\bar{\eta}^*_{R_o} - \bar{\eta}^*_j\right)\int_{\bar{\eta}^*_j}^{\bar{\eta}^*_{Y_R}} \frac{\varphi}{1 - C_{2a}^{\,2}\varphi^2}\, d\bar{\eta}^* + \int_{\bar{\eta}^*_j}^{\bar{\eta}^*_{Y_R}} \frac{\varphi\, \bar{\eta}^*\, d\bar{\eta}^*}{1 - C_{2a}^{\,2}\varphi^2}\right] \qquad \text{(A-13)}$$

For convenience, the following shorthand notation is now introduced:

$$I_1 = (1 - C_{2a}^{\,2}) \int \frac{\varphi}{1 - C_{2a}^{\,2}\varphi^2}\, d\eta \qquad I_3 = (1 - C_{2a}^{\,2}) \int \frac{\varphi^2}{1 - C_{2a}^{\,2}\varphi^2}\, d\eta$$

$$I_2 = (1 - C_{2a}^{\,2}) \int \frac{\varphi\,\eta}{1 - C_{2a}^{\,2}\varphi^2}\, d\eta \qquad I_4 = (1 - C_{2a}^{\,2}) \int \frac{\varphi^2\eta}{1 - C_{2a}^{\,2}\varphi^2}\, d\eta$$

Equations A-11 and A-13 are combined to yield:

$$\bar{\eta}_j^* = \bar{\eta}_{R_o}^* + \bar{A} \tag{A-14}$$

where

$$\bar{A} = \frac{I_2 \Big|_{\bar{\eta}_j^*}^{\bar{\eta}_{Y_R}^*} - I_4 \Big|_{-\infty}^{\bar{\eta}_{Y_R}^*}}{I_1 \Big|_{\bar{\eta}_j^*}^{\bar{\eta}_{Y_R}^*} - I_3 \Big|_{-\infty}^{\bar{\eta}_{Y_R}^*}} \tag{A-15}$$

and

$$\bar{\eta}_m^* = \bar{B} + (\bar{B}^2 - \bar{C})^{1/2} \tag{A-16}$$

where

$$\bar{B} = \bar{\eta}_j^* - \bar{\eta}_{R_o}^* - \bar{\eta}_{Y_R}^* \tag{A-17}$$

$$\bar{C} = -\,6\,\bar{\eta}_{R_o}^* - 9 + 2\,(\bar{\eta}_{R_o}^* - \bar{\eta}_j^*)\; I_1 \Big|_{\bar{\eta}_j^*}^{\bar{\eta}_{Y_R}^*} + 2I_2 \Big|_{\bar{\eta}_j^*}^{\bar{\eta}_{Y_R}^*} \tag{A-18}$$

Equation A14 is solved by iteration and the resulting value of $\bar{\eta}_j^*$ is substituted into Eq. A-6 to determine $\bar{\eta}_m^*$. For computational purposes, $\bar{\eta}_{Y_R}^*$ is chosen to be 3.0 because little changes in the error function arise when $\eta < -3.0$ or $\eta > 3.0$.

Because the mass flow between any two streamlines in the actual shear layer is equal to the corresponding quantity in the hypothetical shear layer, calculations can be made by considering only the latter geometry. In general,

$$\dot{w} = \int_{\bar{y}_I^*}^{\bar{y}_{II}^*} 2\pi \bar{r}^* \rho u \, d\bar{y}^* = 2\pi \int_{\bar{y}_I^*}^{\bar{y}_{II}^*} \rho u \left(R_o - \bar{y}_j^* + \bar{y}^*\right) d\bar{y}^* \tag{A-19}$$

where $\bar{y}_I^*$ and $\bar{y}_{II}^*$ represent arbitrary streamlines.

Application of operations discussed previously yields:

$$\dot{w} = \frac{2\pi \rho_{2a} u_{2a} \bar{x}^{*2}}{\sigma^2} (1 - C_{2a}{}^2) \int_{\bar{\eta}_I^*}^{\bar{\eta}_{II}^*} \frac{\varphi}{1 - C_{2a}{}^2 \varphi^2} \left(\bar{\eta}_{R_o}^* - \bar{\eta}_j^* + \bar{\eta}^*\right) d\bar{\eta}' \tag{A-20}$$

or

$$\dot{w} = \frac{2\pi \rho_{2a} u_{2a} \bar{x}^* R_o}{\sigma} \left[\left(1 - \frac{\bar{\eta}_j^*}{\bar{\eta}_{R_o}^*}\right) I_1 \Bigg|_{\bar{\eta}_I^*}^{\bar{\eta}_{II}^*} + \frac{1}{\bar{\eta}_{R_o}^*} I_2 \Bigg|_{\bar{\eta}_I^*}^{\bar{\eta}_{II}^*} \right] \tag{A-21}$$

EFFECT OF THE INITIAL BOUNDARY LAYER

The effect of the initial boundary layer is accounted for by the method of Kirk (Ref. A-3). An equivalent shear layer is postualed so that its momentum thickness at the point of separation is equal to that of the initial boundary layer (Fig. A-7).

The momentum thickness of the two-dimensional shear layer is given by:

$$\theta = \frac{x}{\sigma} (1 - C_{2a}{}^2) \int_{-\infty}^{\infty} \frac{\varphi(1-\varphi)}{1 - C_{2a}{}^2 \varphi^2} d\eta \tag{A-22}$$

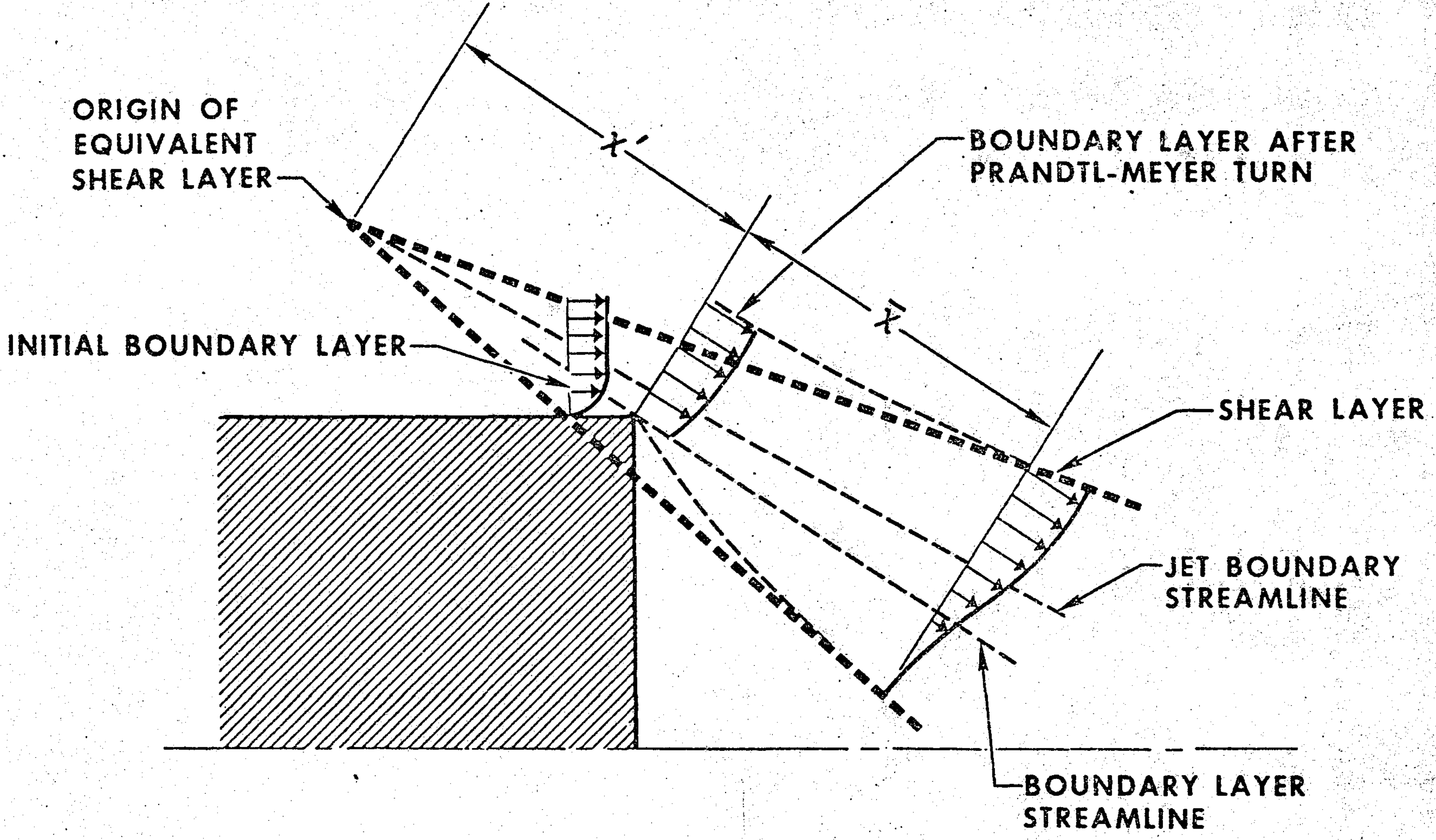

Figure A-7. The Equivalent Shear Layer Model of Kirk

Therefore, the length of the equivalent shear layer up to the point of separation is:

$$x' = \frac{\theta_2 \sigma}{(1-C_{2a}^{\,2})\displaystyle\int_{-\infty}^{\infty} \frac{\varphi\,(1-\varphi)}{1-C_{2a}^{\,2}\varphi^2}\, d\eta} = \frac{\theta_1 \sigma}{I_1\Big|_{-\infty}^{\infty} - I_3\Big|_{-\infty}^{\infty}} \qquad \text{(A-23)}$$

where θ_2 is the momentum thickness of the initial boundary layer at the point of separation after expansion to the base pressure, $P_B = P_2$. The change in boundary layer momentum thickness caused by expansion from P_1 to P_2 is given by (Ref. A-4)

$$\theta_2 = \theta_1 \left\{ \frac{ \dfrac{M_{1a}\left[1 + \frac{\gamma-1}{2} M_{2a}^{\,2}\right]^{\frac{\gamma+1}{2(\gamma-1)}}}{M_{2a}\left[1 + \frac{\gamma-1}{2} M_{1a}^{\,2}\right]^{\frac{\gamma+1}{2(\gamma-1)}}} \left[\displaystyle\int_0^1 \frac{\varphi^n d\varphi}{1-C_{1a}^{\,2}\varphi^2} - \int_0^1 \frac{\left[KC_{1a}^{\,2}\,\varphi^2 - (K-1)\right]^{1/2} \varphi^n d\,\varphi}{\left[KC_{1a}^{\,2} - (K-1)\right]^{1/2} (1-C_{1a}^{\,2}\,\varphi^2)} \right] }{ \displaystyle\int_0^1 \frac{(1-\varphi)\,\varphi^n d\varphi}{(1-C_{1a}^{\,2}\varphi^2)} } \right. \qquad \text{(A-24)}$$

where

$$K = \left[\frac{(P_2/P_o)}{(P_1/P_o)}\right]^{\frac{\gamma-1}{\gamma}}$$

P_o = the stagnation pressure of the flow and n is the exponent in the power-law boundary layer velocity profile (chosen as n = 7 for turbulent flow), i.e.,

$$\frac{y_1}{\delta_1} = \varphi_1^n$$

Therefore, the total length of the equivalent shear layer is:

$$x^* = x' + \bar{x} \tag{A-25}$$

where $\bar{x}$ is the length of the free jet boundary for no initial boundary layer.

From the two-dimensional shear layer relationships (Ref. A-1):

$$I_1 \Big|_{-\infty}^{\eta_j} = I_1 \Big|_{-\infty}^{\infty} - I_3 \Big|_{-\infty}^{\infty} \tag{A-26}$$

Substitution of Eq. A-26 into Eq. A-23 yields:

$$I_1 \Big|_{-\infty}^{\eta_j} = \frac{\theta_1 \sigma}{x'} \tag{A-27}$$

In a two-dimensional shear layer, the mass flow per unit width between streamlines is given by:

$$\dot{w} = \frac{\rho_{2a}\, u_{2a}\, x}{\sigma}\, I_1 \Big|_{\eta_I}^{\eta_{II}} \tag{A-28}$$

Therefore, the mass flow per unit width below the jet boundary streamline of the equivalent shear layer at $\bar{x} = 0$ (point of actual flow separation) is given by:

$$\dot{w} = \frac{\rho_{2a}\, u_{2a}\, x'}{\sigma}\, I_1 \Big|_{-\infty}^{\eta_j} = \rho_{2a}\, u_{2a}\, \theta_2 \tag{A-29}$$

Because there is no flow across streamlines, that amount of mass flow will remain between the jet boundary streamline of the equivalent shear layer (η_j) and the streamline originating at the point of actual flow separation ($\bar{\eta}_j$) for all valves of x. That is,

$$I_1 \Big|_{\eta_B}^{\eta_j} = \frac{\theta_2 \sigma}{x} \tag{A-30}$$

where η_B in the equivalent shear layer corresponds to $\bar{\eta}_j$ in the shear layer which originates at separation.

In the present approach, the foregoing concepts are applied to the hypothetical shear layer. At the point of flow separation ($r = R_o$), the momentum thickness, θ_2, is small compared to R_o, and the two-dimensional Eq. A-22 through A-25 can be applied.

COMBINED SHEAR LAYER MODEL

The effect of combining the hypothetical shear layer ($\bar{y}_j^*$ at constant R_o) with the equivalent shear layer concept is to displace the jet boundary streamline (y_j^*) in the hypothetical equivalent shear layer above the streamline originating at the corner (Fig. A-8) by:

$$y_j^* - y_B^* = \frac{x^*}{\sigma} \left(\eta_j^* - \eta_B^* \right) \tag{A-31}$$

Therefore,

$$r^* = R_o - y_B^* + y^* \tag{A-32}$$

The area relationships discussed previously, between the hypothetical equivalent shear layer and the shear layer following the corresponding inviscid jet boundary are preserved. The analog to Eq. A-21 for the mass flow between any two streamlines is given by:

$$\dot{w} = \frac{2\pi \rho_{2a} u_{2a} x^* R_o}{\sigma} \left[\left(1 - \frac{\eta_B^*}{\eta_{R_o}^*} \right) I_1 \Big|_{\eta_I^*}^{\eta_{II}^*} + \frac{1}{\eta_{R_o}^*} I_2 \Big|_{\eta_I^*}^{\eta_{II}^*} \right] \tag{A-33}$$

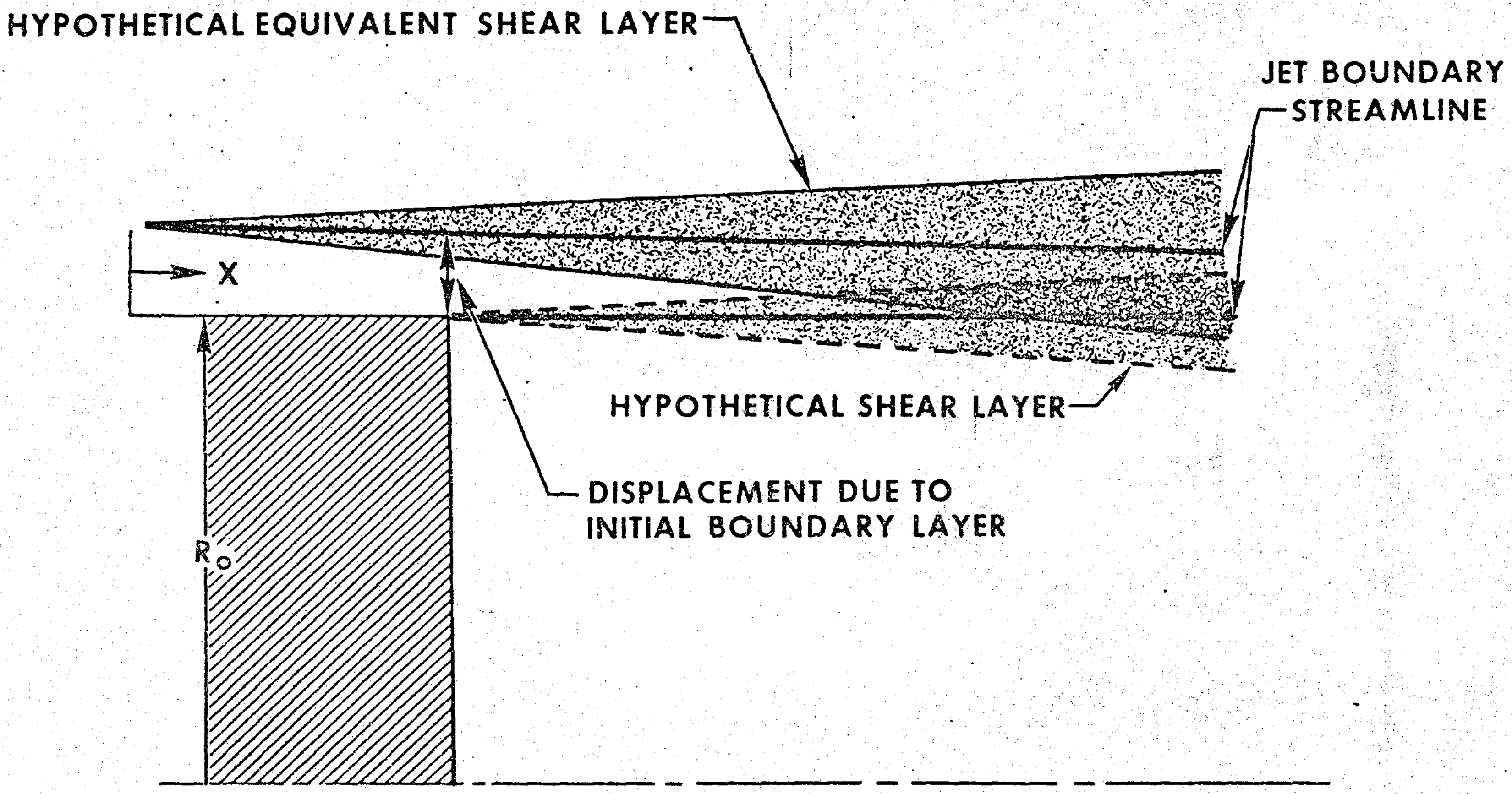

Figure A-8. Hypothetical Equivalent Shear Layer

In particular, the axisymmetric form of Eq. A-30 is:

$$\left(1 - \frac{\eta_B^*}{\eta_{R_o}^*}\right) I_1 \Bigg|_{\eta_B^*}^{\eta_j^*} + \frac{1}{\eta_{R_o}^*} I_2 \Bigg|_{\eta_B^*}^{\eta_j^*} = \frac{\theta_2 \sigma}{x^*} \qquad \text{(A-34)}$$

In practice, $\bar{\eta}_j^*$ and $\bar{\eta}_m^*$ for the hypothetical shear layer are calculated using Eq. A-14 and A-16, and these values are assigned to the corresponding quantities (η_j^* and η_m^*) of the hypothetical equivalent shear layer. As long as the upward translation of the shear layer, as given by Eq. A-31, is small compared to R_o, this approximation is valid.

RECOMPRESSION MODEL

To close the base pressure solution, the identity of the discriminating streamline must be determined by energy relationships in the recompression region. In the two-dimensional model, Korst postulated that the energy on the discriminating streamline, in terms of the ratio of stagnation pressure to static pressure, is equal to the pressure rise associated with the turning of the inviscid flow behind the near wake (Fig. A-2). The axisymmetric case presents unique problems, however, because the flow angle along the corresponding inviscid jet boundary is constantly changing as a function of X. Therefore, considerable emphasis has been placed on defining the flow geometry in the aft portion of the near wake to determine the value of X at which recompression effectively occurs.

As the inviscid flow, with the superimposed shear layer, approaches the axis, a point will be reached at which the forward-moving velocity profile intersects the reverse flow (Fig. A-9). Because of spatial considerations, the inviscid flow must subsequently turn, causing an associated pressure rise (recompression). This adverse pressure gradient is imposed on the viscous flow, causing the less energetic elements to reverse direction progressively and join the recirculating stream. Because there is only a small pressure rise associated with the flow reversal of the low-velocity "tail" of the error-function profile, recompression is not

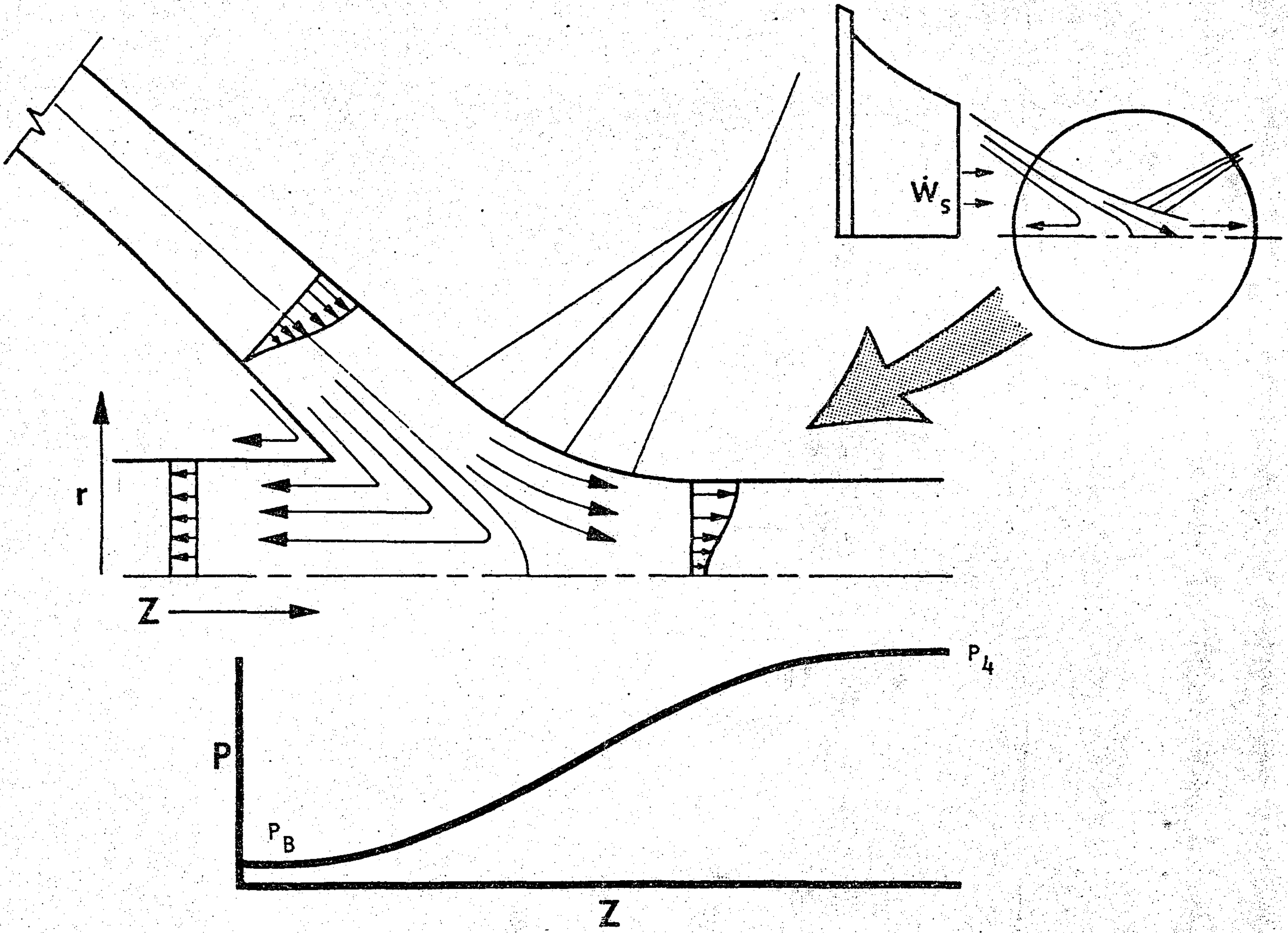

Figure A-9. Recompression

considered to begin until the lower portion of the profile has been turned back and the slope of the static pressure curve becomes more discernible (Fig. A-9). At that point, part of the remaining profile also will have been distorted by viscous forces. As an approximation, it is assumed that the upper portion retains its error-function form, but that the lower portion assumes the shape of the tangent to the original profile at its midpoint or point of inflection (Fig. A-10). The resulting point of zero velocity is now located at a correspondingly higher value of the dimensionless coordinate, η (i.e., $\eta = -\sqrt{\pi/2}$). The reverse-flow portion of the profile contains a mass flowrate equal to that below the discriminating streamline in the forward-moving portion. During the flow reversal process, some mixing will occur in the recirculating stream. The simplifying assumption is made that the mixing is complete, resulting in uniform velocity and density.

CALCULATIONS IN THE RECOMPRESSION ZONE

Based on the foregoing assumptions, the point on the free jet boundary at which recompression begins can be determined. It corresponds to the unique point at which the outer radius of the recirculating stream (r_s) is equal to the inner radius of the forward-moving profile (r_{-R}), radius of the forward-moving profile (r_{-R}), as shown in Fig. A-11.

For the recirculating stream, the assumption of constant-pressure flow uniformization along the axis yields the following equations (Fig. A-12):

Conservation of Mass

$$\frac{2\pi \rho_{2a} u_{2a} x^* R_o}{\sigma} \left[\left(1 - \frac{\eta_B^*}{\eta_{R_o}^*}\right) I_1' \Bigg|_{-\sqrt{\frac{\pi}{2}}}^{\eta_d^*} + \frac{1}{\eta_{R_o}^*} I_2' \Bigg|_{-\sqrt{\frac{\pi}{2}}}^{\eta_d^*} \right] = \rho_{3b} u_{3b} \pi r_s^2 \qquad \text{(A-35)}$$

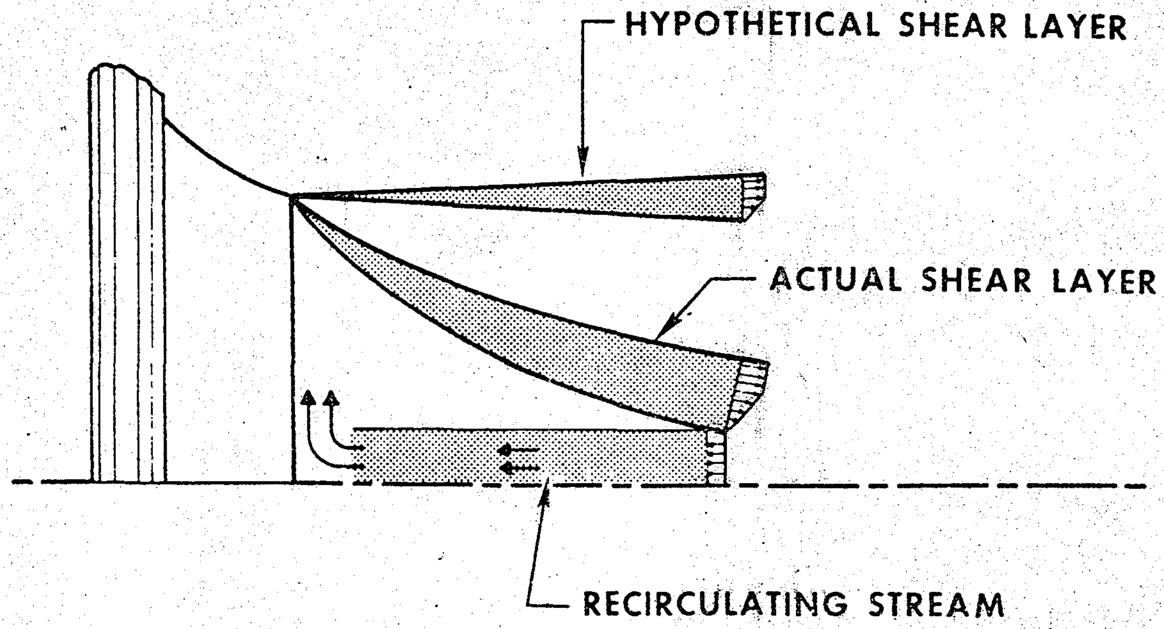

Figure A-11.Location of the Start of Recompression

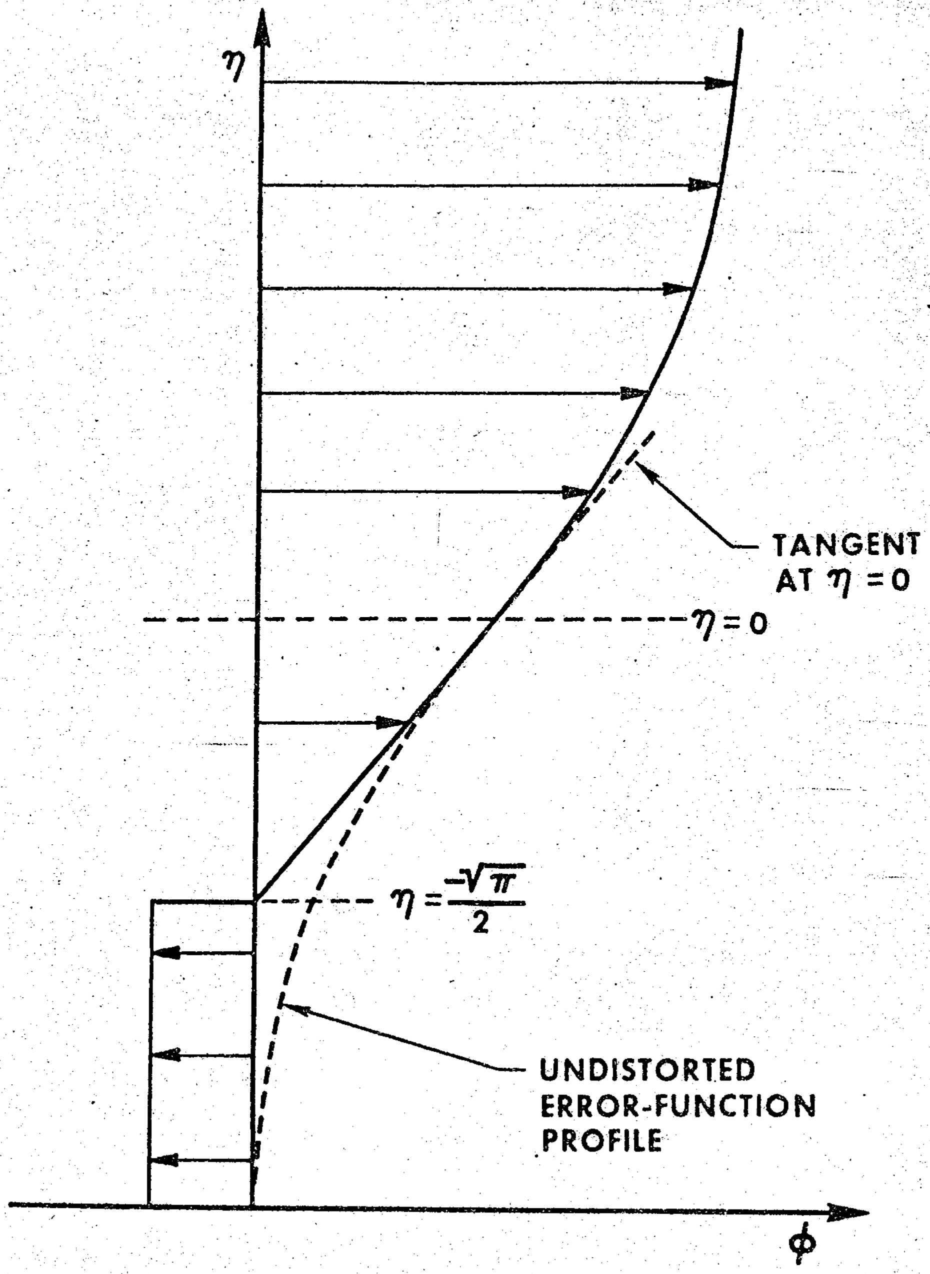

Figure A-10. Velocity Profile Just Upstream of Recompression

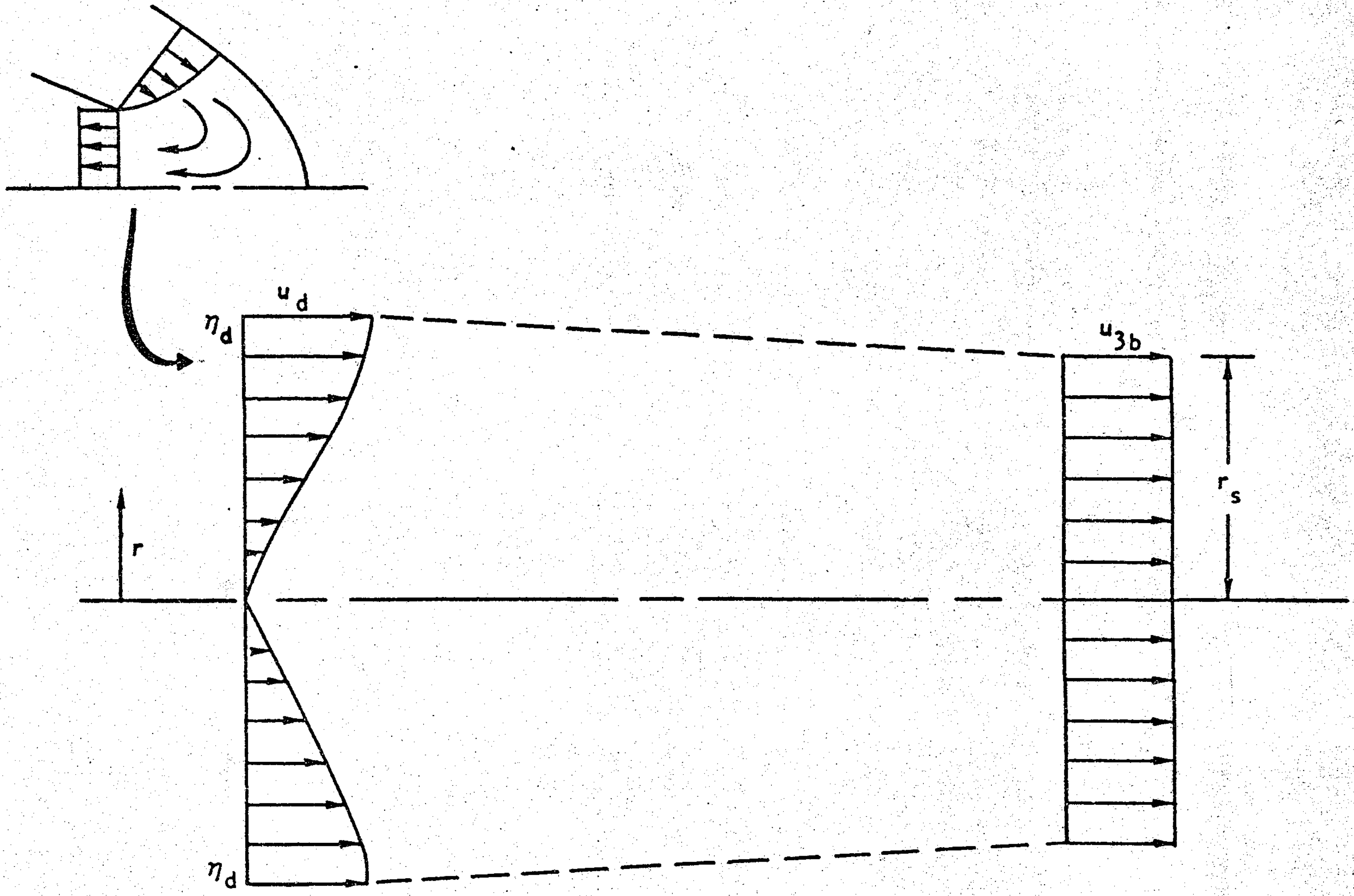

Figure A-12. Recirculating Stream: Control Volume for Constant-Pressure Uniformization Calculations where I′ has the same form as the corresponding integral defined after Eq. A-13), but the velocity profile is that shows in Fig. A-10:

$$\varphi = \frac{\eta}{\sqrt{\pi}} + 0.5 \quad (\eta \leq 0)$$

$$\varphi = \frac{1}{2}\,(1 + \mathrm{erf}\ \eta) \quad (\eta > 0) \qquad \text{(A-30)}$$

Conservation of Momentum

$$2\pi \ \frac{\rho_{2a}\ u_{2a}^{2}\, x^{*}R_{o}}{\sigma} \left[\left(1 - \frac{\eta_B^{*}}{\eta_{R_o}^{*}}\right) I_3' \Bigg|_{-\frac{\sqrt{\pi}}{2}}^{\eta_d^{*}} + \frac{1}{\eta_{R_o}^{*}}\ I_4' \Bigg|_{-\frac{\sqrt{\pi}}{2}}^{\eta_d^{*}} \right] = \rho_{3b}\ u_{3b}^{2}\ \pi\ r_s^{2} \qquad \text{(A-37}$$

where η_d^* represents the discriminating streamline in the hypothetical equivalent shear layer. For the case in which a sting is present in the base region, these equations become:

$$\frac{2\pi\ \rho_{2a}\ u_{2a}\, x^{*}R_{o}}{\sigma} \left[\left(1 - \frac{\eta_B^{*}}{\eta_{R_o}^{*}}\right) I_1' \Bigg|_{-\frac{\sqrt{\pi}}{2}}^{\eta_d^{*}} + \frac{1}{\eta_{R_o}^{*}}\ I_2' \Bigg|_{-\frac{\sqrt{\pi}}{2}}^{\eta_d^{*}} \right] = \rho_{3b}\ u_{3b}\, \pi\ (r_s^{2} - r_{st}^{2}) \qquad \text{(A-38)}$$

and

$$\frac{2\pi\ \rho_{2a}\ u_{2a}^{2}\, x^{*}R_{o}}{\sigma} \left[\left(1 - \frac{\eta_B^{*}}{\eta_{R_o}^{*}}\right) I_3' \Bigg|_{-\frac{\sqrt{\pi}}{2}}^{\eta_d^{*}} + \frac{1}{\eta_{R_o}^{*}}\ I_4' \Bigg|_{-\frac{\sqrt{\pi}}{2}}^{\eta_d^{*}} = \rho_{3b}\ u_{3b}^{2}\ \pi\ (r_s^{2} - r_{st}^{2}) \right] \qquad \text{(A-39)}$$

where r_{st} is the sting radius.

The conservation of energy can now be used to obtain the following relations (ideal gas, constant T_o):

Relationships Between Velocity and Crocco Number

$$C^2 = \frac{u^2}{2c_p T_o} = 1 - \frac{T}{T_o}$$

$$u_{3b}^2 = 2c_p \ (T_o - T_{3b})$$

$$u_{2a}^2 = 2c_p \ (T_o - T_{2a})$$

$$\frac{u_{3b}^2}{u_{2a}^2} = \frac{\left(1 - \frac{T_{3b}}{T_o}\right)}{\left(1 - \frac{T_{2a}}{T_o}\right)} = \frac{C_{3b}^2}{C_{2a}^2} \qquad \text{(A-40)}$$

Relationship Between Density and Crocco Number

$$\frac{\rho_{3b}}{\rho_{2a}} = \frac{T_{2a}/T_o}{T_{3b}/T_o}$$

$$= \frac{1 - C_{2a}^2}{1 - C_{3b}^2} = \frac{\frac{1}{C_{2a}^2} - 1}{\frac{1}{C_{2a}^2} - \frac{C_{3b}^2}{C_{2a}^2}} \qquad \text{(A-41)}$$

Equations A-38 and A-39 can be combined to give:

$$\frac{\rho_{3b}}{\rho_{2a}} = \frac{\frac{1}{C_{2a}^2} - 1}{\frac{1}{C_{2a}^2} - \frac{u_{3b}^2}{u_{2a}^2}} \qquad \text{(A-42)}$$

The value of $\frac{u_{3b}}{u_{2a}}$ required for Eq. A-40 is obtained through division of Eq. A-37 by Eq. A-35:

$$\frac{u_{3b}}{u_{2a}} = \frac{\left[\left(1 - \frac{\eta_B^*}{\eta_{R_o}^*}\right) I_3' \Big|_{-\frac{\sqrt{\pi}}{2}}^{\eta_d^*} + \frac{1}{\eta_{R_o}^*} I_4' \Big|_{-\frac{\sqrt{\pi}}{2}}^{\eta_d^*}\right]}{\left[\left(1 - \frac{\eta_B^*}{\eta_{R_o}^*}\right) I_1' \Big|_{-\frac{\sqrt{\pi}}{2}}^{\eta_d^*} + \frac{1}{\eta_{R_o}^*} I_2' \Big|_{-\frac{\sqrt{\pi}}{2}}^{\eta_d^*}\right]} \qquad \text{(A-43)}$$

Or, for the case in which a sting is present, Eq. A-38 and A-39 can be used to obtain the same result.

The outer radius of the recirculating stream, r_s, is then found from Eq. A-35 or A-38 using the values of ρ_{3b}/ρ_{2a} and u_{3b}/u_{2a} from Eq. A-42 and A-43, i.e.,

$$r_s^2 = r_{st}^2 + 2\,\frac{\rho_{2a}\; u_{2a}\; x^* R_o}{\rho_{3b}\; u_{3b}\; \sigma}\left[\left(1 - \frac{\eta_B^*}{\eta_{R_o}^*}\right) I_1' \Big|_{-\frac{\sqrt{\pi}}{2}}^{\eta_d^*} + \frac{1}{\eta_{R_o}^*} I_2' \Big|_{-\frac{\pi}{2}}^{\eta_d^*}\right] \qquad \text{(A-44)}$$

The value of $\bar{r}_{-R}$, the radial position of the streamline at η_{-R} in the forward-moving shear layer, is determined by the equality annular flow areas between given streamlines in the hypothetical equivalent shear layer and in the shear layer which is superimposed on the inviscid jet boundary. The geometric relationships are depicted in Fig. A-11 . The radius of the inviscid jet boundary, $\bar{r}_{JB}$, is known as a function of its length, x. The flow area between $\bar{r}_{JB}$ and $\bar{r}_{-R}$ is given by:

$$A_{JB-R} = \pi \left(\bar{r}_{JB}^{\,2} - \bar{r}_{-R}^{\,2}\right) / \text{Cos}\; \bar{\theta}_{JB} \qquad \text{(A-45)}$$

The corresponding flow area in the hypothetical equivalent shear layer is given by:

$$A_{JB-R}^* = \pi\,(r_{JB}^{*2} - r_{-R}^{*2}) \qquad \text{(A-46)}$$

From Eq. A-32, the value of r_{JB}^* is given by:

$$r_{JB}^* = R_o - y_b^* + y_m^* \qquad \text{(A-47)}$$

or, alternatively,

$$r_{JB}^* = R_o + \frac{x^*}{\sigma}(\eta_m^* - \eta_b^*) \qquad \text{(A-48)}$$

Similarly, r_{-R}^* can be expressed as:

$$r_{-R}^* = R_o + \frac{x^*}{\sigma}(\eta_{-R}^* - \eta_b^*) \qquad \text{(A-49)}$$

By use of the fact that A_{JB-R} and A_{JB-R}^* are equal, the above equations can be combined to yield:

$$\bar{r}_{-R}^2 = \bar{r}_{JB}^2 - \text{Cos}\ \bar{\theta}_{JB} \left\{ \left[R_o + \frac{x^*}{\sigma}(\eta_m^* - \eta_b^*)\right]^2 - \left[R_o + \frac{x^*}{\sigma}(\eta_R^* - \eta_b^*)\right]^2 \right\} \qquad \text{(A-50)}$$

The above equation can be rearranged to give:

$$\bar{r}_{-R}^2 = \bar{r}_{JB}^2 - \text{Cos}\ \bar{\theta}_{JB} \left\{ \frac{x^*}{\sigma}(\eta_m^* - \eta_b^*)\left[2R_o + \frac{x^*}{\sigma}(\eta_m^* - \eta_b^*)\right] - \frac{x^*}{\sigma}(\eta_{-R}^* - \eta_b^*)\left[2R_o + \frac{x^*}{\sigma}(\eta_{-R}^* - \eta_b^*)\right] \right\} \qquad \text{(A-51)}$$

Equations A-44 and A-51 are now solved simultaneously with an iteration performed on $\bar{r}_{JB}$ (with corresponding $\bar{\theta}_{JB}$ and x) so that:

$$\bar{r}_{-R} = r_s \qquad \text{(A-52)}$$

At that point, recompression is said to begin. The adjacent inviscid field is then assumed to undergo an isentropic recompression as it turns from $\bar{\theta}_{JB}$ back to the axial direction. This results in a pressure rise from P_B to P_4. The recompression waves then coalesce into a trailing shock farther out in the flow field (Fig. A-9).

A recompression factor, N, as defined by Nash (Ref. A-5), is used to relate the pressure on the discriminating streamline (in terms of the ratio of stagnation pressure to static pressure) to the total pressure rise associated with the turning of the fluid along the inviscid jet boundary:

$$N = \frac{\left(\frac{P_o}{P}\right)_d - 1}{\frac{P_4}{P_{\underline{\underline{B}}}} - 1} \qquad \text{(A-53)}$$

Then, in terms of this N factor, the pressure ratio on the discriminating streamline is given by:

$$\left(\frac{P_o}{P}\right)_d = N\left[\frac{P_4}{P_{\underline{\underline{B}}}} - 1\right] + 1 \qquad \text{(A-54)}$$

The value of $\eta_d{}^*$ is then found from the following relationships

$$\varphi_d = \frac{M_d{}^*}{M_{2a}{}^*} = \frac{1}{M_{2a}{}^*}\left\{\frac{\gamma+1}{\gamma-1}\left[1 - \left(\frac{P}{P_o}\right)_d^{\frac{\gamma-1}{\gamma}}\right]\right\}^{1/2} \qquad \text{(A-55)}$$

$$\varphi_d = \frac{1}{2}\,(1 + \text{erf}\ \eta_d{}^*) \qquad \text{(A-56)}$$

DETERMINATION OF BASE BLEED

From the definitions of η_d and η_B, the mass flowrate between the two streamlines represents fluid added to the near wake (base bleed in Fig. A-1).

From Eq. A-33 , the bleed flowrate can be calculated as:

$$\dot{w}_s = \frac{2\pi \rho_{2a} u_{2a} x^* R_o}{\sigma} \left[\left(1 - \frac{\eta_B^*}{\eta_{R_o}^*} \right) I_1 \Bigg|_{\eta_d^*}^{\eta_B^*} + \frac{1}{\eta_{R_o}^*} I_2 \Bigg|_{\eta_d^*}^{\eta_B^*} \right] \quad \text{(A-57)}$$

The primary flowrate is given by:

$$\dot{w}_p = \rho_{2a} u_{2a} A_{2a} \quad \text{(A-58)}$$

where A_{2a} is an effective area for the primary flow. If an effective throat radius, r_t, is defined by:

$$A_{2a}^* = \pi r_t^2 \quad \text{(A-59)}$$

then the ratio of secondary to primary flowrate is found to be:

$$\frac{\dot{w}_s}{\dot{w}_p} = \frac{2\left(\frac{x^*}{r_t}\right)\left(\frac{R_o}{r_t}\right)}{\sigma \, (A/A^*)_{2a}} \left[\left(1 - \frac{\eta_B^*}{\eta_{R_o}^*} \right) I_1 \Bigg|_{\eta_d^*}^{\eta_B^*} + \frac{1}{\eta_{R_o}^*} I_2 \Bigg|_{\eta_d^*}^{\eta_B^*} \right] \quad \text{(A-60)}$$

It should be pointed out that the valve of $\dot{w}_s/\dot{w}_p$ for which this model is applicable is limited to the total mass flow in the shear layer below the η_B^* streamline. Once the N-factor has been chosen, the above equations can be used to obtain η_d^*, φ_d, and, finally, the secondary flowrate necessary to yield a given base pressure.

N-FACTOR CORRELATION

Application of the theory to experimental data for aerospike base flows has yielded the empirical correlation of Fig. A-13. Similar curves have been obtained for flow over two-dimensional backsteps and for flow over cylinders (Fig. A-13). The N-factor has been found to be a function of

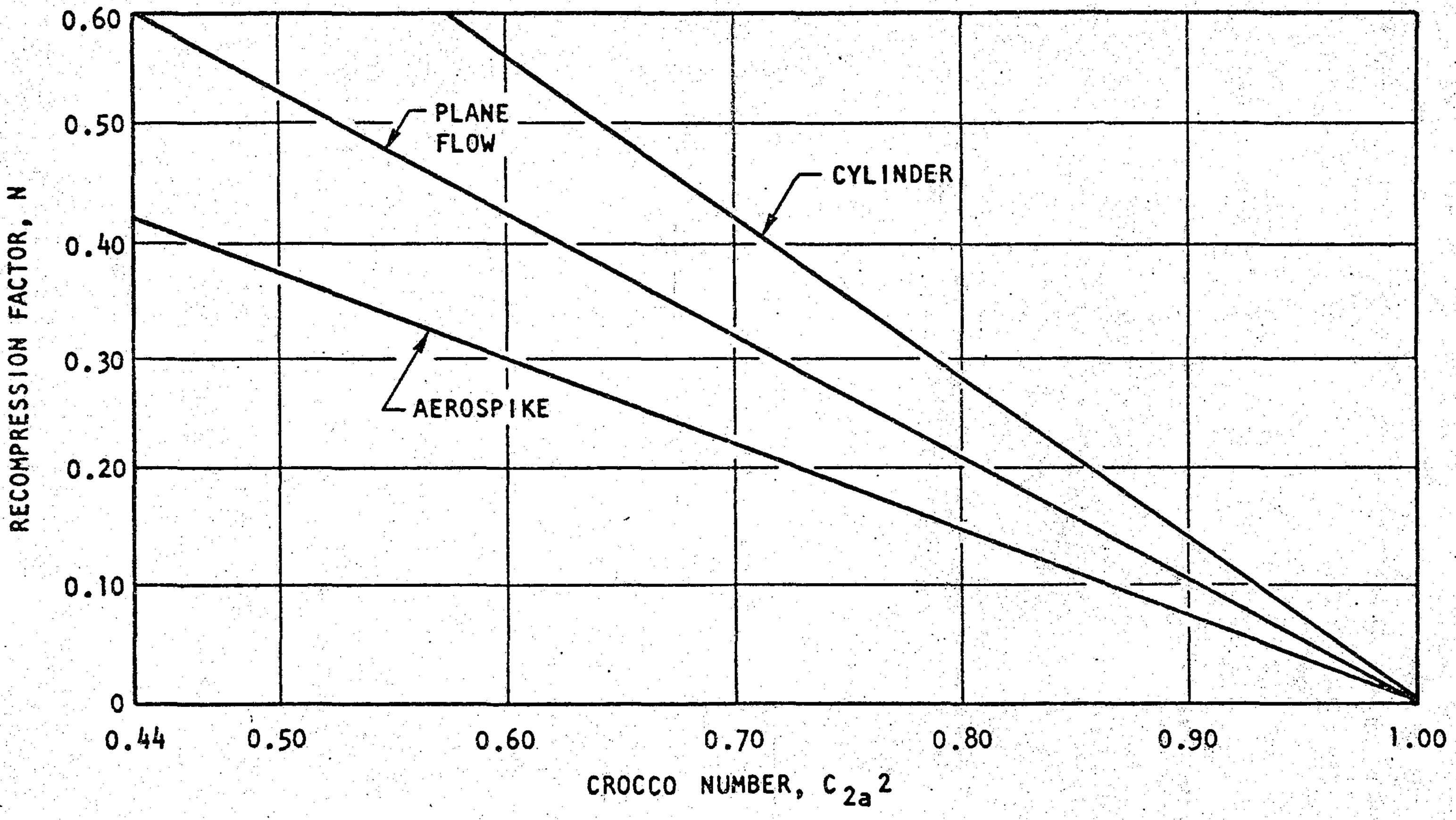

Figure A-13. Correlation of Recompression Factor, N

Crocco number on the inviscid jet boundary. This functional relationship appears to be most affected by the general shape of the inviscid jet boundary. For two-dimensional flow the jet boundary is relatively straight (Fig.A-14a); for parallel uniform flow over cylinders, it has the shape shown in Fig.A-14b; and, for aerospike flow fields, it has the shape shown in Fig.A-14c. The more the constant-pressure free jet boundary tends to "dive" into the axis, the higher the N-factor for a given Crocco number.

The experimental data used to obtain the N-factor correlations covered a wide variety of flow conditions, i.e., gas compositions, free stream Mach number, initial boundary layer moment thickness, degree of nonuniformity of the free stream flow amount of base bleed, and base geometries including stings. The straight line correlation curves shown in Fig. A-13 were then chosen for the N-factor determination for the various geometries and free stream Crocco numbers. Use of these N-factors for base pressure calculations for cases not used for the N-factor correlation has given results which agree quite well with experimental data. In addition, where experimental data have been available, the location of the point at which recompression begins, the pressure at reattachment, and the peak pressure rise have been compared for theory and experiment. Comparisons of this type are shown in Fig. A-15 through A-17. The experimental data, taken from Ref. A-6 , extended over various free stream Mach numbers and ratios of sting radii to base radii. For some of these data, the momentum thickness of the initial boundary layer was substantial when compared with the step height. Nevertheless, the theory was able to predict the base pressure and the location of the point at which recompression begins quite accurately.

It should be emphasized that the N-factors were determined as the proper values to force the theory to give the correct base pressures for given base bleed flowrates, and were not defined from detailed experimental data in the recompression region. The fact that these N-factors do predict the location of the start of recompression and the pressure level at reattachment lends support to the validity of the theory.

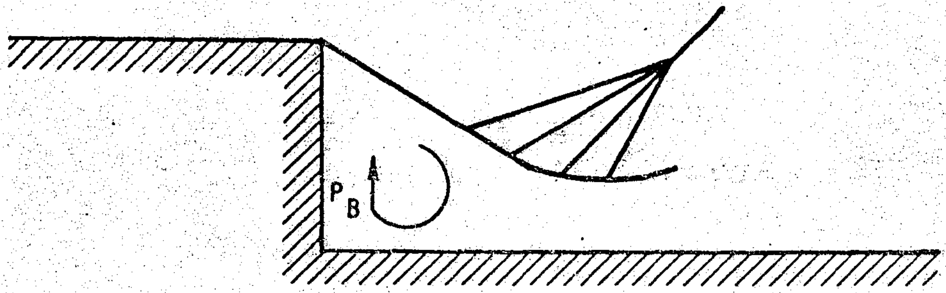

(a) FLOW OVER TWO-DIMENSIONAL BACKSTEP

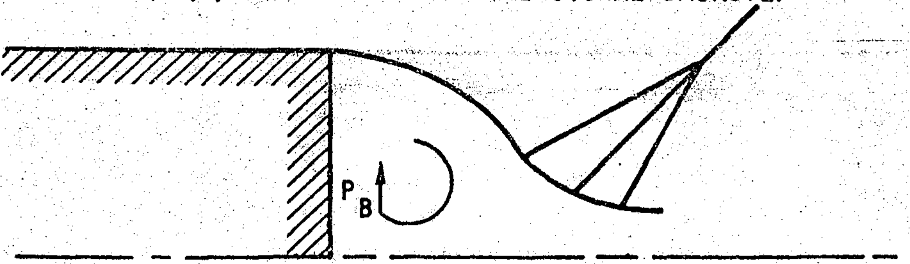

(b) FLOW OVER CYLINDER

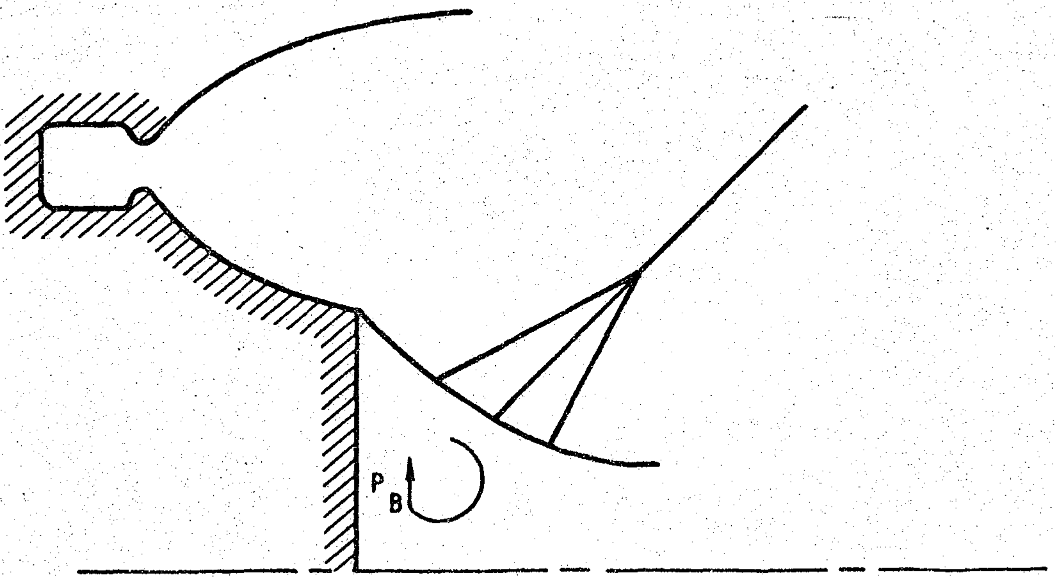

(c) AEROSPIKE BASE FLOW

Figure A-14. Base Flow Free Jet Boundaries

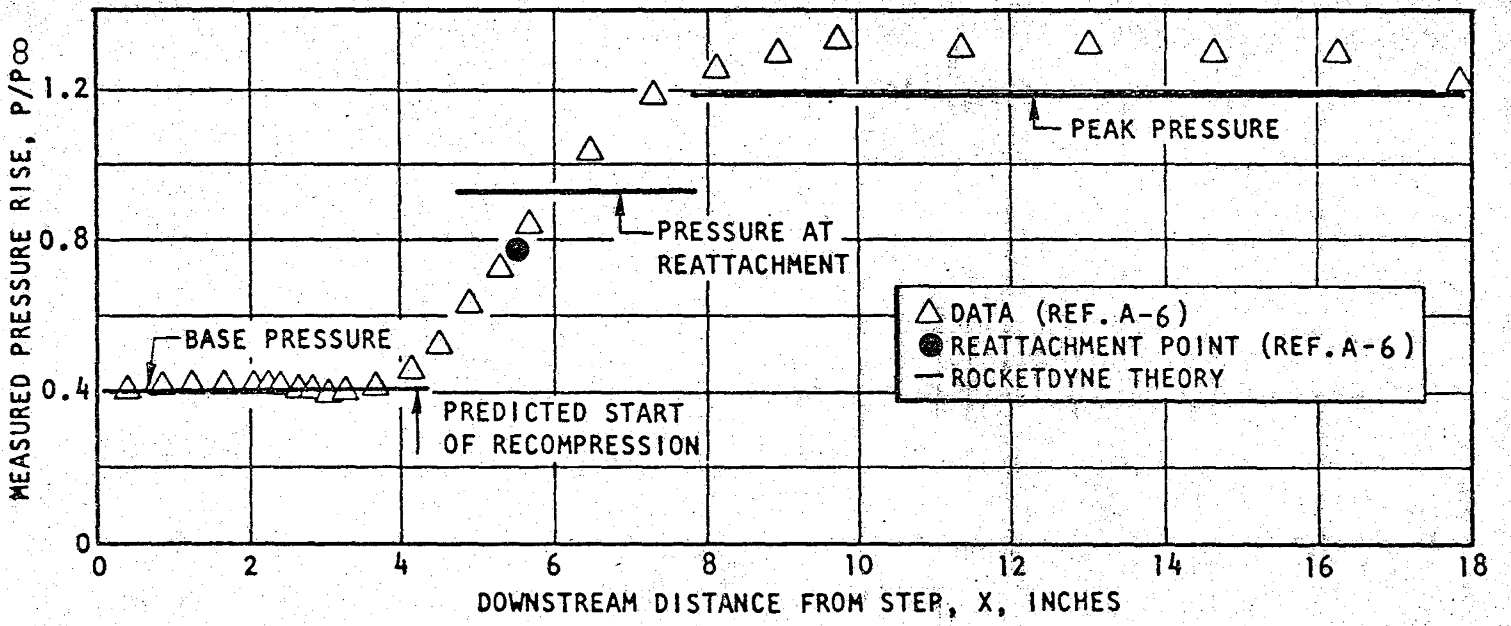

Figure A-15. Comparison of Theory and Experiment, $M_\infty = 2.09$, $r_{st}/R_o = 0.721$

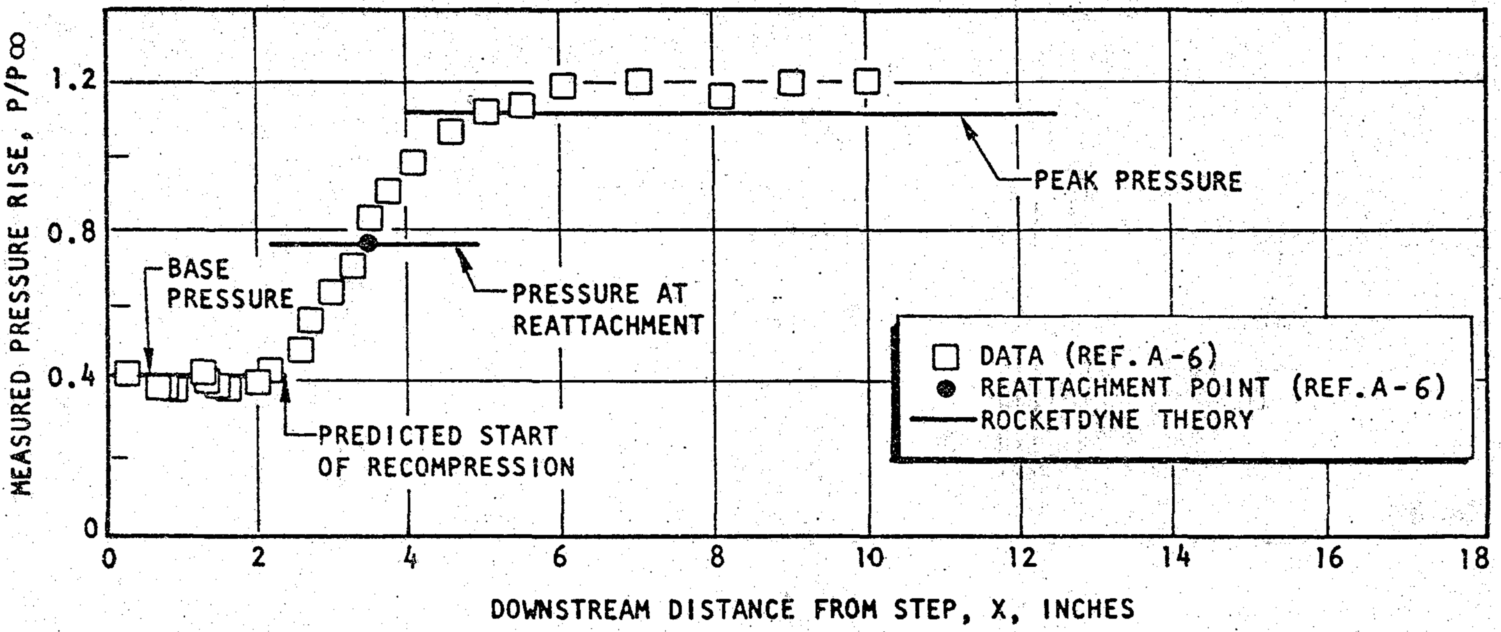

Figure A-16. Comparison of Theory and Experiment, $M_\infty = 2.09$, $r_{st}/R_o = 0.830$

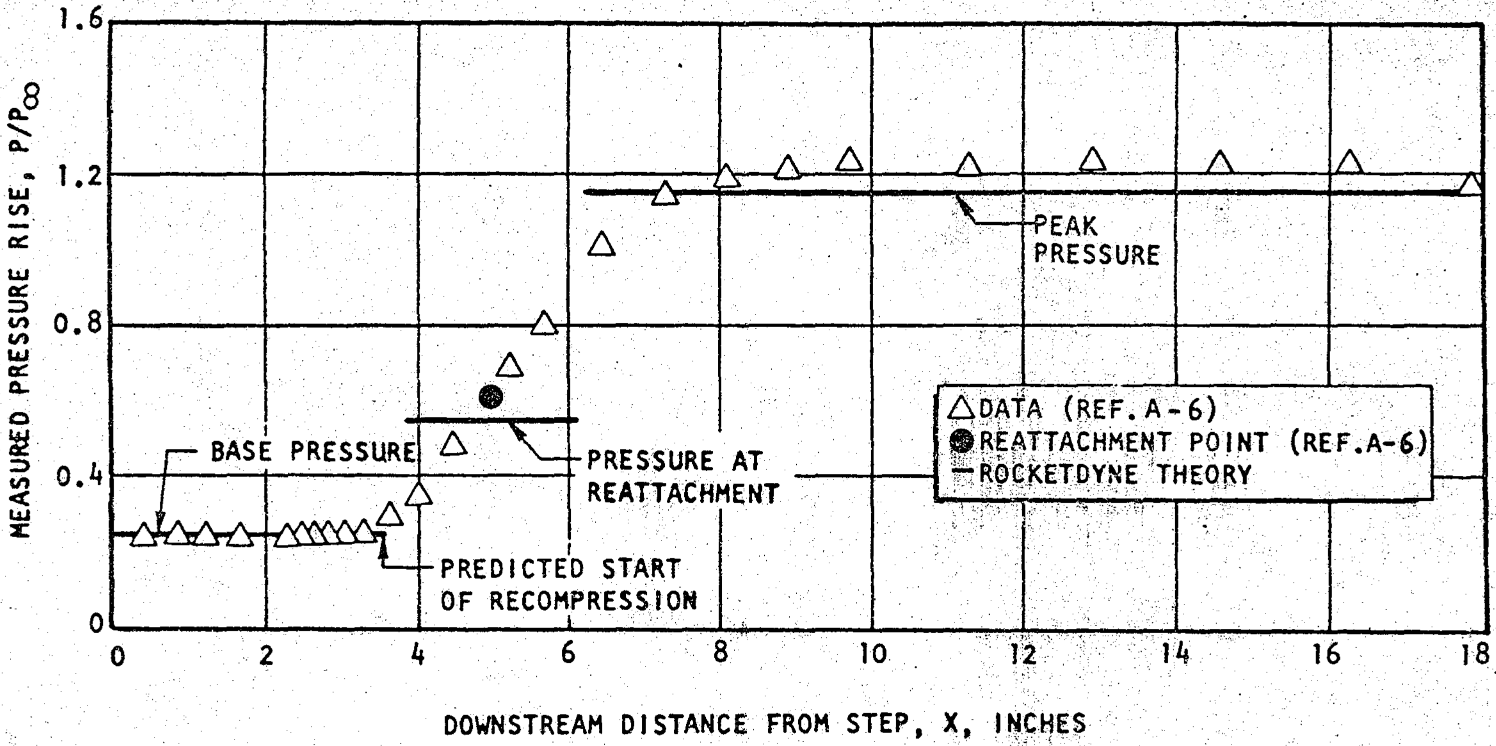

Figure A-17. Comparison of Theory and Experiment, $M_\infty = 3.02$, $r_{st}/R_o = 0.721$

A comparison of theory and experiment for base pressure when bleed is present is shown in Fig. A-18. The experimental data were obtained from cold-flow wind tunnel tests for aerospike nozzle with various amounts of base bleed. Similar comparisons have been obtained for other aerospike configurations.

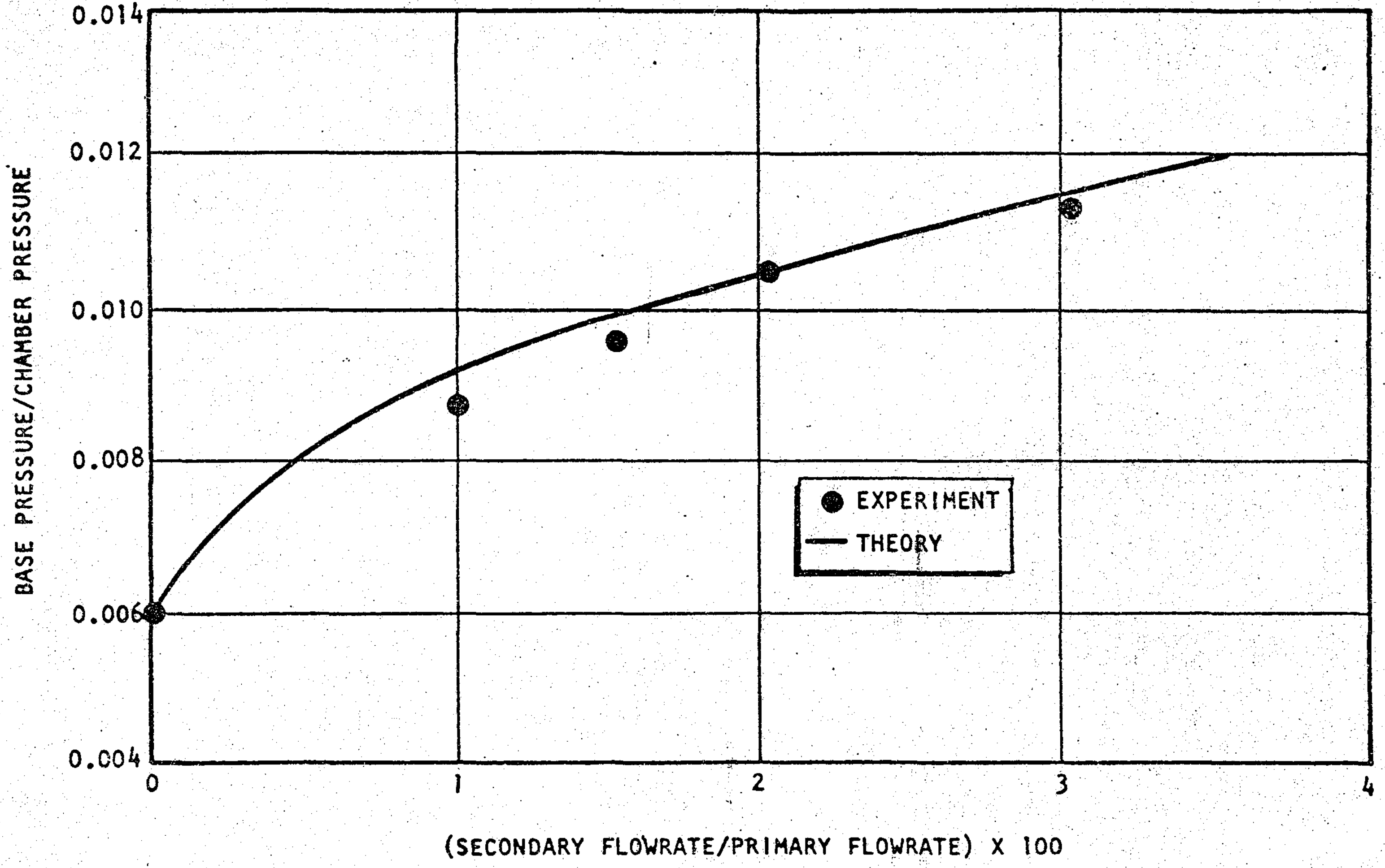

Figure A-18. Base Pressure for Contoured Aerospike

APPENDIX A REFERENCES

A-1. Korst, H. H., W. L. Chow, and G. W. Zumwalt: Research on Transonic and Supersonic Flow of a Real Fluid at Abrupt Increases in Cross Section (with Special Consideration of Base Drag Problems), Final Report, University of Illinois, ME-TN-392-5, December 1959.

A-2. Channapragada, R. S.: "Compressible Jet Spread Parameter for Mixing Zone Analyses," AIAA Journal, Vol. 1, No. 9, p. 2188.

A-3. Kirk, F. N.: "An Approximate Theory of Base Pressure in Two-Dimensional Flow at Supersonic Speed," R.A.E. Technical Note Aero 2377, December 1959.

A-4. Roberts, J. B.: "On the Prediction of Base Pressure in Two-Dimensional Supersonic Turbulent Flow," N.G.T.E. R 265, November 1964; A.R.C. 26 - F.M. 3571, November 1964.

A-5. Nash, J. F.: An Analysis of Two-Dimensional Base Flow, Including the Effect of the Approaching Boundary Layer, N.P.L. Aero Report 1036, 1963.

A-6. Roshko, A. and G. J. Thomke: Observations of Turbulent Reattachment Behind an Axisymmetric Downstream-Facing Step in Supersonic Flow, Douglas Report SM-43069, April 1965.

APPENDIX B

TEST DATA REDUCTION AT AEDC

The test configuration at AEDC has been designed to provide sufficient data for evaluation of both full scale engine performance and vehicle drag. To accomplish this, pressure profiles along the vehicle forebody and boattail, and engine expansion surfaces will be measured in addition to flow engine parameters and overall thrust. Model instrumentation is shown in Fig. B-1.

A list of equations useful in monitoring the on-line test-to-test integrity of each data point is presented in Table B-I. The constants used in the equations of Table B-I are presented in Table B-II. Items 1-7 indicate average flow parameters for each run. Freestream flow conditions and thrust contributions from various portions of the vehicle and engine are provided by Items 8-22. Characteristic velocity of the primary and secondary streams can be computed as indicated in Items 23-26. Fliegner's constant data for air has been furnished to AEDC in separate cover. The engine throat Reynold's number determined in Item 27 is used to obtain the primary throat area (Item 28) from Rocketdyne calibration data presented in Fig. B-2. This will provide a consistent comparison with AEDC flow measurements by means of Item 29. Pressure ratios calculated in Items 30-32 form the basis for obtaining the thrust coefficients in Items 33 and 34. The relationship between pressure ratio and thrust coefficient is shown in equation below. The quantities in Items 35-37 will aid in computing engine and vehicle scale parameters. The remaining quantities should help to evaluate overall engine and vehicle performance characteristics.

$$C_F = \sqrt{\frac{2\gamma^2}{\gamma-1}\left[\frac{2}{\gamma+1}\right]^{\frac{\gamma+1}{\gamma-1}}\left[1-\left[\frac{P_e}{P_c}\right]^{\frac{\gamma-1}{\ }}\right]}$$

Supplemental data reduction requested from AEDC is outlined in Table B-III. Thrust readings corrected for variations in freestream conditions are indicated by Items 1-10. The starred items should also be determined on-line if possible to enable immediate data evaluation. Model scale coefficients are provided by Items 11-15. All raw data taken during each test should be printed out on-line along with numerical items in Tables B-I, and B-III. Nomenclature lists are provided in Tables B-IV and B-V. A schematic of the model with pertinent area parameters is shown in Fig. B-3.

TABLE B-I

ON LINE DATA REDUCTION

ITEM	SYMBOL	UNITS	EQUATION
1	P_c	psia	$P_c = K_{51}\ (P1+P2)$
2	$\overline{P}_{cav}$	psia	$\overline{P}_{cav} = K_{51}\ (P130+P131)$
3	P_s	psia	$P_s = K_{51}\ (P19+P20)$
4	T_c	°R	$T_c = K_{51}\ (T136+T137)$
5	T_s	°R	$T_s = K_{51}\ (T134+T135)$
6	$\dot{w}_p$	lbs/sec	Primary Flowrate (Facility
7	$\dot{w}_s$	lbs/sec	Secondary Flowrate (Facility)
8	P	psia	Freestream Static Pressure (Facility)
9	q	psia	Freestream Dynamic Pressure (Facility)
10	M	—	Freestream Mach Number (Facility)
11	F	lbf	Force Balance Reading (F133)
12	$\overline{P}_F$	psia	$\overline{P}_F = K_1\ (P56+P71) + K_2\ (P57+P72)$ $+ K_3\ (P58+P73) + K_4\ (P59+P74)$ $+ K_5\ (P60+P75) + K_6\ (P61+P76)$ $+ K_7\ (P62+P77) + K_8\ (P63+P78)$ $+ K_9\ (P64+P79) + K_{10}(P65+P80)$ $+ K_{11}(P66+P81) + K_{12}(P67+P82)$ $+ K_{13}(P68+P83) + K_{14}(P69+P84)$ $+ K_{15}(P70+P85)$
13	$\overline{P}_{B_v}$	psia	$\overline{P}_{B_v} = K_{16}(P102+P106) + K_{17}(P103+P107)$ $+ K_{18}(P104+P108) + K_{19}(P105+P109)$
14	$\overline{P}_{B_{v_o}}$	psia	$\overline{P}_{B_{v_o}} = K_{20}(P3+P4) + K_{21}(P5+P6) + K_{22}(P7+P8)$ $+ K_{23}(P9+P10) + K_{24}(P11+P12)$ $+ K_{25}(P13+P14) + K_{25}(P15+P16)$ $+ K_{27}(P17+P18) + K_{61}\ \left.\overline{P}_{B_e}\right)_o$

TABLE B-I

ON LINE DATA REDUCTION (Continued)

ITEM	SYMBOL	UNITS	EQUATION
15	$\overline{P}_{B_{VDB}}$	psia	$\overline{P}_{B_{VDB}} = K_{28}(P139+P148) + K_{29}(P140+P149)$ $+ K_{30}(P141+P150) + K_{31}(P142+P151)$ $+ K_{32}(P143+P152) + K_{53}(P144+P153)$ $+ K_{54}(P145+P154) + K_{55}(P146+K155)$
16	$\overline{P}_{B_{VDU}}$	psia	$\overline{P}_{B_{VDU}} = K_{33}(P156+P164) + K_{34}(P157+P165)$ $+ K_{35}(P158+P166) + K_{36}(P159+P167)$ $+ K_{37}(P160+P168) + K_{56}(P161+P169)$ $+ K_{57}(P162+P170) + K_{58}(P163+P171)$
17	$\overline{P}_{B_D}$	psia	$\overline{P}_{B_D} = \overline{P}_{B_V} + K_{59}\,\overline{P}_{B_{VDB}} - K_{60}\,\overline{P}_{B_{VDU}}$
18	$\overline{P}_{B_e}\Big)_1$	psia	$\overline{P}_{B_e}\Big)_1 = K_{38}(P21+P22) + K_{39}(P23+P32+P36+P44+P48)$ $+ K_{40}(P24+P37+P49)$ $+ K_{41}(P25+P33+P38+P45+P50)$ $+ K_{42}(P26+P39+P51)$ $+ K_{43}(P27+P34+P40+P46+P52)$ $+ K_{44}(P28+P41+P53)$ $+ K_{45}(P29+P35+P42+P47+P54)$ $+ K_{46}(P30+P43+P55) + K_{47}(P31)$
19	D_{F_o}	lbs	$D_{F_o} = F_o + K_{48}\,\overline{P}_{B_{D_o}} + K_{49}\,\overline{P}_{B_{v_o}}$
20	F_e	lbs	$F_e = F - K_{48}\,\overline{P}_{B_D}$
21	F_{B_v}	lbs	$F_{B_v} = K_{49}\,\overline{P}_{B_v}$
22	F_∞	lbs	$F_\infty = K_{49}\,P_\infty$
23	f_{K_p}	$\sqrt{{}^oR\text{-}sec^2/ft^2}$	$f_{K_p} = f(P_c, T_c)$
24	C^*_p	ft/sec	$C^*_p = (32.174)\sqrt{T_c}/f_{K_p}$

TABLE B-I

ON LINE DATA REDUCTION (Continued)

ITEM	SYMBOL	UNITS	EQUATION
25	f_{K_s}	$\sqrt{{}^{o}R\text{-sec}^2/ft^2}$	$f_{K_s} = f(P_s, T_s)$
26	C^*_s	ft/sec	$C^*_s = (32.174)\sqrt{T_s}/f_{K_s}$
27	R_e	–	$R_e = K_{50}\ P_c/T_c$
28	A^*_R	in^2	$A^*_R = f(R_e)$
29	A^*_A	in^2	$A^*_A = \dot{w}_p C^*_p/(32.174)\ P_c$
30	PR_{v_o}	–	$PR_{v_o} = P_c/\overline{P}_{B_{v_o}}$
31	PR_{BV}	–	$PR_{v} = P_c/\overline{P}_{B_v}$
32	PR_∞	–	$PR_\infty = P_c/P_\infty$
33	$C_{F_{BV}}$	–	$C_{F_{BV}} = f(PR_v)$
34	C_{F_∞}	–	$C_{F_\infty} = f(PR_\infty)$
35	F_t	lbs	$F_t = P_c\ A^*\ (1 + \dot{w}_s C^*_s/\dot{w}_p C^*_p)$
36	$F_{i_{BV}}$	lbs	$F_{i_{BV}} = C_{F_{BV}}\ F_t$
37	F_{i_∞}	lbs	$F_{i_\infty} = C_{F_\infty}\ F_t$
38	C_{p_v}	–	$C_{p_v} = (\overline{P}_{B_v} - P_\infty)/q_\infty$
39	C_{p_D}	–	$C_{p_D} = (\overline{P}_{B_D} - P_\infty)/q_\infty$
40	$(\overline{P}_{B_e}/P_c)_1$	–	$(\overline{P}_{B_e}/P_c)_1 = \overline{P}_{B_e}/P_c$
41	$\overline{P}_{B_v}/P_\infty$	–	$\overline{P}_{B_v}/P_\infty = \overline{P}_{B_v}/P_\infty$
42	$\overline{P}_{B_D}/P_\infty$	–	$\overline{P}_{B_D}/P_\infty = \overline{P}_{B_D}/P_\infty$
43	$\dot{w}_s C^*_s/\dot{w}_p C^*_p$	–	$\dot{w}_s C^*_s/\dot{w}_p C^*_p = \dot{w}_s C^*_s/\dot{w}_p C^*_p$

TABLE B-II

CONSTANTS USED IN EQUATIONS OF TABLE B-II

K_1 = .01740

K_2 = .02737

K_3 = .03323

K_4 = .03909

K_5 = .04495

K_6 = .04108

K_7 = .03035

K_8 = .02691

K_9 = .02802

K_{10} = .02929

K_{11} = .03060

K_{12} = .03188

K_{13} = .03312

K_{14} = .02732

K_{15} = .05945

K_{16} = .08545

K_{17} = .1074

K_{18} = .1417

K_{19} = .1655

K_{20} = .02415

K_{21} = .00957

K_{22} = .01371

K_{23} = .01336

K_{24} = .0101

K_{25} = .009525

K_{26} = .01212

K_{27} = .00906

K_{28} = .050

K_{29} = .050

K_{30} = .050

K_{31} = .050

K_{32} = .050

K_{33} = .050

K_{34} = .050

K_{35} = .050

K_{36} = .050

K_{37} = .050

K_{38} = .05530

K_{39} = .03082

K_{40} = .03577

K_{41} = .02272

K_{42} = .03890

K_{43} = .02446

K_{44} = .03953

K_{45} = .02823

K_{46} = .01763

K_{47} = .01910

K_{48} = 48.270

K_{49} = 524.283

K_{50} = 1.0

K_{51} = 0.5

K_{52} = 0.0000288

K_{53} = .075

K_{54} = .100

K_{55} = .075

K_{56} = .075

K_{57} = .100

K_{58} = .075

K_{59} = 2.5909

K_{60} = 2.2519

K_{61} = .79591

K_{62} = 572.557 (no doors)
589.303 (with doors)

K_{63} = 417.285

K_{64} = 36.692

TABLE B- III

SUPPLEMENTAL DATA REDUCTION

ITEM	SYMBOL	UNIT	EQUATION	
1*	$\overline{F}_{e_1}$	lbs	$\overline{F}_{e_1} = F_{e_1} + (q_{\infty_1}/q_{\infty_o})\, D_{F_o}$	
2*	$\overline{F}_{e_2}$	lbs	$\overline{F}_{e_2} = F_{e_2} + (q_{\infty_2}/q_{\infty_o}) D_{F_o}$	
3*	$F_{e_{v_1}}$	lbs	$F_{e_{v_1}} = \overline{F}_{e_1} - (K_{49}\, \overline{P}_{B_{v_o}})\, (P_{\infty_1}\, P_{\infty_o})$	
4*	$F_{e_{v_2}}$	lbs	$F_{e_{v_2}} = \overline{F}_{e_2} - (K_{49}\, \overline{P}_{B_{v_o}})\, (P_{\infty_2}/P_{\infty_o})$	
5	$F_{e_{BV_1}}$	lbs	$F_{e_{BV_1}} = \overline{F}_{e_1} - (K_{49}\, \overline{P}_{B_{v_1}})$	
6	$F_{e_{BV_2}}$	lbs	$F_{e_{BV_2}} = \overline{F}_{e_2} - (K_{49}\, \overline{P}_{B_{v_2}})$	
7*	$F_{e_{\infty_1}}$	lbs	$F_{e_{1}} = \overline{F}_{e_1} - (K_{49}\, P_{\infty_1})$	
8*	$F_{e_{\infty_2}}$	lbs	$F_{e_{2}} = F_{e_2} - (K_{49}\, P_{\infty_2})$	
9	F_{N_1}	lbs	$F_{N_1} = F_1 + F_o\, (q_{\infty_1}/q_{\infty_o})$	
10	F_{N_2}	lbs	$F_{N_2} = F_2 + F_o\, (q_{\infty_2}/q_{\infty_o})$	
11*	$\overline{PR}_{v_{o_1}}$	—	$\overline{PR}_{v_{o_1}} = PR_{v_o}\, (P_{\infty_o}/P_{\infty_1})$	
12*	$\overline{PR}_{v_{o_2}}$	—	$\overline{PR}_{v_{o_2}} = PR_{v_o}\, (P_{\infty_o}/P_{\infty_2})$	
13*	C_{F_v}		$C_{F_v} = f(\overline{PR}_{v_o})$	1 & 2
14*	Φ_v	—	$\Phi_v = F_{e_v}/C_{F_v} F_t$	1 & 2
15	Φ_{BV}	—	$\Phi_{BV} = F_{e_{BV}}/F_{i_{BV}}$	1 & 2

TABLE B-III

SUPPLEMENTAL DATA REDUCTION (Continued)

ITEM	SYMBOL	UNIT	EQUATION	
16*	Φ_∞	–	$\Phi_\infty = F_e / F_i$	1 & 2
17	Φ_N		$\Phi_N = F_N / C_{F_v} \; F_t$	1 & 2
18	C		$C = \left[D_{F_o} - K_{64} (P_{cav} - P_\infty) \right] / q_{\infty_o} K_{62} - \bar{P}_{B_D} K_{48} \, q_\infty \, K_{62}$	1&2
19	C_v		$C_v = C - (\bar{P}_{B_{v_o}} \; K_{49}) \; P_\infty / q_\infty \; P_{\infty_o} K_{62}$	1 & 2
20	C_{BV}		$C_{BV} = C - (\bar{P}_{B_v} \; K_{49}) / q_\infty \, K_{62}$	1 & 2
21	C		$C = C - (P_\infty K_{49}) / q_\infty K_{62}$	1 & 2
22	C_N		$C_N = \left[F_o - K_{64} (P_{cav} - P_\infty) \right] / q_{\infty_o} \; K_{62}$	
23	$D\overline{PR}_{v_o}$		$D\overline{PR}_{v_o} = K_{52} \; \overline{PR}_{v_o}$	1 & 2
24	DRP_{BV}		$DPR_{BV} = K_{52} \; PR_{BV}$	1 & 2
25	DPR		$DPR = K_{52} \; PR_\infty$	1 & 2
26	C_{F_e}		$C_{F_e} = F_e / F_t$	1 & 2
27	$P_{B_e} / P_c \big)_2$	–	$\left. \frac{P_{B_e}}{P_c} \right)_2 = \left. \frac{\bar{P}_{B_e}}{P_c} \right)_1 + \frac{\left(\frac{\bar{P}_{B_{v_1}} \; P_{c_1} \; A_1^*}{\bar{P}_{B_{v_2}} \; P_{c_2} \; A_2^*} \right) F_{e_2} - F_{e_1}}{P_{c_1} \; K_{63}}$	2

TABLE B- IV

NOMENCLATURE FOR ON-LINE DATA REDUCTION

ITEM	SYMBOL	DESCRIPTION
1	P_c	Nozzle primary chamber supply pressure
2	P_{cav}	Average pressure inside the cavity containing the force balance, which is formed by the vehicle and nozzle shell
3	P_s	Nozzle secondary supply pressure
4	T_c	Nozzle primary chamber supply temperature
5	T_s	Nozzle secondary supply temperature
6	$\dot{w}_p$	Nozzle primary weight flowrate
7	$\dot{w}_s$	Nozzle secondary weight flowrate
8	P	Freestream static pressure
9	q	Freestream dynamic pressure
10	M	Freestream Mach number
11	F	Force balance reading (absolute)
12	$\bar{P}_F$	Average forebody pressure from the sting slot to the maximum vehicle diameter
13	$\bar{P}_{B_V}$	Average pressure acting along the face of the nozzle outer cowl (Fig.). This is the engine-on vehicle base pressure when the doors are removed
14	$\bar{P}_{B_{V_o}}$	Average engine-off pressure acting over the portion of the vehicle base occupied by the engine. This parameter only has meaning when the engine is not running, and need be computed only during the first of each set of three runs
15	$\bar{P}_{B_{VDB}}$	Average pressure acting over the rearward or boattail portion of the vehicle doors (Fig.)
16	$\bar{P}_{B_{VDU}}$	Average pressure acting over the internal surface of the vehicle door (Fig.)
17	$\bar{P}_{B_D}$	Effective boattail pressure. When multiplied by the vehicle base area exclusive of the doors (i.e., base surface area of the nozzle outer cowl) this provides a value for vehicle base thrust with doors removed, and vehicle base plus door thrust with doors installed

TABLE B-IV

NOMENCLATURE FOR ON-LINE DATA REDUCTION (Continued)

ITEM	SYMBOL	DESCRIPTION
18	$\overline{P}_{B_{e_1}}$	Average engine base pressure when the engine is running without secondary flow
19	D_{F_o}	Vehicle forebody drag with the engine off
20	F_e	Net thrust exclusive of boattail drag with the engine running. Used for computational purposes only
21	F_{B_V}	Engine-off thrust over the portion of the vehicle occupied by the engine
22	F_∞	Thrust produced by the freestream static pressure acting over the portion of the vehicle occupied by the engine in a direction opposite to the engine thrust
23	f_{K_p}	Primary flow real gas Fliegners constant
24	C^*_P	Primary flow characteristic velocity
25	f_{K_s}	Secondary flow real gas Fliegners constant
26	C^*_s	Secondary flow characteristic velocity
27	R_e	Primary flow throat Reynolds number. This parameter will be used to correlate aerodynamic throat area test data obtained at Rocketdyne
28	A^*_R	Aerodynamic throat area determined at Rocketdyne
29	A^*_A	Aerodynamic throat area determined at AEDC
30	PR_{V_o}	Ratio of chamber pressure to the average engine-off pressure acting on the engine area
31	PR_{BV}	Ratio of chamber pressure to the average pressure acting over the face of the nozzle outer cowl
32	PR_∞	Ratio of chamber pressure to freestream static pressure
33	$C_{F_{BV}}$	Optimum thrust coefficient based upon air properties and the pressure ratio, PR_{BV}

TABLE B- IV

NOMENCLATURE FOR ON-LINE DATA REDUCTION (Continued)

ITEM	SYMBOL	DESCRIPTION
34	C_F	Optimum thrust coefficient based upon air properties and the pressure ratio, PR_∞
35	F_t	Thrust parameter used for computational purposes
36	$F_{i_{BV}}$	Ideal thrust of the primary and secondary streams based on the optimum thrust coefficient, $C_{F_{BV}}$
37	F_i	Ideal thrust of the primary and secondary streams based on the optimum thrust coefficient, C_F
38	C_{P_V}	Pressure coefficient for the average pressure acting over the face of the nozzle outer cowl (Item 13)
39	C_{P_D}	Pressure coefficient for the effective boattail pressure (Item 17)
40	$\left.\overline{P}_{B_e}/P_c\right)_1$	Engine base-to-chamber pressure ratio without secondary flow
41	$\overline{P}_{B_V}/P_\infty$	Average outer cowl face pressure-to-freestream static pressure ratio
42	$\overline{P}_{BD}/P_\infty$	Effective boattail pressure-to-freestream static pressure ratio

TABLE B- V

NOMENCLATURE FOR ADDITIONAL DATA REDUCTION

ITEM	SYMBOL	DESCRIPTION
1	F_{e_1}	Intrinsic thrust of the engine without secondary flow (i.e., exclusive of a pressure force acting in opposition to the engine thrust) with a correction for variations in freestream conditions from the first data slice (engine-off) to the second data slice (engine-on without secondary flow)
2	F_{e_2}	Intrinsic thrust of the engine with secondary flow (third data slice) and with a correction for variation in free-stream conditions from the first to the third data slice. These corrections are performed such that all data is corrected to conditions occurring during the current data slice.
3 & 4	F_{e_V}	Engine thrust relative to the engine-off vehicle base pressure force over the area occupied by the engine
5 & 6	$F_{e_{BV}}$	Engine thrust relative to the engine-on vehicle base pressure force over the area occupied by the engine
7 & 8	F_{e_∞}	Engine thrust relative to the freestream pressure force over the area occupied by the engine
9 & 10	F_N	Engine thrust relative to the engine-off vehicle base pressure force over the area occupied by the engine including the influence of the engine-on boattail thrust
11 & 12	$\overline{PR}_{V_o}$	Ratio of chamber pressure to the average engine-off pressure acting on the engine area with appropriate corrections for variations in freestream conditions
13	C_{F_V}	Optimum thrust coefficient based upon air properties and the pressure ratio, $\overline{PR}_{V_o}$
14	Φ_V	Nozzle scale coefficient based upon the engine-off vehicle base pressure. This parameter will be used indirectly to establish fullscale hot flow specific impulse for engine operation in a slipstream relative to the engine-off vehicle base pressure
15	Φ_{BV}	Nozzle scale coefficient based upon the engine-on vehicle base pressure. This parameter will be used primarily to correlate test data with the engine-on vehicle base pressure ratio

TABLE B-V

NOMENCLATURE FOR ADDITIONAL DATA REDUCTION (Continued)

ITEM	SYMBOL	DESCRIPTION
16	Φ_∞	Nozzle scale coefficient based upon the freestream static pressure. This parameter will be used for scaling and data analysis purposes
17	Φ_N	Nozzle scale coefficient based upon the engine-off vehicle base pressure including the influence of the engine on boattail thrust. Scaling by means of this parameter is less correct than by means of the parameters in Items 14-16, but it may provide the only acceptable information at an angle-of-attack since an elaborate pressure-area integration is not required.
18	C	Corrected vehicle forebody-minus-engine-on-boattail drag coefficient
19-22	C_V, C_{BV}, C_∞ , C_N	These are vehicle scale coefficients which when combined with appropriate nozzle scale coefficients, engine characteristics, and vehicle geometry provide net vehicle thrust uncorrected for model sting effects
23	$D\overline{PR}_{V_o}$	Ratio of $\overline{PR}_{B_o}$ (Items 11 and 12) to the nozzle design pressure ratio
24	DPR_{BV}	Ratio of PR_{BV} (Item 31 in the previous table) to the nozzle design pressure ratio
25	DPR_∞	Ratio of PR (Item 32 in the previous table) to the nozzle design pressure ratio
26	C_{F_e}	Intrinsic nozzle thrust coefficient (see Items 1 and 2)
27	$\left.\overline{P}_{B_e}/P_c\right)_2$	Effective nozzle base pressure with secondary flow

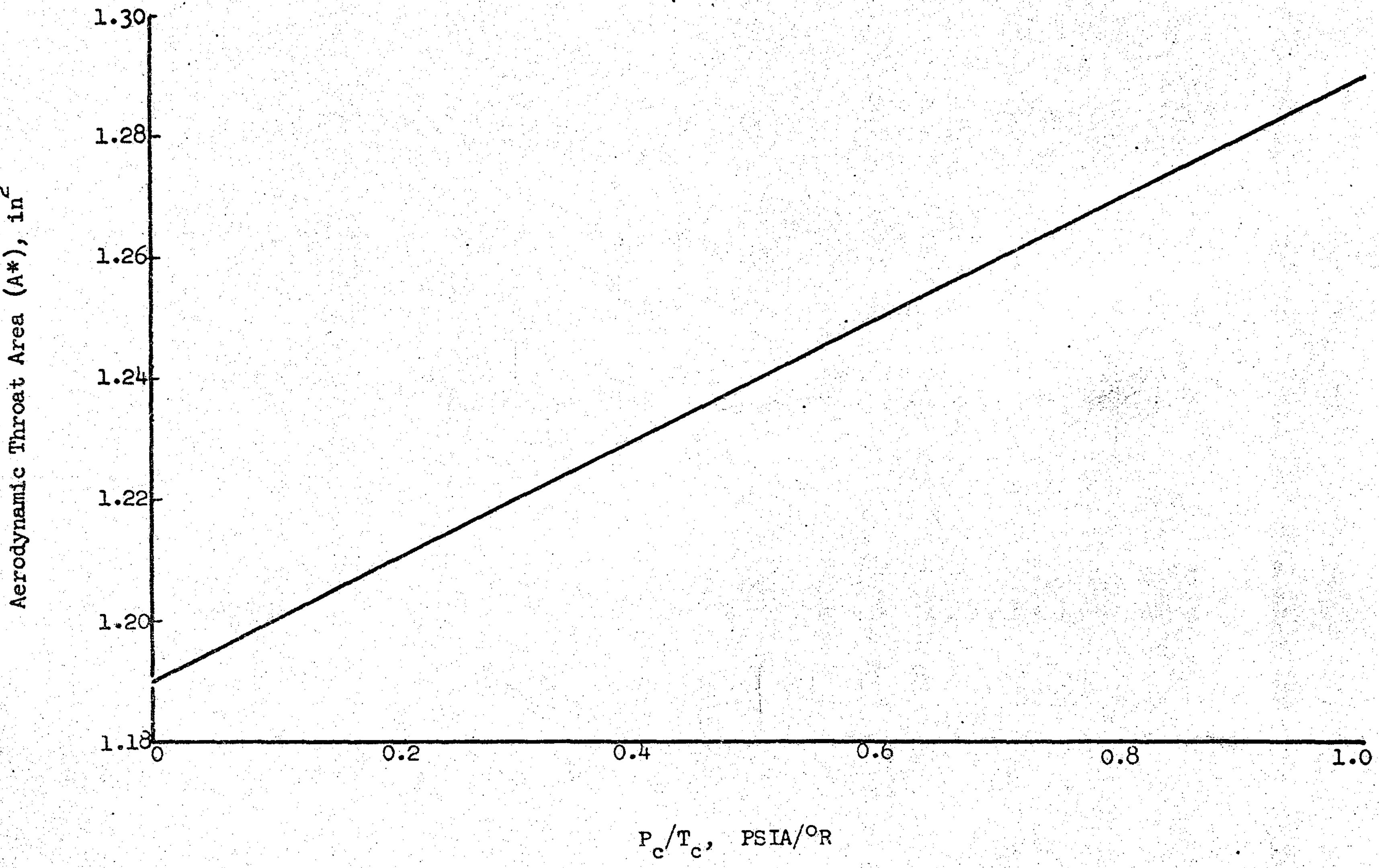

Fig.B-2. SERV Cold Flow Model Aerodynamic Throat Area as Function of Chamber Pressure and Temperature

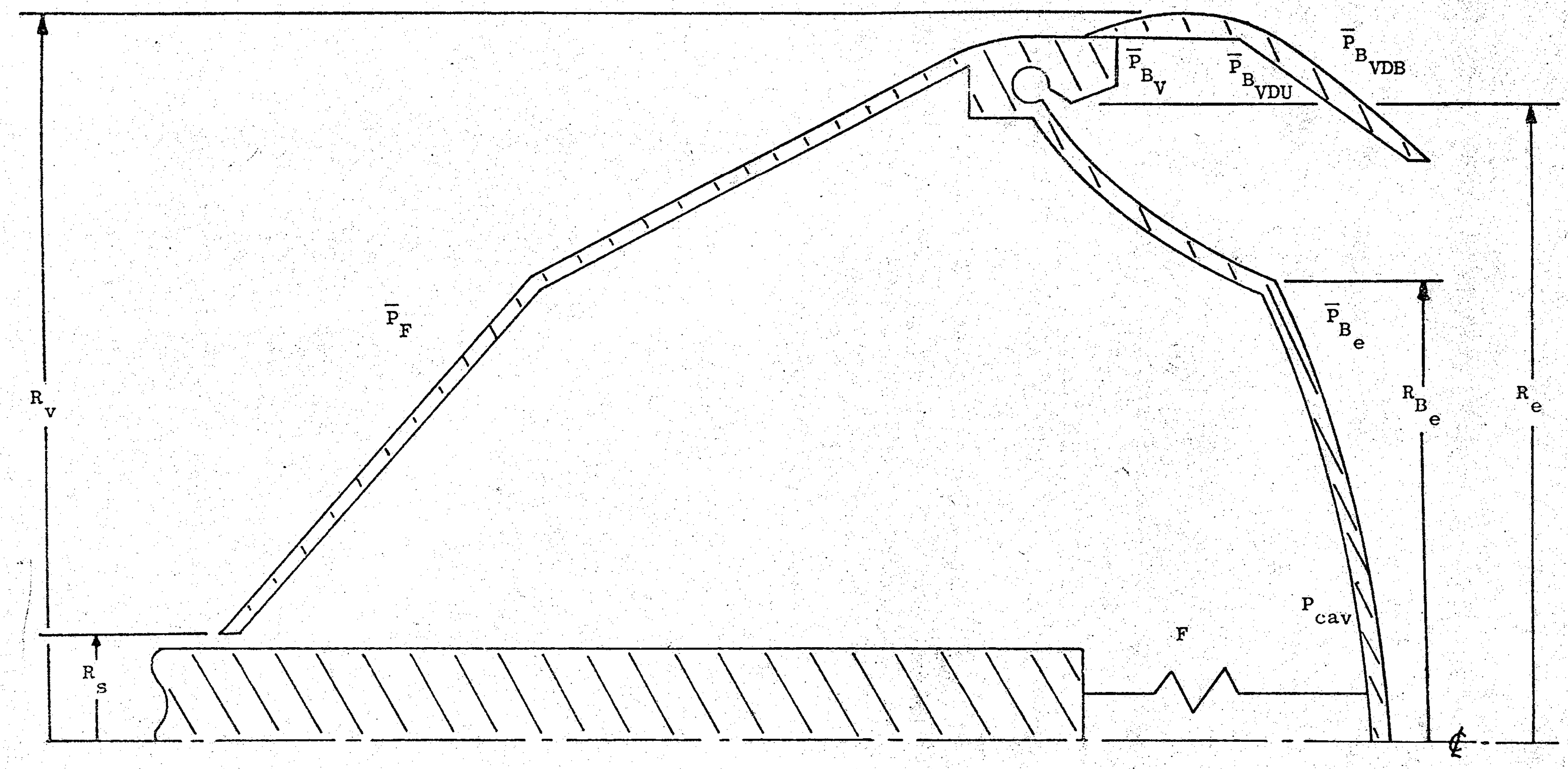

Figure B-3. Test Model Schematic

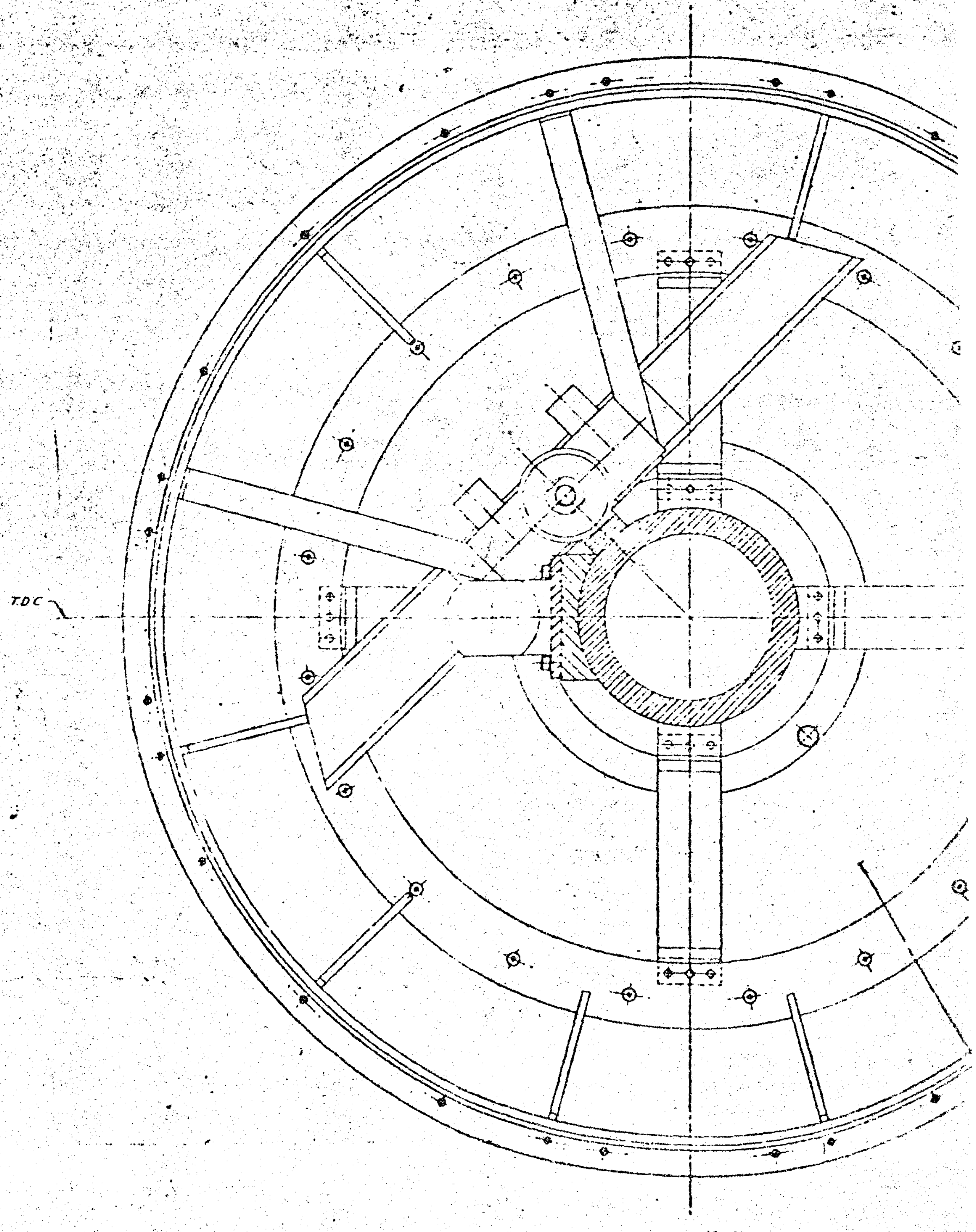

SECTION D-D

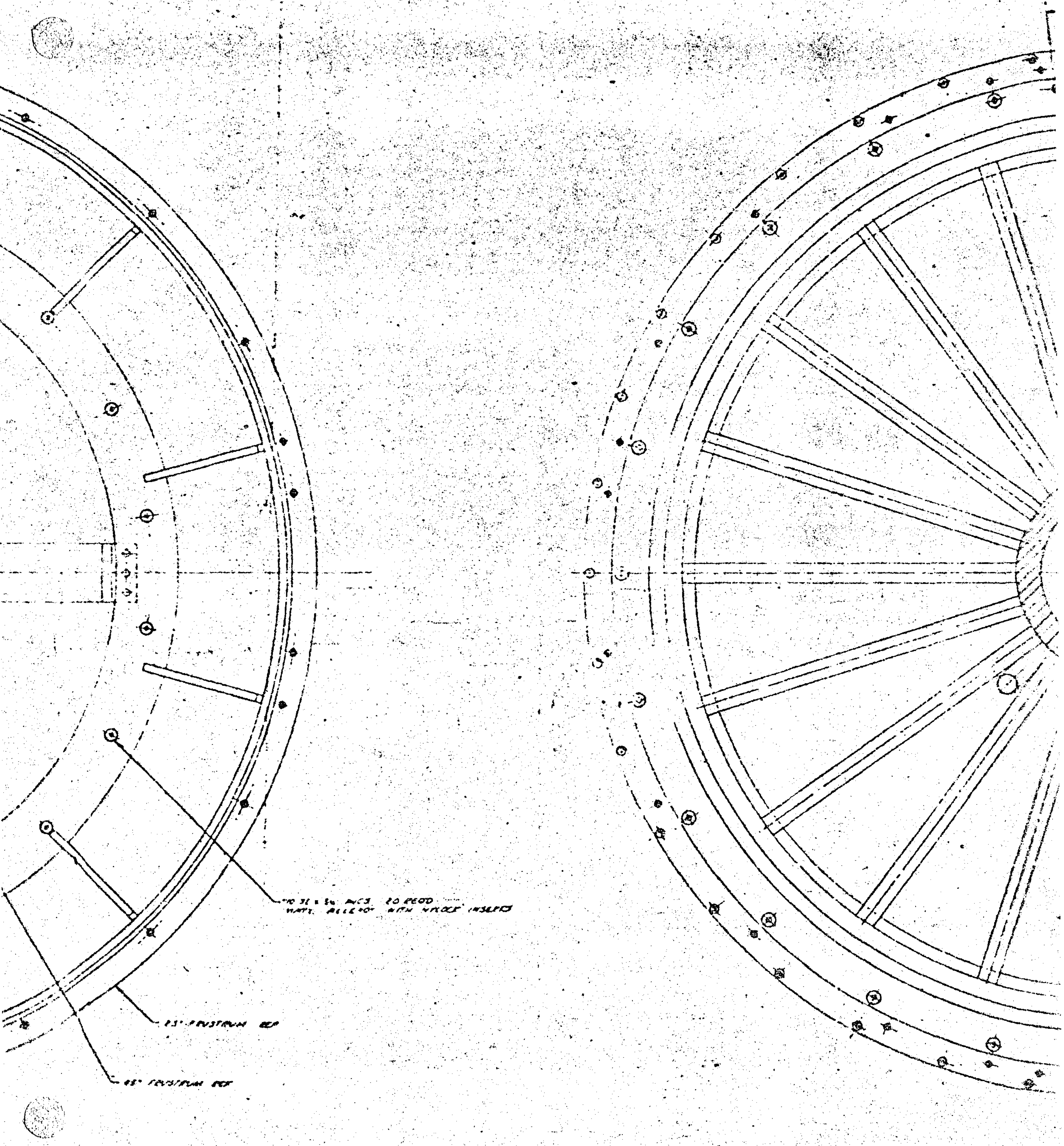
#10-32 x 3/4 HCS 20 REQD
MAT'L ALLOY WITH NYLOK INSERTS
23° FRUSTRUM REF
45° FRUSTRUM REF

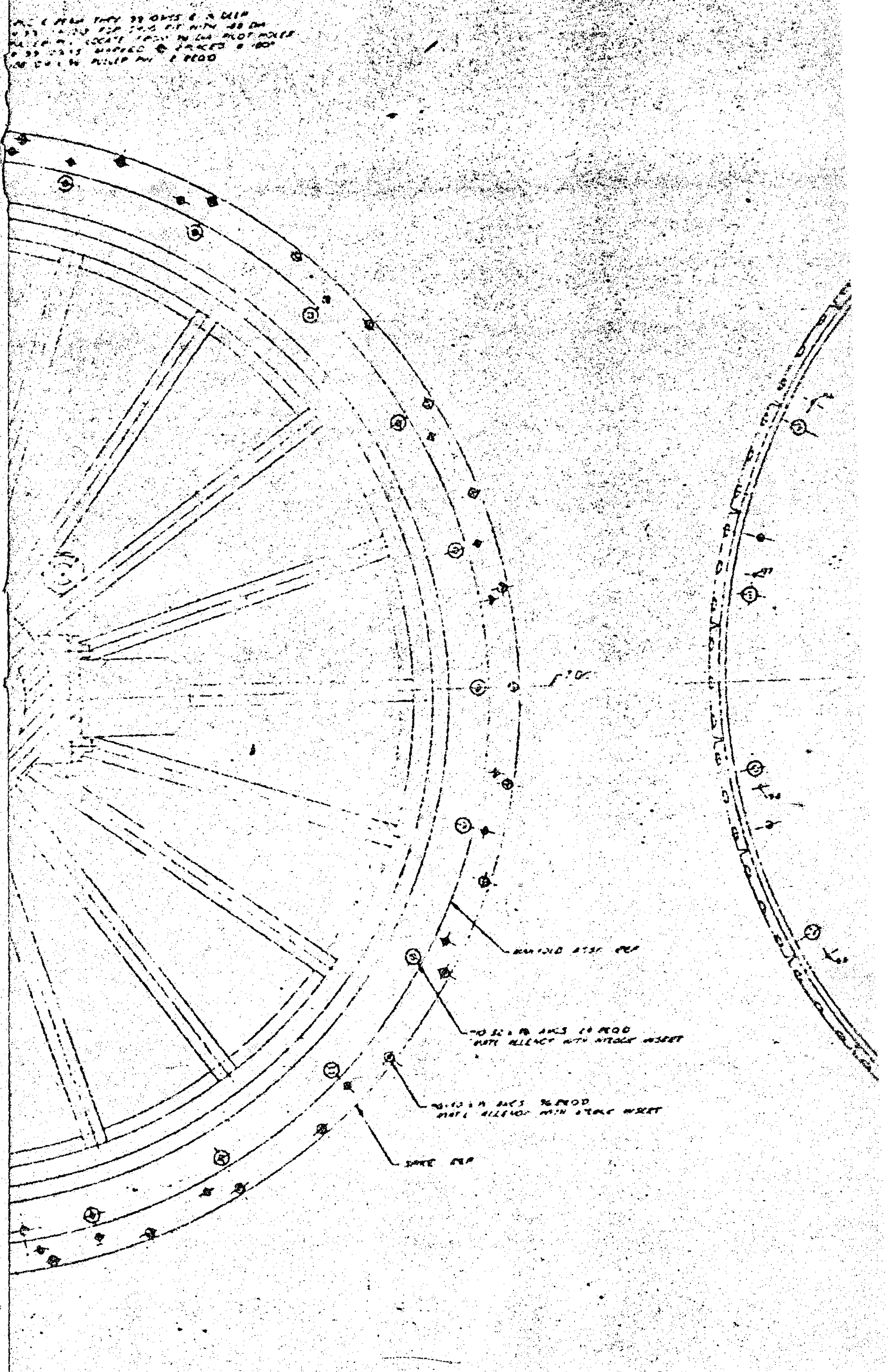

PROD
INSERT
PROD
INSERT
SPOKE REF

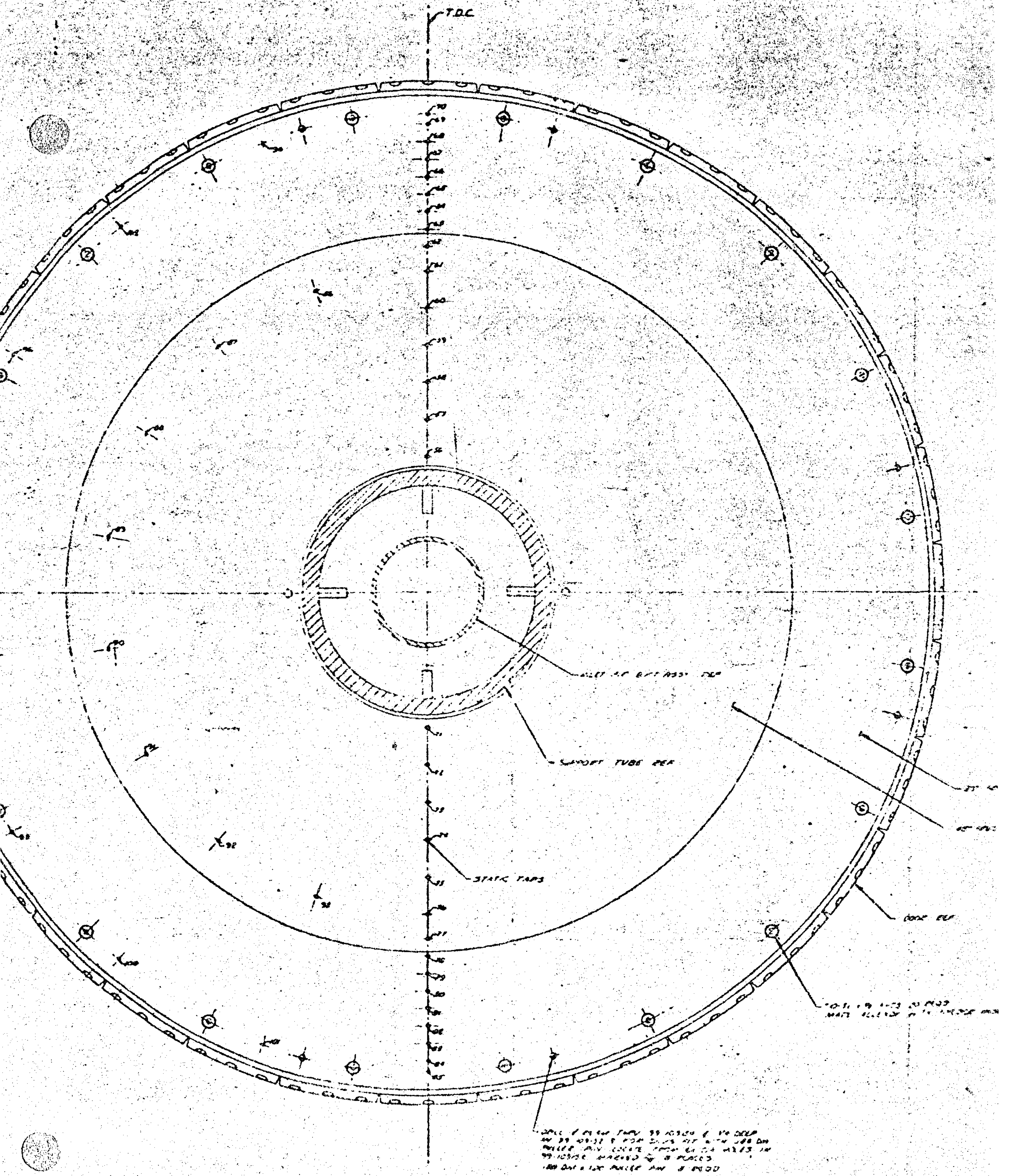
TDC
INLET AIR EXIT ASSY REF
SUPPORT TUBE REF
STATIC TAPS
CONE REF

SECTION B-B

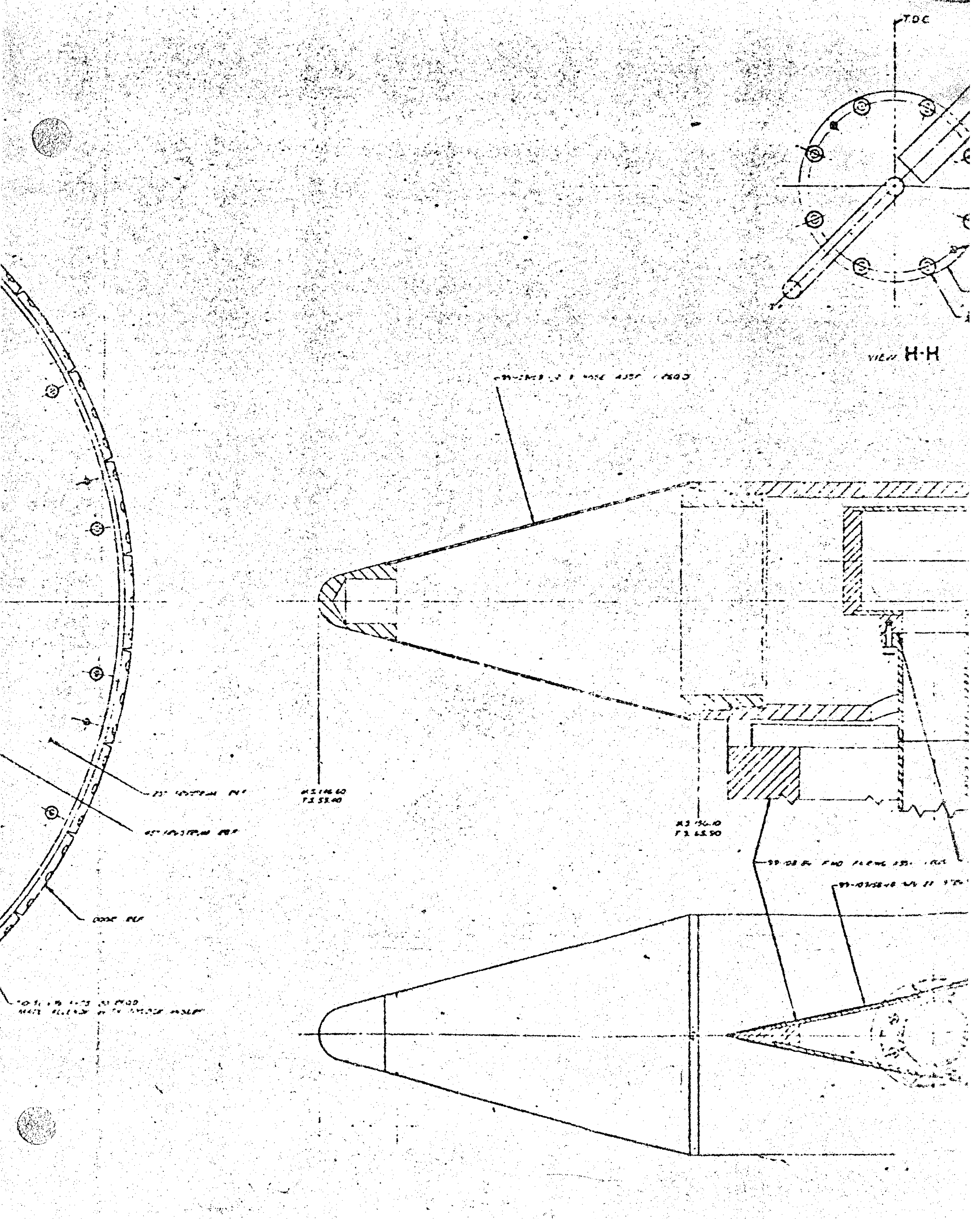
TDC
VIEW H-H
XS 146.60
ZS 53.40
XS 156.10
ZS 65.90
25° UPSTREAM REF
45° UPSTREAM REF
DOOR REF

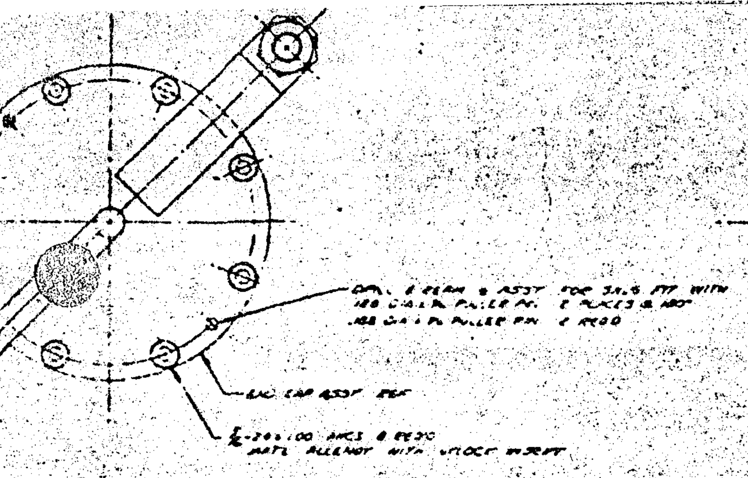

VIEW H-H

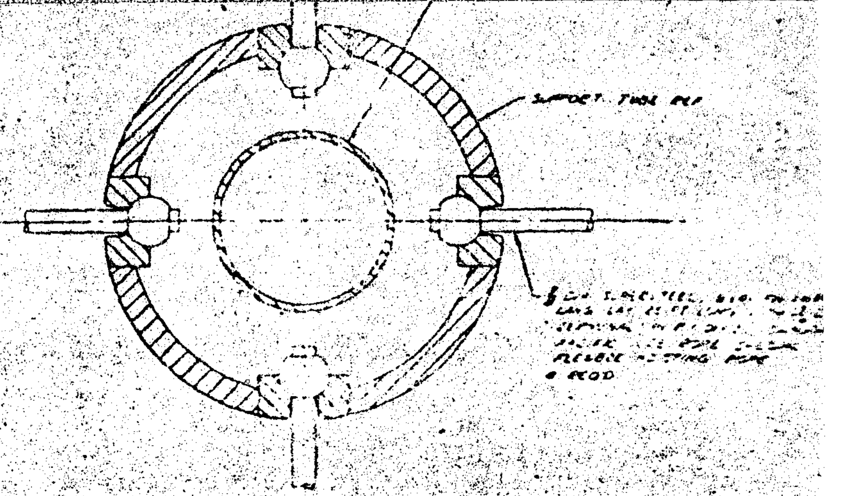

SECTION G G

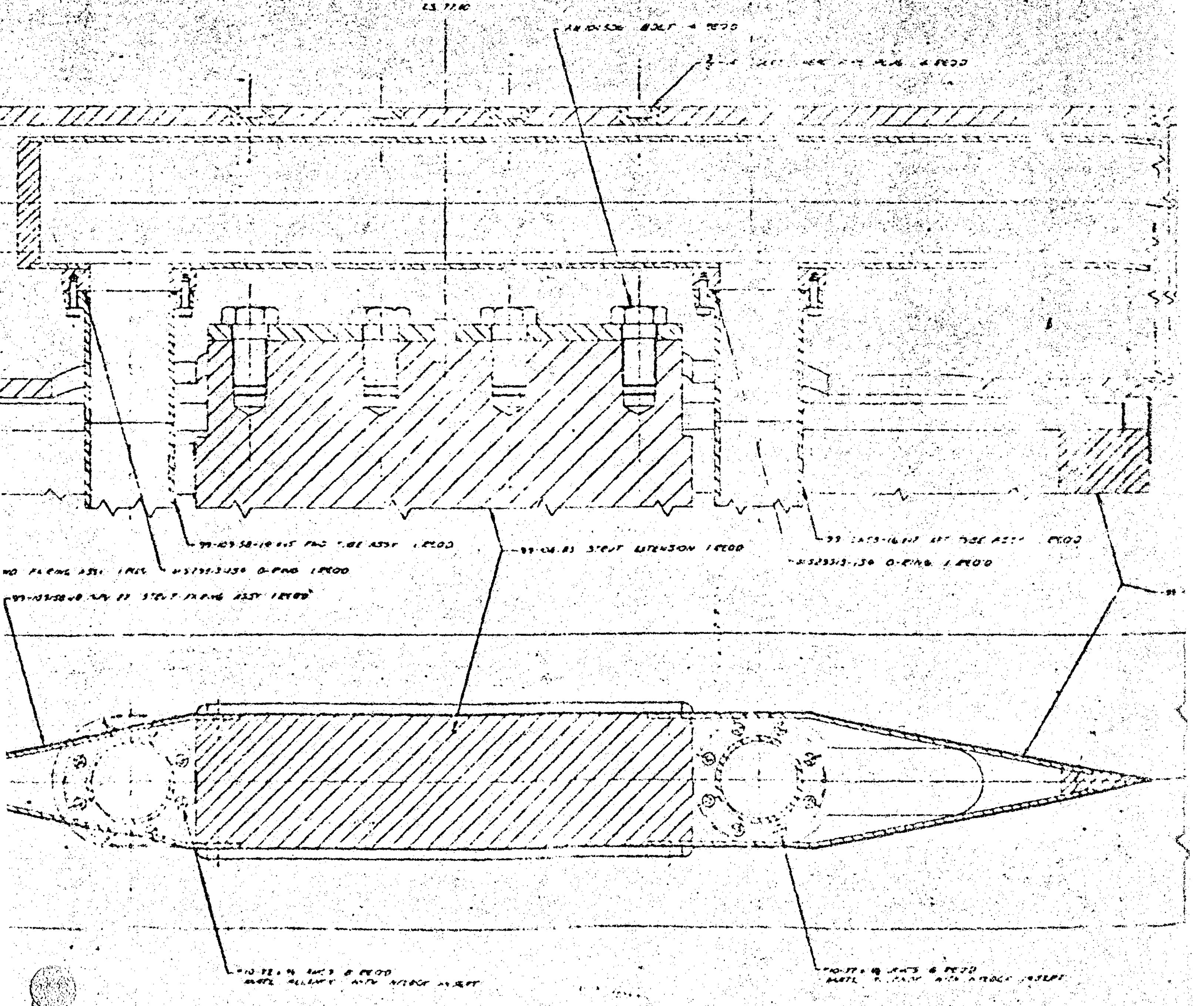

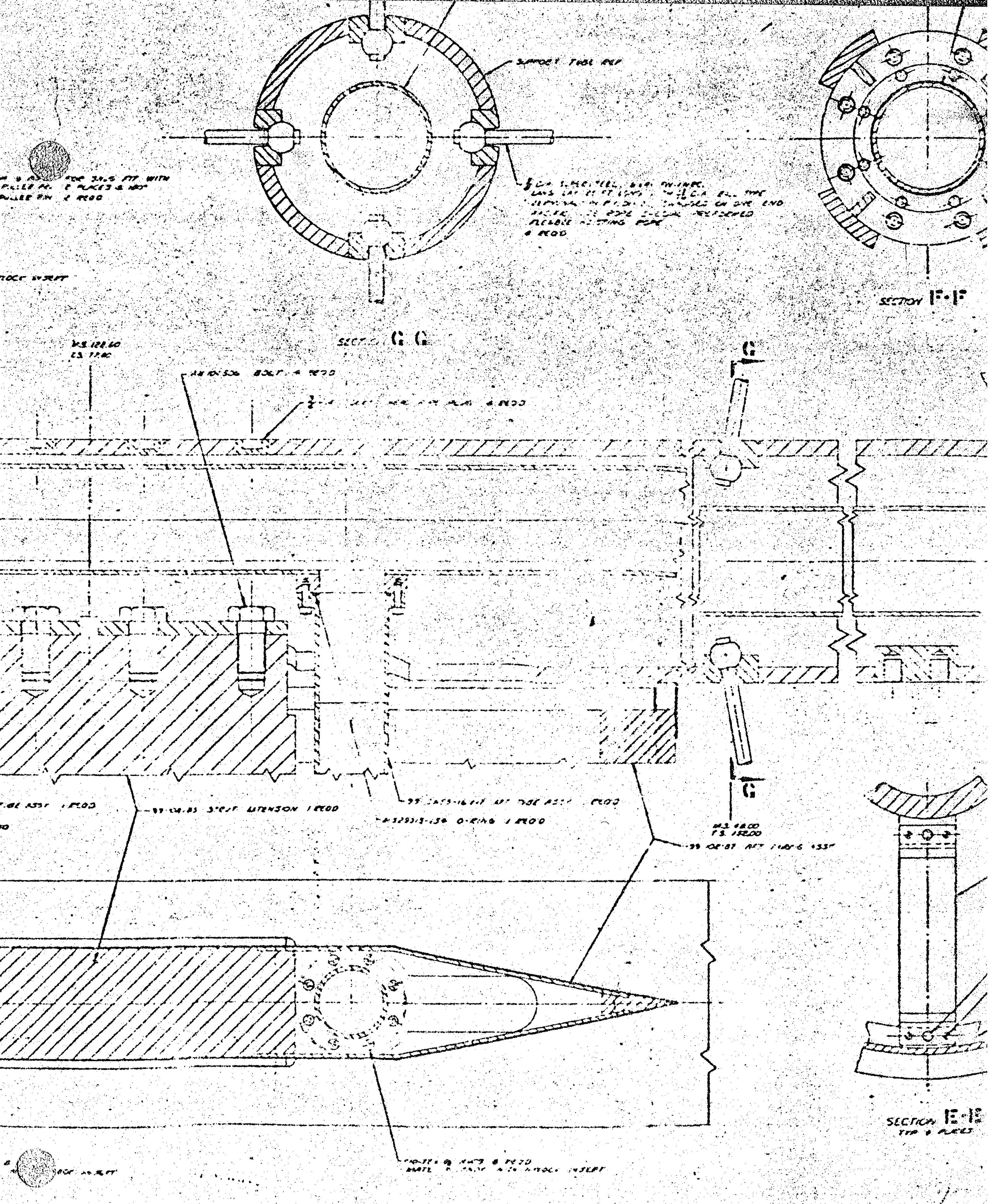
SUPPORT TUBE ASY
4 REQD
SECTION F-F
SECTION G G
G
G
W.S. 122.60
ES 77.60
AN 10-536 BOLT 4 REQD
4 REQD
STRUT EXTENSION 1 REQD
O-RING 1 REQD
W.S. 48.00
FS 152.00
1 REQD
INSERT
SECTION E-E
TYP 4 PLACES

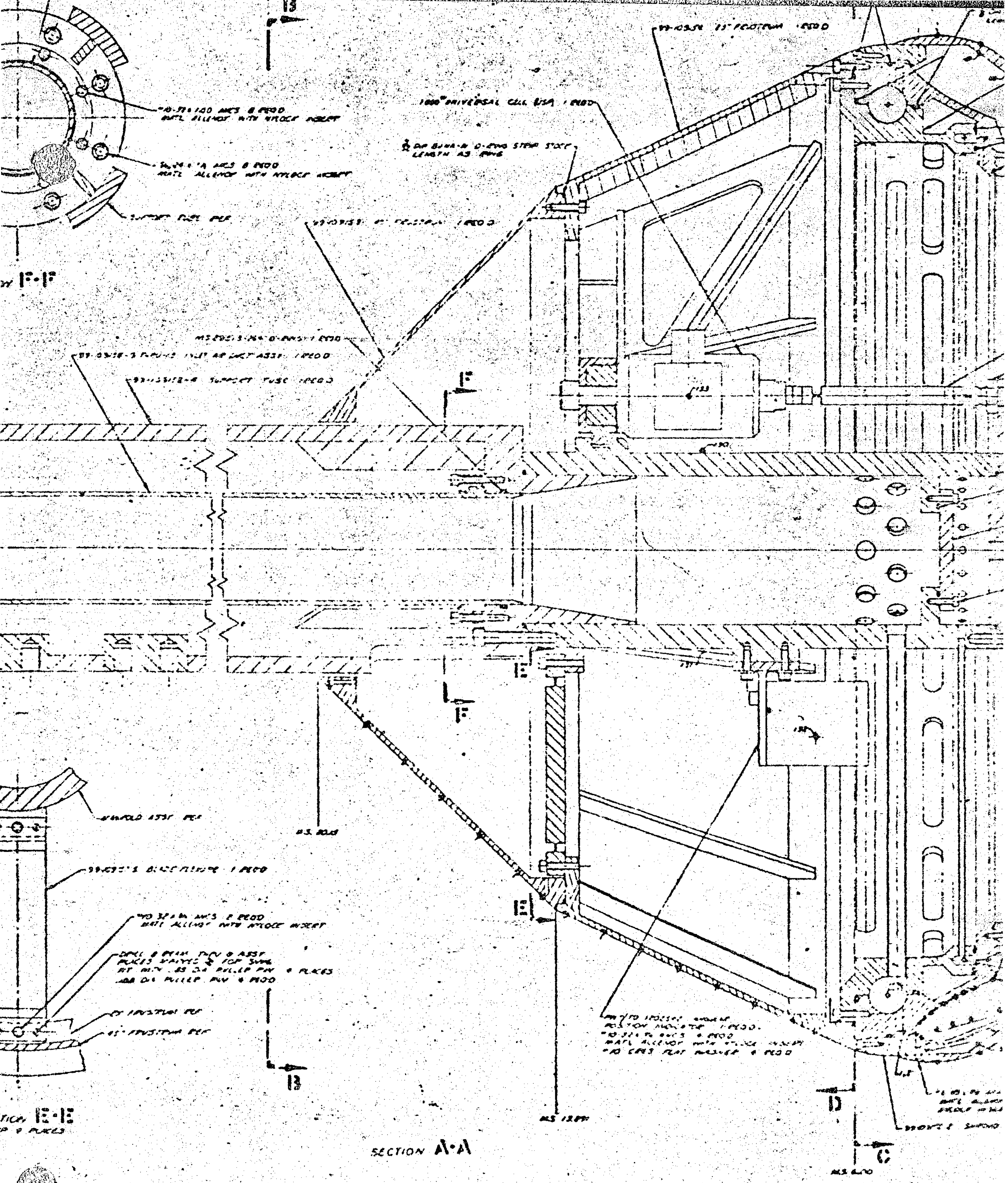
SECTION A-A
E-E
F-F
B
C
D
E
F
1000" UNIVERSAL CELL USA 1 REQD
23" FRUSTUM 1 REQD
O-RING STRIP STOCK LENGTH AS REQ
SUPPORT TUBE REF
SUPPORT TUBE 1 REQD
INLET AIR DUCT ASSY 1 REQD
MATL ALLOY WITH NYLOCK INSERT
MANIFOLD ASSY REF
8 PLACES
FRUSTUM REF
45° FRUSTUM REF
FLAT WASHER
SHROUD
MS 12.89
MS 6.70
MS 20.0

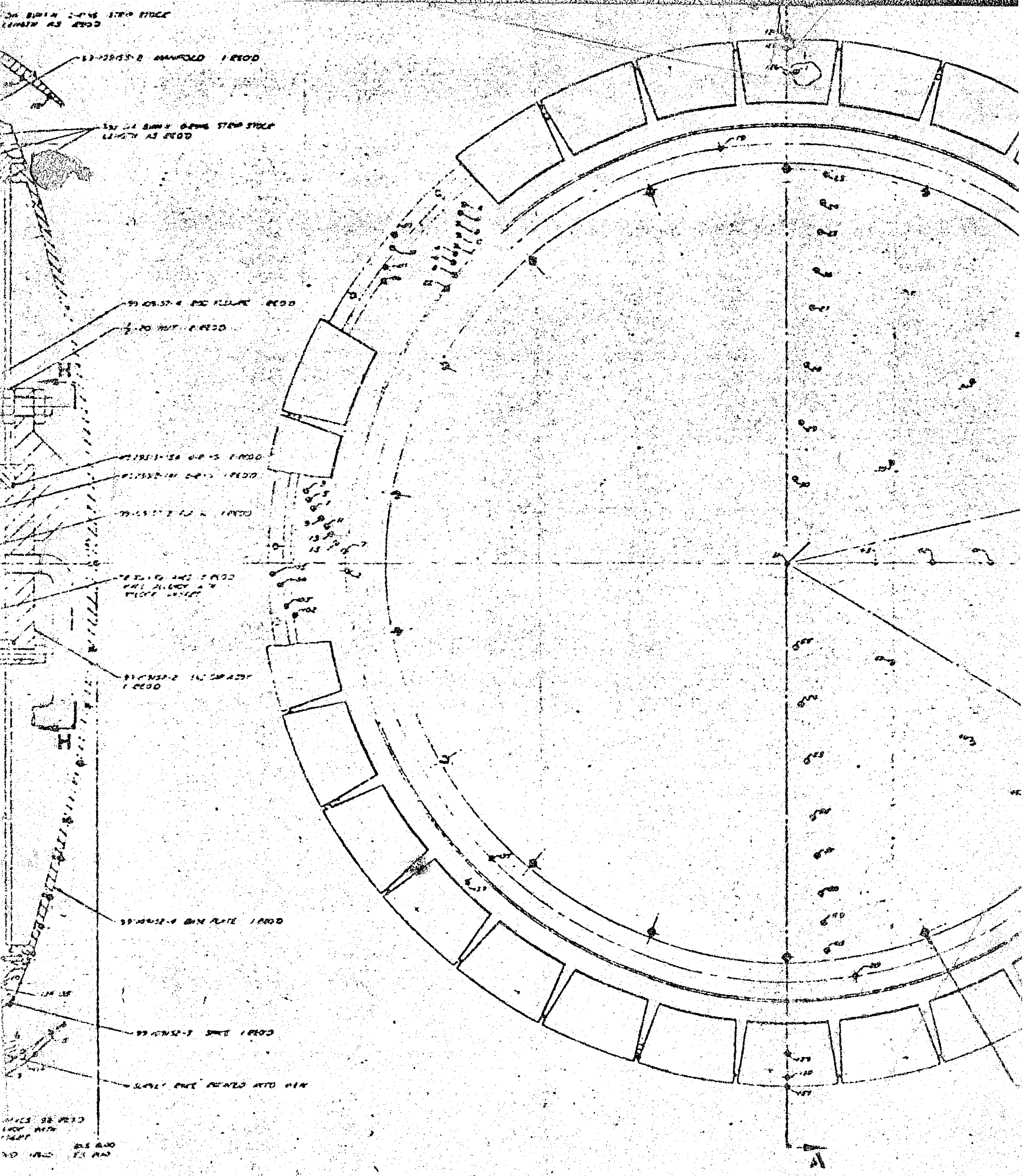
BRASS STRIP STOCK
LENGTH AS REQD
53-129153-8 MANIFOLD 1 REQD
3/32 X 1/4 BRASS O-RING STRIP STOCK
LENGTH AS REQD
99-105.57-4 RING FLANGE REQD
1/2-20 NUT REQD
1 REQD
1 REQD
1 REQD
REQD
1 REQD
BASE PLATE 1 REQD
SPACER 1 REQD
MADE INTO
H
H
A

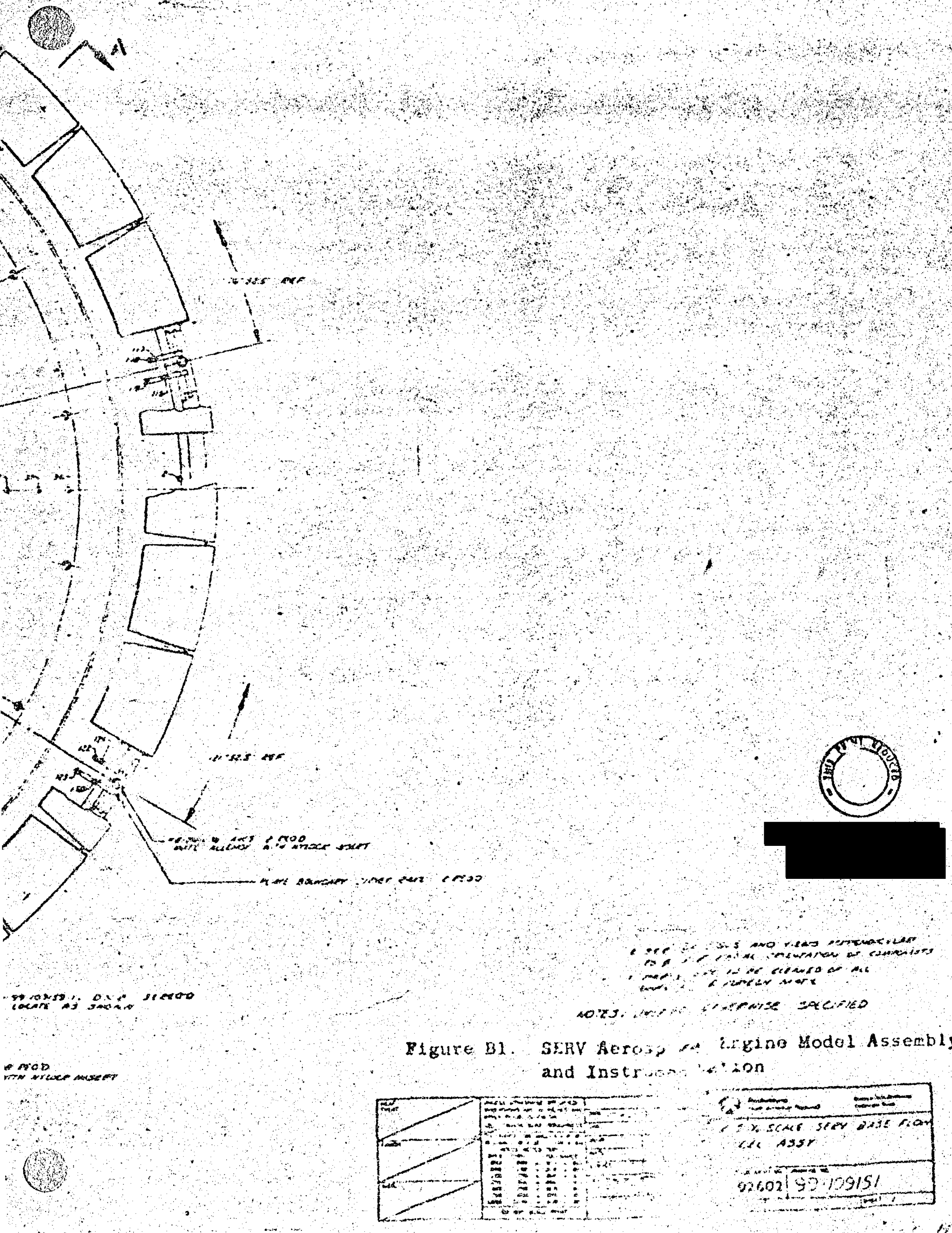

[redacted]

Figure B1. SERV Aerospike Engine Model Assembly and Instrumentation